eXPRESS Polymer Letters Vol.10, No.11 (2016) 873
Available online at www.expresspolymlett.com
DOI: 10.3144/expresspolymlett.2016.81

Editorial corner – a personal view
Cleaner, greener routes for polyurethanes

*B. K. Kim**

Distinguished Professor of Research College of Engineering, Pusan National University Busan 609-735, Korea

Polyurethanes (PUs) are multiblock copolymers containing repeated urethane groups which are formed from the stepwise addition reaction of polyol with isocyanate. Depending on the type and composition of raw materials, a most broad property spectrum from elastomer to rigid plastics is tailored, and most widely used as coating, adhesive, sealant, elastomer, and various types of foam with an annual production over 18 million tons 2015.

Since they are closely related to our daily life, particular attentions have been paid to reduce the environmental impacts and enhance sustainability. Earlier attempt was to replace petroleum based polyols by bio-based ones using vegetable oils which are 'broken', 'functionalized', and 'polymerized into polyols'. They are greenhouse gas neutral with virtually no odors from the end products giving much reduced volatile organic compounds (VOC) during manufacturing, and are more sustainable through the life cycle. However, generally poor properties of bio-based polyol PU are to be enhanced by proper techniques.

More harmful than polyols is isocyanates whose synthetic route involves phosgene which is highly toxic. So, an isocyanate-free route to synthesize PU has recently gained great interests. The route is based on an old reaction of dicyclocarbonates and diamines, where isocyanate group is not present at any step. Hydroxyl groups at the β-carbon atom of the urethane moiety increase adhesion. Rich intra- and intermolecular hydrogen bonds and the absence of unstable biuret and allophanate units augment thermal stability and chemical resistance to non-polar solvents.

Isocyanate-free PU based on multicyclic carbonates and polyamines is fabricated using toxic solvent at high temperature, which poses difficulties for industrial application. One promising way is that they can be used to modify epoxy matrix for coating application in industry. They are solvent-free, cured at low temperatures, based on renewable raw materials, and show resistance to weathering, abrasion, and solvents. The lack of commercially available multifunctional cyclic carbonates is a fundamental problem to be resolved.

A most significant way to reduce VOC was to replace organic solvent by water.

Waterborne PU was introduced in market in 1980s and steadily replaces solvent-borne type in many applications although the market is yet to expand. Certain inferior properties pertinent to ionomer nature should be resolved by molecular architecture and hybridization.

Much care was paid to foam production regarding blowing agent. Use of chlorine-containing ones was restricted by Montreal Protocol (1987) and Kyoto Protocol (1997). Carbon dioxide, pentane, HFC-134a and HFC-245fa steadily expand their usage to reduce ozone depletion potential and global warming potential. Global spread of non-emission and non-fugitive catalysts contributes to cleaner atmosphere. All the efforts are expected to continue for cleaner and greener environment.

Prof. Dr. Byung Kyu Kim
Member of International Advisory Board

*Corresponding author, e-mail: bkkim@pnu.edu

eXPRESS Polymer Letters Vol.10, No.11 (2016) 874–882
Available online at www.expresspolymlett.com
DOI: 10.3144/expresspolymlett.2016.82

Using maleic anhydride functionalized graphene oxide for improving the interfacial properties of carbon fiber/BMI composites

W. Li, Y. Z. Yue, M. Y. Wang, Q. Li, R. Ren*

Faculty of Aerospace Engineering, Shenyang Aerospace University, Liaoning Key Laboratory of High Performance Polymer Matrix Composites, 110136 Shenyang, China

Received 11 April 2016; accepted in revised form 16 June 2016

Abstract. Maleic anhydride functionalized graphene oxide (MAH-GO) was synthesized and then introduced into carbon fiber (CF) reinforced bismaleimide (BMI) composites, with the aim of improving the interfacial adhesion strength between CF and BMI resin. Various characterization techniques including Fourier transform infrared spectroscopy (FT-IR), X-ray photoelectron spectra (XPS) and thermogravimetric analysis (TGA) demonstrated that the maleic anhydride has been successfully grafted onto the GO surfaces. The study showed that the interlaminar shear strength (ILSS) and flexural properties of CF/BMI composites were all improved by the incorporation of GO and MAH-GO, and the MAH-GO showed the substantially improved effect due to the strong interaction between the MAH-GO and the resin matrix. The maximum increment of the ILSS, flexural strength and flexural modulus of composites were 24.4, 28.7 and 49.7%, respectively. Scanning electron microscope (SEM) photographs of the fracture surfaces revealed that the interfacial bonding between CF and resin matrix was significantly strengthened by the addition of MAH-GO. The results suggest that this feasible method may be an ideal substitute for the traditional method in the interfacial modification of composites.

Keywords: *polymer composites, interfacial bonding, graphene, covalent functionalization, bismaleimide*

1. Introduction

Carbon fiber (CF) reinforced polymer composites have been widely used in aerospace, automobiles, constructions and other industry fields because of their excellent mechanical properties, such as high specific strength, specific modulus and damping capacity [1–3]. As well known, the mechanical properties of fiber reinforced composites are largely dominated by the fiber-matrix interfacial adhesion. Good interfacial bonding is essential to ensure the load transfer from the matrix to the fiber reinforcements, which is helpful to reduce the stress concentrations and improve the overall mechanical properties of final composite products. However, the fiber-matrix interfacial adhesion tends to be weak since the CFs surfaces are smooth, non-polar and chemical inert [4, 5]. In order to improve the interfacial bonding properties, a series of effective methods have been successfully developed for surface modification of CFs, such as chemical oxidation, high-energy radiation, grafting, and plasma treatment, etc. [5–8].

Recently, the utility of graphene oxide (GO) or functionalized GO as additives to enhance the interfacial properties of CF reinforced polymer composites has begun to attract more attention [2, 9]. Because the functionalized GO has various functional groups and large specific surface area, it can be uniformly dispersed and firmly adsorbed on the surface of CFs to prepare a new hierarchical reinforcement. Therefore, the interfacial adhesion of composites can be im-

*Corresponding author, e-mail: liwei@sau.edu.cn

proved by this new hierarchical reinforcement due to consuming much more energy by pulling out the functionalized GO from the matrix or breakage of them. On the other hand, the introduction of the functionalized GO can increase the modulus of polymer matrix significantly [10–12], that is to say, it can reduce the modulus difference between matrix and fiber, which is also beneficial for the applied load transferring more effectively from matrix to CFs.

CF reinforced bismaleimide (BMI) composites have been widely used as one of advanced composites owing to their superior mechanical and thermal properties [13, 14]. Nevertheless, the properties need to be further improved when they are used in some specific environments. Nowadays, GO or functionalized GO have been used for modifying the BMI resin by some researchers. For example, Yan and coworkers [15, 16] grafted hyperbranched polysilane (HBPSi) and hyperbranched polytriazine (HBPT) onto the reduced GO surfaces, respectively. The results revealed that the introduction of HBPSi (or HBPT) functionalized reduced GO could decrease the frictional coefficient and the wear rate of the BMI resin dramatically. Liu *et al,* [13] reported a 39% increase in impact strength by adding 0.3 wt% aniline functionalized graphene nanosheets in BMI resin. Our previous work [17] also found that the suitable addition of silane functionalized GO (MPTS-GO) could significantly improve the mechanical properties of the BMI composites. Although substantial research has pointed out that the addition of graphene into polymer matrix can result in the considerable improvements of new or modified properties, there are few reports to study the effect of graphene on enhancing the properties of CF/BMI composites, especially the interfacial adhesion.

Herein, we report the fabrication of a novel covalent functionalized GO by using maleic anhydride. Then the maleic anhydride functionalized GO (MAH-GO) was introduced into the CF/BMI composite system to improve the mechanical properties. Because the carbon-carbon bond of maleic anhydride is high reactive activity, the MAH-GO is easy to participate in the curing reaction of BMI resin, and thus improving its dispersibility and strengthening the interaction with the resin. The aim of the current investigation is to determine the role of MAH-GO on the interfacial adhesion of CF/BMI composites.

2. Experimental section

2.1. Materials

The BMI resin used was the 4,4′-bismaleimide diphenyl methane (BDM) modified with the O,O′-diallyl bisphenol A (DBA). BDM and DBA were both supplied by Honghu New Materials Technical Co. LTD., China. Unidirectional carbon fiber (T700SC-12k, diameter: 7 μm) was purchased from Toray Industries, Inc., Japan. Pristine graphite powder was obtained from Qingdao Jinrilai Graphite Co., Ltd., China. Maleic anhydride (MAH), ethanol, acetone, and dimethylformamide (DMF) were of analytical grade and obtained from Sinopram Chemical Reagent Co., Ltd., China.

2.2. Fabrication of GO and MAH functionalized GO (MAH-GO)

GO was prepared by oxidizing natural graphite powder based on a modified Hummers method [17, 18]. To functionalize GO, 0.5 g GO was placed in a 250 mL dried beaker with 100 mL DMF and sonicated for 1 h to form a homogeneous solution. 15 g MAH was then added into the mixture solution and transferred into a three-necked flask with refluxing at 80 °C for 1 h. After the reaction finished, the product was washed with ethanol several times to remove all the unreacted MAH. The solid was finally dried under vacuum to obtain the MAH-GO. The preparation process of MAH-GO is shown in Figure 1.

2.3. Fabrication of CF reinforced BMI composites

According to the different weight ratios, the MAH-GO was firstly added into 100 mL ethanol and sonicated for 1 h to promote its dispersion. 51 g DBA was then added into the ethanol solutions and sonicated for another 1 h. In order to remove all the ethanol, the mixture container was transferred into an oil bath and distilled according to the scheduled process: 80 °C for 1 h, 100 °C for 2 h, 120 °C for 1 h, and 140 °C for 6 h. Then, 68 g BDM was added to the mixture, and this was followed by prepolymerization for 30 min at 140 °C. The molar ratio of DBA to BDM was 0.87:1. 150 mL acetone was added into the resultant prepolymer under refluxing for 1 h to obtain a homogenous thin resin solution. The unidirectional CF was impregnated by passing through this resin solution. Two glass bars were used to scrape off excess

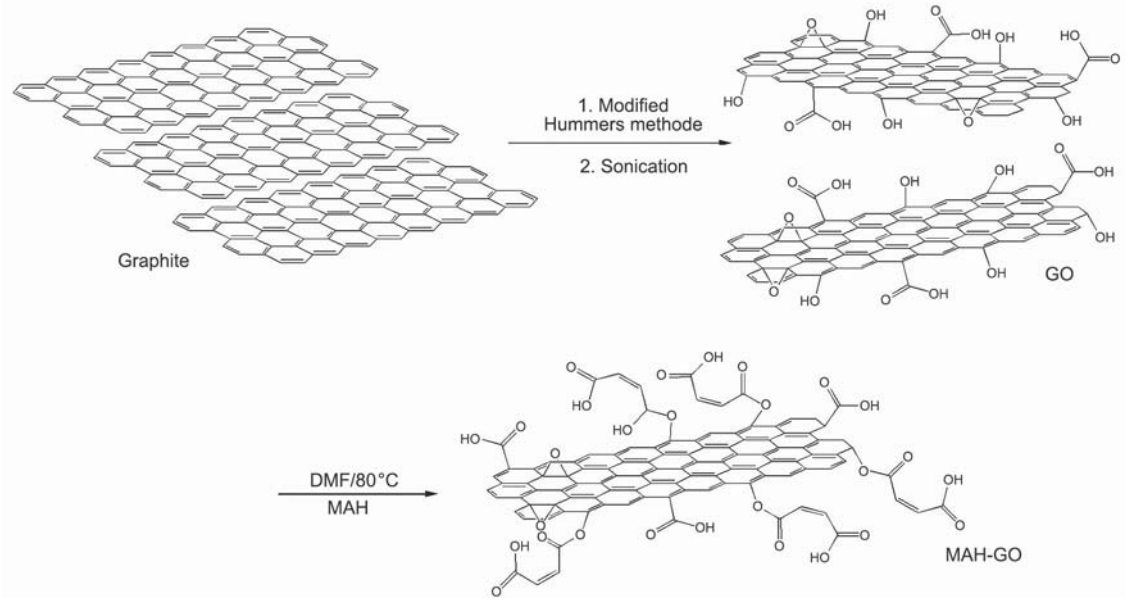

Figure 1. Schematic of preparation process of MAH-GO

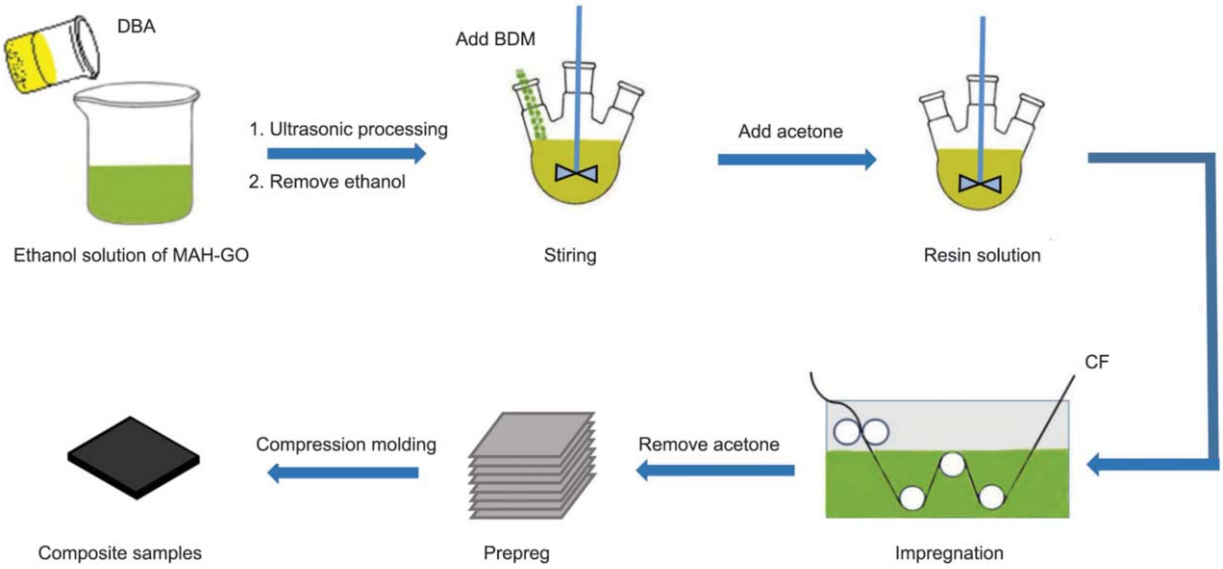

Figure 2. Fabrication process of CF/MAH-GO/BMI composites

resin solution from the CF carefully, and then the solvent was removed in a vacuum oven at 80 °C to obtain the prepregs. The composites were prepared by using compression molding method. The preparation procedure of CF composites is represented in Figure 2. The referential CF/GO/BMI composites were also prepared in the same procedure.

2.4. Characterization

Transmission electron microscopy (TEM) micrographs were used to observe the morphologies of GO and MAH-GO sheets by using a TEM instrument (TecnaiG220, FEI, USA). The sheets were firstly dispersed in de-ionized water by sonication for 30 min and then some pieces were collected on carbon-coated copper grids for TEM observation.

Fourier transform infrared (FT-IR) spectra were recorded on a spectrometer (Spectrum 100, Perkin Elmer, USA) using KBr pellets at room temperature. The frequency range of FT-IR was 4000–400 cm^{-1}.

X-ray photoelectron spectroscopy (XPS) measurements were used to determine the surface groups of GO and MAH-GO by using an XPS instrument (ESCALAB 250, Thermo, USA). The nonlinear least squares fitting (NLLSF) program with a Gaussian-Lorentzian production function was used for curve

fitting of C1s spectra. The surface chemical composition was calculated from the areas of relevant spectra peaks.

Thermogravimetric analysis (TGA) were measured under a nitrogen atmosphere from 60 to 700 ° with a thermal analyzer (TGA-7, Perkin Elmer, USA) at a heating rate of 10 °C·min^{-1}.

Scanning electron microscopy (SEM) observations were conducted with a scanning electron microscope (∑IGMA, Carl Zeiss, Germany). Each sample was coated with gold prior to SEM observation.

The interlaminar shear strength (ILSS) of CF composites was carried out by the short beam three point bending test on a universal testing machine (WOW 1000, Jinan Shidai Shijin Testing machine Group Co., Ltd., China) according to the ASTM D2344. The cross-head speed was 2 mm·min^{-1}. The width of test specimen was 6 mm and the thickness was 2.4 mm. A span-to-depth ratio of 5:1 was used.

The flexural properties of composites specimens were carried out using three-point bending mode on the above mentioned WOW1000 testing machine according to ASTM D-790. The crosshead rate was 2 mm·min^{-1}. The length between supports span was 16 times the depth of test specimen. At least seven samples were tested in each experiment and the average value was reported.

3. Results and discussion

3.1. Characterization of GO and MAH-GO

TEM micrographs of the GO and MAH-GO sheets are given in Figure 3. The GO and MAH-GO sheets show almost similar structures with a few thin ripples in their surfaces. FT-IR, XPS and TGA analysis were used to testify the surface functionalization of GO. Figure 4 illustrates a comparison of FT-IR spectra of GO and MAH-GO. In the case of GO, the peak located at 1716, 1637, 1375, 1227 and 1048 cm^{-1} are assigned to the stretching vibrations of C=O of carboxylic and carbonyl groups, C=C, –OH of the carboxyl group, C–O of the epoxy group and C–OH group, respectively. Similar patterns were observed in other studies [10, 19]. These observations indicate that the GO contains abundant oxygen-containing functional groups. After surface covalent functionalization, the bands at 1716, 1637 and 1375 cm^{-1} became stronger. Meanwhile, the new band appeared at 860 cm^{-1}, correspond to the in-plane bending vibration of C–H of CH=CH group. Another two new bands at 1100 and 1172 cm^{-1} are assigned to the stretching vibration of C–O of the ester group. The appearance of ester group clearly implies that the MAH molecules were reacted with the electrophilic groups of the GO surfaces, which provided more evidence for this successful chemical functionalization.

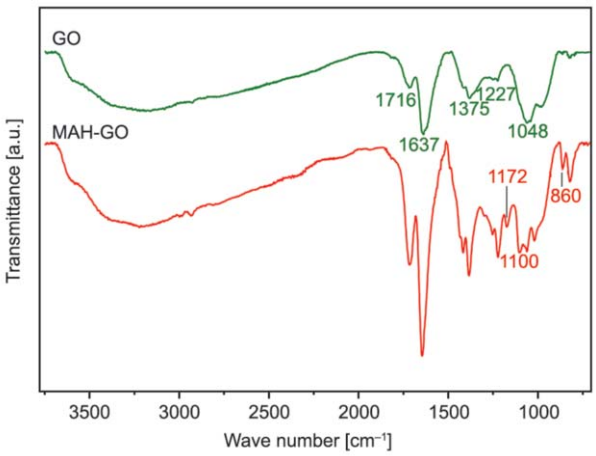

Figure 4. FT-IR spectra of GO and MAH-GO

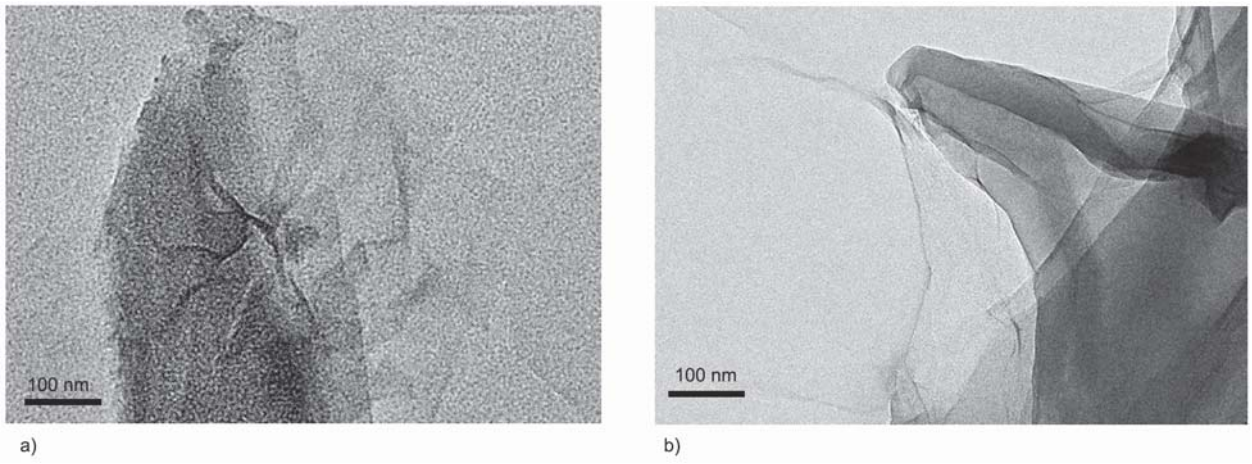

Figure 3. TEM images of (a) GO and (b) MAH-GO

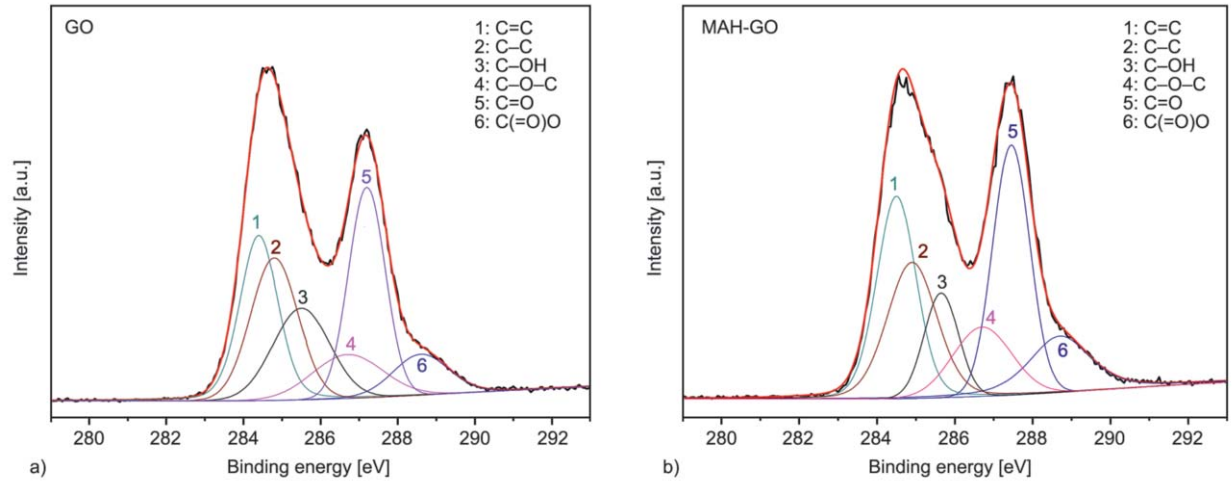

Figure 5. C1s XPS spectra of (a) GO and (b) MAH-GO

Table 1. The chemical compositions of GO and MAH-GO

Samples	O/C	Contents of chemical groups [%]					
		C=C	C–C	C–OH	C–O–C	C=O	C(=O)O
GO	0.378	21.14	20.68	15.98	12.44	20.13	9.63
MAH-GO	0.397	23.10	19.70	9.79	11.03	25.24	11.14

XPS is a useful tool in determining the chemical compositions of graphene surfaces. Figure 5 shows the XPS C1s spectra of GO and MAH-GO. It is shown that both of the C1s spectra contain six peaks, which are assigned to C=C (284.4 eV), C–C (284.8 eV), C–OH (285.6 eV), C–O–C (286.7 eV), C=O (287.3 eV) and C(=O)O (288.6 eV) group, respectively. However, as shown in Table 1, the O/C ratio of GO increased slightly from 0.378 to 0.397 after interacting with MAH, which may be caused by the higher oxygen atom concentration in the MAH molecules. Moreover, it is noted that the concentration of C–OH group decreased from 15.98 to 9.79%, and the concentrations of C=O and C(=O)O groups increased from 20.13 to 25.24% and 9.63 to 11.14%, respectively. The change of these functional group concentrations are caused by the grafting of MAH molecules onto the GO surface. Meanwhile, it may be concluded that the C–OH groups acted as electrophilic groups and reacted with the MAH molecules (see the Figure 1) in the light of the significant decrease of its content.

Figure 6 presents the TGA and DTG curves of graphite, GO and MAH-GO. As can be seen, the pristine graphite is thermally stable. After oxidation, the GO show significant decomposition at approximately 230 °C, which is likely due to the decomposition of labile oxygen-containing functional groups [9, 10, 20], yielding CO, CO_2 and H_2O. From the DTG curve of MAH-GO, it is clearly shown that there are two weight loss peaks appeared at 176 and 256 °C, re-

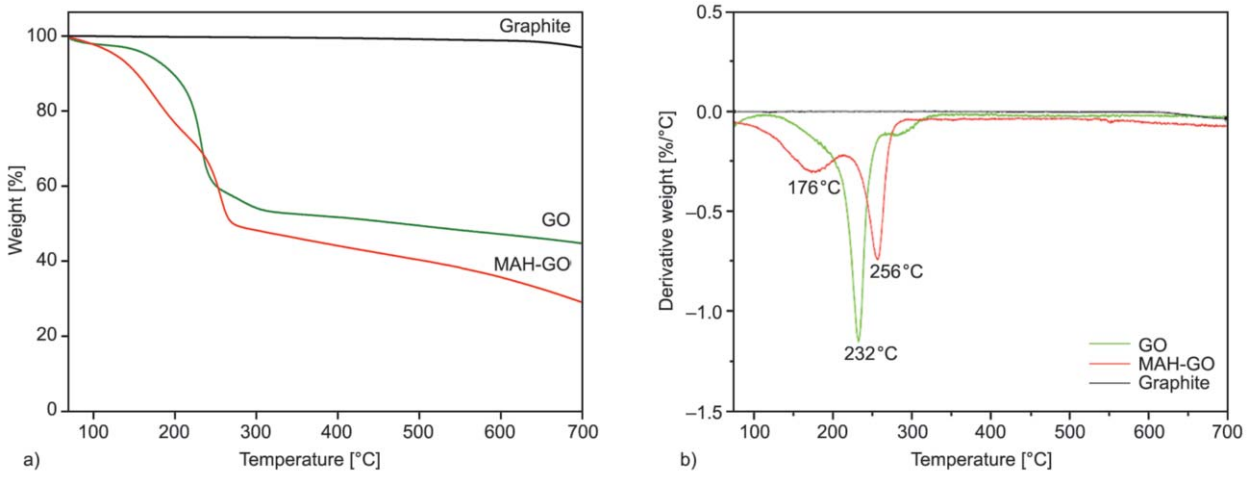

Figure 6. (a) TGA and (b) DTG curves of graphite, GO and MAH-GO

spectively. This result may be caused by the difference of thermal stability between the grafted MAH molecules and the original labile groups. However, the MAH-GO does not exhibit excessive highly thermal stability, which is explained by the fact that the grafted MAH are also small molecules. By comparison, the weight loss of MAH-GO observed up to 700 °C (about 71.1%) is higher than that of GO (about 55.3%), which further alludes to the successful grafting of MAH molecules onto the GO surfaces. The result is consistent with that derived from FT-IR and XPS analysis.

In this study, the aim of covalent functionalization of GO by using MAH is to react the MAH-GO with the BMI resin so as to improve the dispersibility of functionalized GO in the resin matrix. According to the literatures [21, 22], the ene reaction and Diels-Alder reaction have been proposed to be involved in the curing process of BDM and DBA. In view of the high activity of carbon-carbon double bond of grafted MAH, it may be concluded that the MAH-GO could participate in the curing reaction of BMI resin. In order to testify whether the reaction between them occurred or not, the maleic acid was used to react with DBA based on the molecular structure of grafted MAH. Figure 7 shows the FT-IR spectra of maleic acid and DBA before and after reaction.

In the spectrum of maleic acid, the peaks located at 863, 1587 and 1705 cm^{-1} are assigned to the in-plane bending vibration of C–H of CH=CH group, the stretching vibrations of C=C and C=O, respectively. After react with DBA, the peaks at 1587 and 863 cm^{-1} are disappeared. This phenomenon indicated that the carbon-carbon double bond of maleic acid reacted with the DBA molecules. Therefore, the conjugation effect between the C=O and C=C was not existed. As a result, the characteristic band of the C=O stretching mode of MA split into two peaks (1718 and 1778 cm^{-1}). These results confirmed that the MAH-GO could take part in the curing reaction of BMI resin.

3.2. Effect of MAH-GO on the interfacial property of CF/BMI composites

The ILSS test is an effective method for evaluating the interfacial adhesion property of fiber composites. The effects of GO and MAH-GO on the ILSS of CF/BMI composites are shown in Figure 8. It is shown that the ILSS of CF/BMI composites increased firstly and then decreased with the increase of filler loading. At 0.1 wt% loading of GO, the ILSS of composites reached the maximum value of 88.5 MPa, corresponding to a slight increase of 5.3% compared to the CF/BMI composite. It is exciting that the maximum improvement of ILSS obtained in the composites containing MAH-GO is far higher than the GO counterparts, which is 24.4% at 0.15 wt% loading. The corresponding ILSS value is 104.6 MPa. The result indicted that the interfacial bonding between the carbon fibers and BMI resin was enhanced by the introduction of GO and MAH-GO, and the MAH-GO showed a substantially improved effect.

Although the further increase in the MAH-GO content lead to the decrease of ILSS, which is possibly attributed to the agglomeration of excessive filler, it is still much better than that of the CF/BMI compos-

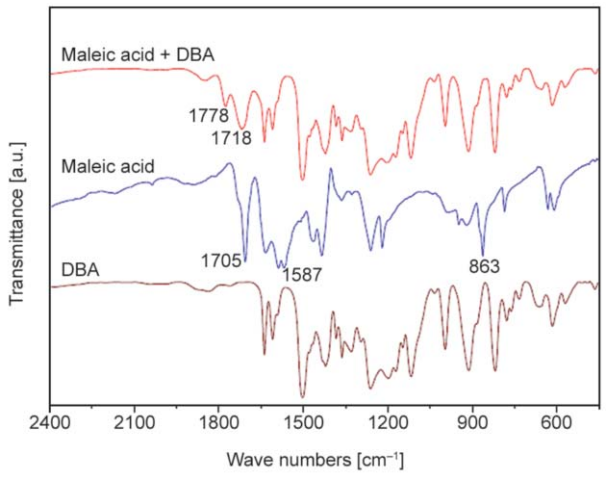

Figure 7. FT-IR spectra of maleic acid and DBA before and after reaction

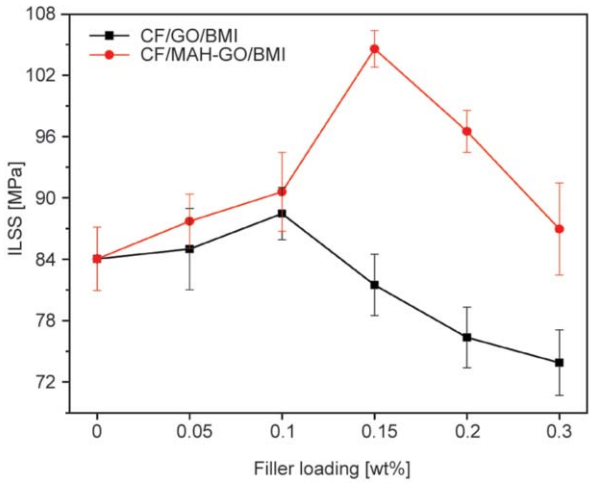

Figure 8. ILSS of neat BMI resin and its composites with different filler loading

ite. Meanwhile, it is also noted that the ILSS of composites decrease severely when the GO content beyond its optimum value. Based on the above results, it is safe to conclude that the dispersion of MAH-GO in the resin was superior to that of GO due to the chemical interaction between the grafted MAH molecules and the BMI resin. Moreover, the MAH-GO nanosheets bring this advantage into the CF/BMI composites to enhance the interfacial adhesion.

To better understand the addition of GO and MAH-GO in enhancing the interfacial adhesion of the CF/BMI composites, the fracture morphologies of the composites were studied by using SEM, as shown in Figure 9. For the CF/BMI composite, quite a number of fibers have smooth surfaces and there is little resin adhered on the surfaces (see the red box in Figure 9a). In addition, it is clearly shown that many CFs are pulled out from the resin matrix and the gaps between CFs and resin are quite large (see the red arrows in Figure 9d). These phenomena indicate that the interfacial adhesion of the CF/BMI composite is weak and the fiber debonding occurs easily. When the GO or MAH-GO was introduced into the composite system, the fracture morphologies are obviously different (Figure 9b, 9e and Figure 9c, 9f). Especially for the CF/MAH-GO/BMI composite, the fibers are tightly surrounded by the resin and there are no pulled-out fibers. A large amount of matrix is attached on the CFs surfaces. Moreover, Figure 9g shows that many MAH-GO nanofillers (see the red arrows) are adsorbed on the surface of CFs although few of MAH-GO agglomerates (see the blue arrow) are also existed. Therefore, the interfacial adhesion of composites was improved because more energy was consumed by pulling out the MAH-GO nanofillers from the matrix.

3.3. Flexural properties of CF/BMI composites

The flexural properties of CF/BMI composites were measured and illustrated in Figure 10. The flexural

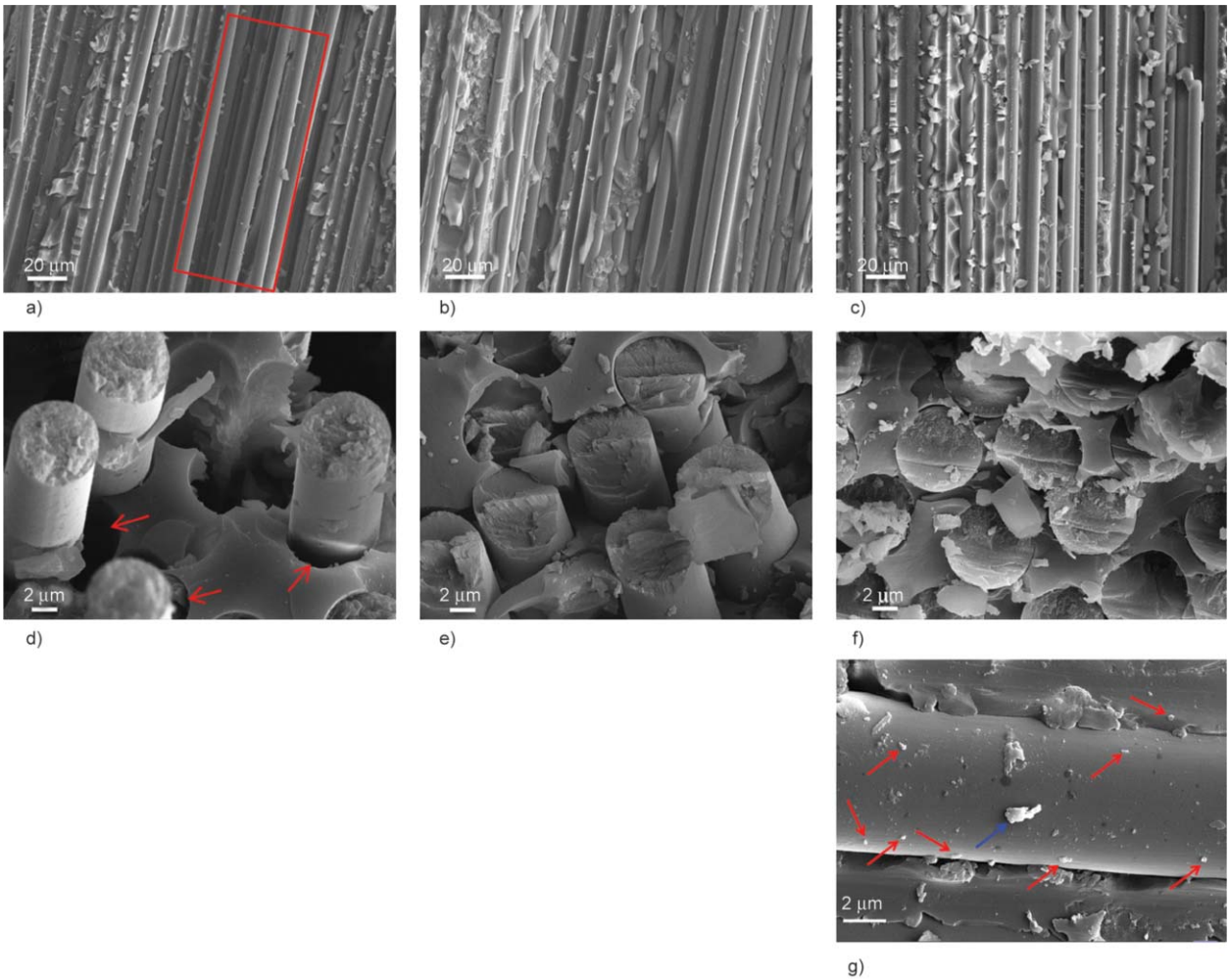

Figure 9. Fracture morphologies of the composites: (a), (d) CF/BMI; (b), (e) CF/BMI with 0.1 wt% GO; (c), (f), (g) CF/BMI with 0.15 wt% MAH-GO

strength for CF/BMI composite was 1.36 GPa. With the increase of filler loading, the flexural strength increased firstly and then decreased. This tendency is similar to that of the ILSS of the composites. The flexural strength of CF/GO/BMI and CF/MAH-GO/BMI composites reached the maximum values of 1.51 and 1.75 GPa when the GO and MAH-GO content was 0.1 and 0.15 wt%, 11.0 and 28.7% improvement more than that of the CF/BMI composite, respectively.

The improvement of flexural strength should be attributed to the enhancement of the interfacial adhesion between the CFs and MAH-GO (or GO). The enhanced interfacial adhesion allows better load transfer from the resin matrix to the CFs [2, 23]. Another possible reason is the synergistic effects [24] of microscopic CFs and nanoscale MAH-GO (or GO). The CFs and the MAH-GO (or GO) might act as a good combination of reinforcement and to carry the load during the flexural deformation of resin matrix.

Figure 10b shows the effects of GO and MAH-GO content on the flexural modulus of CF/BMI composites. It is obviously that the incorporation of GO and MAH-GO yielded an improvement of the composites stiffness and the MAH-GO enhanced the flexural modulus of composites greatly compared with the GO. When the filler content was 0.1 wt%, the flexural modulus of CF/GO/BMI and CF/MAH-GO/BMI composites reached the maxium values of 84.63 and 98.87 GPa, which increased 27.9 and 49.7% with respect to that of CF/BMI composite, respectively. The study also indicates that excessive GO and MAH-GO gave the negative effects to the flexural properties of composites due to the agglomeration. The agglomeration will decrease the surficial contact area of the graphene filler and thus give bad effect in improving the mechanical properties of the CF composites.

4. Conclusions

In this study, we have demonstrated a novel and facile method for improving the interfacial adhesion property of CF/BMI composites. Firstly, the covalent functionalized GO was synthesized by grafting MAH onto the GO surfaces. Then, the CF/BMI composites with both the GO and MAH-GO at different loadings were prepared. The effects of GO and MAH-GO on the interfacial adhesion of CF/BMI composites were investigated and compared. Due to the high reactivity of carbon-carbon double bond in the grafted MAH molecules, the MAH-GO reacted with the BMI resin during the curing process. This strong chemical interaction between the MAH-GO and the resin matrix gave a substantial increase in the ILSS and flexural properties of CF/BMI composite. The enhancement of interfacial adhesion was testified by SEM images of the fracture morphologies.

References

[1] Zhao F., Huang Y., Liu L., Bai Y., Xu L.: Formation of a carbon fiber/polyhedral oligomeric silsesquioxane/carbon nanotube hybrid reinforcement and its effect on the interfacial properties of carbon fiber/epoxy composites. Carbon, **49**, 2624–2632 (2011). DOI: 10.1016/j.carbon.2011.02.026

[2] Ashori A., Rahmani H., Bahrami R.: Preparation and characterization of functionalized graphene oxide/carbon fiber/epoxy nanocomposites. Polymer Testing, **48**, 82–88 (2015). DOI: 10.1016/j.polymertesting.2015.09.010

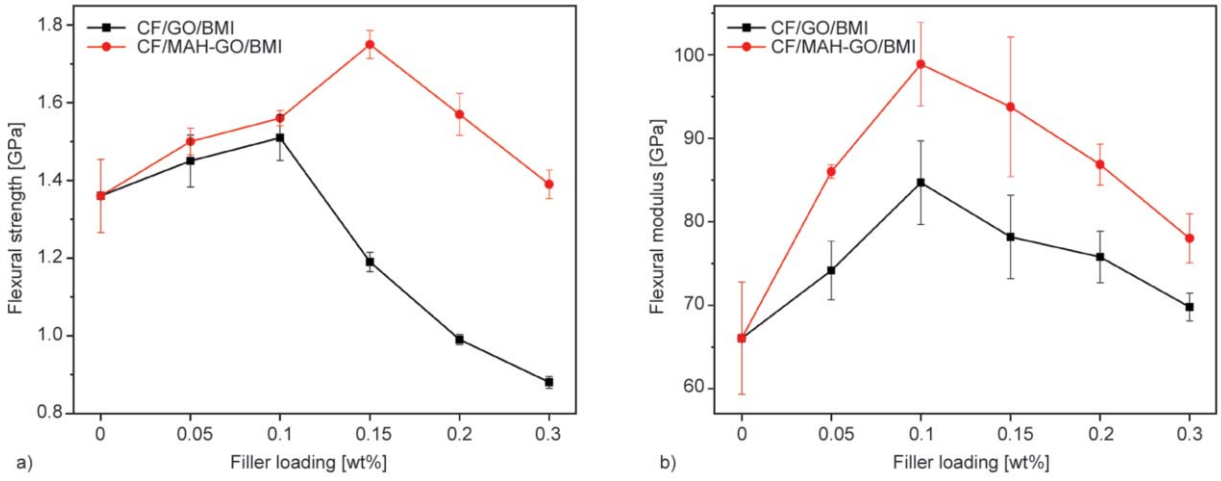

Figure 10. (a) flexural strength and (b) flexural modulus of neat BMI resin and its composites with different filler loading

[3] Deng S. H., Zhou X. D., Zhu M. Q., Fan C. J., Lin Q. F.: Interfacial toughening and consequent improvement in fracture toughness of carbon fiber reinforced epoxy resin composites: Induced by diblock copolymers. Express Polymer Letters, **7**, 925–935 (2013). DOI: 10.3144/expresspolymlett.2013.90

[4] Li Y., Peng Q., He X., Hu P., Wang C., Shang Y., Wang R., Jiao W., Lv H.: Synthesis and characterization of a new hierarchical reinforcement by chemically grafting graphene oxide onto carbon fibers. Journal of Materials Chemistry, **22**, 18748–18752 (2012). DOI: 10.1039/c2jm32596a

[5] Li W., Yao S. Y., Ma K. M., Chen P.: Effect of plasma modification on the mechanical properties of carbon fiber/phenolphthalein polyaryletherketone composites. Polymer Composites, **34**, 368–375 (2013). DOI: 10.1002/pc.22385

[6] Liu L., Jia C., He J., Zhao F., Fan D., Xing L., Wang M., Wang F., Jiang Z., Huang Y.: Interfacial characterization, control and modification of carbon fiber reinforced polymer composites. Composites Science and Technology, **121**, 56–72 (2015). DOI: 10.1016/j.compscitech.2015.08.002

[7] Wu G., Ma L., Wang Y., Liu L., Huang Y.: Interfacial properties and impact toughness of methylphenylsilicone resin composites by chemically grafting POSS and tetraethylenepentamine onto carbon fibers. Composites Part A: Applied Science and Manufacturing, **84**, 1–8 (2016). DOI: 10.1016/j.compositesa.2015.12.015

[8] Fukunaga A., Ueda S.: Anodic surface oxidation for pitch-based carbon fibers and the interfacial bond strengths in epoxy matrices. Composites Science and Technology, **60**, 249–254 (2000). DOI: 10.1016/S0266-3538(99)00118-9

[9] Lee C. Y., Bae J-H., Kim T-Y., Chang S-H., Kim S. Y.: Using silane-functionalized graphene oxides for enhancing the interfacial bonding strength of carbon/epoxy composites. Composites Part A: Applied Science and Manufacturing, **75**, 11–17 (2015). DOI: 10.1016/j.compositesa.2015.04.013

[10] Wan Y-J., Gong L-X., Tang L-C., Wu L-B., Jiang J-X.: Mechanical properties of epoxy composites filled with silane-functionalized graphene oxide. Composites Part A: Applied Science and Manufacturing, **64**, 79–89 (2014). DOI: 10.1016/j.compositesa.2014.04.023

[11] Lim M-Y., Oh J., Kim H. J., Kim K Y., Lee S-S., Lee J-C.: Effect of antioxidant grafted graphene oxides on the mechanical and thermal properties of polyketone composites. European Polymer Journal, **69**, 156–167 (2015). DOI: 10.1016/j.eurpolymj.2015.06.009

[12] Chatterjee S., Wang J. W., Kuo W. S., Tai N. H., Salzmann C., Li W. L., Hollertz R., Nüesch F. A., Chu B. T. T.: Mechanical reinforcement and thermal conductivity in expanded graphene nanoplatelets reinforced epoxy composites. Chemical Physics Letters, **531**, 6–10 (2012). DOI: 10.1016/j.cplett.2012.02.006

[13] Liu M., Duan Y., Wang Y., Zhao Y.: Diazonium functionalization of graphene nanosheets and impact response of aniline modified graphene/bismaleimide nanocomposites. Materials and Design, **53**, 466–474 (2014). DOI: 10.1016/j.matdes.2013.07.027

[14] Rozenberg B. A., Dzhavadyan E. A., Morgan R., Shin E.: High-performance bismaleimide matrices: Cure kinetics and mechanism. Polymers for Advanced Technology, **13**, 837–844 (2002). DOI: 10.1002/pat.230

[15] Yan H., Li S., Jia Y., Ma X. Y.: Hyperbranched polysiloxane grafted graphene for improved tribological performance of bismaleimide composites. RSC Advances, **5**, 12578–12582 (2015). DOI: 10.1039/C4RA13134G

[16] Liu C., Yan H., Chen Z., Yuan L., Lv Q.: Effect of surface-functionalized reduced graphene oxide on mechanical and tribological properties of bismaleimide composites. RSC Advances, **5**, 46632–46639 (2015). DOI: 10.1039/C5RA06009E

[17] Li W., Zhou B., Wang M., Li Z., Ren R.: Silane functionalization of graphene oxide and its use as a reinforcement in bismaleimide composites. Journal of Materials Science, **50**, 5402–5410 (2015). DOI: 10.1007/s10853-015-9084-z

[18] Hummers Jr. W. S., Offerman R. E.: Preparation of graphitic oxide. Journal of the American Chemical Society, **80**, 1339 (1958). DOI: 10.1021/ja01539a017

[19] Wang X., Xing W., Zhang P., Song L., Yang H., Hua Y.: Covalent functionalization of graphene with organosilane and its use as a reinforcement in epoxy composites. Composites Science and Technology, **72**, 737–743 (2012). DOI: 10.1016/j.compscitech.2012.01.027

[20] Yang H., Li F., Shan C., Han D., Zhang Q., Niu L., Ivaska A.: Covalent functionalization of chemically converted graphene sheets *via* silane and its reinforcement. Journal of Materials Chemistry, **19**, 4632–4638 (2009). DOI: 10.1039/b901421g

[21] Hu X., Meng J.: Effect of organoclay on the curing reactions in bismaleimide/diallyl bisphenol A resin. Journal of Polymer Science Part A: Polymer Chemistry, **43**, 994–1006 (2005). DOI: 10.1002/pola.20521

[22] Li J. J.: Alder ene reaction. in 'Name reactions' (ed.: Li J. J.) Springer, New York, 1–2 (2014). DOI: 10.1007/978-3-319-03979-4_1

[23] Song K., Zhang Y., Minus M. L.: Polymer interphase self-reinforcement and strengthening mechanisms in low-loaded nanocomposite fibers. Macromolecular Chemistry and Physics, **216**, 1313–1320 (2015). DOI: 10.1002/macp.201500011

[24] Pedrazzoli D., Pegoretti A., Kalaitzidou K.: Synergistic effect of exfoliated graphite nanoplatelets and short glass fiber on the mechanical and interfacial properties of epoxy composites. Composites Science and Technology, **98**, 15–21 (2014). DOI: 10.1016/j.compscitech.2014.04.019

eXPRESS Polymer Letters Vol.10, No.11 (2016) 883–894
Available online at www.expresspolymlett.com
DOI: 10.3144/expresspolymlett.2016.83

Influence of cadmium sulfide nanoparticles on structural and electrical properties of polyvinyl alcohol films

J. Koteswararao[1], *R. Abhishek*[1] , *S. V. Satyanarayana*[2], *G. M. Madhu*[1*], *V. Venkatesham*[1]

[1]Department of Chemical Engineering, M S Ramaiah Institute of Technology, 560054 Bangalore, Karnataka, India
[2]Department of Chemical Engineering, Jawaharlal Nehru Technological University Anantapur, Anantapuramu – 515002, Andhra Pradesh, India

Received 1 January 2016; accepted in revised form 20 June 2016

Abstract. Cadmium sulfide (CdS) nanoparticles have been synthesized by hydrothermal method and dispersed in poly vinyl alcohol (PVA) matrix in varying amounts by weight. Subsequently, PVA/CdS nanocomposites have been synthesized with the objective of investigating the effect of CdS nanoparticles on structural and electrical properties of PVA films. Structural properties were analyzed by Fourier transform infrared spectroscopy (FTIR), X-ray diffraction (XRD) and scanning electron microscopy (SEM) techniques. Differential scanning calorimetry (DSC) was used to investigate thermal properties of PVA/CdS nanocomposites. Electrical properties were measured by using high frequency LCR meter and were found to be strongly dependent on frequency and nano CdS content. Dielectric constant decreased with increase in frequency and with increase in nanofiller concentration. AC conductivity and dielectric loss increased with frequency and decreased with increase in nano CdS content.

Keywords: *nanocomposites, cadmium sulfide, electrical properties, polyvinyl alcohol*

1. Introduction

Use of nanoparticles in numerous applications has become a major area of interdisciplinary research in recent times. The method of nanoparticle synthesis is an important factor in determining the type of application. The research, particularly on semiconductor nanoparticles is motivated by its possible uses in various fields like nonlinear optics, solar cells, light-emitting devices, electronics, biological labels, and catalysis. The size-dependent mechanical, optical and electronic properties are very much essential. When a particle approaches the size of a few nanometers, its diameter becomes equal to or less than the bulk semiconductor exciton diameter (for cadmium sulfide it is 5–6 nm [1]), such that quantum confinement of electron-hole pairs increase the band gap relative to that in the bulk materials. Hence, the control of particle size allows tuning of the band gap which gives the desired above mentioned electronic and optical properties. Reinforcement of inorganic nanoparticles inside solid polymer matrices are attracting increased attention because the combination of both these materials provides a simple route to stable and processable materials having properties of both components incorporated in the matrix [1].

However, these composites normally cannot be re-dissolved while protecting the colloidal state of nanoparticles. The single polymer molecule represents an important type because isolated nanocomposites based on a single molecule can be obtained, which have very desirable processing characteristics. Mainly, all the applications which are based on single polymer molecule can be applied to the single molecule-nanoparticle composites also. In most of these cases, the nano-

*Corresponding author, e-mail: gmmadhu@gmail.com

composites were further used in various applications in their thin-film form [1].

Composite materials consisting of metal nanoparticles embedded in transparent host matrix have attracted the attention of researchers as advanced technological materials for use in solar cells for photoelectric conversion, transistors for electronic switches [2–6] because of their unique optical, electronic [7], mechanical [8] and structural [9] properties. Large interfacial area between the nanofiller and polymer matrix is a key advantage of nanocomposites since the nanomaterials have high aspect ratio and high surface area. Similarly the dielectric properties of polymers doped with micro and nano fillers have also attracted considerable attention, due to their technological importance for devices such as heating elements, electrical igniters, electrodes for fuel cells and crucibles for vacuum induction furnaces and electric feed [10]. Polymer nanocomposites are known to possess good barrier, mechanical properties, reduced flammability, increased heat distortion temperature and reduced solvent uptake [11].

The study of the effect of temperature on dielectric and frequency is one of the most convenient and sensitive methods of investigating polymer structure. The polarization of dielectric is contributed by dielectric, polar and ionic means [12]. Electronic polarization occurs during very short intervals of time, ionic polarization in the range of a few seconds whereas the dipole polarization takes relatively longer durations.

In this study, poly vinyl alcohol (PVA) has been used as a host matrix for incorporating cadmium sulfide (CdS) nanoparticles due to its water soluble, transparent and highly durable nature. It is a semi-crystalline hydrophilic polymer with a 1,3 glycol structure. Due to its biodegradability and non-toxicity it is highly suitable for environmental processes [13, 14]. The primary focus here is to explore the effects of CdS nanoparticles loading on properties of PVA/CdS composite films. Crystallinity of pure CdS nanopowder and prepared PVA/CdS nanocomposites was studied by X-ray diffraction (XRD) analysis. Scanning electron microscopy (SEM) and Fourier transform infrared spectroscopy (FTIR) techniques were used to investigate the surface morphology of prepared films and influence of CdS nanoparticles on structural characteristics of PVA films. The dielectric constant, dielectric loss and conductivity of PVA/CdS nanocomposite films at different frequencies were studied in order to probe the role of nanofiller in PVA matrix. Also, the effect of CdS content on thermal properties of PVA/CdS nanocomposites was investigated in detail.

2. Experimental procedure

2.1. Reagents and materials

All chemicals used were of analytical grade and used without further purification. Cadmium nitrate, [$Cd(NO_3)_2 \cdot 4H_2O$ (≥99%)], Nice Chemicals Pvt. Ltd, Cochin, India, Thiourea [NH2CSNH2] AR grade (≥99%), and L-valine [$C_5H_{11}NO_2$] BO grade were obtained from SDFCL (SD Fine–CHEM LIMITED), Mumbai, India. PVA [$(C_2H_4O)_n$] LR grade having molecular weight from 85 000 to 124 000 (86–89%) was obtained in powder form from SDFCL (SD Fine – CHEM LIMITED), Mumbai, India. Double distilled water was used for dissolution and casting of PVA films.

2.2. Synthesis and characterization of CdS nanoparticles

CdS nanoparticles were prepared using hydrothermal method [15, 17]. An aqueous solution was prepared by mixing 3.08 g of Cadmium nitrate ($Cd(NO_3)_2 \cdot 4H_2O$), 2.285 g of Thiourea (NH_2CSNH_2) and 0.3518 g of L-valine ($C_5H_{11}NO_2$) were dissolved in 80 mL of distilled water to form a solution. Here, thiourea and L-valine act as fuel and stabilizer respectively. The fuel used here supplies required energy for the reaction. The solution is kept in teflon lined stainless steel container and stirred for 30 minutes. Then the container was placed in an autoclave at a temperature of 180–200 °C, for 4 hours, and later allowed to cool to room temperature. The product was then washed thoroughly with distilled water and ethanol, and centrifuged. The residue was heated at 80 °C for an hour to produce nano powder of CdS. The overall reaction can be represented as shown by Equation (1):

$$Cd(NO_3)_2 + NH_2CSNH_2 \rightarrow CdS + 2N_2O + 2H_2O + CO_2 \quad (1)$$

2.3. Fabrication of PVA/CdS nanocomposite films

PVA/CdS nanocomposite films were prepared by solution intercalation film casting method. Films were cast from a CdS water suspension, in which PVA was dissolved by heating at 75–80 °C for 4 hr with constant stirring on a water bath. The solid content of the PVA solution was maintained at 7.5% by wt. The solution was then ultrasonicated at 80–90 °C for 30–40 min for uniform distribution of nanomaterial in the solution and to minimize any possible agglomeration and immediately poured into a clean glass mould and then dried at room temperature for 48 hours. PVA nanocomposite films were cast with different solutions containing varying amounts viz. 0.5, 1, 1.5 and 2 wt% of CdS nanoparticles. The casted films were free from air bubbles with uniformly dispersed CdS nanoparticles in PVA matrix. The thickness of the nanocomposite film samples casted were in the range of 0.18–0.22 mm [16].

2.4. Measurements

FTIR spectra of the samples were measured in the spectral range of 4000–500 cm^{-1} using FTIR in transmittance mode with resolution of 4 cm^{-1}. XRD analysis was recorded using Brucker's D-8 advanced wide-angle X-ray diffractometer. The X-ray source was Ni-filtered Cu-Kα radiation (40 kV, 30 mA). The dried membranes of uniform thickness (~200 μm) were mounted on a sample holder and the X-ray tracings were recorded in the range of 0–80° at a speed of 8° per min. Surface images were recorded by SEM (Model JSM-5910-JEOL JAPAN) at an operating voltage of 5 kV. For the electrical characterization of composites, high frequency LCR meter (Agilent 4294A) was employed having a frequency range from 4 kHz to 1 MHz. The test was carried out at constant voltage of 1 V and at room temperature. DSC measurements of neat PVA and PVA/CdS nanocomposites were performed using a NETZSCH DSC 200F3 instrument in the temperature range of 30 to 250 °C in nitrogen atmosphere. Both the heating and cooling rates were maintained at 10 °C·min^{-1}.

3. Results and discussion

3.1. Fourier transform-infrared spectroscopy (FTIR)

Any possible interaction between PVA matrix and CdS nanoparticles can be understood by FTIR analysis. The FTIR spectra of PVA and CdS reinforced PVA nanocomposite films are shown in Figure 1. The spectrum shows peaks at 3285, 2923, 1724, 1373, 1239, 1087, and 842 cm^{-1}. The broad peak around 3285 cm^{-1} indicates stretching of hydroxyl groups(O–H) [40] and peaks at 2923 and 2850 cm^{-1} are due to C–H asymmetric stretching vibration. The peaks observed at 1724 and 1373 cm^{-1} correspond to C=O stretching (of vinyl acetate group of PVA), out-of-phase deformation and in-plane deformation of the methyl group respectively. The peak at 1239 cm^{-1} corresponds to the C–O–C out of phase stretching and the peak at 1087 cm^{-1} was due to the COS stretching vibration mode and also indicates the C–O stretch of secondary alcoholic groups. Out-of-

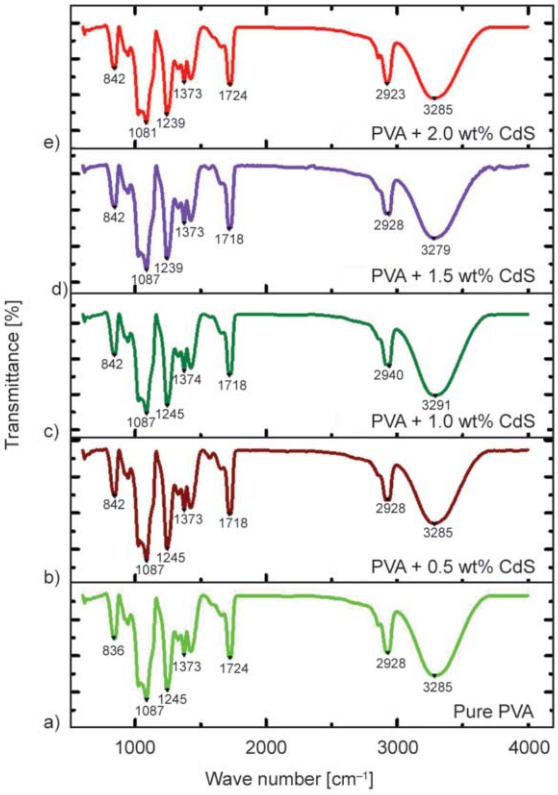

Figure 1. FTIR samples of PVA loaded with CdS nanoparticles at (a) 0 wt%, (b) 0.5 wt%, (c) 1.0 wt% (d) 1.5 wt%, (e) 2 wt%

phase stretching vibration was observed at 842 cm^{-1} due to sulfate ions in are linked with water molecules by hydrogen bonding [41].

The vibration absorption peak of Cd–S bond at 405 cm^{-1} is observed in the spectrum. The observed at peak at 3285 cm^{-1} is very broad when compared to the as synthesized complex, which is purely due to the adsorbed moisture by the sample. The peak observed at 2923 cm^{-1} evidences the capping of alkyl group over the formed CdS. There was no form of additional peak in IR spectra; however a small shift in the peak position of the band is observed (which is not considerable) corresponding to C=O stretch and C–O–C stretch vibrations indicates physical interaction between hydroxyl groups of PVA and nano CdS. The hydroxyl groups of PVA have a very strong tendency to form charge-transfer complex with CdS nanoparticles through chelation.

3.2. X-ray diffraction analysis

Figure 2 shows XRD patterns of the synthesized CdS nanoparticles. Comparison with the standard (JCPDS No 41- 4019) [15] clearly revealed the formation of single phase CdS with a hexagonal crystal structure. The crystalline nature of pure nano CdS was observed by various sharp peaks shown in Figure 2. Seven separate diffraction peaks can be seen at the 2θ values of 24.98, 26.5, 28.14, 31.8, 43.8, 48.2 and 51.9°. It was observed that varying the solvent during synthesis of nano CdS presented preferential growth in different crystalline directions [18]. Similarly it can be believed that a less pronounced preferential growth occurred in the nanocomposite film samples of this study.

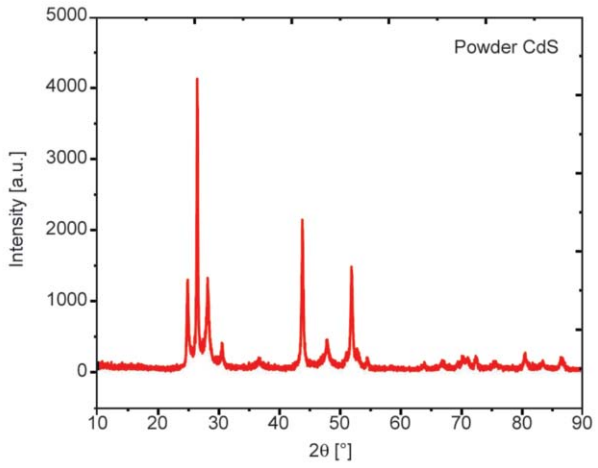

Figure 2. XRD profile of pure CdS nanoparticles

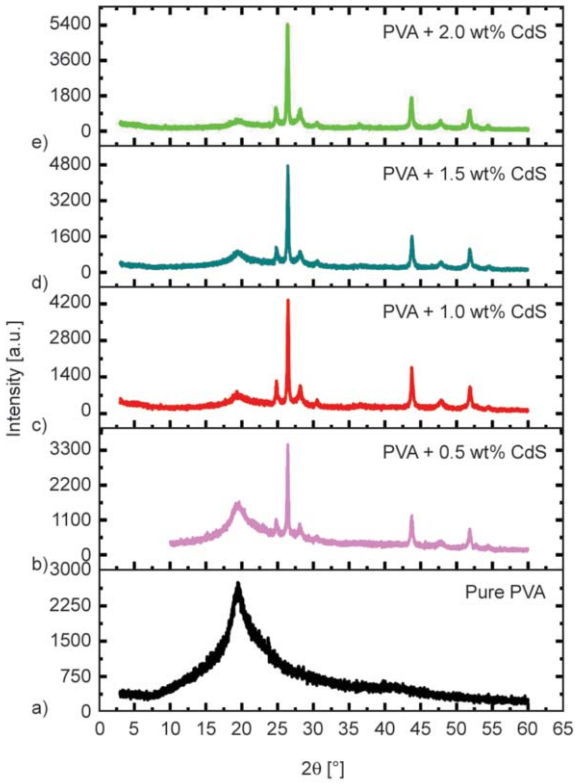

Figure 3. XRD profiles of (a) 0 wt%, (b) 0.5 wt%, (c) 1 wt%, (d) 1.5 wt%, (e) 2 wt% CdS nanoparticles loaded PVA nanocomposites

XRD patterns of pure polyvinyl alcohol and PVA/CdS nanocomposites having 0.5, 1, 1.5 and 2 wt% of CdS respectively are shown in Figure 3. All the composites showed a peak at approximately 2θ = 19.4° [19] corresponding to (1 0 1) crystal plane for polyvinyl alcohol, which indicates the semi-crystalline nature of PVA. The crystalline nature of PVA results from the strong intermolecular interaction between PVA polymer networks. The mean particle size of synthesized nano CdS calculated by using Scherrer equation was found to be 37.68 nm.

XRD profiles of the composites showed no shifting or broadening of peak at 2θ = 19.4°, but showed appearance of smaller new peaks at 24.98, 26.4, 28.16, 30.65, 44.33, 47.92, 51.81 and 54.48° which clearly indicated the presence of CdS nanoparticles inside the PVA matrix.

3.3. Thermal characterization of the PVA/CdS nanocomposites

Differential scanning calorimetry (DSC)

The thermal properties of PVA/CdS composite films were analyzed by DSC [39] to investigate the effect of CdS filler content on glass transition temperature

(T_g), melting temperature (T_m), heat of fusion (ΔH), percentage crystallinity (% x_c) and crystallization temperature (T_c) of PVA. DSC analysis was performed in successive cycles of heating and cooling as shown in Figure 4. Outline of the DSC data corresponding to these curves is shown in Table 1.

During heating of a sample, for example, from room temperature to its decomposition temperature, peaks with positive and negative $\Delta dH/dt$ may be recorded; each peak corresponds to a heat effect associated with a specific process, such as crystallization or melting. The important information from DSC curves is the temperature at which process occurs and the peak temperature is associated and the temperature at which maximum reaction rate occurs.

The analysis was carried out from 25 to 250 °C of temperature at a rate of 10 °C/min. All peak values have been shown in Table 1. The incorporation of CdS nanoparticles decreased the T_g and T_m of PVA. This decrease may be due to the agglomeration of CdS nanoparticles, which decreases the polymeric network strength and also the intermolecular interaction between PVA chains. The values of T_g and T_m do not vary much with the content of CdS in the matrix which indicates that the PVA barely interacts with the nanoparticles. It may be due to increase in the free volume (which may also be due to adsorption because of the limited mobility of the adsorbed chains). The suppressed melting point shows that the interaction with the nanofiller hampers crystallization. This may also explain the larger supercooling (lower T_c).

Although an increase in the nanoparticle content does not affect crystallinity (melting enthalpies in Table 1 are almost unchanged), it can be concluded that the presence of the CdS-nanofiller prevents crystal thickening. The observed effects can be explained by the reduced mobility of the PVA chains attached to the surface of the CdS nanoparticles. This is also supported by the FTIR data given above.

The glass transition, strictly speaking, is not a true phase transition, because the first derivative of the heat capacity curve is a continuous function of temperature as shown by phase-modulated DSC measurements. This means that the polymer shows signs of a spectrum of glass transition temperatures, each corresponding to different segmental relaxations. Figure 4 tells not just a shift of the slope in the heat capacity curve to higher temperatures with an increase of the content of the inorganic phase, but also a lengthening of its temperature range. It seems that incorporation of CdS into the polymer matrix affects the distribution of chain segments, most likely due to a change in chain packing density in the surrounding area of the surface of the nanofillers.

Table 1. Thermal properties of PVA/CdS nanocomposites showing T_g, T_m, ΔH_m, % x_c and T_c as a function of CdS content in PVA matrix

Composition [wt%]		T_g [°C]	T_m [°C]	ΔH_m [J/g]	% x_c	T_c [°C]
PVA	CdS					
100.0	0.0	81.6	224.3	40.54	4.390	189.8
99.5	0.5	71.3	189.1	40.89	5.768	95.2
99.0	1.0	68.4	190.2	41.49	4.572	118.5
98.5	1.5	71.2	191.5	37.29	4.408	109.9
98.0	2.0	69.2	190.0	35.72	4.171	118.6

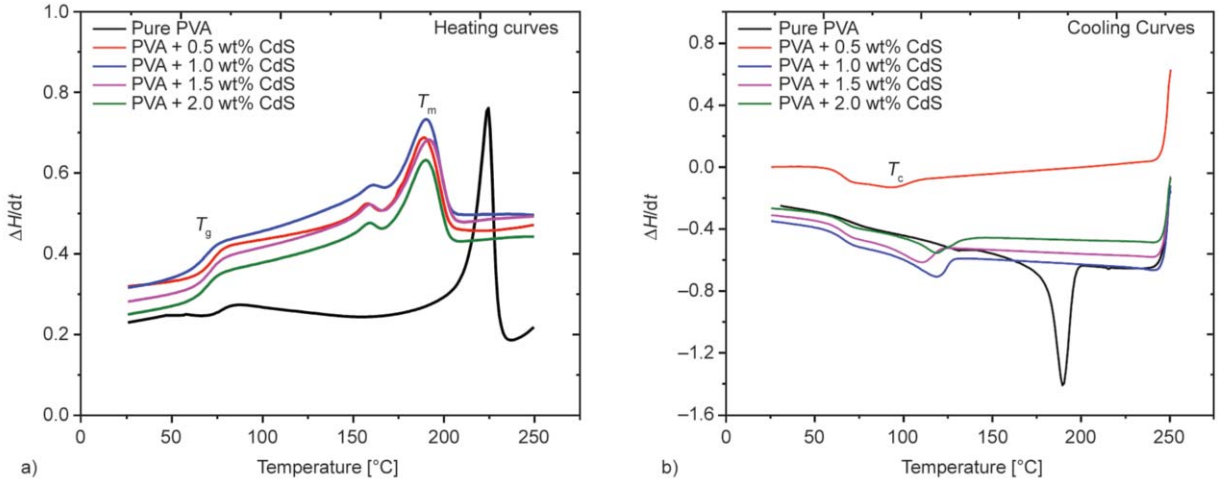

Figure 4. (a) DSC heating curve and (b) cooling curve of pure PVA and PVA/CdS nanocomposites

3.4. Scanning electron microscopy (SEM)

Surface morphology of PVA and PVA/CdS nanocomposite films was understood from the SEM images shown in Figures 5. The images clearly show CdS nanoparticles which have porous, agglomerated, acicular (Needle like components) structure, size below 80 nm and also confirmed from the images reported elsewhere [20, 21]. The varying sizes obtained may be due to agglomeration of the nanoparticles which takes place in order to minimise the high surface energy that exists in individual nanoparticles. Figure 6 shows SEM images of (a) neat PVA, (b) PVA–0.5 wt% CdS, (c) PVA–1.0 wt% CdS, (d) PVA–1.5 wt% CdS, (e) PVA–2.0 wt% CdS. From these images, it was observed that nanoparticles were aglomerated at all concentrations at varying degree. These agglomerated CdS nanoparticles were seen homogeneously distributed throughout the PVA matrix at lower concentrations. Agglomeration of these nanoparticles lead to big masses as seen in some of the images such as in Figure 6b–6e. The white spots shown in all the SEM images (Figure 6) are CdS nanoparticles. As a result of agglomeration, the particle sizes were seen to increase with increase in filler concentration. The mean particle size obtained from the images was 40 nm (approxmately same as obtained from Scherrer formula) while the largest particle size obtained due to agglomeration was 240 nm. The nanoparticles were seen to be dispersed closely to each other in PVA matrix with increase in nanofiller concentration from 0.5 to 2.0 wt%. This is because with increase in nanofiller loading, the number of particles increases and so the interparticle distance decreases.

3.5. Effect of CdS nanoparticles addition on different electrical properties of PVA matrix

3.5.1. Dielectric permittivity

The effective dielectric permittivity in nanocomposites is determined by dielectric division in the bulk of the composite material. In the present case, these are: polarization associated with PVA as well as CdS nano particles and interfacial polarization at the PVA-nanoparticle interfaces. The prepared nanocomposites have a large volume fraction of interfaces where interfacial polarizations are most likely to occur. Several dielectric properties of polymer nanocomposites have been evaluated in the past and the permittivity values in nanocomposites are reported to be lower than that of base polymers when insulating oxides are used as the fillers [12, 22–25].

In order to investigate the effect of nanoparticles on PVA matrix, CdS nanoparticles were incorporated into PVA matrix and analyzed for dielectric properties. Measurements of capacitance C (in Farad) and loss tangent were made over the range from 4 Hz to 1 MHz. The dielectric constant (ε_r or ε'), dielectric loss (ε'') and electrical conductivity values were calculated from capacitance and loss tangent using the Equations (1)–(3). The frequency-dependent ε', ε'' and $\tan\delta$ values of the PVA/CdS nanocomposites at different filler concentrations are presented in Figure 7 and 8, respectively.

The dielectric parameter as a function of frequency is described by the complex permittivity in the form given by Equation (2):

$$\varepsilon^*(\omega) = \varepsilon'(\omega) - i\varepsilon''(\omega) \tag{2}$$

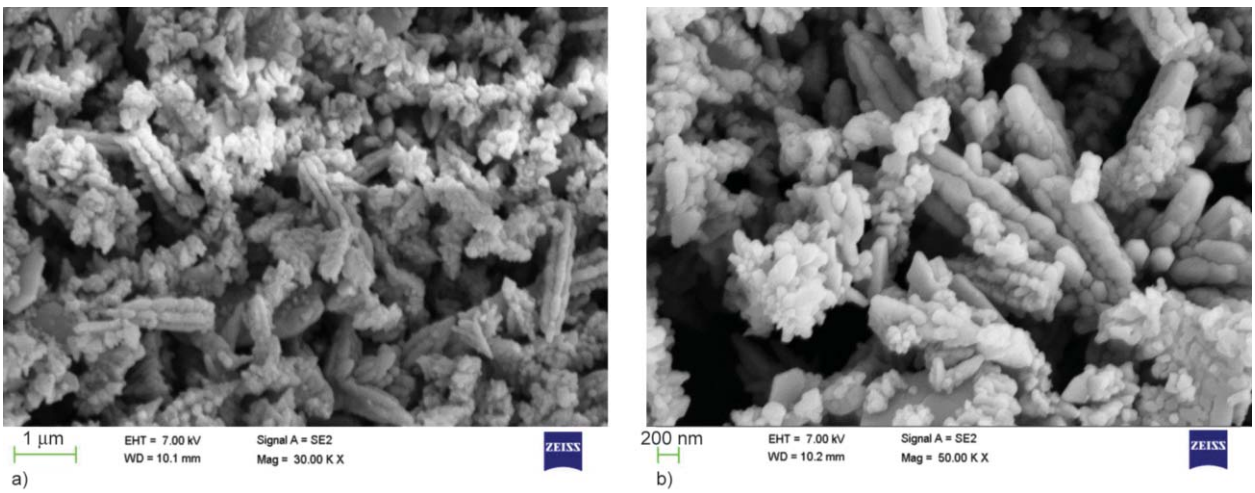

Figure 5. SEM image of CdS nanoparticles taken at (a) micrometre and (b) nanometre scale

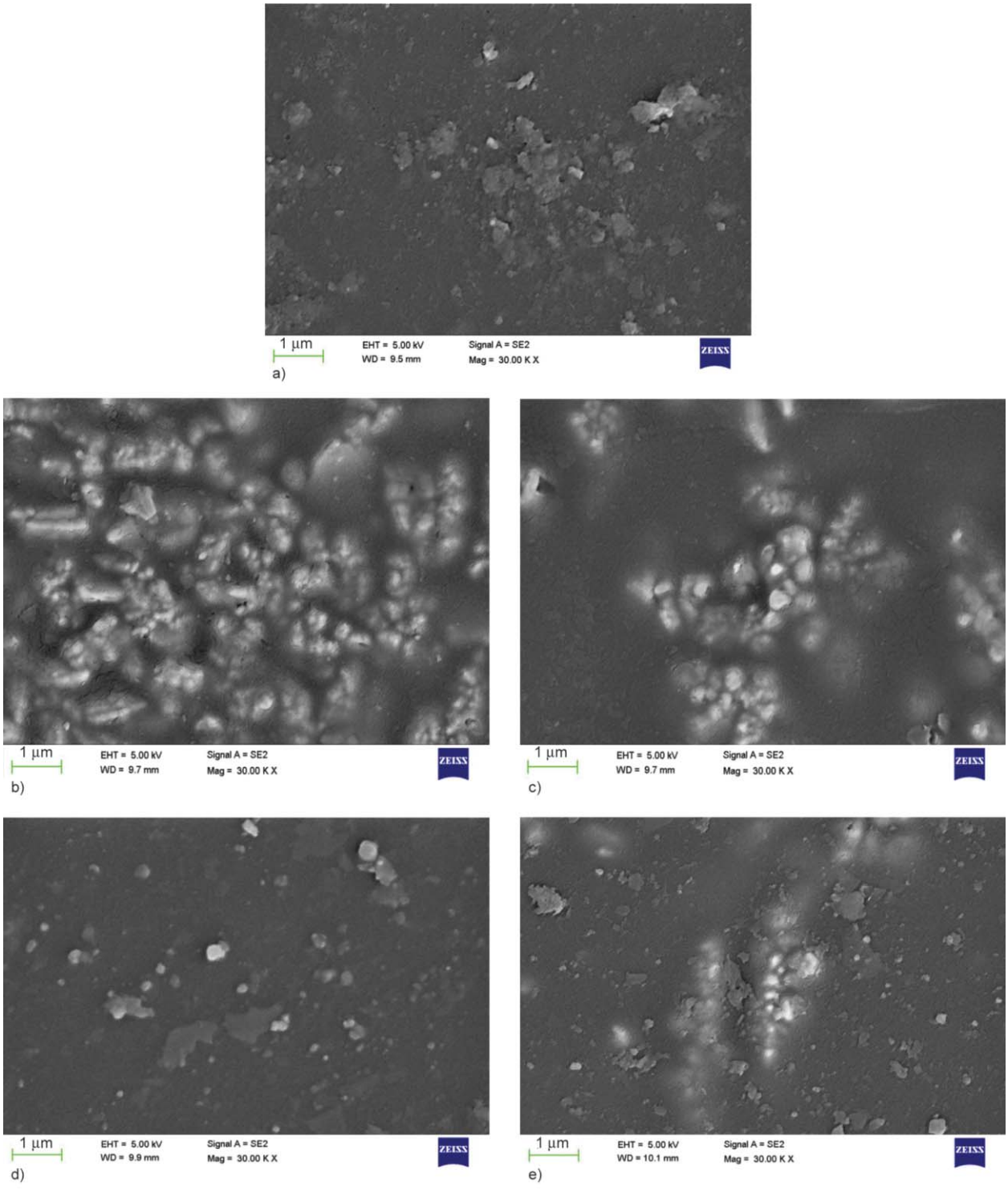

Figure 6. SEM photomicrographs of PVA loaded with CdS nanoparticles at (a) 0 wt%, (b) 0.5 wt%, (c) 1.0 wt%, (d) 1.5 wt%, (e) 2.0 wt%

where $\varepsilon'(\omega)$ is real part and $\varepsilon''(\omega)$ imaginary part are the components for energy storage and energy loss respectively in each cycle of the electric field.

The measured capacitance C was used to calculate the dielectric constant, $\varepsilon'(\omega)$ using the Equation (3):

$$\varepsilon'(\omega) = \frac{C \cdot t}{A \cdot \varepsilon_0} \tag{3}$$

where t is the film thickness in [m], A is surface area of sample in [m^2], ε_0 is the permittivity of air ($8.85 \cdot 10^{-12}$ F/m) and ω is the angular frequency in [s^{-1}] given by $\omega = 2\pi f$; and f is frequency in [s^{-1}].

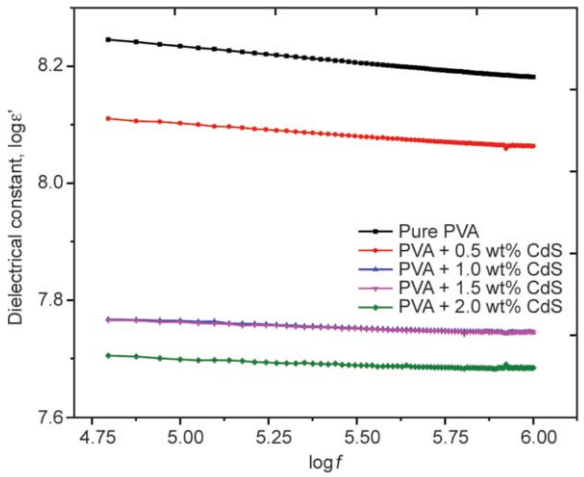

Figure 7. Dielectric constant of PVA/CdS nanocomposites as a function of log frequency

Whereas, the dielectric loss $\varepsilon''(\omega)$ is given by Equation (4):

$$\varepsilon''(\omega) = \varepsilon'(\omega)\tan\delta(\omega) \quad (4)$$

where $\tan\delta(\omega)$ is tangent delta and $\varepsilon'(\omega)$ is dielectric constant.

The dielectric properties of materials are mainly determined by their abilities to polarize at a given frequency. For multi component systems, when free charge carriers migrate through the material, space charges build up at the interfaces of the components remaining to the mismatch of the conductivities and dielectric constants of the materials at the interfaces [26, 27]. This is called interfacial polarization. The interfacial polarization in polymers having structural in homogeneities (such as nanoparticles) can be identified by low-frequency dielectric measurement based on Maxwell-Wagner-Sillar's method [27–29]. The changes in the permittivity values as a function of frequency are attributed to dielectric relaxations especially at low frequency which is due to micro-Brownian motion of the whole chain (segmental movement). Nevertheless, these changes are also affected by the interfacial polarization process known as Maxwell-Wagner-Sillar, exist in heterogeneous dielectric materials and are produced by the travelling of charge carriers [30, 31].

It is observed from Figure 7 and Figure 8 that the values of ε', ε'' and $\tan\delta$ were found to be strongly influenced by frequency. The value of ε', decreased with increasing frequency whereas the dielectric loss ε'' increased with frequency. This shows that strong low-frequency dispersion takes place that characterizes the frequency dependence of ε' and ε'' in PVA/CdS nanocomposite films. In general, there are four possible mechanisms that could contribute to the low-frequency dielectric behaviour of PVA/CdS nanocomposites: electrode interface, AC electrical conductivity, dipole orientation and charge carriers. In principle, at low frequencies and temperatures, all four types of polarization mechanisms contribute to the values of ε' and ε''. As the frequency increases, the contributions of interfacial, dipolar, and ionic polarizations become ineffective, leaving behind only the AC electrical conductivity parameter. Furthermore, decrease in ε' with increasing frequency can be explained by the fact that as the frequency increased, the interfacial dipoles had less time to orient themselves in the direction of the alternating field. However, the value of ε'' increased with increasing frequency, which can be credited to the high interfacial traps formed at the PVA/CdS interface that negatively influences the electrical properties [32] that illustrate the dependence of various dielectric behaviors on CdS content and on the frequency of the applied AC field.

From Figure 7 it is observed that ε' value gradually decreased with increase in CdS loading from 0.5 to 1 wt% in the PVA matrix and further increase in CdS content had no effect and ε' was observed to be constant for 1 and 1.5 wt%. Also, less difference was observed between ε' values for 1, 1.5 and 2.0 wt% as compared to the ε' values for 0, 0.5 and 1.0 wt% CdS content. These results suggest that there is an existing threshold CdS content for the dielectric behavior of these nanocomposites.

As shown by Figure 5, the majority of nano-sized CdS particles were well-dispersed in the PVA matrix when the CdS content exceeded 1 wt% and these well-dispersed particles emerge as mini-capacitors within the composites (Figure 5d and 5e). Hence it can be said that the high values of dielectric constant for PVA/CdS composite films observed is the result of the accumulation of these nano-sized capacitors. Since these particles were fixed within the PVA matrix, the charge associated with an individual particle was confined to a small area surrounding the particle and could not jump to adjacent particles. In the investigation of a CdS/PVA composite material pre-

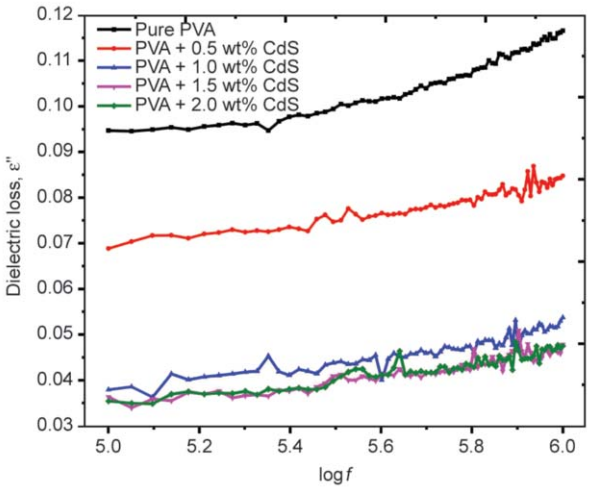

Figure 8. Dielectric loss of PVA/CdS nanocomposites as a function of log frequency

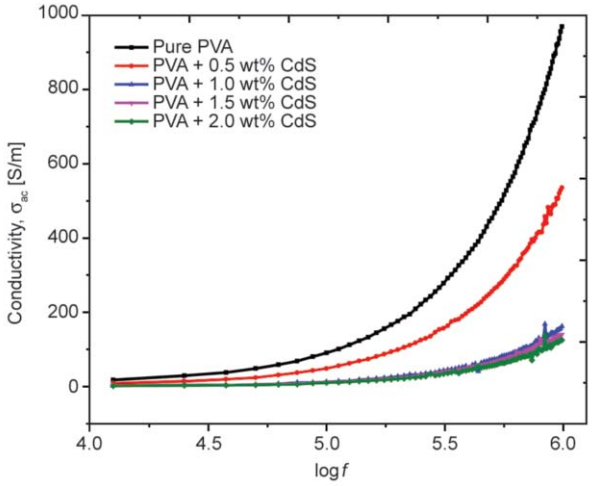

Figure 9. AC Conductivity of PVA/CdS nanocomposites as a function of log frequency

pared by sonication in present study, it is found that that the CdS nano-crystalline domains (~90 nm) can give rise to large dielectric constants.

3.5.2. Dielectric loss

Dielectric loss is the portion of energy of an alternating electric field in a dielectric medium that is converted into heat. It can be expressed in terms of either the loss angle (D) or corresponding loss tangent ($\tan\delta$). Figure 8 shows the effect of frequency on dielectric loss for PVA/CdS nanocomposites. It is seen that the dielectric loss increases with increase in frequency. This increase is substantial at high frequencies in the range of 10^5–10^6 Hz and may be due to heat generated within the composite as a result of rapid alignment of dipoles with the rapidly changing direction of electric field. The dielectric losses may have also increased because of increase in conduction losses with increase in frequency. In spite of these factors, the dielectric loss behaviour with frequency seems to be quite complicated and requires further study.

3.5.3. AC conductivity

AC conductivity is the alternating conductivity of sample that arises from the motion of charge carriers through the polymer and is measured using the Equation (5) [33–35]:

$$\sigma_{ac} = \frac{G_p \cdot t}{A} \tag{5}$$

where G_p is the conductance, t is the film thickness [m], A is surface area of sample [m^2].

Figure 9 illustrates the dependence of AC electrical conductivity (σ_{ac}) on frequency [36]. The variation is studied in the frequency range from 4 kHz to 1 MHz at room temperature for the PVA/CdS composites. It can be noted that the AC electrical conductivity generally increased with increasing frequency; in particular, a sharp increase in σ_{ac} is found beyond 1 kHz frequency. This may be due to increased electronic interaction processes taking place inside the composites as a result of which the composites became more relatively conductive. In PVA, as the bond rotates with increased frequency, the existing flexible polar groups cause dielectric transitions. This changes the composition of the polymer chains due to the formation of charge transfer complexes. The AC conductivity increases [37] and polymer chains become more flexible.

3.5.4. Loss tangent (D or $\tan\delta$)

Variation in loss tangent ($\tan\delta$) of PVA/CdS composites as a function of frequency is shown in Figure 10. It can be seen from the figure that tanδ decreased initially and then increased with increasing frequency in the range from 4 Hz to 1 MHz passing through a minimum at $6.5 \cdot 10^4$ Hz frequency gradually. The decrease was seen at lower concentrations of CdS nanofiller. The increase in this value indicates the increase in loss storage ratio and hence the composite becomes a semi-conductor and is similar to the ob-

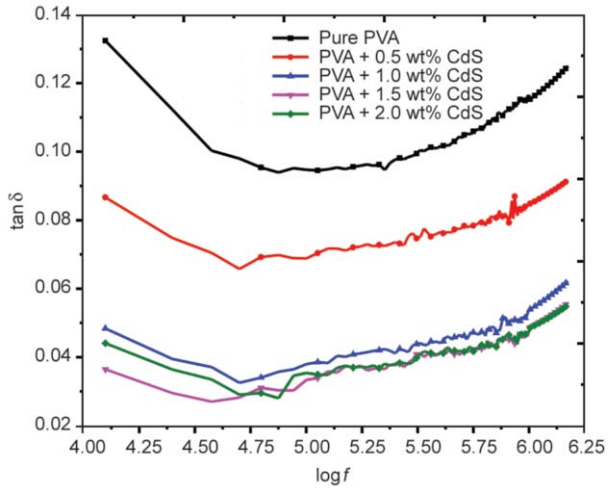

Figure 10. Loss tangent of PVA/CdS nanocomposites as a function of log frequency

servations made by Chao-Hsien Ho *et al.* [38] from the studies on PANI–DBSA/PAA (polyaniline, dodecyl-benzene sulfonate and poly-acrylic acid) films. These experimental results show that ε', ε'' and $\tan\delta$ had a strong dependence on the measured frequency. The capacitance of the PVA/CdS composites at high frequencies in the accumulation region was basically controlled by the dielectric properties of the bulk insulator.

4. Conclusions

PVA/CdS nanocomposites containing varying weight percentages of CdS nanoparticles were prepared by solution intercalation technique. Effects of CdS nanoparticles on structural and electrical properties of PVA films were observed. Various peaks obtained in FTIR analysis showed good physical interaction between PVA matrix and nano CdS. SEM analysis showed porous and acicular CdS nanoparticles which tend to agglomerate at higher concentrations in the polymer matrix. DSC analysis shows that presence of nanoparticles in PVA matrix influence thermal properties like T_g and T_m and heat capacity. Electrical properties of PVA/CdS nanocomposites have been reported for the first time probably by hydrothermal method of synthesizing the nanomaterial. These properties were observed to be strongly dependent upon applied frequency and CdS nanofiller content. Dielectric constant decreased with increase in frequency and with increase in filler concentration; AC conductivity and dielectric loss increased with frequency and decreased with increase in CdS content. The loss tangent increased with increase in concentration of nanofiller showed that the CdS/PVA nanocomposite films can be good semiconductors.

Acknowledgements

The authors would like to extend their kind gratitude towards Department of Chemistry, MSRIT for providing the necessary facilities to synthesize the materials. They would also like to thank MSRIT Alumni Association for providing funds required to carry out this research study. A portion of this research was also performed using facilities at CeNSE, funded by Department of Information Technology, Govt. of India located at Indian Institute of Science, Bangalore. DSC analysis was carried out at NETZSCH Technologies India Pvt. Ltd-Analysis and Testing located in Chennai, Tamil Nadu.

References

[1] Zhang M., Dreschler M., Müller A. H. E.: Template-controlled synthesis of wire-like cadmium sulfide nanoparticle assemblies within core–shell cylindrical polymer brushes. Chemistry of Materials, **16**, 537–543 (2004).
DOI: 10.1021/cm034760v

[2] Zhao H., Douglas E. P.: Preparation of corona-embedded CdS nanoparticles. Chemistry of Materials, **14**, 1418–1423 (2002).
DOI: 10.1021/cm011581

[3] Kim J-Y., Kim H-M., Shin D-H., Ihn K-J.: Synthesis of CdS nanoparticles dispersed within poly(urethane acrylate-*co*-styrene) films using an amphiphilic urethane acrylate nonionomer. Macromolecular Chemistry and Physics, **207**, 925–932 (2006).
DOI: 10.1002/macp.200600031

[4] Pardhan B., Sharma A. K., Ray A. K.: Conduction studies on chemical bath-deposited nanocrystalline CdS thin films. Journal of Crystal Growth, **304**, 388–392 (2007).
DOI: 10.1016/j.jcrysgro.2007.03.041

[5] Pattabi M., Amma B. S., Manzoor K., Sanjeev G.: Effect of 8 MeV electron irradiation on the optical properties of PVP capped CdS nanoparticles in PVA matrix. Solar Energy Materials and Solar Cells, **91**, 1403–1407 (2007).
DOI: 10.1016/j.solmat.2007.04.015

[6] Wang H., Fang P., Chen Z., Wang S.: Synthesis and characterization of CdS/PVA nanocomposite films. Applied Surface Science, **253**, 8495–8499 (2007).
DOI: 10.1016/j.apsusc.2007.04.020

[7] Rao J. K., Raizada A., Ganguly D., Mankad M. M., Satayanarayna S. V., Madhu G. M.: Investigation of structural and electrical properties of novel CuO–PVA nanocomposite films. Journal of Materials Science, **50**, 7064–7074 (2015).
DOI: 10.1007/s10853-015-9261-0

[8] Rao J. K., Raizada A., Ganguly D., Mankad M. M., Satayanarayna S. V., Madhu G. M.: Enhanced mechanical properties of polyvinyl alcohol composite films containing copper oxide nanoparticles as filler. Polymer Bulletin, **72**, 2033–2047 (2015).
DOI: 10.1007/s00289-015-1386-4

[9] Rashmi S. H., Raizada A., Madhu G. M., Kittur A. A., Suresh R., Sudhina H. K.: Influence of zinc oxide nanoparticles on structural and electrical properties of polyvinyl alcohol films. Plastics, Rubber and Composites: Macromolecular Engineering, **44**, 33–39 (2015).
DOI: 10.1179/1743289814Y.0000000115

[10] Maeda S., Armes S. P.: Surface area measurements on conducting polymer-inorganic oxide nanocomposites. Synthetic Metals, **73**, 151–155 (1995).
DOI: 10.1016/0379-6779(95)03315-7

[11] Huang J-C., Zhu Z-K., Yin J., Qian X-F., Sun Y-Y.: Poly(etherimide)/montmorillonite nanocomposites prepared by melt intercalation: Morphology, solvent resistance properties and thermal properties. Polymer, **42**, 873–877 (2001).
DOI: 10.1016/S0032-3861(00)00411-0

[12] Tanaka T.: Dielectric nanocomposites with insulating properties. IEEE Transactions on Dielectrics and Electrical Insulation, **12**, 914–928 (2005).
DOI: 10.1109/TDEI.2005.1522186

[13] Jayasekara R., Harding I., Bowater I., Christie G. B. Y., Lonergan G. T.: Preparation, surface modification and characterisation of solution cast starch PVA blended films. Polymer Testing, **23**, 17–27 (2004).
DOI: 10.1016/S0142-9418(03)00049-7

[14] Kokabi M., Sirousazar M., Hassan Z. M.: PVA–clay nanocomposite hydrogels for wound dressing. European Polymer Journal, **43**, 773–781 (2007).
DOI: 10.1016/j.eurpolymj.2006.11.030

[15] Datta A., Panda S. K., Chaudhuri S.: Synthesis and optical and electrical properties of CdS/ZnS core/shell nanorods. The Journal of Physical Chemistry C, **111**, 17260–17264 (2007).
DOI: 10.1021/jp076093p

[16] Rudko G. Y., Kovalchuk A. O., Bondarenko V. A., Fediv V. I., Gule E. G.: Tunable electrophysical properties of composites nano-CdS/polyvinyl alcohol. Materials Chemistry and Physics, **148**, 77–81 (2014).
DOI: 10.1016/j.matchemphys.2014.07.014

[17] Madhu G. M., Raj M. A. L. A., Pai K. V. K., Rao S.: Photodegradation of methylene blue dye using UV/$BaTiO_3$, UV/H_2O_2 and UV/H_2O_2/$BaTiO_3$ oxidation processes. Indian Journal of Chemical Technology, **14**, 139–144 (2007).

[18] Oliveira J. F. A., Milão T. M., Araújo V. D., Moreira M. L., Longo E., Bernardi M. I. B.: Influence of different solvents on the structural, optical and morphological properties of CdS nanoparticles. Journal of Alloys and Compounds, **509**, 6880–6883 (2011).
DOI: 10.1016/j.jallcom.2011.03.171

[19] Bhadra J., Sarkar D.: Electrical and optical properties of polyaniline polyvinyl alcohol composite films. Indian Journal of Pure and Applied Physics, **48**, 425–428 (2010).

[20] Aneeqa S., Saadat A. S., Salamat A.: Fabrication and characterization of CdS nanoparticles annealed by using different radiations. International Journal of Chemical, Molecular, Nuclear, Materials and Metallurgical Engineering, **4**, 532–539 (2010).

[21] Raut B. T., Chougule M. A., Ghanwat A. A., Pawar R. C., Lee C. S., Patil V. B.: Polyaniline–CdS nanocomposites: Effect of camphor sulfonic acid doping on structural, microstructural, optical and electrical properties. Journal of Materials Science: Materials in Electronics, **23**, 2104–2109 (2012).
DOI: 10.1007/s10854-012-0708-7

[22] Zhang L., Wu P., Li Y., Cheng Z-Y., Brewer J. C.: Preparation process and dielectric properties of $Ba_{0.5}Sr_{0.5}TiO_3$–P(VDF–CTFE) nanocomposites. Composites Part B: Engineering, **56**, 284–289 (2014).
DOI: 10.1016/j.compositesb.2013.08.029

[23] Dang Z-M., Yuan J-K., Zha J-W., Zhou T., Li S-T., Hu G-H.: Fundamentals, processes and applications of high-permittivity polymer–matrix composites. Progress in Materials Science, **57**, 660–723 (2012).
DOI: 10.1016/j.pmatsci.2011.08.001

[24] Panda M., Srinivas V., Thakur A. K.: On the question of percolation threshold in polyvinylidene fluoride/nanocrystalline nickel composites. Applied Physics Letters, **92**, 132905/1–132905/4 (2008).
DOI: 10.1063/1.2900710

[25] Cao Y., Irwin P. C., Younsi K.: The future of nanodielectrics in the electrical power industry. IEEE Transactions on Dielectrics and Electrical Insulation, **11**, 797–807 (2004).
DOI: 10.1109/TDEI.2004.1349785

[26] Li D., Leung Y. H., Djurišić A. B., Liu Z. T., Xie M. H., Gao J., Chan W. K.: CuO nanostructures prepared by a chemical method. Journal of Crystal Growth, **282**, 105–111 (2005).
DOI: 10.1016/j.jcrysgro.2005.04.090

[27] Ku C. C., Liepins R.: Electrical properties of polymers: Chemical principles. Hanser, Munich (1987).

[28] Maxwell J. C.: A Treatise on electricity and magnetism. Clarendon Press, Oxford (1954).

[29] Wagner K. W.: Zur Theorie der unvollkommenen Dielektrika. Annalen der Physik Wiley, **40**, 817–855 (1913).
DOI: 10.1002/andp.19133450502

[30] Latif I., AL-Abodi E. E., Dhefaf H. B., Al Khafagi J.: Preparation, characterization and electrical study of (carboxymethylated polyvinyl alcohol/ZnO) nanocomposites. American Journal of Polymer Science, **2**, 135–140 (2012).
DOI: 10.5923/j.ajps.20120206.01

[31] Patsidis G. C., Psarras A.: Dielectric behaviour and functionality of polymer matrix-ceramic $BaTiO_3$ composites. Express Polymer Letters, **2**, 718–726 (2008).
DOI: 10.3144/expresspolymlett.2008.85

[32] Zhang L. D., Zhang H. F., Wang G. Z., Mo C. M., Zhang Y.: Dielectric behaviour of nano-TiO_2 bulks. Physica Status Solidi (a), **157**, 483–491 (1996).
DOI: 10.1002/pssa.2211570232

[33] Dyre J. C., Schrøder T. B.: Universality of AC conduction in disordered solids. Reviews of Modern Physics, **72**, 873–892 (2000).
DOI: 10.1103/RevModPhys.72.873

[34] Harun M. H., Saion E., Kassim A., Hussain M. Y., Mustafa I. S., Omer M. A. A.: Temperature dependence of AC electrical conductivity of PVA-PPy-$FeCl_3$ composite polymer films. Malaysian Polymer Jounal, **3**, 24–31 (2008).

[35] Meera J., Sumithra V., Seethu R., Prajeshkumar J. M.: Dielectric properties of nanocrystalline ZnS. SB Academic Review, **1**, 93–100 (2010).

[36] Tripathi R., Kumar A., Sinha T. P.: Dielectric properties of CdS nanoparticles synthesized by soft chemical route. Pramana: Journal of Physics, **72**, 969–978 (2009).
DOI: 10.1007/s12043-009-0089-5

[37] Bhajanti R. F., Ravindrachary V., Harisha A., Ranganathiah G., Kumaraswamy G. N.: Effect of barium chloride doping on PVA microstructure: Positron annihilation study. Applied Physics A, **87**, 797–805 (2007).
DOI: 10.1007/s00339-007-3923-y

[38] Ho C-H., Liu C-D., Hsieh C-H., Hsieh K-H., Lee S-N.: High dielectric constant polyaniline/poly(acrylic acid) composites prepared by in situ polymerization. Synthetic Metals, **158**, 630–637 (2008).
DOI: 10.1016/j.synthmet.2008.04.014

[39] El-Tantawy F., Abdel-Kader K. M., Kaneko F., Sung Y. K.: Physical properties of CdS-poly (vinyl alcohol) nanoconducting composite synthesized by organosol techniques and novel application potential. European Polymer Journal, **40**, 415–430 (2004).
DOI: 10.1016/j.eurpolymj.2003.10.013

[40] Pal K., Banthia A. K., Majumdar D. K.: Preparation and characterization of polyvinyl alcohol-gelatin hydrogel membranes for biomedical applications. AAPS PharmSciTech, **8**, E142–E146 (2007).
DOI: 10.1208/pt080121

[41] Giribabu K., Suresh R., Manigandan R., Vijayaraj A., Prabu R., Narayanan V.: Cadmium sulphide nanorods: Synthesis, characterization and their photocatalytic activity. Bulletin of the Korean Chemical Society, **33**, 2910–2916 (2012).
DOI: 10.5012/bkcs.2012.33.9.2910

eXPRESS Polymer Letters Vol.10, No.11 (2016) 895–913
Available online at www.expresspolymlett.com
DOI: 10.3144/expresspolymlett.2016.84

Polymeric nanoparticles: Recent development in synthesis and application

S. Mallakpour[1,2,3*], *V. Behranvand*[1]

[1]Organic Polymer Chemistry Research Laboratory, Department of Chemistry, Isfahan University of Technology, 84156-83111 Isfahan, Islamic Republic of Iran
[2]Nanotechnology and Advanced Materials Institute, Isfahan University of Technology, 84156-83111 Isfahan, Islamic Republic of Iran
[3]Center of Excellence in Sensors and Green Chemistry, Department of Chemistry, Isfahan University of Technology, 84156-83111 Isfahan, Islamic Republic of Iran

Received 18 April 2016; accepted in revised form 25 June 2016

Abstract. Nanosized particles have attractive characteristics, which have received considerable attention in the last decade. Polymeric nanoparticles (PNP)s are solid particles or particulate dispersions with size in the range of 10–1000 nm. Due to the very small size, the surface area is very large so the percentage of atoms or molecules on the surface is significantly increased, which is expected to have extensive applications in various fields such as drug delivery systems, biosensors, catalysts, nanocomposites, agriculture and environment. The aim of the present paper is to critically review enhancement in the field of synthesis and different application of novel PNPs in various area from drug delivery to composite fabrication. Literature sources were mainly taken from the publications of 2011 and later; though, for a basic depiction of the structural principles, older publications have also been cited.

Keywords: *biopolymers, biocomposites, polymeric nanoparticles, drug delivery systems, biosensors*

1. Introduction to polymer nanoparticles (PNP)s

Particles with diameters below the micron dimension: generally, in the range 10–100 nm are nanoparticles (NP)s [1]. Polymer-based NP (PNP) is a collective term which is given to any kind of polymer NP, but specifically is applied for nanospheres and nanocapsules [2]. The historical development of PNPs was created by Paul Ehrlich with the first experimental efforts by Ursula Scheffel. Extensive works were conducted by the group of Peter Speiser at ETH Zürich in the late 1960s and early 1970s [3].

The field of PNPs is quickly growing and playing a key role in extensive field of areas ranging from photonics, electronics, sensors, medicine, pollution control and environmental technology. PNPs have long been used as main components in established everyday coatings, paints and adhesives products. More recently, they have found applications in biomedical fields such as bio-imaging, drug delivery and diagnostics. PNP-based materials with unique physical and chemical characteristics might become future commands for the progress of new nanomaterials [4–7].

As a contribution to updating the state of knowledge and due to importance of PNPs, the present review focuses on PNPs. The aim of this review article is primarily to provide short information about traditional preparation ways of PNPs. Then, we would like to show some recently reported methods like using ultrasonic and microwave tools as other environmentally friendly approaches for the PNPs preparation in the first section. From our point of view, the use

*Corresponding author, e-mail: mallak@cc.iut.ac.ir

of these methods as low cost and safe ways should be highlighted. Furthermore, their importance according to their applications discusses. We will also show some properties of them such as morphology and biological activity.

2. Green techniques in synthesis of NPs

The manufacturing techniques of PNPs are classified due to whether the particle formation involves a polymerization reaction or NPs are produced directly from a preformed polymer or by direct polymerization of monomers using classical polymerization or polyreactions [7, 8]. Direct polymerization of monomers can be accomplished through different polymerization techniques such as micro-emulsion, mini-emulsion, surfactant-free emulsion and interfacial polymerization. The preparation of PNPs from preformed polymers can be carried out via methods like solvent evaporation, salting-out, dialysis and supercritical fluid technology. Methods like rapid expansion of supercritical solution and rapid expansion of supercritical solution into liquid solvent and surfactant-free emulsion polymerization can be successfully applied for manufacturing surfactant-free PNPs and moreover they are environment friendly [2]. In this section we want to introduce ultrasonic and microwave tools as another environmentally friendly approaches for the PNPs preparation.

2.1. Ultrasonication

Ultrasound (US) is presently a common laboratory tool applied to disperse NPs and colloids and to nebulize solutions into fine mixtures [9]. This method is advantageous because it is nontoxic, rapid in reaction rate, and produces very small particles [10]. US provides rather unusual reaction conditions (such as: temperatures of ~5000 K, pressures of ~1 GPa, and cooling rates of ~1010 $K \cdot s^{-1}$) in contrast to the traditional energy sources. In fact, acoustic cavitation causes sonochemistry. Irradiation of liquids with acoustic waves of US creates the bubbles and makes the bubbles to oscillate. The bubbles collect ultrasonic energy while growing. A bubble can overgrow and collapse within a very short lifetime and a large energy concentration is attained. Consequently, various chemical reactions can proceed at room temperature using US irradiation [11, 12]. For example, the synthesis of colloidal silver NPs by using starch as reducing and stabilizing agent under sonication was accomplished by Kumar *et al*. [13]. Sonochemical reduction showed a remarkable potential for producing desired particle size colloidal silver NPs. It was more environmentally friendly and safer than other synthetic methodology. A variety of 1,3,5-triaryl-1,3,5-hexahydrotriazine was synthesized using ultrasound assisted reactions from the reactions of aryl amines with aqueous formaldehyde by Singh *et al*. [14]. The use of ultrasound provided an efficient, clean and rapid methodology for the synthesis of various 1,3,5-hexahydrotriazine derivatives. In addition, it caused greater yields than the previously reported conventional methods.

2.2. Microwave (MW)

A fast technique of heating materials for industrial, domestic, and medical usages is MW heating. Reduction of the reaction time, controlling the reaction conditions, monitoring of temperature, pressure, and reaction times, higher yields in shorter reaction time are key advantages of MW apparatus [15, 16]. Medium needs to have a high dielectric constant for performing reaction in a solvent under MW irradiations. There are excellent organic solvents such as 1-methyl-2-pyrrolidone (NMP), dimethylsulfoxide (DMSO) and *N,N*-dimethylformamide (DMF) for carrying out the reaction but solvents should be removed at the end of the reaction and they are also toxic [16, 17]. Room temperature ionic liquids (IL)s efficiently absorb MW energy due to their high polarity. ILs are green organic salts consisting only of ionic species that melt being below 100 °C or even at room temperature which have attracted much attention as solvent for the polymerization [18]. The combination of MW-assisted reactions with IL has been applied for the synthesis of various nanomaterials [19].

Recently, Sun *et al*. [20] synthesized fluorescent carbon dots using single precursor, ammonium citrate dibasic using cheap home-use microwave oven as a facile and ultrafast method for the first time. In 2015, Hasanpoor *et al*. [21] obtained ultrafine zinc oxide (ZnO) particles with controlled morphology using microwave irradiation by various methods. They examined the effect of precursor type as well as the time and the microwave irradiation power on the structure and size of ZnO NPs. By increasing the time of synthesis needle-shaped particles with a diameter of 50–

150 nm could be attained and with increasing the microwave power flower-shaped particles were obtained.

3. Recent development in synthesis of PNPs

In this section, novel and modified processes for the production of PNPs through the polymerization of monomers are discussed. Till 2013, emulsion polymerization is the best-proven and most generally used method [22]. In nano-emulsion formation, the spontaneous emulsification occurs with mixing of an aqueous phase and organic phase. The aqueous phase consists of hydrophilic surfactant and water, whereas the organic phase is a homogeneous solution of lipophilic surfactant, oil and water-miscible solvent. At the end of the reaction, PNPs with very small droplets (50–100 nm) will form [23]. It is known that this method requires large amounts of surfactant/co-surfactant to make small NPs which increases cost and causes difficulty of purification [8]. So, 'acoustic emulsification' as one of the powerful tools for fast and environmentally friendly emulsion production was applied by Nakabayashi *et al*. [22] to obtain size-controlled poly(methyl methacrylate) (PMMA) NPs. They developed a novel synthesis method for size-controlled PNPs under surfactant free conditions using sequential ultrasonic irradiation. Figure 1 shows sequential ultrasonic irradiation (20 kHz → 500 kHz → 1.6 MHz → 2.4 MHz) steps for acoustic emulsification of a water insoluble monomer methylmethacrylate (MMA) in an aqueous medium. Polymerization happened by the addition of initiator [ammonium peroxodisulfate (APS)] and to stop the polymerization, the reaction vessel was cooled to 25 °C. PMMA

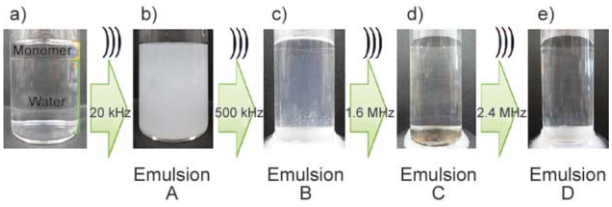

Figure 1. Photographic observations of tandem acoustic emulsification of MMA in aqueous solution. Photograph (a) represents the original MMA in aqueous solution mixture. Emulsification conditions were (b) 20 kHz, 8 min; (c) 20 kHz, 8 min → 500 kHz, 10 min; (d) 20 kHz, 8 min → 500 kHz, 10 min → 1.6 MHz, 10 min; and (e) 20 kHz, 8 min → 500 kHz, 10 min → 1.6 MHz, 10 min → 2.4 MHz, 10 min [22].

samples which were synthesized from emulsion (a) showed average particle size of 241 nm. Ultrasonication with 2.4 MHz after 20 kHz, 500 kHz, and 1.6 MHz produced particles with size of 23 nm. Higher frequency of ultrasonication could break up the larger droplets to create smaller droplets.

Recently, Mallakpour and coworkers [24] reported in detail the use of MW irradiation for the polycondensation of diacids containing different amino acids such as phenylalanine, leucine, isoleucine, valine and alanine with aromatic diamine. Step-growth polymerization reactions were carried out in molten tetra-n-butylammonium bromide salt (TBAB) and IL/triphenyl phosphite (TPP) under MW irradiation. Under this conditions, poly(amide-imide) (PAI) nanostructures were obtained. According to field emission scanning electron microscopy (FE-SEM) micrographs, the PAI was obtained with the particle size of smaller than 45 nm in more cases. Then, the effect of ultrasonic irradiation on the size and shape of PAI NPs was investigated. FE-SEM micrographs showed that after sonication process, the size of PAI particles was decreased and reached to 28–38 nm (Figure 2).

The influence of sonication and MW irradiations on the morphology and shape of different poly(ester-imide)s (PEI)s and PAIs containing natural amino acids was investigated and novel PNPs obtained by our group. Due to the presence of amino acids in their backbones, these polymers are expected to be biodegradable and hence could be categorized under environmental benign materials [25–32]. In 2013, the synthesis of several chiral nanostructure PAIs was performed under conventional heating and MW irradiation in IL media by Mallakpour and Dinari [33] to highlight the effect of MW heating. To provide the optimum reaction conditions, the influence of MW power levels and duration of heating was inspected and the results were summarized in Table 1. The best inherent viscosity and yield were obtained after 3 min at 90% (810 W) of MW power level according to this Table. The inherent viscosities of the resulting polymers under oil bath conditions (conventional heating) were in the range of 0.41–0.58 $dL \cdot g^{-1}$ and the yields were 83–94%. The FE-SEM images of the resultant PAIs prepared by MW irradiation showed nanostructure morphology of PAI with size smaller than 60 nm while the size of PAI synthesized under conventional heating was smaller than 70 nm.

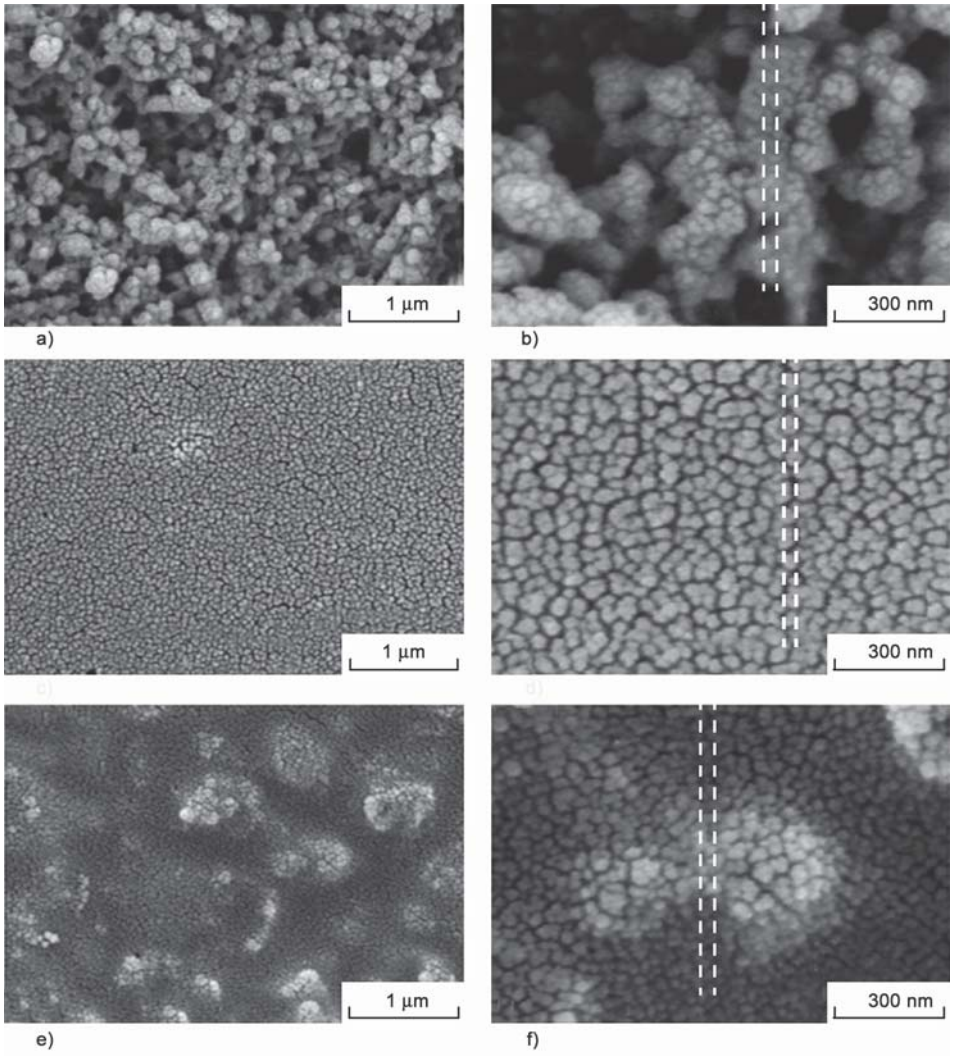

Figure 2. FE-SEM micrographs of (a and b) PAI-5a, (c and d) PAI-5b, and (e and f) PAI-5c after sonication process [24]

Table 1. Optimization of reaction conditions for the preparation of PAI1a using MW irradiation in molten TBAB [33].

Polymer	Microwave power	Reaction time [s]	Yield [%]	η_{inh}[a] [dL/g]	$[\alpha]_D^{25}$ [a]
PAI1a	100	60	67	0.32	–46.64
PAI1a	100	120	62	0.32	–47.02
PAI1a	100	180	58	0.31	–47.00
PAI1a	100	240[b]	–	–	–
PAI1a	90	60	74	0.32	–50.80
PAI1a	90	120	78	0.38	–52.41
PAI1a	90	180	92	0.47	–52.43
PAI1a	90	240[b]	–	–	–
PAI1a	80	60	50	0.30	–49.47
PAI1a	80	120	57	0.31	–50.52
PAI1a	80	180	59	0.34	–50.14
PAI1a	80	210	63	0.35	–49.87

[a]Measured at a concentration of 0.5 g/dL in DMF at 25 °C,
[b]Decomposition occurred at higher power or extended irradiation time

Mallakpour and coworkers [34, 35] prepared the optically active and biodegradable polymers containing S-valine and L-leucine amino acids under MW irradiations. The obtained PAIs showed relatively spherical morphology with particle size smaller than 50 nm in more cases. The results showed that the diacids and aforesaid polymers were all nontoxic to fungal growth and all samples were colonized by fungal mycelia. The resulting samples showed weight loss due to fungal degradation while no weight loss could be detected in bisphenol-A (BPA) as control. Figure 3a demonstrates that BPA completely inhibited wheat seedling growth compared to grown seedling in control soil and lastly killed the plantlet because of its toxicity for plant growth. On the other hand, wheat seedling growth in soil containing the monomers and PAIs proposed that polymeric products have not substantial inhibition influence on normal plant growth (Figures 3b–e).

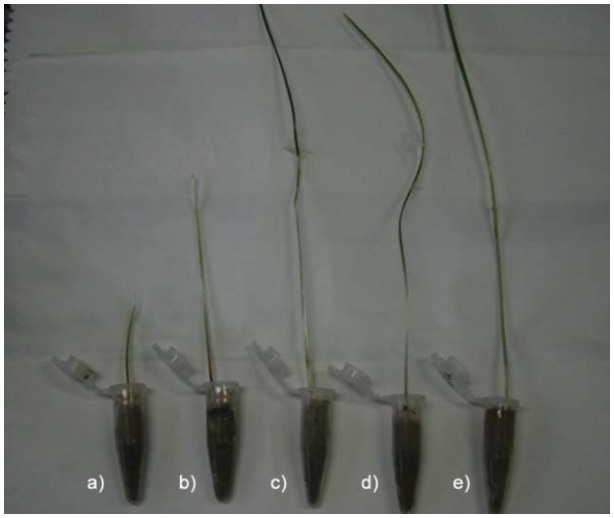

Figure 3. Effect of (b) PAI2, (c) diacid 7b, (d) diacid 7a and (e) PAI1 compared with (a) BPA on survival and growth of wheat seedlings [35]

The facile preparation of diverse and functional NPs with negatively and positively charged functionalities derived from a CO_2-based triblock amphiphilic polycarbonate system from a sequential copolymerization and chemical transformation strategy was reported by Wang *et al*. in 2015 (Figure 4) [36].

The results indicated that polymer **5** have not formed shell–core structure. In contrast, the dynamic light scattering (DLS) studies of anionic block polymer **4** and cationic polymer **6** presented that they underwent gathering to form NPs with high uniformity, giving a similar intensity-averaged hydrodynamic diameters of 26±15 nm. Both displayed a similar critical micelle concentration (CMC) of 66 mg·mL^{-1} in DI water. They expressed that these CO_2-based polycarbonates could afford a powerful platform for biomedical applications.

In 2015, Crucho and Barros [37] reported preparation of PNPs from the chemical modification of poly (D,L-lactide-co-glycolide) (PLGA) with sucrose and a cholic acid moieties (abbreviated as Suc-PLGA-Chol). They expressed that altering the polymer backbone not only can improve the physicochemical features of the PNPs but also their safety in biomedical applications. The synthesis of Suc-PLGA-Chol polymer conjugates was done through esterification. Virtually perfect spheres of lyophilized Suc-PLGA-Chol PNPs with a mean particle size of 260±50 nm were observed in SEM image. Several experimental parameters such as polymer concentration, organic solvent and evaporation rate were examined too. To evaluate dependence of the size of PNPs on the solubility parameters, acetone, acetonitrile, tetrahydrofuran as organic solvents were used for the preparation of Suc-PLGA-Chol PNPs. Using the most water miscible solvent (acetone) smaller particles were obtained. It could be ascribed to a more effectual solvent diffusion and faster polymer dispersion into water. The mean particle size of PNPs increased with increasing polymer concentration which is attributed to the slower solvent diffusion and formation of larger droplets during phase mixing. In 2015, Kumar's group reported an effective and simple technique for synthesizing highly fluorescent, protein-based NPs [38]. Figure 5 shows current approach of the synthesis of Prodots which made from bovine serum albumin (nBSA), glucose oxidase (nGO), horseradish perox-

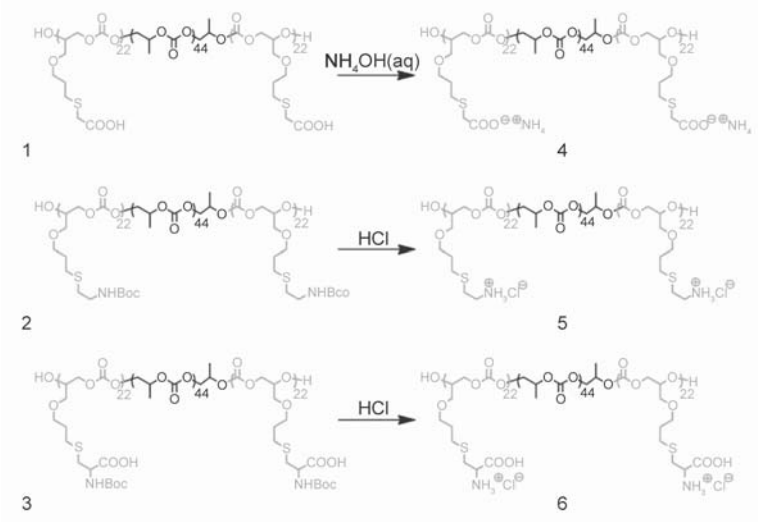

Figure 4. Synthesis of amphiphilic block polycarbonates with different charges. Boc = tert-butoxycarbonyl [36]

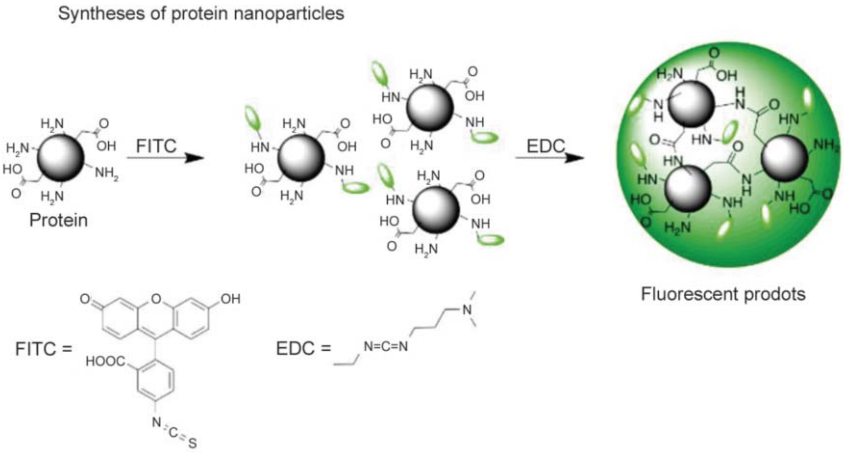

Figure 5. Prodot synthesis by FITC labeling followed by EDC cross-linking of the resulting protein clusters [38]

idase (nHRP), catalase (nCatalase), and lipase (nLipase). The amino groups of the lysine residues of proteins were coupled with fluorescein isothiocyanate (FITC) followed by controlled aggregation of proteins. Then, cross-linking the protein units was done by 1-ethyl-3-(-3-dimethylaminopropyl) carbodiimide (EDC). In this study, FITC labeling of proteins was accomplished to cross-link these clusters and form stable particles.

Transmission electron microscopy (TEM) micrographs showed nGO particles with size ~10 nm, while nHRP had a diameter of ~20 nm and nLipase a diameter of ~15 nm. Prodots showed enhanced thermal stabilities and improved half-life besides to conserved biological activity, and these unique properties may facilitate their usage in imaging. Their aim of producing stable, fluorescent, functional, biocompatible Prodots of controllable size was testing the potential of the Prodots for cellular imaging. The results showed enhanced thermal stabilities and improved half-life besides to conserved biological activity of Prodots, and these unique properties may facilitate their usage in imaging.

Klymchenko's group [39] investigated the effect of one to two charged groups per polymer chain to obtain ultrasmall PNPs as nanocarriers. Positively charged trimethylammonium groups or negatively charged carboxylate and sulfonate were introduced into the PLGA, PMMA, and polycaprolactone (PCL). They concluded that the existence of charged groups per polymer chain can strongly decrease the size of PNPs made by nanoprecipitation(PPN). As it could be observed from TEM images, the size of particles made from uncharged chains was largest for all three polymers (above 100 nm). The TEM images of uncharged and carboxy PMMA particles represented a strong affinity of aggregation. Trimethylammonium and sulfonate-bearing polymers obtained the smallest particles (below 25 nm). They further exhibited that small NPs of 15 nm size preserve the capacity to encapsulate capably large quantities of ionic dyes with bulky counterions which creates PNPs 10-fold brighter than quantum dots of the same size.

Kausar and coworkers [40] synthesized polystyrene (PS) NPs through modified nanoprecipitation cosolvent evaporation technique (NcoSE) and two widely used strategies, i.e., solvent evaporation and NPP to examine the scope of the novel technique. The usage of modified NcoSE method improved several material properties such as the simplicity of fabrication, effectiveness, homogeneous and uniform morphology, narrow size distribution, and suitability for the composite fabrication compared to other extensively used techniques. FE-SEM image showed the spherical morphology, uniform size distribution and ordered nanostructures for obtained PSNPs/SiNPs by NcoSE method while the rough and unclear surface topology of grafted NPs were observed for PSNPs/SiNPs synthesized through NPP and solvent evaporation methods. Silica NPs and graphite were incorporated into the obtained PS NPs to study the scope of this novel method. The results revealed the improved conductivity and thermal properties of PS and Si NP-grafted graphite CNs.

In 2015, polyamic acid (PAA) formation was attained using precipitation with a compressed fluid antisolvent technique [41]. The particle size of obtained PAA was decreased with decreased PAA con-

centration, decreased temperature and increased pressure. Subsequently, the polyimide NPs synthesized by thermal imidization treatment of PAA.

4. Application of PNPs

Due to the attendance of characteristic properties presented by PNPs, these materials exhibit important roles in several applications including NCs preparation, optoelectronic and drug delivery. In this section, the design, morphology examination as well as application of two classes of PNPs are reviewed in detail: conducting polymers including polypyrrole, polyaniline (PANi), polyacetylene, poly(p-phenylene-vinylene) and polythiophene which have been a popular subject of exploration [42] and biosafe PNPs that are another important class of polymers and have many advantages such as biocompatibility and biodegradability. They are easily removed from the body by the normal metabolic path or they can have susceptibility to fungal enzymatic degradation [43–45].

4.1. Application of conductive nanostructure polymers

Conducting micro-/nano-structure polymers received increasing attention due to their specific electronic properties and potential applications in rechargeable batteries, electrochromic displays [46], corrosion inhibition and camouflage [47]. Conductive polymers are polymers with highly unpaired (π) conjugated polymeric chains. In comparison to their bulk forms nanostructured conductive polymers, provide several advantageous features, such as large surface areas, improved mechanical properties for strain housing and shortened paths for charge/mass/ion transport [48].

Among the conducting polymers, polypyrrole (PPy), is one of the most widely studied electronic materials which have potential applications in drug delivery, sensors and corrosion protection [49, 50]. Samanta *et al*. [51] synthesized PPy NPs without the use of dopants. They loaded these PPy NPs with fluorescein sodium salt, a negatively charged model drug, and rhodamine 6G, a positively charged model drug. PPy was used because it is an electrically conducting polymer which is both nontoxic and biocompatible. The obtained NPs exhibited good drug loading capacity. They showed that PPy NPs can be adjusted to release drugs at both acidic and basic pH by varying the pH. In other work, Chen *et al*. [52] synthesized PPy NPs with size of 50 nm as a metal-free ultraviolet (UV)/

near-infrared (NIR) shielding material and mixed them with polyacrylic acid (PAA) resin for the preparation of PPy–PAA full-polymer films. Their results showed that PPy–PAA films have great potential as novel coating in the application of cost-efficient energy-saving windows without potential pollution.

Alizadeh *et al*. [53] synthesized two types of potentiometric sensors, based on the nano-sized molecularly imprinted polymer (MIP) for high selective determination of promethazine. Two different methods containing microemulsion polymerization and suspension polymerization in silicon oil were applied to prepare nano-MIP(1) and nano-MIP(2), respectively. SEM images of the obtained polymers showed very small and spherically shaped particles. The results of the rebinding experiments represented that the binding sites of the nano-MIP(2) obtained by suspension polymerization in silicon oil had more affinity to target molecules, comparison to those of the nano-MIP(1). The results of the rebinding experiments for both MIPs in aqueous phase are shown in Table 2. It can be observed that in the case of promethazine, the adsorption ability of the nano-MIP(2) is more than that of the nano-MIP(1). In addition, it is clear that the difference between the adsorption capability of the chlorpromethazine and promethazine on the MIP(1) is more than that of nano-MIP(2), demonstrating higher selectivity of nano-MIP(2), compared to nano-MIP(1). Also, the nano-MIP(2) based sensor, displayed higher selectivity and sensitivity, compared to the nano-MIP(1) based electrode.

Vaitkuviene *et al*. [54] synthesized pure polypyrrole (Ppy NPs) by one-step oxidative polymerization and in order to study about biocompatibility of Ppy, their cyto-compatibility was assessed. The effect of different concentration of Ppy NPs on primary mouse

Table 2. Adsorption capabilities of promethazine and chlorpromethazine to the nano-MIP(1) and nano-MIP(2) and their relevant NIPs [53]

Polymer type	Adsorption amount [mmol/g]	
	Promethazine	Chlorpromethazine
nano-MIP(1)	0.51	0.36
nano-MIP(1)	0.47	0.23
nano-MIP(2)	0.85	0.47
nano-MIP(2)	0.37	0.26

embryonic fibroblasts (MEF), mouse hepatoma cell line (MH-22A), and human T lymphocyte Jurkat cell line was examined. Achieved results exhibited that Ppy NPs at low concentrations are biocompatible, whereas at high concentrations they got cytotoxic for MEF, Jurkat and MH-22A cells, and it was concluded that cytotoxic effect is dose-dependent.

Polyaniline (PANi) is one of the oldest known and the most widely studied conducting polymer due to unique doping mechanism, its relative ease in preparation, low specific mass, good environmental stability and controllable conductivity [55–57]. It has numerous applications in rechargeable batteries, anticorrosion coatings, energy storage, photovoltaic devices, catalyst, electrochromic displays and electronic switches [58, 59]. Berti *et al*. [60] developed and characterized conductive PANi nanostructures for applications in electrochemical biosensing. PANi nanotubes were arranged in an ordered structure directly on an electrode surface using nanoporous alumina membranes as nano-mould. Then, grafting of PANi was done with a MIP receptor to create a model sensor for catechol detection. Actually, PANi nanostructures as conductive nanowire system allowed direct electrical connection between the synthetic receptor (MIP) and the electrode. A significantly lower detection limit for catechol attained, thus representing that the nanostructures are capable of improving the analytical performance of the sensor. A simple chemical route for synthesizing highly crystalline PANi NPs was proposed by Mahato *et al*. [61]. It was carried out by an *in-situ* polymerization of aniline monomers in a hot and dilute aqueous acidic solution. The particles with diameter ranging from 15 to 30 nm appeared as circular disk like structures in TEM image (Figure 6). The polymer exhibited good thermal stability. The PANi NPs were utilized for preparing composite with graphene NPs (2wt% loading). It was tested as a coating material for protection of mild steel from corrosion in 0.1 N HCl. Still surface with composite coating (thickness of ~0.5 mm) showed good corrosion protection to mild steel surface in acidic environment.

Recently, Hong *et al*. [62] demonstrated an acidic environmental sensing technique based on PANi NPs. In this regards, PNs were immobilized to an aminated glass substrate to sense environmental pH conditions. The fabricated PANi NPs showed outstanding capabilities to sense acidic environments at the single NP level. In 2016, Luo *et al*. [63] reported the design and production of a novel MIP conductive PANi NPs using polymeric micelle as nanoreactor for enhanced paracetamol (PCM) detection. The obtained PANi sensor showed high selectivity toward PCM. It also revealed a wider linear range over PCM concentration which was attributed to numerous effective recognition sites among the PANi matrix and it was due to the large specific surface area of PANi NPs. Considerably lower detection limit was obtained compared to previously reported PCM electrochemical sensors that should be attributed to the electrical conductivity of PANi.

4.2. Application of biodegradable nanostructure polymers

Biodegradable polymers can be classified as artificial or natural. Polysaccharides, nucleic acids and proteins are the illustrative natural biodegradable

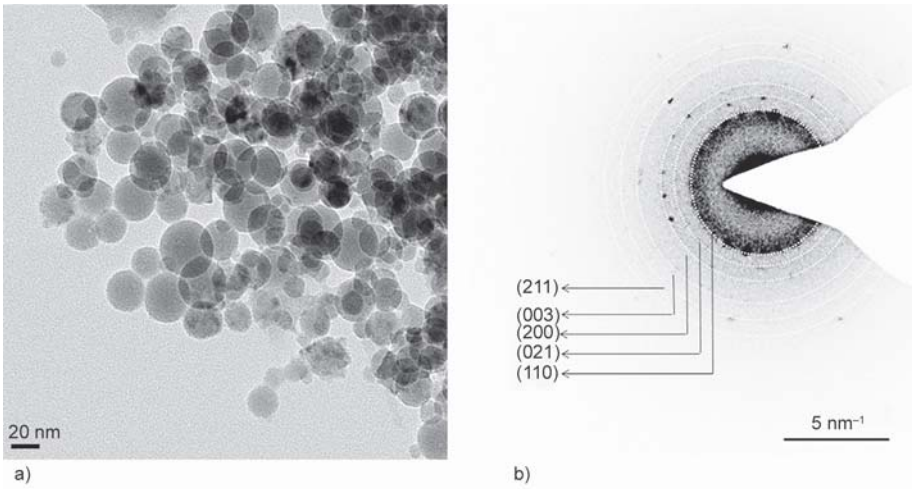

Figure 6. (a) TEM image and (b) selected area diffraction pattern of the PANi NPs [51]

polymers. Polyesters and polyamides are typical examples for the artificial polymers [64]. Due to their biodegradability, good biocompatibility and minimal side effects, usage of biodegradable polymers for biomedical applications has increased in recent decades. The biodegradable polymeric NPs provide controlled release of bioactive compounds, and improve properties such as stability and bioavailability [65]. Nano-particulate delivery system can effectively control particle size, surface character; it enhances permeation, solubility, flexibility, and release therapeutically active agents to reach the target and attain specific activity at a predetermined rate and time [66, 67]. PLGA is one of the most successfully applied biodegradable nanosystem for the development of nanomedicines because it is a copolymer and can hydrolyze in the body to produce the biodegradable metabolite monomers, lactide and glycolide that are finally removed from the body by the citric acid cycle [68]. Poly(lactic acid) (PLA) is one of the most popular members of biodegradable polymers that can be naturally degraded in compost or soil by enzymes or fungi [69]. Surface grafting copolymerization of glycidyl methacrylate (GMA) on PLA NPs was accomplished through emulsion/evaporation procedure as a novel method by Li *et al*. [70]. Rhodamine B (RhB) initially interacts with sodium dodecyl sulfate (SDS) through electrostatic interaction to generate hydrophobic complex of SDS-RhB. According to the high-affinity of SDS-RhB with GMA, hydrophilic RhB can be successfully joined into PLA NPs. The obtained results indicated that the PLA with particle size smaller than 200 nm can prevent the macrophage uptake. On the other hand, the bigger PLA particles with polyethylene glycol (PEG) surface modification showed the lowest internalization by macrophage comparison to those with poly(ethylene oxide-propylene oxide) copolymer or poly (vinyl alcohol) (PVA) surface. Yoo's group reported synthesis of PLGA NPs with well-defined sizes of ~70 nm (NP70), ~100 nm (NP100), ~200 nm (NP200), ~400 nm (NP400), ~600 nm (NP600) and ~1000 nm (NP1000) [71]. The NPs showed high yield with a narrow size distribution. Uniform size distribution and mean size of 103.7 nm for NP100, 204.6 nm for NP200, 421.1 nm for NP400, 604.8 nm for NP600 and 990.0 nm for NP1000 were obtained. The obtained results showed as particle size becomes

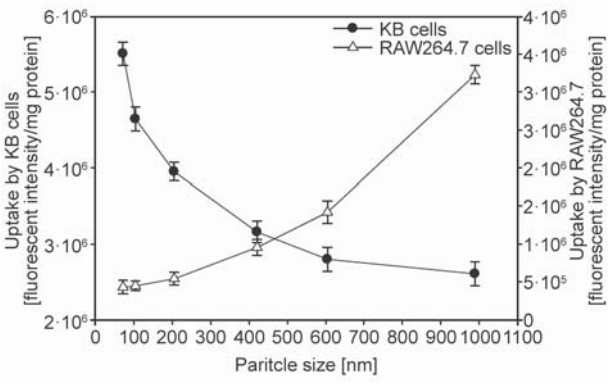

Figure 7. Quantification of the cellular uptake by KB carcinoma cells (closed circle) and RAW264.7 cells (open triangle). Data were expressed as mean ±SD (n = 6) [71]

smaller, cellular uptake and toxicities increased in tumor cells and decreased in macrophages (Figure 7). They also found that paclitaxel (PTX)-loaded NPs showed a size-dependent inhibition of tumor cell growth and the size-dependency was influenced by cellular uptake and PTX release.

Reinforcement of biomolecules within biodegradable NPs and further insertion of such carriers into tissue-engineered scaffolds will provide a controlled-release drug delivery system. With this in mind, Nazemi *et al*. [72] investigated the influence of adding PLGA NPs on a chitosan-bioactive glass (CH–BG) scaffold. They prepared two groups of scaffolds (with and without NPs) and studied drug release. The SEM micrographs showed nearly spherical morphologies of the PLGA NPs which were uniformly distributed on the scaffolds pore walls. According to these images, the PLGA NPs loading into the CH–BG scaffolds did not considerably affect the microarchitecture of the scaffolds. It was reported that the incorporation of these NPs slightly decreased the swelling behavior of the scaffolds whereas increased the mechanical strength. In addition, it was mentioned that the obtained scaffolds containing PLGA NPs could be used as bioactive bone tissue engineering scaffolds with the potential of localized delivery of biological molecules (Figure 8).

Folic acid (FA)-conjugated chitosan (CS)-functionalized PLGA nanocarriers for treatment of prostate cancer were designed by Dhas *et al*. [43]. PLGA NPs were coated using FA–CS conjugates for binding with folate receptors. A cell toxicity assay verified that functionalized PLGA NPs were more effective than un-functionalized ones according to modified

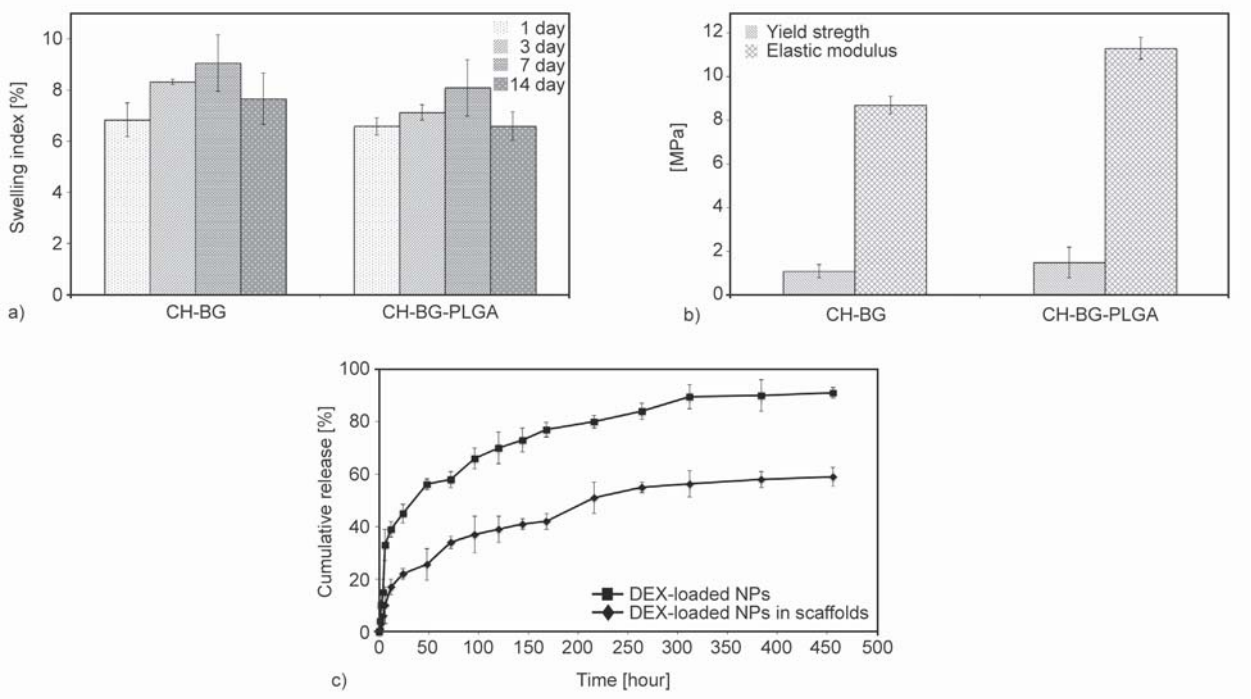

Figure 8. (a) The Swelling behavior in PBS solution, (b) the mechanical behavior of the scaffolds from compression tests, and (c) the *in vitro* release profile of DEX from either free NPs or NPs incorporated within the scaffolds [72]

surface, which can improve the efficiency of NPs by increasing cell targeting and/or tissue targeting and/or site-specific delivery PLGA NPs.

Mallakpour *et al*. [73] designed chiral bioactive PEIs containing L-phenylalanine and L-leucine amino acids with nanoscale size and good thermal stability. In vitro toxicity studies and soil biodegradation test confirmed that synthesized polymers could be decomposed by soil microorganisms hence they were biodegradable. They applied the obtained PEI containing L-leucine amino acid as matrix to prepare multi-walled carbon nanotubes (MWCNT)s bionanocomposites (BNC)s [74]. Thermal analysis showed improvement in thermal stability of the composites compared to the neat PEI by the addition of the CNTs.

Abdolmaleki and coworkers synthesized optically active and potentially biodegradable poly(ester-amide)s (PEAs) based on tyrosine amino acid [75]. Nano spherical-shaped spheres of PEAs with average mean diameter as low as 79 up to 500 nm were obtained in this study. Higher number of colonies was counted from water extracts of soil containing diol and PEA than control treatments (Figure 9). In fact, soil burial test and dehydrogenase activity assay confirmed biodegradability of PEA NPs due to the presence of amino acid in the polymer backbone.

Afterward in 2014, they used from mentioned PEA for the fabrication of PEA/ZnO BNCs. They expressed that the synthesized NCs are expected to categorize as biologically active materials due to using

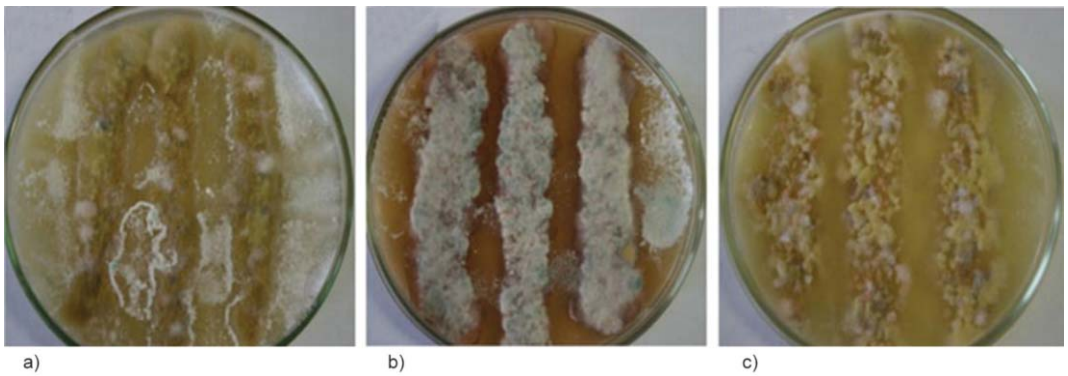

Figure 9. Fungal and bacterial colonies grown from soil water extract, 6 days after inoculation on PDA Petri plates: (a) PEA, (b) diol, and (c) control [75]

polymer based on biodegradable amino acid [76]. Hu *et al*. [77] studied assembled PNPs from gallic acid (GA) grafted chitosan (CS, GA-g-CS for GA grafted CS) and caseinophosphopeptides (CPP) to deliver (–)-epigallocatechin-3-gallate (EGCG) as novel functional foods. GA is a naturally occurring phenolic acid with high antioxidant activity. The GA-g-CS conjugates, compared with CS, exhibited much higher solubility under alkaline and neutral environments. Strong antioxidant activity and cytotoxicity against Caco-2 colon cancer cells were obtained by the GA-g-CS-CPP NPs. Paclitaxel is one of the most effective chemotherapeutic agents but it has poor water solubility and low therapeutic index so it needs an urgent solution to increase therapeutic efficacy of paclitaxel. According to this subject, in 2015, Thu *et al*. [78] designed synthesis of folate decorated paclitaxel loaded PLA-tocopheryl polyethylene glycol 1000 succinate (Fol/PTX/PLA–TPGS) NPs by a modified emulsification/solvent evaporation method. Targeting effect of the samples was evaluated by *in vivo* on tumor bearing mouse and *in vitro* on cancer cells. Research work showed that the cellular uptake of drug into cancer cells are improved by folate decorated NPs [79]. In this study, PTX loaded NPs induced better targeting influence than free PTX, and also the best operative targeting was related to Fol/PTX/PLA NPs. For examination of *in vivo* targeting effect of NPs, PTX in different constructions (free PTX, PTX/PLA–TPGS NPs and Fol/PTX/PLA–TPGS NPs) was intravenously administrated into mouse. The Fol/PTX/PLA–TPGS NPs demonstrated the best tumor growth inhibition after 42 days of treatment (Figure 10).

Barba group synthesized new nanovectors based on copolymer of α, β-poly(N-2- hydroxyethyl)-D,L-aspartamide (PHEA) and PLA to control release of lipophilic drugs [80]. The drug release happened in shorter times in comparison to PLA corresponding to the presence of hydrophilic PHEA, so the produced NPs could be introduced for semi-long term release drug delivery systems. Xu *et al*. [81] introduced novel PEG–PLA–polycaprolactone (PEG–PLA–PCL) NPs/DNA complex as a valid gene vesicle. This complex was even better choice for transfecting rabbit bone marrow stromal cells than con-

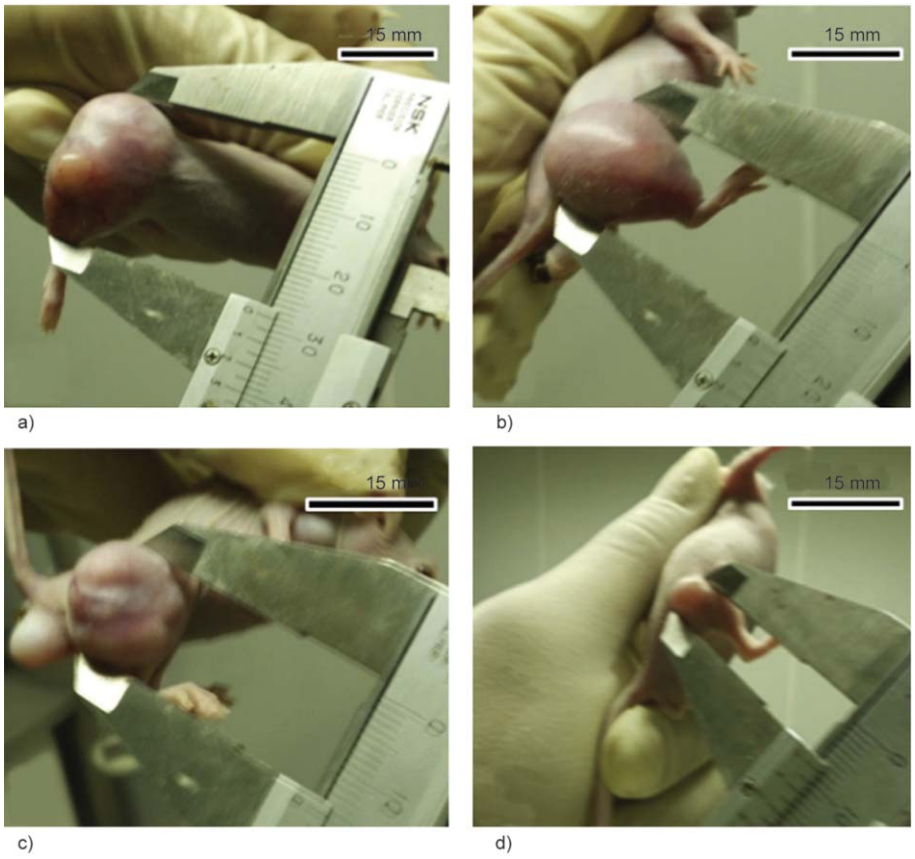

Figure 10. Tumor images of mouse after 42 days of treatment: (a) control, (b) free PTX, (c) PTX/PLA–TPGS NPs and (d) Fol/PTX/PLA–TPGS NPs [79]

ventional liposomes. The synthesized PLA/PCL particles as vehicles through supercritical fluid technology were applied by Moraes group [82]. The use of low PCL fractions (up to 20%) obtained suitable release of 17α-methyltestosterone hormone.

In general, encapsulation of drug happens into the polymeric particle and it is released in a controlled way by diffusion and erosion of the polymeric matrix. However, it was found that the hydrophobic character of the PLGA causes the nonspecific adsorption of plasma proteins directing to the uptake of the particles by the mononuclear phagocyte system and therefore their fast clearance from the body. It is recognized that this problem can be prevented if the particles are surface modified by the adsorption or grafting of hydrophilic polymers such as polyethylene glycol (PEG) or poly(ethylene oxide) (PEO) to improve its surface biocompatibility [83, 84]. In 2016, Gyulai *et al*. [83] with the aim to increase the potential of targeted drug delivery synthesized the end group derivative of Pluronics a promising drug carrier systems. Then, Pluronic and Pluronic-amine stabilized PLGA NPs were prepared by nanoprecipitation. When the Pluronic-amine derivative was applied for the NPs stabilization, intracellular antibacterial effect and in vitro efficiency increased. Also, tuneable surface modification of PLGA NPs had been accomplished by Kiss *et al*. in 2013 [84]. Rhodamine-6G labelled PLGA NPs were prepared by a double emulsion solvent evaporation freeze-drying method by Nkabine *et al*. [85]. The obtained PLGA NPs were non-cytotoxic to three different mammalian cell lines, which confirmed their safe usage as drug carrier systems.

4.3. Application of other class of nanostructure polymers

Amphiphilic poly(dimethylsiloxane) (PDMS)-containing poly(ether amine) (PDMS-gPEA) were synthesized by Di *et al*. [86]. The prepared PDMS-gPEA could directly self-assemble into stable uniform-sized NPs in aqueous solution. Temperature, pH and ionic strength could control their aggregation. The responsive PDMS-gPEA NPs showed the unique selective encapsulation of water-soluble dye and great potential in smart separations. Kuruppuarachchi *et al*. [87] used from polyacrylamide NPs with potential of delivery for photodynamic agents in photodynamic therapy for cancer. Dang *et al*. [88] investigated preparation of PS NPs with dendrimer-Ag shell and studied their application in catalytic reduction of 4-nitrophenol (4-NP). The presence of faintly thin outer layer of PS microsphere was related to the PAMAM dendrimer shell was observed in TEM images. The attached silver NPs onto the fourth PAMAM dendrimer shell were observed too. The synthesized PS@PAMAM-Ag NPs were packed into a column for reduction of 4-NP in the presence of $NaBH_4$ and showed adequate catalytic activity. Their results indicated that reactants could be catalyzed directly by the column system with stable flow rate and column pressure. They mentioned that this approach can decrease the loss of catalyst and prevent tedious and repeated separation using filtration or centrifugation for typical catalytic reactions. So, they concluded that it may also find application in other fields such as for antibacterial materials and in water treatment. Fritzen-Garcia, Creczynski-Pasa and coworkers [89] studied adsorption of peroxidase on PEGylated polyurethane (PU-PEG) NPs using a purified horseradish peroxidase (HRP). TEM image of the PEGylated PU NPs was shown in Figure 11a. Figure 11b displays incubated NPs by HRP with several little 'bubbles' around the NPs. As could be observed in Figure 11c, the localization of HRP molecules labeled with Au particles (dark spots with 10 nm size) is possible. Figure 11d representing the schematic of the TEM image of Figure 11c. This system was used as a modified carbon paste electrode for determination of dopamine in pharmaceutical products that showed improved detection limit and good performance in dopamine determination with less amount of enzyme adsorbed on PU-PEG NPs.

PS NPs with particle size range of 29.4–52.7 nm were manufactured via emulsion polymerization by Kong *et al*. [90]. Due to the lowered water to cement ratio, the use of superplasticizers has drastically altered the properties of concrete including workability, durability, impermeability and strength. Adsorption of polycarboxylate (PCE) superplasticizers on the cement surface creates the steric hindrance and electrostatic repulsion force which leads to better dispersion of cement grains in water media. Obtained results represented that the synthetic PNPs can also provide plasticizing influence to cement mixtures like as the traditional superplasticizers such

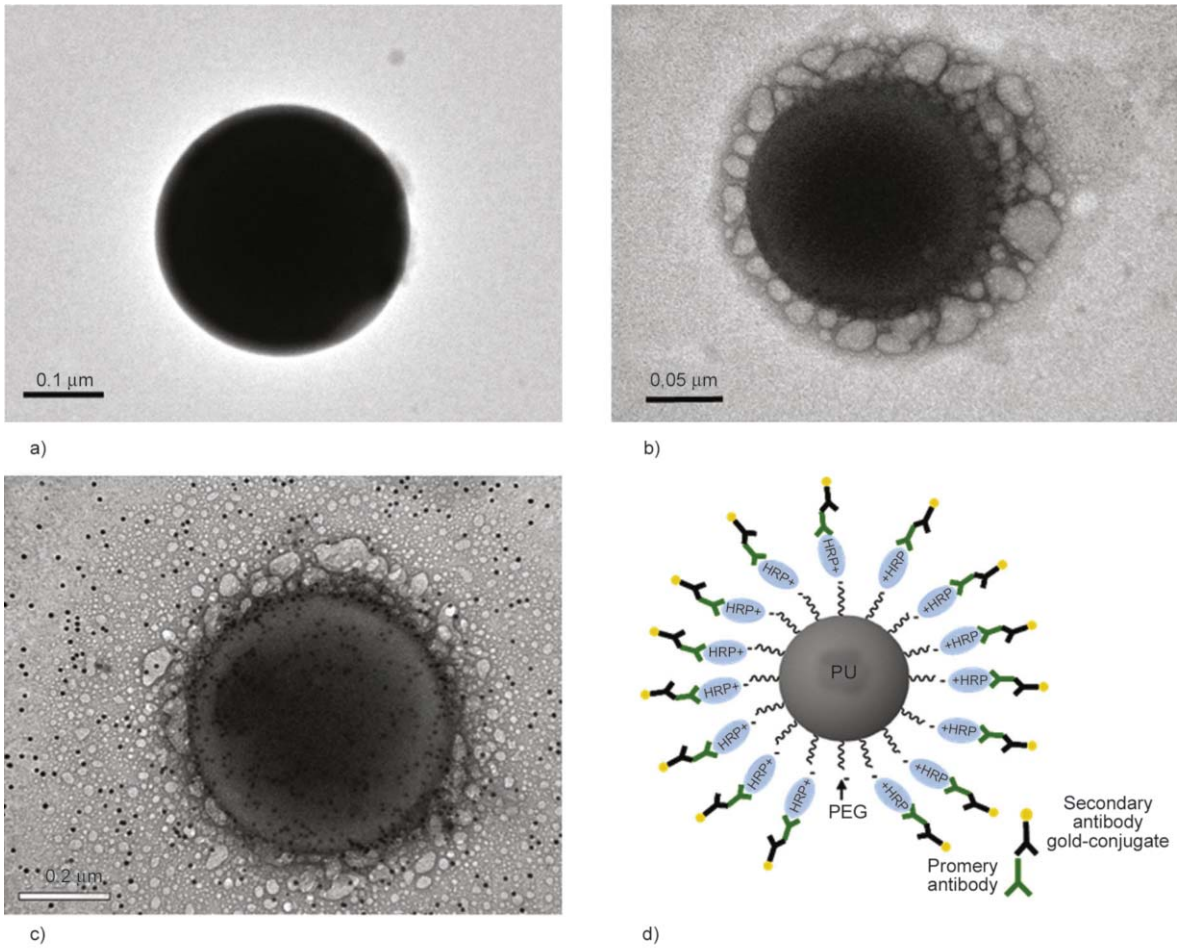

Figure 11. TEM images of (a) PEGylated PU NPs; (b) in the presence of HRP and (c) HRP molecules labeled with Au particles; (d) scheme representing the image 11c [89]

as PCE. TEM image of obtained PS NPs are shown in Figure 12 and displayed narrow particle size distribution of PNPs.

According to their funding, adsorbed PS NPs on the surface of cement grains could improve the fluidity of the fresh cement pastes (fcps) effectively. The fluidity of fcps increased with increase in quantity of PNPs. Also, the plasticizing effectiveness of PNPs was lower than that of PCE, which should be owing to their larger particle size and thicker adsorption layer on the surface of cement. Pu *et al*. [91] introduced semiconducting PNPs (SPNs) as near-infrared photoacoustic contrast agents for photoacoustic molecular imaging. They selected poly(cyclopentadithio-

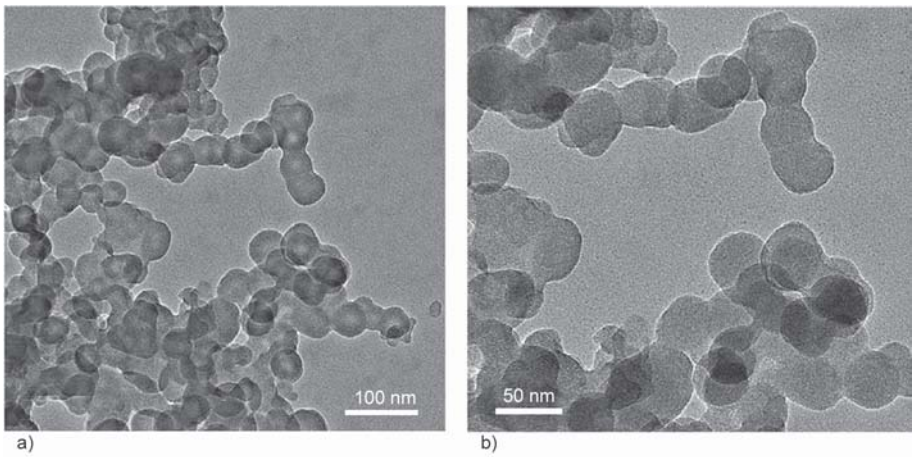

Figure 12. TEM images of the synthesized PS NPs [90]

phene-alt-benzothiadiazole) and poly(acenaphthothienopyrazine-alt-benzodithiophene) for the preparation of SPNs. Results showed that these NPs not only can generate a stronger signal than the usually used gold nanorods and single-walled carbon nanotubes on a per mass basis but also they are an ideal nanoplatform for enhancing photoacoustic molecular probes. Mallakpour *et al*. [92] synthesized poly (amide-benzimidazole-imide) (PABI) nanostructure containing amino acid. FE-SEM images showed nano-patterns of PABI particles with homogenous spherical shape. Then, PABI/Ag BNC was fabricated through in situ procedure. TEM image of obtained PABI/Ag NC represented good dispersion of Ag NPs in the PABI matrix. Also, resulting PABI/Ag NC exhibited antibacterial behavior rather than the pure PABI. Pure PABI was biologically active and undergoes biodegradability in soil burial test due to the presence of amino acid and also nitrogen functional groups in polymer backbone. More antibacterial effectiveness of the BNC rather than the pure PABI was obtained by embedding Ag NPs into the polymer matrix.

Because PS does not decompose in the cellular environment and is biocompatible with cells, it can be used as new drug delivery systems [93]. PS as biocompatible NPs with particle size of 44 nm were used as a model by Arciello and coworkers to analyze the endocytosis and uptake paths in primary human renal cortical epithelial (HRCE) cells [94]. These cells play a key role in the clearance of drugs. Results showed that PS NPs didn't exhibit any toxic influence to renal cells, and they were not released overtime. Therefore, they concluded that NPs could be used at low doses and, could to deliver drugs to specific targets upon functionalization with particular biomolecules. Also, they indicated that PS NPs entered HRCE cells through multiple mechanisms, either energy-independent or energy-dependent (endocytosis).

5. Conclusions

The combination of nanotechnology and polymers will be extremely useful in various applications, producing materials with unique properties. The first section of this review has provided information about recent developments in synthesis of PNPs. The using of ultrasound and MW irradiations as fast and green available methods was introduced for the preparation of PNPs too. Then, this review paper has focused on the properties and application of novel synthesized PNPs. The discussed nanostructured polymers have been applied as nanoreactors, coating materials, electrochemical biosensors, drug delivery, nanocarriers, catalysts and polymer composite fabrication. Due to main applications of PNPs in various fields, the demand for such materials is highly significant, and this is possibly one of the most important fields of research for the future. As could be observed in this review there has been a considerable research interest in the area of drug delivery using PNPs delivery systems as carriers for small and large molecules. The polymers used in delivery systems should be compatible with the body in the terms of adaptability (non-toxicity) and (non-antigenicity) and should be biodegradable and biocompatible. So, toxicity and environmental impact issues of these nanomaterials are of particular concern but are often ignored. Hence, the safety of PNPs, acute as well as long-term toxicity, should be addressed further, and special attention should be paid to off-target effects, demanding careful design and proper controls, as well as extreme caution in interpretation of data from *in vivo* studies. Another key issue about usage of PNPs is their potential effects on global economics, as well as speculation about various doomsday scenarios. These worries have accounted for a discussion among advocacy groups and governments on whether special statutory regulation of nanobiotechnology is warranted.

Acknowledgements

We are grateful for the financial support provided by the Research Affairs Division, Isfahan University of Technology (IUT), Isfahan. Further partial financial support from the Iran Nanotechnology Initiative Council (INIC), National Elite Foundation (NEF) and Center of Excellency in Sensors and Green Chemistry (IUT) is also gratefully acknowledged.

References

[1] Hanemann T., Szabó D. V.: Polymer-nanoparticle composites: From synthesis to modern applications. Materials, **3**, 3468–3517 (2010). DOI: 10.3390/ma3063468

[2] Rao J. P., Geckeler K. E.: Polymer nanoparticles: Preparation techniques and size-control parameters. Progress in Polymer Science, **36**, 887–913 (2011). DOI: 10.1016/j.progpolymsci.2011.01.001

[3] Lu X-Y., Wu D-C., Li Z-J., Chen G-Q.: Polymer nanoparticles. Progress in Molecular Biology and Translational Science, **104**, 299–323 (2011).
DOI: 10.1016/B978-0-12-416020-0.00007-3

[4] Wang Y-J., Larsson M., Huang W-T., Chiou S-H., Nicholls S. J., Chao J-I., Liu D-M.: The use of polymer-based nanoparticles and nanostructured materials in treatment and diagnosis of cardiovascular diseases: Recent advances and emerging designs. Progress in Polymer Science, **57**, 153–178 (2016).
DOI: 10.1016/j.progpolymsci.2016.01.002

[5] Nasir A., Kausar A., Younus A.: A review on preparation, properties and applications of polymeric nanoparticle-based materials. Polymer-Plastics Technology and Engineering, **54**, 325–341 (2015).
DOI: 10.1080/03602559.2014.958780

[6] He G., Pan Q., Rempel G. L.: Synthesis of poly(methyl methacrylate) nanosize particles by differential microemulsion polymerization. Macromolecular Rapid Communications, **24**, 585–588 (2003).
DOI: 10.1002/marc.200390089

[7] Nagavarma B. V. N., Yadav H. K. S., Ayaz A., Vasudha L. S., Shivakumar H. G.: Different techniques for preparation of polymeric nanoparticles – A review. Asian Journal of Pharmaceutical and Clinical Research, **5**, 16–23 (2012).

[8] Zhang G., Niu A., Peng S., Jiang M., Tu Y., Li M., Wu C.: Formation of novel polymeric nanoparticles. Accounts of Chemical Research, **34**, 249–256 (2001).
DOI: 10.1021/ar000011x

[9] Kharissova O. V., Kharisov B. I., Ruíz Valdés J. J., Méndez O. U.: Ultrasound in nanochemistry: Recent advances. Synthesis and Reactivity in Inorganic, Metal-Organic, and Nano-Metal Chemistry, **41**, 429–448 (2011).
DOI: 10.1080/15533174.2011.568424

[10] Zhang J., Du J., Han B., Liu Z., Jiang T., Zhang Z.: Sonochemical formation of single-crystalline gold nanobelts. Angewandte Chemie, **118**, 1134–1137 (2006).
DOI: 10.1002/ange.200503762

[11] Safarifard V., Morsali A.: Applications of ultrasound to the synthesis of nanoscale metal–organic coordination polymers. Coordination Chemistry Reviews, **292**, 1–14 (2015).
DOI: 10.1016/j.ccr.2015.02.014

[12] Bang J. H., Suslick K. S.: Applications of ultrasound to the synthesis of nanostructured materials. Advanced Materials, **118**, 1039–1059 (2010).
DOI: 10.1002/adma.200904093

[13] Kumar B., Smita K., Cumbal L., Debut A., Pathak R. N.: Sonochemical synthesis of silver nanoparticles using starch: A comparison. Bioinorganic Chemistry and Applications, **2014**, 784268/1– 784268/8 (2014).
DOI: 10.1155/2014/784268

[14] Singh A. K., Shukla S. K., Quraishi M. A.: Ultrasound mediated green synthesis of hexa-hydro triazines. Journal of Material Environment Science, **2**, 403–406 (2011).

[15] Dubey R., Moorthy N. S. H. N.: Comparative studies on conventional and microwave assisted synthesis of benzimidazole and their 2-substituted derivative with the effect of salt form of reactant. Chemical and Pharmaceutical Bulletin, **55**, 115–117 (2007).
DOI: 10.1248/cpb.55.115

[16] Mallakpour S., Rafiee Z.: Application of microwave-assisted reactions in step-growth polymerization: A review. Iranian Polymer Journal, **17**, 907–935 (2008).

[17] Leadbeater N. E., Torenius H. M.: A study of the ionic liquid mediated microwave heating of organic solvents. The Journal of Organic Chemistry, **67**, 3145–3148 (2002).
DOI: 10.1021/jo016297g

[18] Mallakpour S., Rafiee Z.: Ionic liquids as environmentally friendly solvents in macromolecules chemistry and technology, Part I. Journal of Polymers and the Environment, **19**, 447–484 (2011).
DOI: 10.1007/s10924-011-0287-3

[19] Mallakpour S., Rafiee Z.: New developments in polymer science and technology using combination of ionic liquids and microwave irradiation. Progress in Polymer Science, **36**, 1754–1765 (2011).
DOI: 10.1016/j.progpolymsci.2011.03.001

[20] Sun X., He J., Meng Y., Zhang L., Zhang S., Ma X., Dey S., Zhao J., Lei Y.: Microwave-assisted ultrafast and facile synthesis of fluorescent carbon nanoparticles from a single precursor: Preparation, characterization and their application for the highly selective detection of explosive picric acid. Journal of Materials Chemistry A, **4**, 4161–4171 (2016).
DOI: 10.1039/C5TA10027E

[21] Hasanpoor M., Aliofkhazraei M., Delavari H.: Microwave-assisted synthesis of zinc oxide nanoparticles. Procedia Materials Science, **11**, 320–325 (2015).
DOI: 10.1016/j.mspro.2015.11.101

[22] Nakabayashi K., Kojima M., Inagi S., Hirai Y., Atobe M.: Size-controlled synthesis of polymer nanoparticles with tandem acoustic emulsification followed by soap-free emulsion polymerization. ACS Macro Letters, **2**, 482–484 (2013).
DOI: 10.1021/mz4001817

[23] Sundar S., Kundu J., Kundu S. C.: Biopolymeric nanoparticles. Science and Technology of Advanced Materials, **11**, 1–13 (2010).
DOI: 10.1088/1468-6996/11/1/014104

[24] Mallakpour S., Zadehnazari A.: Simple and efficient microwave-assisted polycondensation for preparation of chiral poly(amide-imide)s having pendant phenol moiety. Polymer Science Series B, **54**, 314–322 (2012).
DOI: 10.1134/S1560090412060048

[25] Mallakpour S., Zeraatpisheh F.: Novel chiral and organosoluble nanostructure poly(ester–imide)s containing *N*,*N*′-(3,3′,4,4′-benzophenonetetracarboxylic)-3,3′,4,4′-diimido-bis-(L-tyrosine methyl ester) as a new amino acid based diol: Production, morphology, and thermal properties. Designed Monomers and Polymers, **16**, 488–497 (2013).
DOI: 10.1080/15685551.2012.747167

[26] Mallakpour S., Zadehnazari A.: Synergic effects of molten ionic liquid and microwave irradiation in preparation of optically active nanostructured poly(amide-imide)s containing amino acid and dopamine moiety. Polymer-Plastics Technology and Engineering, **51**, 1090–1096 (2012).
DOI: 10.1080/03602559.2012.689059

[27] Mallakpour S., Ahmadizadegan H.: Poly(amide-imide)s obtained from 3,5-diamino-*N*-(thiazol-2-yl)-benzamide and dicarboxylic acids containing various amino acid units: Production, characterization and morphological investigation. High Performance Polymers, **25**, 156–164 (2013).
DOI: 10.1177/0954008312459547

[28] Mallakpour S., Zarei M.: Novel, thermally stable and chiral poly(amide-imide)s derived from a new diamine containing pyridine ring and various amino acid-based diacids: Fabrication and characterization. High Performance Polymers, **25**, 245–253 (2013).
DOI: 10.1177/0954008312461658

[29] Mallakpour S., Dinari M.: Novel nanostructure amino acid-based poly(amide–imide)s enclosing benzimidazole pendant group in green medium: Fabrication and characterization. Amino Acids, **43**, 1605–1613 (2012).
DOI: 10.1007/s00726-012-1236-8

[30] Mallakpour S., Zadehnazari A.: Microwave-assisted synthesis and morphological characterization of chiral poly(amide–imide) nanostructures in molten ionic liquid salt. Advances in Polymer Technology, **32**, 21333/1–21333/12 (2013).
DOI: 10.1002/adv.21333

[31] Mallakpour S., Zadehnazari A.: Tailored synthesis of nanostructured polymer thin films from optically active and thermally stable poly(amide-*co*-imide)s containing hydroxyl pendant groups in a green ionic solvent. Polymer-Plastics Technology and Engineering, **51**, 1097–1105 (2012).
DOI: 10.1080/03602559.2012.689060

[32] Mallakpour S., Zadehnazari A.: New organosoluble, thermally stable, and nanostructured poly(amide-imide)s with dopamine pendant groups: Microwave-assisted synthesis and characterization. International Journal of Polymer Analysis and Characterization, **17**, 408–416 (2012).
DOI: 10.1080/1023666X.2012.669646

[33] Mallakpour S., Dinari M.: Straightforward and green method for the synthesis of nanostructure poly(amide-imide)s-containing benzimidazole and amino acid moieties by microwave irradiation. Polymer Bulletin, **70**, 1049–1064 (2013).
DOI: 10.1007/s00289-012-0875-y

[34] Mallakpour S., Khani M.: Microwave-assisted construction of nanostructured poly(amide-imide)s containing environmentally friendly natural amino acids *via* implementation of molten salt ionic liquid as an activating media. Polymer-Plastics Technology and Engineering, **53**, 38–45 (2014).
DOI: 10.1080/03602559.2013.843687

[35] Mallakpour S., Khani M., Sabzalian M. R.: Synthesis and biodegradability assessment of poly(amide-imide)s containing *N*-trimellitylimido-L-amino acid and 5-(2-benzimidazole)-1,3-phenylenediamine. Polymer Bulletin, **71**, 2159–2172 (2014).
DOI: 10.1007/s00289-014-1179-1

[36] Wang Y., Fan J., Darensbourg D. J.: Construction of versatile and functional nanostructures derived from CO_2-based polycarbonates. Angewandte Chemie International Edition, **54**, 10206–10210 (2015).
DOI: 10.1002/anie.201505076

[37] Crucho C. I. C., Barros M. T.: Formulation of functionalized PLGA polymeric nanoparticles for targeted drug delivery. Polymer, **68**, 41–46 (2015).
DOI: 10.1016/j.polymer.2015.04.083

[38] Deshapriya I. K., Stromer B. S., Pattammattel A., Kim C. S., Iglesias-Bartolome R., Gonzalez-Fajardo L., Patel V., Gutkind J. S., Lu X., Kumar C. V.: Fluorescent, bioactive protein nanoparticles (prodots) for rapid, improved cellular uptake. Bioconjugate Chemistry, **26**, 396–404 (2015).
DOI: 10.1021/bc500621h

[39] Reisch A., Runser A., Arntz Y., Mély Y., Klymchenko A. S.: Charge-controlled nanoprecipitation as a modular approach to ultrasmall polymer nanocarriers: Making bright and stable nanoparticles. ACS Nano, **5**, 5104–5116 (2015).
DOI: 10.1021/acsnano.5b00214

[40] Nasir A., Kausar A., Younus A.: Novel hybrids of polystyrene nanoparticles and silica nanoparticles-grafted-graphite *via* modified technique. Polymer-Plastics Technology and Engineering, **54**, 1122–1134 (2015). DOI: 10.1080/03602559.2014.996904

[41] Lin H-W., Tan C-S.: Preparation of polyamic acid and polyimide nanoparticles by compressed fluid antisolvent and thermal imidization. The Journal of Supercritical Fluids, **99**, 103–111 (2015).
DOI: 10.1016/j.supflu.2015.01.028

[42] Chabukswar V., Dhomase N., Bhavsar S., Horne A., Mohite K., Gaikwad V.: Studies on morphology and conductivity of poly (*N*-methyl aniline) nanoparticles prepared in nonstirred reaction medium. Macromolecular Symposia, **298**, 43–50 (2010).
DOI: 10.1002/masy.201000019

[43] Dhas N. L., Ige P. P., Kudarha R. R.: Design, optimization and *in-vitro* study of folic acid conjugated-chitosan functionalized PLGA nanoparticle for delivery of bicalutamide in prostate cancer. Powder Technology, **283**, 234–245 (2015).
DOI: 10.1016/j.powtec.2015.04.053

[44] Mallakpour S., Behranvand V.: Surface treatment of nano ZnO using 3,4,5,6-tetrabromo-*N*-(4-hydroxyphenyl)-phthalamic acid as novel coupling agent for the preparation of poly(amide–imide)/ZnO nanocomposites. Colloid and Polymer Science, **292**, 2275–2283 (2014).
DOI: 10.1007/s00396-014-3264-2

[45] Mallakpour S., Dinari M.: Progress in synthetic polymers based on natural amino acids. Journal of Macromolecular Science Part A: Pure and Applied Chemistry, **48**, 644–679 (2011).
DOI: 10.1080/15226514.2011.586289

[46] Ashrafi A., Golozar M. A., Mallakpour S.: Morphological investigations of polypyrrole coatings on stainless steel. Synthetic Metals, **156**, 1280–1285 (2006).
DOI: 10.1016/j.synthmet.2006.09.014

[47] Ayad M. M., Salahuddin N., Ali M.: Polyaniline–organoclay nanocomposites as curing agent for epoxy: Preparation and characterization. Polymer Composites, **30**, 467–473 (2009).
DOI: 10.1002/pc.20599

[48] Shi Y., Peng L., Ding Y., Zhao Y., Yu G.: Nanostructured conductive polymers for advanced energy storage. Chemical Society Reviews, **44**, 6684–6696 (2015).
DOI: 10.1039/c5cs00362h

[49] Moghaddam A. B., Nazari T., Badraghi J., Kazemzad M.: Synthesis of ZnO nanoparticles and electrodeposition of polypyrrole/ZnO nanocomposite film. International Journal of Electrochemistry Science, **4**, 247–257 (2009).

[50] Tai H., Jiang Y., Xie G., Yu J., Zhao M.: Self-assembly of TiO_2/polypyrrole nanocomposite ultrathin films and application for an NH_3 gas sensor. International Journal of Environmental Analytical Chemistry, **87**, 539–551 (2007).
DOI: 10.1080/03067310701272954

[51] Samanta D., Meiser J. L., Zare N. R.: Polypyrrole nanoparticles for tunable, pH-sensitive and sustained drug release. Nanoscale, **7**, 9497–9504 (2015).
DOI: 10.1039/c5nr02196k

[52] Chen X., Yu N., Zhang L., Liu Z., Wang Z., Chen Z.: Synthesis of polypyrrole nanoparticles for constructing full-polymer UV/NIR-shielding film. RSC Advances, **5**, 96888–96895 (2015).
DOI: 10.1039/c5ra20164k

[53] Alizadeh T., Ganjali M. R., Akhoundian M.: Synthesis and application of different nano-sized imprinted polymers for the preparation of promethazine membrane electrodes and comparison of their efficiencies. International Journal of Electrochemical Science, **7**, 7655–7674 (2012).

[54] Vaitkuviene A., Kaseta V., Voronovic J., Ramanauskaite G., Biziuleviciene G., Ramanaviciene A., Ramanavicius A.: Evaluation of cytotoxicity of polypyrrole nanoparticles synthesized by oxidative polymerization. Journal of Hazardous Materials, **250–251**, 167–174 (2013).
DOI: 10.1016/j.jhazmat.2013.01.038

[55] Patil S. L., Chougule M. A., Pawar S. G., Sen S., Patil V. B.: Effect of camphor sulfonic acid doping on structural, morphological, optical and electrical transport properties on polyaniline-ZnO nanocomposites. Soft Nanoscience Letters, **2**, 46–53 (2012).
DOI: 10.4236/snl.2012.23009

[56] Phang S. W., Tadokoro M., Watanabe J., Kuramoto N.: Effect of Fe_3O_4 and TiO_2 addition on the microwave absorption property of polyaniline micro/nanocomposites. Polymers for Advanced Technologies, **20**, 550–557 (2009).
DOI: 10.1002/pat.1381

[57] Song E., Choi J-W.: Conducting polyaniline nanowire and its applications in chemiresistive sensing. Nanomaterials, **3**, 498–523 (2013).
DOI: 10.3390/nano3030498

[58] Hu C., Chen Y., Chen X., Zhang B., Yang J., Zhou J., Zhang M. Q.: Enhancement of photoresponse properties of conjugated polymers/inorganic semiconductor nanocomposites by internal micro-magnetic field. Chemistry A European Journal, **18**, 1467–1475 (2012).
DOI: 10.1002/chem.201101769

[59] Bhadra J., Sarkar D.: Size variation of polyaniline nanoparticles dispersed in polyvinyl alcohol matrix. Bulletin of Materials Science, **33**, 519–523 (2010).
DOI: 10.1007/s12034-010-0079-8

[60] Berti F., Todros S., Lakshmi D., Whitcombe M. J., Chianella I., Ferroni M., Piletsky S. A., Turner A. P. F., Marrazza G.: Quasi-monodimensional polyaniline nanostructures for enhanced molecularly imprinted polymer-based sensing. Biosensors and Bioelectronics, **26**, 497–503 (2010).
DOI: 10.1016/j.bios.2010.07.063

[61] Mahato N., Parveen N., Cho M. H.: Synthesis of highly crystalline polyaniline nanoparticles by simple chemical route. Materials Letters, **161**, 372–374 (2015).
DOI: 10.1016/j.matlet.2015.08.138

[62] Hong Y., Hwang S., Yoon D. S., Yang J.: Scattering analysis of single polyaniline nanoparticles for acidic environmental sensing. Sensors and Actuators B: Chemical, **218**, 31–36 (2015).
DOI: 10.1016/j.snb.2015.04.098

[63] Luo J., Sun J., Huang J., Liu X.: Preparation of water-compatible molecular imprinted conductive polyaniline nanoparticles using polymeric micelle as nanoreactor for enhanced paracetamol detection. Chemical Engineering Journal, **283**, 1118–1126 (2016).
DOI: 10.1016/j.cej.2015.08.041

[64] Zhang S., Wu Y., He B., Luo K., Gu Z.: Biodegradable polymeric nanoparticles based on amphiphilic principle: Construction and application in drug delivery. Science China Chemistry, **57**, 461–475 (2014).
DOI: 10.1007/s11426-014-5076-0

[65] Marin E., Briceño M. I., Caballero-George C.: Critical evaluation of biodegradable polymers used in nanodrugs. International Journal of Nanomedicine, **8**, 3071–3091 (2013).
DOI: 10.2147/IJN.S47186

[66] Bennet D., Kim S.: Polymer nanoparticles for smart drug delivery. in 'Application of nanotechnology in drug delivery' (Sezer E. A. D.) InTech, Rijeka, 257–310 (2014).
DOI: 10.5772/58422

[67] Soppimath K. S., Aminabhavi T. M., Kulkarni A. R., Rudzinski W. E.: Biodegradable polymeric nanoparticles as drug delivery devices. Journal of Controlled Release, **70**, 1–20 (2001). DOI: 10.1016/S0168-3659(00)00339-4

[68] Kerimoğlu O., Alarçin E.: Poly(lactic-*co*-glycolic acid) based drug delivery devices for tissue engineering and regenerative medicine. ANKEM Derg, **26**, 86–98 (2012). DOI: 10.5222/ankem.2012.086

[69] Eili M., Shameli K., Ibrahim N. A., Yunus W. M. Z. W.: Degradability enhancement of poly(lactic acid) by stearate-Zn_3Al LDH nanolayers. International Journal of Molecular Sciences, **13**, 7938–7951 (2012). DOI: 10.3390/ijms13077938

[70] Li F., Zhu A., Song X., Ji L., Wang J.: The internalization of fluorescence-labeled PLA nanoparticles by macrophages. International Journal of Pharmaceutics, **453**, 506–513 (2013). DOI: 10.1016/j.ijpharm.2013.06.033

[71] Choi J-S., Cao J., Naeem M., Noh J., Hasan N., Choi H-K., Yoo J-W.: Size-controlled biodegradable nanoparticles: Preparation and size-dependent cellular uptake and tumor cell growth inhibition. Colloids and Surfaces B: Biointerfaces, **122**, 545–551 (2014). DOI: 10.1016/j.colsurfb.2014.07.030

[72] Nazemi K., Azadpour P., Moztarzadeh F., Urbanska A. M., Mozafari M.: Tissue-engineered chitosan/bioactive glass bone scaffolds integrated with PLGA nanoparticles: A therapeutic design for on-demand drug delivery. Materials Letters, **138**, 16–20 (2015). DOI: 10.1016/j.matlet.2014.09.086

[73] Mallakpour S., Soltanian S., Sabzalian M. R.: Fabrication and *in vitro* degradation study of novel optically active polymers derived from amino acid containing diacids and 4,4′-thiobis(2-tert-butyl-5-methylphenol). Journal of Polymer Research, **18**, 1679–1686 (2011). DOI: 10.1007/s10965-011-9573-y

[74] Mallakpour S., Soltanian S.: Functionalized multi-wall carbon nanotube reinforced poly(ester-imide) bionanocomposites containing L-leucine amino acid units. Journal of Polymer Research, **21**, 335–342 (2014). DOI: 10.1007/s10965-013-0335-x

[75] Abdolmaleki A., Mallakpour S., Borandeh S., Sabzalian M. R.: Fabrication of biodegradable poly(ester-amide)s based on tyrosine natural amino acid. Amino Acids, **42**, 1997–2007 (2012). DOI: 10.1007/s00726-011-0931-1

[76] Abdolmaleki A., Mallakpour S., Borandeh S.: Tailored functionalization of ZnO nanoparticle *via* reactive cyclodextrin and its bionanocomposite synthesis. Carbohydrate Polymers, **103**, 32–37 (2014). DOI: 10.1016/j.carbpol.2013.12.013

[77] Hu B., Wang Y., Xie M., Hu G., Ma F., Zeng X.: Polymer nanoparticles composed with gallic acid grafted chitosan and bioactive peptides combined antioxidant, anticancer activities and improved delivery property for labile polyphenols. Journal of Functional Foods, **15**, 593–603 (2015). DOI: 10.1016/j.jff.2015.04.009

[78] Thu H. P., Nam N. H., Quang B. T., Son H. A., Toan N. L., Quang D. T.: *In vitro* and *in vivo* targeting effect of folate decorated paclitaxel loaded PLA–TPGS nanoparticles. Saudi Pharmaceutical Journal, **23**, 683–688 (2015). DOI: 10.1016/j.jsps.2015.02.002

[79] Zhang H., Li F., Yi J., Gu C., Fan L., Qiao Y., Tao Y., Cheng C., Wu H.: Folate-decorated maleilated pullulan–doxorubicin conjugate for active tumor-targeted drug delivery. European Journal of Pharmaceutical Sciences, **42**, 517–526 (2011). DOI: 10.1016/j.ejps.2011.02.006

[80] Cavallaro G., Craparo E. F., Sardo C., Lamberti G., Barba A. A., Dalmoro A.: PHEA–PLA biocompatible nanoparticles by technique of solvent evaporation from multiple emulsions. International Journal of Pharmaceutics, **495**, 719–727 (2015). DOI: 10.1016/j.ijpharm.2015.09.050

[81] Xu X., Yang J., Ding L., Li J.: Bone morphogenetic protein-2-encapsulated grafted-poly-lactic acid–polycaprolactone nanoparticles promote bone repair. Cell Biochemistry and Biophysics, **71**, 215–225 (2015). DOI: 10.1007/s12013-014-0187-y

[82] Sacchetin P. S. C., Setti R. F., de Tarso Vieira e Rosa P., Moraes Â. M.: Properties of PLA/PCL particles as vehicles for oral delivery of the androgen hormone 17α-methyltestosterone. Materials Science and Engineering: C, **58**, 870–881 (2016). DOI: 10.1016/j.msec.2015.09.071

[83] Gyulai G., Magyar A., Rohonczy J., Orosz J., Yamasaki M., Bősze Sz., Kiss É.: Preparation and characterization of cationic pluronic for surface modification and functionalization of polymeric drug delivery nanoparticles. Express Polymer Letters, **10**, 216–226 (2016). DOI: 10.3144/expresspolymlett.2016.20

[84] Kiss É., Gyulai G., Pénzes Cs. B., Idei M., Horváti K., Bacsa B., Bősze Sz.: Tuneable surface modification of PLGA nanoparticles carrying new antitubercular drug candidate. Colloids and Surfaces A: Physicochemical and Engineering Aspects, **458**, 178–186 (2014). DOI: 10.1016/j.colsurfa.2014.05.048

[85] Nkabinde L. A., Shoba-Zikhali L. N. N., Semete-Makokotlela B., Kalombo L., Swai H., Grobler A., Hamman J. H.: Poly (D,L-lactide-*co*-glycolide) nanoparticles: Uptake by epithelial cells and cytotoxicity. Express Polymer Letters, **8**, 197–206 (2014). DOI: 10.3144/expresspolymlett.2014.23

[86] Di C., Jiang X., Wang R., Yin J.: Multi-responsive polymer nanoparticles from the amphiphilic poly(dimethylsiloxane) (PDMS)-containing poly(ether amine) (PDMS-gPEA) and its potential application for smart separation. Journal of Materials Chemistry, **21**, 4416–4423 (2011).
DOI: 10.1039/c0jm03569f

[87] Kuruppuarachchi M., Savoie H., Lowry A., Alonso C., Boyle R. W.: Polyacrylamide nanoparticles as a delivery system in photodynamic therapy. Molecular Pharmaceutics, **8**, 920–931 (2011).
DOI: 10.1021/mp200023y

[88] Dang G., Shi Y., Fu Z., Yang W.: Polymer nanoparticles with dendrimer-Ag shell and its application in catalysis. Particuology, **11**, 346–352 (2013).
DOI: 10.1016/j.partic.2011.06.012

[89] Fritzen-Garcia M. B., Monteiro F. F., Cristofolini T., Acuña J. J. S., Zanetti-Ramos B. G., Oliveira I. R. W. Z., Soldi V., Pasa A. A., Creczynski-Pasa T. B.: Characterization of horseradish peroxidase immobilized on PEGylated polyurethane nanoparticles and its application for dopamine detection. Sensors and Actuators B: Chemical, **182**, 264–272 (2013).
DOI: 10.1016/j.snb.2013.02.107

[90] Kong X., Shi Z., Lu Z.: Synthesis of novel polymer nano-particles and their interaction with cement. Construction and Building Materials, **68**, 434–443 (2014).
DOI: 10.1016/j.conbuildmat.2014.06.086

[91] Pu K., Shuhendler A. J., Jokerst J. V., Mei J., Gambhir S. S., Bao Z., Rao J.: Semiconducting polymer nanoparticles as photoacoustic molecular imaging probes in living mice. Nature Nanotechnology, **9**, 233–239 (2014).
DOI: 10.1038/nnano.2013.302

[92] Mallakpour S., Abdolmaleki A., Borandeh S., Sabzalian M. R.: One pot fabrication of optically active and efficient antibacterial poly(amide-benzimidazole-imide)/Ag bionanocomposite. Journal of Polymer Research, **22**, 129–136 (2015).
DOI: 10.1007/s10965-015-0743-1

[93] Loos C., Syrovets T., Musyanovych A., Mailänder V., Landfester K., Nienhaus G. U., Simmet T.: Functionalized polystyrene nanoparticles as a platform for studying bio–nano interactions. Beilstein Journal of Nanotechnology, **5**, 2403–2412 (2014).
DOI: 10.3762/bjnano.5.250

[94] Monti D. M., Guarnieri D., Napolitano G., Piccoli R., Netti P., Fusco S., Arciello A.: Biocompatibility, uptake and endocytosis pathways of polystyrene nanoparticles in primary human renal epithelial cells. Journal of Biotechnology, **193**, 3–10 (2015).
DOI: 10.1016/j.jbiotec.2014.11.004

eXPRESS Polymer Letters Vol.10, No.11 (2016) 914–926
Available online at www.expresspolymlett.com
DOI: 10.3144/expresspolymlett.2016.85

Mode II fracture toughening and healing of composites using supramolecular polymer interlayers

V. Kostopoulos[1*], *A. Kotrotsos*[1], *A. Baltopoulos*[1], *S. Tsantzalis*[1], *P. Tsokanas*[1], *T. Loutas*[1], *A. W. Bosman*[2]

[1]Applied Mechanics Laboratory, Department of Mechanical Engineering and Aeronautics, University of Patras, 26504 Rio-Patras, Greece
[2]SupraPolix BV, Horsten 1, 5612 AX Eindhoven, The Netherlands

Received 18 May 2016; accepted in revised form 25 June 2016

Abstract. This study focuses on the transfer of the healing functionality of supramolecular polymers (SP) to fibre reinforced composites through interleaving. SPs exhibiting self-healing based on hydrogen bonds were formed into films and were successfully incorporated into carbon fibre composites. The effect of the SP interleaves on in-plane fracture toughness and the subsequent healing capability of the hybrid composites were investigated under mode II fracture loading. The fracture toughness showed considerable increase since the maximum load (P_{max}) of the hybrid composite approximately doubled, and consequently the mode II interlaminar fracture toughness energy (G_{IIC}) exhibited an increase reaching nearly 100% compared to the reference composite. The healing component was activated using external heat. P_{max} and G_{IIC} recovery after activation were measured, exhibiting a healing efficiency after the first healing cycle close to 85% for Pmax and 100% for G_{IIC}, eventually dropping to 80% for P_{max} while G_{IIC} was retained around 100% even after the fourth healing cycle. Acoustic Emission activity during the tests was monitored and was found to be strongly reduced due to the presence of the SP.

Keywords: *smart polymers, CFRPs, supramolecular polymers, fracture toughness, self-healing*

1. Introduction

High performance structural composites are year by year replacing metals in load-critical structures of aircrafts and other industrial applications. This tendency is clearly driven by the need for structural materials with superior mechanical properties, low specific weight and corrosion resistance. On the other hand, during their service life, multi-layered composites are prone to delaminations, as a result of out of plane loads. The presence of delaminations dramatically decreases their residual compression properties and also affects other in-plane properties of the composite. Additionally, polymer matrix composites are sensitive to microcracking formation within the polymer phase due to service-induced loading or even during the manufacturing. Under fatigue loading conditions that a real-world structure experiences on its service life, the initially minor microcracks are linked together to create significantly larger cracks. Cracks and delaminations work together to result in remarkable suppression of the load-bearing capacity of the composite part, even with minimal visual indication of damage being present.

The interlaminar fracture toughness is the key-characteristic in initiation and propagation of delaminations in fibre reinforced polymer (FRP) composites. A constant concern of various researchers has been the enhancement of the fracture behavior of high performance structural composites, especially carbon fibre reinforced polymers (CFRP). In this direc-

*Corresponding author, e-mail: kostopoulos@mech.upatras.gr

tion, a series of approaches has been proposed including thermoplastic interleaves, micro- and nanoparticles, other microfibres, z-pins etc [1–5]. However, the most common and widespread approach is the interleaving. The incorporation of very thin layers can be a feasible way to enhance the interlaminar properties without compromising other mechanical properties. For example, Magniez *et al*. [6] succeeded in the toughening of the CFRPs by interleaving a thin layer (~20 μm) of electrospun poly(hydroxyether of bisphenol A). This type of enhancement improved the fracture toughness in mode I and mode II by up to 150 and 30% respectively. Aksoy and Carlsson [7] achieved toughening of graphite/epoxy composites using thermoplastic and thermoset interleaves with various thicknesses. Both types of interleaves enhanced the interlaminar fracture toughness to a great extent, although thermoplastic interleaves were more effective than the thermoset interleaves because of the larger energy-absorbing capability of the thermoplastic polymer. Molnár *et al*. [8] investigated the interleaving effect of polyacrylonitrile electrospun mats on interlaminar shear stress and impact tests of unidirectional and woven CFRPs. It was shown that the interlaminar shear strength of the woven and unidirectional CFRPs was enhanced at the rate of 7 and 11% respectively. In the case of impact tests carried out on woven CFRPs the absorbed energy was increased at the rate of 64% compared to the neat ones. Drakonakis *et al*. [9] investigated the role of the host matrix and the micro-particle interleaving effect to the multilayer structures. From the three different matrices which were utilized, it was shown that the dicyanate was the toughest epoxy while the mode II fracture characteristics were considerably increased with the incorporation of Nylon 6 micro-particles.

Conventional repair techniques of composites are expensive, require extensive human work, and cannot repair defects deep inside the material. Thus, utilization of composites in human safety critical components has always to be accompanied with damage diagnostic tools. It is also of note that conventional damage detection equipment is in some cases not able to detect tiny defects deep inside the material. However, these defects could rapidly propagate between two periodical inspections and lead the composite part to catastrophic failure. This challenging situation acted as an inspiration for the seeking of new repair methods; cheaper and applicable at the early stages of damage evolution. With an aim to address some principal weak points of conventional repair techniques, an emerging approach called 'self-healing polymers' [10] has been proposed but not yet been applied to commercial composites. This smart technology aims to in-situ and autonomously repair damage and thus to lead to extension of the effective life-span of composite structures. Self-healing composites promise to mitigate the importance for detecting damage and to reduce the frequency of scheduled inspections.

An alternative approach to the 'conventional' damage tolerance design philosophy is to provide a material with the ability to self-repair. To this direction, scientists have drawn inspirations by the ability of the biological systems to repair external wounds in order to develop similar repair systems within the material. Two main ways for implementing the healing functionality within a material have been reported over the past two decades: a) the extrinsic one, e.g. [11, 12], where the healing agent is liquid and stored in advance within the material, and b) the intrinsic one, e.g. [13, 14], where the inherently thermally reversible bonds of the material create the healing effect under external heating.

However a more effective way to address the long-standing problem of weak through-the-thickness strength of structural composites is probably the development of new composites that combine high interlaminar fracture toughness with the ability to self-heal. For example, Wang *et al*. [15] investigated the combined self-healing and toughening performance of CFRP interleaved with patches of two thermoplastics. The hybrid composite had enhanced mode I but reduced interlaminar shear properties while reasonable mechanical property recovery after healing was achieved via both thermoplastics in both loading cases. In addition, Yang *et al*. [16] proposed a new type of self-healing composite material containing a three-dimensional thermoplastic (EMAA) fibre system created by stitching. The hybrid composite was tougher than the reference and high recovery of the mode I fracture characteristics was achieved after multiple healing cycles. Very recently, Kotrotsos *et al*. [17] proposed a hybrid composite with a matrix modified with thermoplastic micro-particles. The com-

posite had enhanced mode II fracture toughness and was able to significantly restore the mode II fracture characteristics after healing.

A more promising approach for self-healing composites might be found by merging reversible bonds into epoxide networks, since this approach allows the healing to be unlimited as no chemicals are consumed. A new technology that could be beneficial for self-healing in composites has been built on supramolecular polymers (SP) [18–20]. Especially those based on reversible hydrogen bonding arrays show great promise for self-healing materials [21–24], since these materials can typically withstand multiple healing cycles without substantial loss of performance, as a consequence of the highly directional and fully reversible non-covalent interactions present within the polymer matrix. In this study, we have employed the ureiodypyrimidone hydrogen bonding unit (UPy) as developed by Sijbesma *et al*. [25] because of its strong self-association, its synthetic accessibility, and the highly dynamic nature of low T_g-polymers comprising the UPy [26]. Most interestingly, UPy-polymers have recently been shown to give unprecedented toughening in polybutadiene based interpenetrating networks [27]. In recent investigation, Zhang *et al*. [28] discussed the state of our understanding about ionomers and the historical applications of these nanostructured polymers. It was also discussed the modern methods for synthesizing new ionomers and described a number of relatively new applications for ionomers and the potential use of these materials in contemporary technologies, including, shape memory and self-healing materials and supramolecular polymer systems.

The scope of the present work is the use of flexible SP comprising UPy-moieties as interleaves into conventional CFRPs in order to enhance the fracture properties of these hybrid composites and to take advantage of the SP's healing capability. This study is presenting an overview of the role of the SP in the fracture behavior and the repeatable ability to heal the cracks into CFRPs. It is complementing and extending the work of study [29] where mode I fracture was investigated. Here, reference as well as the hybrid composites were subjected to mode II interlaminar fracture toughness tests and compared. After the fracture, the hybrid composites were subjected to heating under controlled loading in order to activate the SP interleave and the cracks to be healed. The healing process was repeated up to four times. Finally acoustic emission (AE) monitoring was implemented during the testing. Recordings led to better understanding of the involved failure mechanisms as well as some conclusions regarding the healing mechanism.

2. Experimental

2.1. Materials

The composite materials which were used in this study were fabricated from UD carbon fibre-epoxy pre-preg CE-1007 150-38. The pre-preg tape was supplied by SGL Group, Germany. The SP was developed and supplied by Suprapolix. The supplied material (batch identification code: SPSH01) is based on a low T_g (–66 °C) polymer modified with UPy-moieties, and was chosen to play the toughening and healing role as an interleaf in the present study. This polymer owes its mechanical properties to the reversible, non-covalent interactions, such as hydrogen bonding, between the macromolecules.

2.2. Preparation of SP interleaf and composite manufacturing

The as-received polymer piece was converted into a thin film by a two-step heating/pressing treatment using a hot press machine [29]. Firstly, the bulk SP block was pressed under 5 kN at 90 °C for 30 min. Then, heating was stopped and the SP material was left under 25 kN mechanical load overnight to cool-down and reach its final form. Consequently, a thin film of SP was obtained. The thickness of the film was measured to be approximately 120 μm with no significant thickness variations, using a digital caliper. Finally, the SP film was cut into 20 mm wide strip using a conventional film cutter. The selected strip's width, based on experience ensures that the crack propagation would not overcome the healing agent area during the mode II experiments. The melting temperature (T_m) of the SP material was measured to be 77 °C, using the Perkin-Elmer DSC 8500 differential scanning calorimeter. The DSC samples were heated from ambient temperature to 150 °C at a rate of 5 °C/min. Above this temperature, the UPy-UPy hydrogen bonding interactions start to diminish significantly and thereby the interactions between adjacent polymer chains of the material [26].

Two UD laminated plates made of 22 pre-preg layers were manufactured for the needs of the current study; the reference laminate and the hybrid laminate containing the SP interleaf on the mid-plane, both appropriate for deriving mode II interlaminar fracture specimens. Figure 1 shows schematically the plate configuration with respect to the fracture pre-crack and the healing agent location. During the manufacturing process two 13 μm-thick sheets of polytetrafluoroethylene (PTFE) film were placed in the mid-thickness plane of both laminates as shown in Figure 1 to act as initial pre-crack according to the request of the interlaminar fracture test. In the case of the hybrid laminate, a SP strip was carefully placed on the mid-plane as shown in Figure 1b, 1c. Following the lay-up, the laminates were vacuum bagged and cured in autoclave for 2 h at 130 °C under 6 bar pressure, according to the pre-preg supplier guidelines. The dimensions of the plates were 300 mm×150 mm×3 mm. Ultrasonic C-scan inspection was performed on the produced plates. A Physical Acoustics Corporation (PAC) UT C-Scan system was used with a 5 MHz transducer. Five mode I (double cantilever beam, DCB) samples were cut from both the reference and the hybrid plate.

2.3. Mechanical testing and AE monitoring

Quasi-static interlaminar fracture toughness tests were performed at a 25 kN Instron Universal testing machine at room temperature conditions. Two aluminium tabs were glued on the DCB specimen outer surfaces (Figure 2a) using a two-component epoxy adhesive in order to bear the peel forces from the load cell. Both the reference and the hybrid DCB specimens were tested in mode I according to AITM 1.0005 [30] standard of Airbus defence and space, to create a natural sharp pre-crack. After the testing, the fractured samples were cut into mode II (ENF) specimens according to AITM 1.0006 [31] standard of Airbus. ENF specimen dimensions and experimental set-up are both illustrated in Figure 2b, 2c. The pre-cracked ENF test specimens were loaded in 3-point bending, at a cross-head speed of 1 mm/min. Five replicates were tested for each fracture toughness assessment. The G_{IIC} was determined using the Areas method [31], and calculated using the Equation (1):

$$G_{IIC} = \frac{9Pa^2d}{2w\left(\frac{1}{4}L^3 + 3a^3\right)} \left[\frac{\text{kJ}}{\text{m}^2}\right] \quad (1)$$

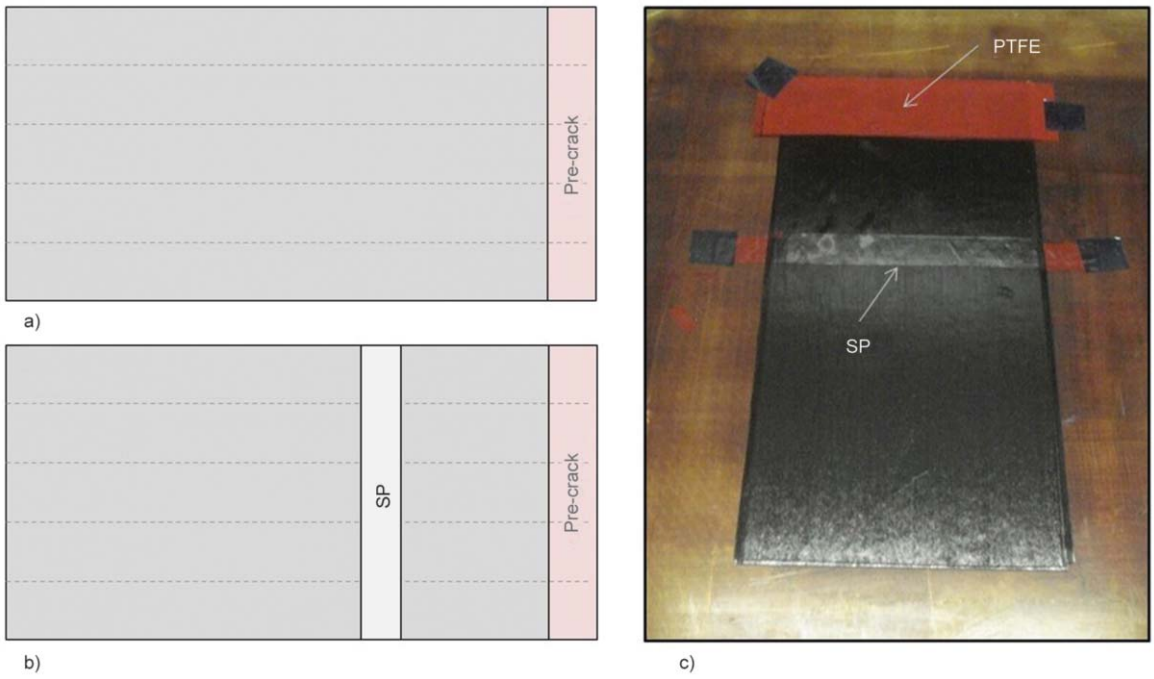

Figure 1. Schematic representation of the mid-plane of (a) the reference plate and (b) the SP containing hybrid plate. (c) Photograph of the mid-plane of the hybrid plate, where a SP strip was carefully positioned, together with the PTFE film.

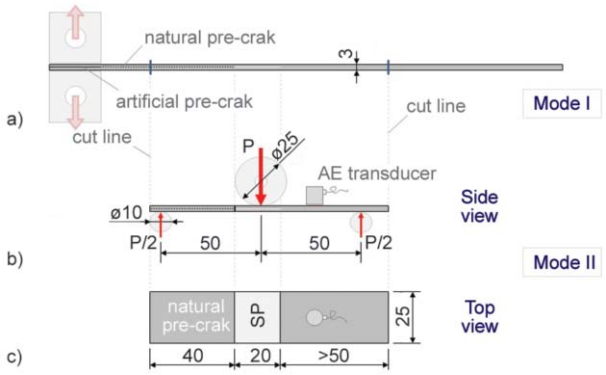

Figure 2. Schematic depiction of the hybrid ENF test specimen configuration as derived from DCB specimen as well as the topology of the AE transducer. (a) DCB specimen, (b) Side view of the ENF specimen, (c) Top view of the ENF specimen. Dimensions in mm.

where d is the cross-head displacement at crack delamination onset, P is the critical load to start the crack, a is the initial crack length (from the support point to the end of the crack), w is the width of the specimen and L is the span length (L = 100 mm).

Based on Equation (1), the crack length (a) has to be known in order the G_{IIC} value to be calculated. For brittle materials the moment of unstable crack growth can be clearly determined; P_{max} is attributed to the critical load at the onset of crack growth. On the other hand, for hybrid materials containing ductile interleaves in which the crack is growing through the ductile interleaved layer [29], the crack initiation occurs long before P_{max}. In addition, in mode II loading of the pre-cracked specimen the crack tends to close which hinder a clear visualization of its tip. Thus, mode II fracture characterization of CFRPs with a ductile interlayer remains a major challenge including uncertainties on the results. Based on these, whereas for the reference case CFRPs the G_{IIC} calculations were extracted directly from the *P-d* data without any concern, for the hybrid CFRPs the monitoring of the crack growth using high resolution digital camera system was carried out. It is suggested that the crack initiation point of the hybrid CFRPs corresponds to the onset of the visual deviation of linearity in *P-d* curves. In addition, a vertical line with pencil was marked at the end of the starter film, as shown in Figure 2b. It is suggested that the separation of the line into two lines corresponds to the crack initiation.

In addition, during the tests the AE activity of the samples was monitored. AE is an ideally suited non-destructive technique for the on-line monitoring of the crack propagation. In this test campaign AE was utilized to support the extraction of useful conclusions, regarding the damage mechanisms activated during the mechanical experiments and investigate any changes due to the presence of the healing agent in the system. An AE sensor was mounted on the specimens' surface as shown in Figure 2b, 2c. The sensor type is wideband WD 100–900 kHz manufactured by PAC, USA. The transducer was attached on the specimens' surface using a suitable glycerine-based coupling agent. AE signal acquisition was performed via a four channel 16 bit PCI/DSP-4 by PAC data acquisition system. Pre-amplification of 40 dB and band-bass filtering of 20–1200 kHz was performed using general purpose voltage preamplifiers with 0/20/40 dB variable gain (2/4/6-AST Auto Sensor Testing Preamplifiers by PAC). A threshold of 40 dB was chosen and the timing parameters were set at Peak Definition Time (PDT) = 50 μs, Hit Definition Time (HDT) = 100 μs and Hit Lockout Time (HLT) = 300 μs. HDT is defined as the maximum duration time of a signal to avoid the monitoring of its reflections. HLT is the waiting time of the system after the last threshold overcoming, to start the new recording. PDT identifies the maximum time between the peaks of two consecutive signals.

The study is deployed in two levels. The first level covers the assessment of the performance change due to the introduction of the healing agent in the reference CFRP system. It is possible that the approach to introduce the healing functionality may jeopardize the load-bearing capacity of the composite. This change in performance is commonly referred to as the knock-down effect. The second level of this study deals with the healing functionality of the composite system and its performance. Essentially, once the healing agent has been incorporated, the system is expected to have a healing functionality; meaning the capability to heal damage in the form of cracks (intrinsic or externally activated). The extent to which this functionality delivers its purposes is assessed in the second level of this work. Details on the procedure are given in the next paragraph.

2.4. Healing procedure and healing efficiency calculations

After the testing procedure, the composites were subjected to a simple healing cycle. The healing cycle activated the healing agent in order to bridge the created crack and heal the system to recover its mechanical performance. The cycle comprised a 15 min dwell at 100 °C under loading of 1 kN using a hot press machine. The aforementioned healing characteristics were chosen in order to be sure that the healing agent would flow along the crack area. The samples were then left to cool-down to room temperature. After the healing process, the samples were retested using the same configurations and procedures described previously. The testing-healing process was repeated until the specimens had received 5 tests and 4 healing events. Reference composites were tested on their original state (un-healed). The calculations of the healing efficiency (H.E.) of the estimated system were based on Equation (2):

$$\text{H.E.} = \frac{a_{\text{healed}}}{a_{\text{hybrid}}} \cdot 100\% \quad (2)$$

where a is the property under examination (i.e., $P_{\max}$ or G_{IIC}), a_{healed} refers to the value of the property after healing and a_{hybrid} refers to the property before healing. The H.E. value refers only to the composites with healing functionality.

3. Results and discussion

3.1. Production and quality issues of composites with healing functionality

Forming the SP material in film form was straightforward as it was easy to process it using processes similar to those used in thermoplastics forming. The handling of the SP film did not create any special concerns. At room temperature the film was stable and did not exhibit tackiness. During composite processing it did not create any problem. The tackiness of the pre-preg was sufficient for holding the film in position. The incorporation of the SP film in the mid-plane of the hybrid laminate did not appear to have a significant effect on the thicknesses of the samples. C-scan images confirmed CFRP plates' quality and showed the absence of manufacturing induced porosity or delaminations, as can be seen in Figure 3. In both plates the rectangular-shaped PTFE strip, which was positioned in the mid-plane of the laminate is clearly distinguished. Additionally, Figure 3b shows clearly the position of the SP film insert, which was incorporated in the mid-plane of the hybrid laminate. The fiber volume fraction of all manufactured plates was calculated to be close to 60%.

3.2. Mode II fracture toughness: Reference vs. hybrid CFRP

The introduction of the healing agent in the CFRP architecture is expected to have an impact on the material performance. At this part of the work the impact on mode II fracture toughness is assessed. The mechanical response of the reference and the hybrid CFRP to mode II fracture loading in combination with AE monitoring and crack evolution camera recording was studied.

Typical load-displacement (*P-d*) curves for the reference and the hybrid plate are given in Figure 4a. All specimens within each set showed a similar behavior. The average values and standard deviation for the two material sets are shown in Figure 4b. As previously mentioned, the *P-d* behavior of the two material sets differs. For the reference material, the applied load increases linearly until the onset of the pre-crack propagation where the load drops abruptly. On the other hand, for the hybrid CFRP the initially linear *P-d* relation is followed by a distinguishable deviation from linearity and much latter the load drop appears. Whereas the load drop for the reference case is attributed to the crack evolution onset, for the hy-

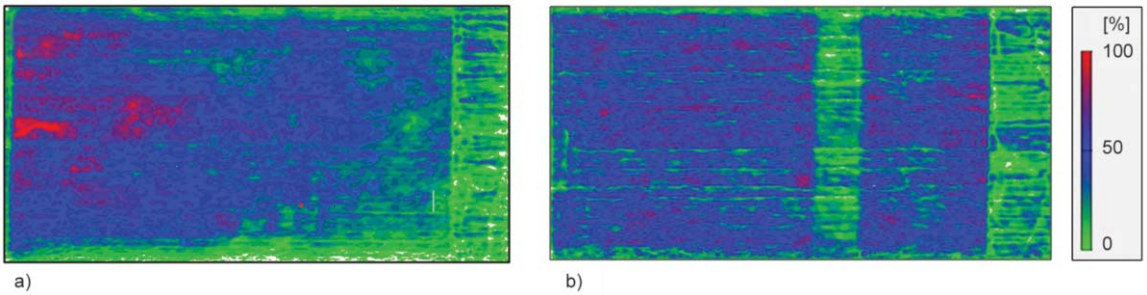

Figure 3. C-scan inspection image of the produced plates: (a) Reference CFRP, (b) Hybrid CFRP

brid CFRP the P_{max} indicates the load bearing capacity of the composite before undergoing major damages. Interestingly, the hybrid laminate exhibits a significantly higher P_{max} and respective displacement. As seen in the Figure 4a, P_{max} is more than double that of the reference CFRP (120% increase) while the displacement at failure is approximately 4 times larger than the reference. From the recorded mechanical data the G_{IIC} was calculated. For the calculation, the displacement (d) at crack propagation onset is needed to be known. The crack initiation points for the reference and the hybrid CFRP, determined as described in section 2.3, are marked in Figure 4a. The snapshot of Figure 4a corresponds to the marked crack initiation point for the hybrid specimen. In this snapshot a slight separation of the pencil line into two lines is observed. The G_{IIC} for both material sets was calculated using in Equation (1) the (P, d) values that correspond to the indicated points of the curve. The average values and standard deviation are shown in Figure 4b. The G_{IIC} values for the hybrid CFRP exhibit an increase of 100% which is related both to the slightly higher corresponding load (P) recorded but also to the displacement (d) at that instance. Nevertheless, this important toughening takes place at a cost of the laminate bending stiffness; a 40% decrease at the linear portion of the curve between the reference and the hybrid CFRP is observed.

AE was recorded during the tests for both materials to support the investigation and are summarized in Figure 5. The AE characteristics in terms of cumulative AE hits and energy were calculated at the threshold of crack initiation (i.e., P_{ini}) for both types of samples as well as at the P_{max} point for the hybrid samples. It is important to highlight that the brittle nature of the reference composite made the P_{ini} and P_{max} points to coincide while in the case of the hybrid ductile samples these points differ significantly, as shown in Figure 4a. It is evident in Figure 5 that the AE activity is significantly less in the hybrid case despite the fact that the test lasts much longer and the specimen experiences much higher loading and displacement. A similar behavior was observed in a previous work [29] in which the AE characteristics were strongly reduced during mode I experiments of hybrid CFRPs containing the same material interleaf. For the hybrid samples the AE activity is much higher at the fracture point in comparison to the point in which the crack initiates as anticipated. The AE activity almost doubled for both the AE characteristics (energy and hits) after the crack initiation point. Apparently, the viscoelastic SP interleaf plays a crucial

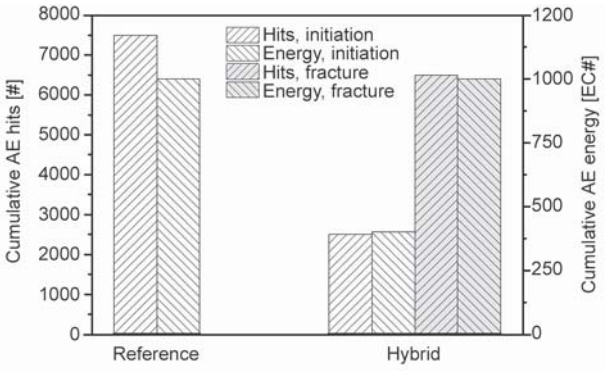

Figure 5. AE activity during mode II interlaminar fracture toughness tests of the reference and the hybrid CFRP at crack initiation and at fracture point

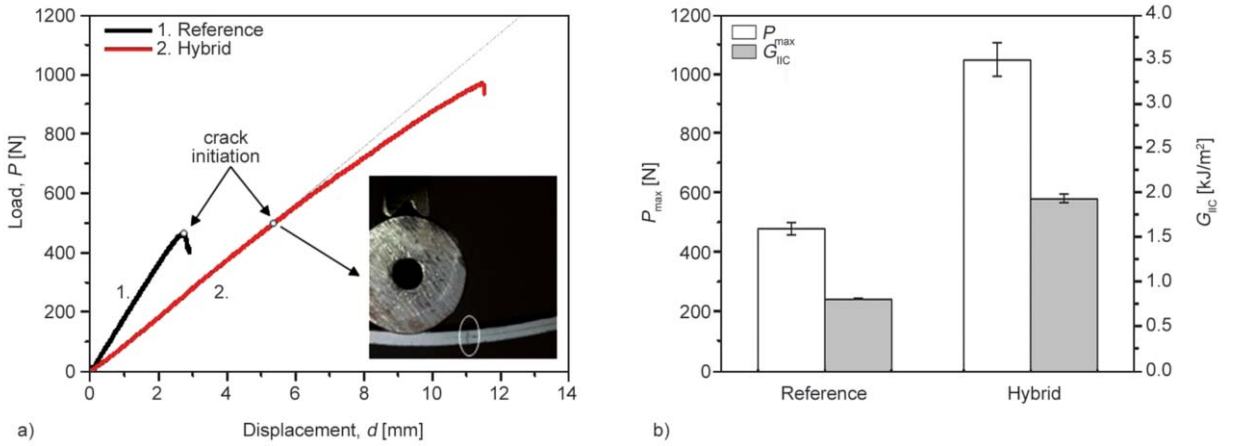

Figure 4. (a) Mode II interlaminar fracture toughness test: representative load-displacement curves for the reference and hybrid CFRPs. (b) Comparison between the reference and the hybrid CFRP, for the maximum load (P_{max}) and the mode II interlaminar fracture toughness energy (G_{IIC})

role in suppressing damage mechanisms otherwise activated at much lower loads/displacements as in the reference case composite material. The macroscopic bending stiffness of the hybrid composite decreases as a knock-down effect but in return the SP interleaf offers extra resistance to the crack initiation as well as larger capacity of strain energy storage (much larger displacements).

As post-tests inspection revealed, the in-plane crack propagated through the SP interleaf rather than along the SP-epoxy interface. This observation indicates that the interface of the interleaf to the host matrix is stronger than the properties of the interleaf, thus guiding the crack to a lower energy path through the interleaf [29]. This behavior essentially maximizes the effectiveness of the interleaf and explains the higher resistance to crack propagation. In addition, high displacements are recorded while the load increased steadily. This can be related to the SP's ductile behavior in combination with its strength. Even when the crack initiated, the presence of the SP interleaf arrested the crack and prevented propagation due to the developed bridging [29] within the crack sides. This results in a lowering of the stress at the crack tip, and consequently in an increased mode II interlaminar fracture toughness. As a matter of fact, similar findings have been reported in by Aksoy and Carlsson where thermoplastics were investigated for interleave toughening. The high deformation of the interleaf resulted in the creation of 'shear-lips'. The deformation mechanism of the interleaf is believed to be similar to the formation of 'shear lips' in mode II fracture of ductile thermoplastic polymers [7]. The same toughening mechanism was also observed and analyzed in detail in the preceding work [29] where support from optical microscopy micrographs from both the cross-section and the fractured surfaces was provided. In Groleau *et al*. [33] investigation a similar mechanism is described in which the interlayered nylon particles played the role of toughening agent into the composite while exhibited plastic deformation and bridging. During the bridging process the particles absorbed energy through extensive plastic deformation and thus the G_{IIC} value was increased.

As mentioned earlier, the flexural stiffness of the hybrid CFRP is lower than that of the reference material. The interleaf has lower stiffness than the UD composite plies and thus results in reducing the equivalent global stiffness of the CFRP plate. Following classical lamination theory this effect, affected by the supramolecular polymer's mechanical properties and the thickness of the interleaf, can be quantified. This is confirmed in fact by studies where thermoplastic interleaves are used to design composites with controllable stiffness [32].

SP provide a unique combination of properties as a material system. Many similarities exist between SP and elastomers, in terms of mechanical behavior, as well as with thermoplastics, primarily in terms of handling and processing. This gives rise to assess SP as engineering materials in general. Thus, on top of the healing functionality SP have repeatedly exhibited on polymer level [33] and which is later on fibre reinforced composite level, SP offer a complementary option in material selection which can deliver improved in-plane fracture toughness as described earlier based on the collected experimental data.

The results from the first study level clearly show that the presence of the supramolecular interleave in the composite resulted in a considerable increase of the mode II interlaminar fracture toughness characteristics. On the physical side, it is believed that the mechanisms delivering this increase in the exhibited fracture toughness are related both to the SP-epoxy interface as well as the structural properties of the interleaf itself. Thus, it is obvious that the fracture toughness characteristics of the composite have been enhanced significantly by the introduction of the SP interleaf. On the contrary, the performance of the CFRP is greatly enhanced. It can be concluded that, regardless of the healing functionality performance, this finding is extremely positive and of great interest.

3.3. Assessment of healing functionality of composites

The healing functionality of these supramolecular interleaves into CFRP composites was assessed by subjecting the samples to a healing cycle consisting of heating and compression as described in section 2.4. Indeed, a large recovery of the interlaminar characteristics (P_{max} and G_{IIC}) during the repeated mode II experiments was observed when the fractured samples had been subjected to multiply healing cycles.

In Figure 6a the recorded load-displacement data are shown for a representative hybrid CFRP specimen. There are five curves; one for the initial test (before healing) and one after each consecutive healing event. In all curves the general trend is the same; the initially linear *P-d* relation is followed by a visual deviation from linearity. In subsequent healing cycles, the sample exhibited a drop for the P_{max}. Nevertheless the lowest value still remains well above that of the reference value (approximately 80% higher). In Figure 6a a magnification of the curve at the crack initiation points is given and for each curve the points are marked. In the histogram of Figure 6b the effect of the number of healing cycles on the mode II fracture characteristics (P_{max} and G_{IIC}) of the hybrid CFRP is seen. As for the P_{max}, the four healing cycles were able to reduce the recorded P_{max} value at a rate of approximately 33%. After the first healing activation the P_{max} of the hybrid CFRP showed a decrease of approximately 16%. The same behavior was observed after the second healing cycle when compared to the first one. Following the third healing cycle the decrease of the P_{max} was calculated to be close to 4% comparing to the second one while the same decrease proportion was calculated after the fourth healing event. On the other hand the G_{IIC} values exhibit a slight increase with increasing the number of healing activations; the G_{IIC} value after the fourth healing cycle is 14% higher than that in the original (no-healed) situation. This behavior is attributed to the fact that the displacement value at crack propagation onset increases as the healing cycles increase (see Equation (1)). In Figure 6c the actual H.E. values for the two magnitudes of interest, calculated based on Equation (2), are given as a function of the number of healing cycles. In subsequent healing cycles a drop for the $H.E._{P_{max}}$ is observed. Nevertheless the lowest value still remains above 70% of the reference value. On the other hand a slight total increase for the $H.E._{G_{IIC}}$ at the rate of approximately

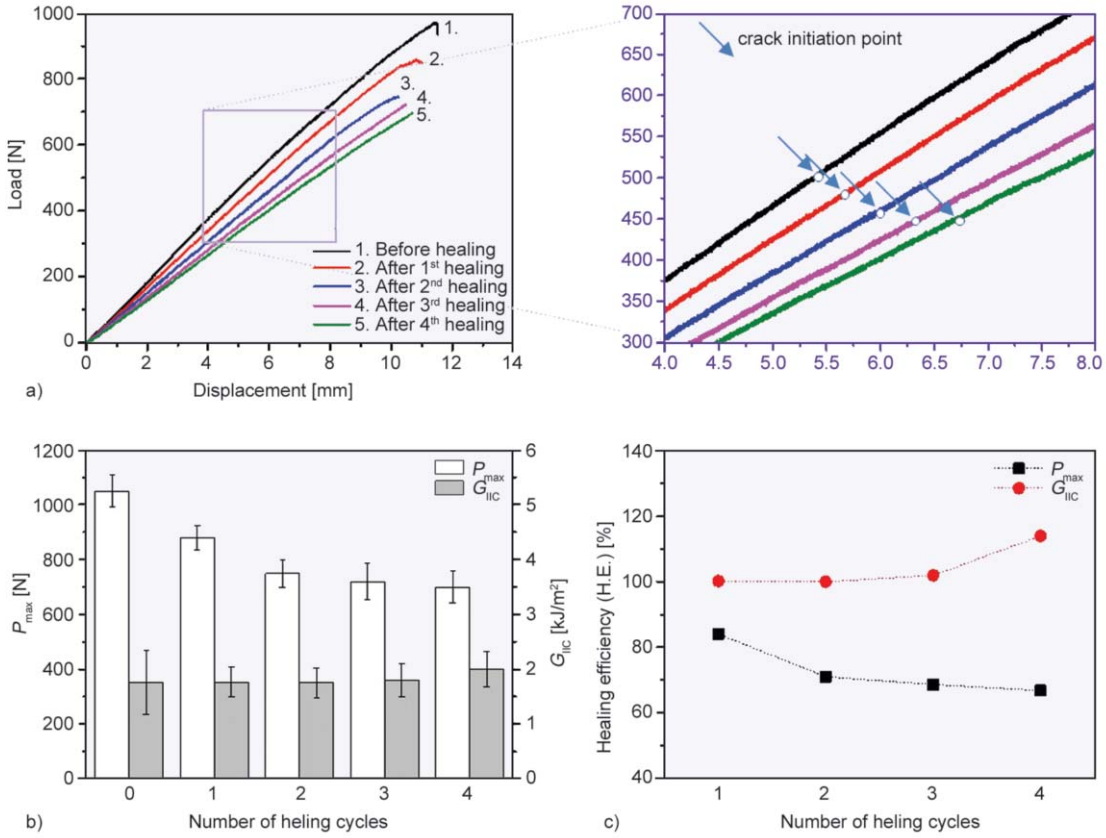

Figure 6. (a) Mode II interlaminar fracture toughness test: representative load-displacement curves for the hybrid CFRP before and after the healing cycles and determination of the crack initiation point. (b) Bar diagrams for the maximum load (P_{max}) and mode II interlaminar fracture toughness energy (G_{IIC}) values of the hybrid CFRP, before and after the healing cycles. (c) The effect of the number of healing cycles on the healing efficiency of the hybrid CFRP, in terms of the P_{max} and the G_{IIC}.

7% is observed. The bending stiffness of the hybrid laminate presents a gradual decrease with increasing number of healing activations.

The repeatability of the healing effect is confirmed by the repetitive behavior of AE monitored during the healing cycles. This is more evident in the results of the bar chart in Figure 7 in which the cumulative AE hits and the cumulative AE energy values are depicted for both the crack initiation and fracture points. As clearly shown in this bar chart, the AE activity is reduced after the first healing cycle for both points and stayed rather stable after each consecutive healing cycle for the crack initiation point. For the fracture point a slight reduction of the AE characteristics after each healing cycle is the general trend whereas a slight increase was observed after the fourth healing cycle. The aforementioned behavior is a solid indication of the fact that the H.E. for the P_{max} value is reduced after each healing cycle. The ability of the SP material to partially remedy previously damaged sites in the vicinity of the crack path and thus produce new AE events (from the healed sites under re-loading) is finite and with a decreasing trend.

The partial recovery may is associated with the degradation of the epoxy-SP interface after each loading cycle which is only partially healed after the subsequent healing. Snapshots of the sample during the mode II experiments at the crack initiation and fracture points before and after the healing cycles are illustrated in Figure 8a.

The high H.E. proportions and the ability of the supramolecular interleaf to heal the cracks are attributed to the SP material's chains that have the ability

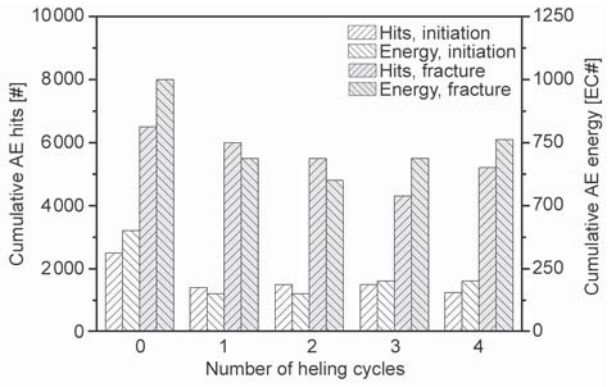

Figure 7. AE activity during mode II interlaminar fracture toughness tests of the hybrid CFRP at crack initiation and just before failure, before and after multiple healing cycles

to reconnect themselves after the mechanical rapture during the mode II experiments. Critical parameters are a good coverage of the fractured surfaces by the SP material and a sufficiently low viscosity of the reversible polymer at 100 °C in order to be able to flow into the crack flanks and to reposition itself equally over the debonded surface. Therefore, the observed reduction in the P_{max} value with increasing number of healing cycles can probably be attributed to an uneven spreading of the SP interleaf over the fracture surface during the healing cycle. An important point to note is the observation that the apparent flexural stiffness of the system decreases after multiple healing activations. A number of reasons have been identified to answer to this observation. Firstly, the tests extended to very large deformation which can lead to the breakage of the fibres on the outer layers. As a matter of fact, Figure 8b shows evidence of broken fibres on the loading cross-head side. It is proposed that these excessive damages were reflected as portion reduction in the load vs. displacement curve. Secondly, during the healing agent activation it is possible that not the complete interface surface of the crack is recovered and bridged. Thus the system cannot recover the stiffness it formerly had. Finally, the healing functionality of the SP may degrade after multiple activations; an observation also noted in [29] with the same material. According to this work the bulk SP material is able to withstand at least seven healing cycles with excellent healing recoveries (still higher toughness values compared to the reference one), but in this loading case and because of the carbon fiber rupture the experiments were stopped after the fourth loading cycle. The post-testing examination of the fracture surface of the healed laminates revealed that the healing agent was clearly separated between the two adjacent fracture surfaces. Thus, the healing effect of the SP material was fully utilized.

4. Conclusions

In this work, the use of supramolecular polymers was investigated in the form of interleaves in CFRP as a means to integrate healing functionality to the composite. Mode II interlaminar fracture toughness tests were performed to assess the effects the SP material brings to the composite. It was shown that the SP interlayer which was introduced at the mid-plane of

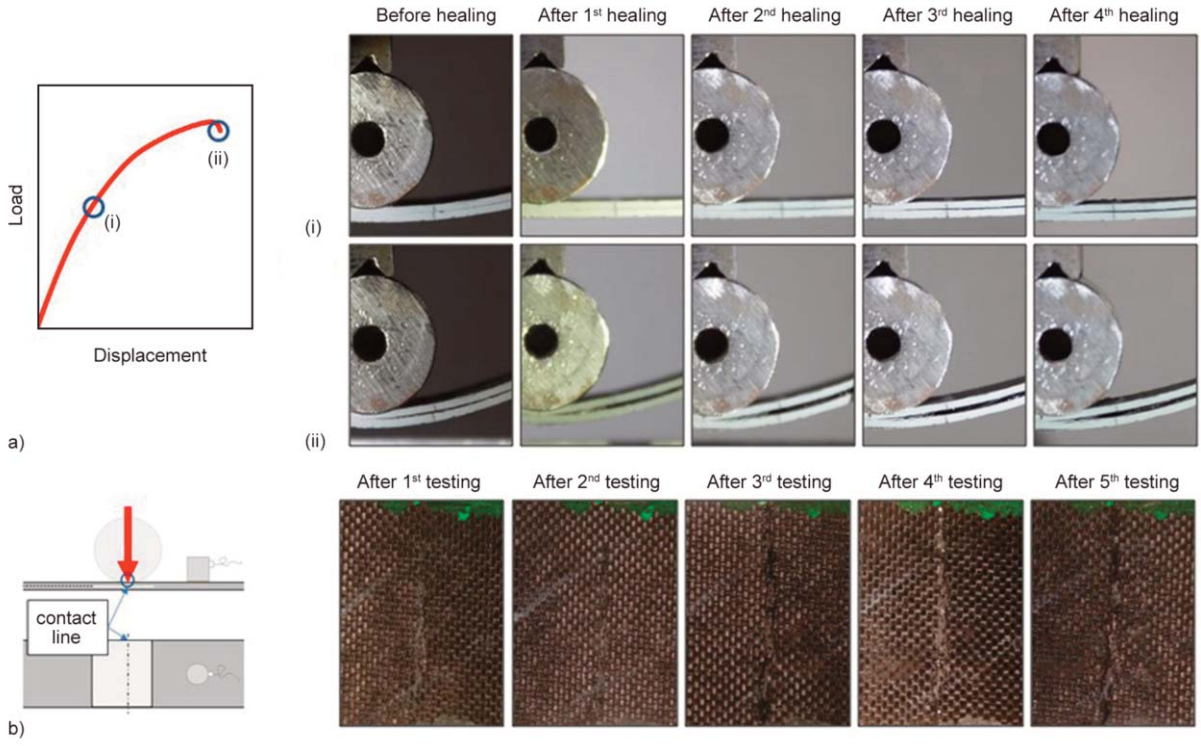

Figure 8. (a) Snapshot during the mode II interlaminar fracture toughness testing of the hybrid CFRP (i) just after crack propagation onset and (ii) just before failure (i.e. $P \sim P_{max}$), before and after healing. (b) Photographs showing the progressive damage accumulation on the upper layers of the hybrid CFRP during the mode II testing, with increasing the number of testing cycles. The damaged line is the contact line between the specimen and the loading cylinder

the lay-up notably increased the fracture toughness of the hybrid composite system, when compared to the reference one. The P_{max} doubled while the G_{IIC} multiplied two times. SP have incorporated a healing functionality to the composite. This has been justified by the effective recovery of more than 85% of the maximum load and 100% of the fracture toughness of the hybrid composite. A decreasing healing ability was observed in terms of load bearing capacity. AE has been utilized in-situ during the tests offering useful insights to the deformation and failure mechanisms taking place in the various materials involved i.e. hybrid, reference, before-after healing explaining inconsistencies or differences in their macroscopical behavior. These findings are considered very interesting for applications where damage tolerance is desired, such as in aeronautics. Such hybrid composite materials could dramatically decrease the repair down time of aircrafts.

Acknowledgements

The present work has been supported by the 7th Framework Program of the European Commission under the project: Self-healing polymers for concepts on self-repaired aeronautical composites – HIPOCRATES (ACP3-GA-2013-605412).

References

[1] Yasaee M., Bond I. P., Trask R. S., Greenhalgh E. S.: Mode II interfacial toughening through discontinuous interleaves for damage suppression and control. Composites Part A: Applied Science and Manufacturing, **43**, 121–128 (2012).
DOI: 10.1016/j.compositesa.2011.09.026

[2] Ahmadi-Moghadam B., Taheri F.: Fracture and toughening mechanisms of GNP-based nanocomposites in modes I and II fracture. Engineering Fracture Mechanics, **131**, 329–339 (2014).
DOI: 10.1016/j.engfracmech.2014.08.008

[3] Zeng Y., Liu H-Y., Mai Y-W., Du X-S.: Effect of nanoparticle modification on composite mode II delamination. in '13th International Conference on Fracture, Beijing, China' p.9 (2013).

[4] Kostopoulos V., Karapappas P., Loutas T., Vavouliotis A., Paipetis A., Tsotra P.: Interlaminar fracture toughness of carbon fibre-reinforced polymer laminates with nano- and micro-fillers. Strain, **47**, 269–282 (2011).
DOI: 10.1111/j.1475-1305.2008.00612.x

[5] Mouritz A. P.: Review of z-pinned composite laminates. Composites Part A: Applied Science and Manufacturing, **38**, 2383–2397 (2007).
DOI: 10.1016/j.compositesa.2007.08.016

[6] Magniez K., Chaffraix T., Fox B.: Toughening of a carbon-fibre composite using electrospun poly(hydroxyether of bisphenol A) nanofibrous membranes through inverse phase separation and inter-domain etherification. Materials, **4**, 1967–1984 (2011).
DOI: 10.3390/ma4111967

[7] Aksoy A., Carlsson L. A.: Interlaminar shear fracture of interleaved graphite/epoxy composites. Composites Science and Technology, **43**, 55–69 (1992).
DOI: 10.1016/0266-3538(92)90133-N

[8] Molnár K., Koštáková E., Mészaros L.: The effect of needleless electrospun nanofibrous interleaves on mechanical properties of carbon fabrics/epoxy laminates. Express Polymer Letters, **8**, 62–72 (2014).
DOI: 10.3144/expresspolymlett.2014.8

[9] Drakonakis V. M., Velisaris C. N., Seferis J. C., Doumanidis C. C., Wardle B. L., Papanicolaou G. C.: Matrix hybridization in the interlayer for carbon fiber reinforced composites. Polymer Composites, **31**, 1965–1976 (2010).
DOI: 10.1002/pc.20996

[10] Wu D. Y., Meure S., Solomon D.: Self-healing polymeric materials: A review of recent developments. Progress in Polymer Science, **33**, 479–522 (2008).
DOI: 10.1016/j.progpolymsci.2008.02.001

[11] White S. R., Sottos N. R., Geubelle P. H., Moore J. S., Kessler M. R., Sriram S. R., Brown E. N., Viswanathan S.: Autonomic healing of polymer composites. Nature, **409**, 794–797 (2001).
DOI: 10.1038/35057232

[12] Diesendruck C. E., Sottos N. R., Moore J. S., White S. R.: Biomimetic self-healing. Angewandte Chemie International Edition, **127**, 10572–10593 (2015).
DOI: 10.1002/anie.201500484

[13] Hayes S. A., Zhang W., Branthwaite M., Jones F. R.: Self-healing of damage in fibre-reinforced polymer-matrix composites. Journal of the Royal Society, Interface, **4**, 381–387 (2007).
DOI: 10.1098/rsif.2006.0209

[14] Pingkarawat K., Bhat T., Craze D. A., Wang C. H., Varley R. J., Mouritz A. P.: Healing of carbon fibre–epoxy composites using thermoplastic additives. Polymer Chemistry, **4**, 5007–5015 (2015).
DOI: 10.1039/C3PY00459G

[15] Wang C. H., Sidhu K., Yang T., Zhang J., Shanks R.: Interlayer self-healing and toughening of carbon fibre/epoxy composites using copolymer films. Composites Part A: Applied Science and Manufacturing, **43**, 512–518 (2012).
DOI: 10.1016/j.compositesa.2011.11.020

[16] Yang T., Wang C. H., Zhang J., He S., Mouritz A. P.: Toughening and self-healing of epoxy matrix laminates using mendable polymer stitching. Composites Science and Technology, **72**, 1396–1401 (2012).
DOI: 10.1016/j.compscitech.2012.05.012

[17] Kotrotsos A., Baltopoulos A., Tsantzalis S., Tsilimigkra X., Tsokanas P., Kostopoulos V.: Experimental investigation on self-healing efficiency of doped fiber reinforced plastics with PET micro-particles. UPB Scientific Bulletin Series D: Mechanical Engineering, **78**, 67–76 (2016).

[18] Brunsveld L., Folmer B. J. B., Meijer E. W., Sijbesma R. P.: Supramolecular polymers. Chemical Reviews, **101**, 4071–4098 (2001).
DOI: 10.1021/cr990125q

[19] Bosman A. W., Sijbesma R. P., Meijer E. W.: Supramolecular polymers at work. Materials Today, **7**, 34–39 (2004).
DOI: 10.1016/S1369-7021(04)00187-7

[20] de Greef T. F. A., Meijer E. W.: Materials science: Supramolecular polymers. Nature, **453**, 171–173 (2008).
DOI: 10.1038/453171a

[21] Palmer L. C., Velichko Y. S., de la Cruz M. O., Stupp S. I.: Supramolecular self-assembly codes for functional structures. Philosophical Transactions of the Royal Society A, **365**, 1417–1433 (2007).
DOI: 10.1098/rsta.2007.2024

[22] Stendahl J. C., Li L., Zubarev E. R., Chen Y-R., Stupp S. I.: Toughening of polymers by self-assembling molecules. Advanced Materials, **14**, 1540–1543 (2002).
DOI: 10.1002/1521-4095(20021104)14:21<1540::AID-ADMA1540>3.0.CO;2-T

[23] Brunsveld L., Folmer B. J. B., Meijer E. W.: Supramolecular polymers. MRS Bulletin, **25**, 49–53 (2000).
DOI: 10.1557/mrs2000.29

[24] Cordier P., Tournilhac F., Soulié-Ziakovic C., Leibler L.: Self-healing and thermoreversible rubber from supramolecular assembly. Nature, **451**, 977–980 (2008).
DOI: 10.1038/nature06669

[25] Sijbesma R. P., Beijer F. H., Brunsveld L., Folmer B. J. B., Hirschberg J. H. K. K., Lange R. F. M., Lowe J. K. L., Meijer E. W.: Reversible polymers formed from self-complementary monomers using quadruple hydrogen bonding. Science, **278**, 1601–1604 (1997).
DOI: 10.1126/science.278.5343.1601

[26] Söntjens S. H. M., Renken R. E. R., van Gemert G. M. L., Engels T. A. P., Bosman W. A., Janssen H. M., Govaert L. E., Baaijens F. P. T.: Thermoplastic elastomers based on strong and well-defined hydrogen-bonding interactions. Macromolecules, **41**, 5703–5708 (2008).
DOI: 10.1021/ma800744c

[27] Monemian S., Korley L. T. J.: Exploring the role of supramolecular associations in mechanical toughening of interpenetrating polymer networks. Macromolecules, **48**, 7146–7155 (2015).
DOI: 10.1021/acs.macromol.5b01752

[28] Zhang L., Brostowitz N. R., Cavicchi K. A., Weiss R. A.: Perspective: Ionomer research and applications. Macromolecular Reaction Engineering, **8**, 81–99 (2014).
DOI: 10.1002/mren.201300181

[29] Kostopoulos V., Kotrotsos A., Tsantzalis S., Tsokanas P., Loutas T., Bosman A.W.: Toughening and healing of continuous fibre reinforced composites by supramolecular polymers. Composites Science and Technology, **128**, 84–93 (2016).
DOI: 10.1016/j.compscitech.2016.03.021

[30] AITM 1.0005: Carbon fiber reinforced plastics. Determination of interlaminar fracture toughness energy. Mode I (1994).

[31] AITM 1.0006: Carbon fiber reinforced plastics. Determination of interlaminar fracture toughness energy. Mode II (1994).

[32] Maples H. A., Wakefield S., Robinson P., Bismarck A.: High performance carbon fibre reinforced epoxy composites with controllable stiffness. Composites Science and Technology, **105**, 134–143 (2014).
DOI: 10.1016/j.compscitech.2014.09.008

[33] Groleau M. R., Shi Y-B., Yee A. F., Bertram J. L., Sue H. J., Yang P. C.: Mode II fracture of composites interlayered with nylon particles. Composites Science and Technology, **56**, 1223–1240 (1996).
DOI: 10.1016/S0266-3538(96)00080-2

[34] van Gemert G. M. L., Peeters J. W., Söntjens S. H. M., Janssen H. M., Bosman A. W.: Self-healing supramolecular polymers in action. Macromolecular Chemistry and Physics, **213**, 234–242 (2012).
DOI: 10.1002/macp.201100559

eXPRESS Polymer Letters Vol.10, No.11 (2016) 927–940
Available online at www.expresspolymlett.com
DOI: 10.3144/expresspolymlett.2016.86

Bio-based polyurethane prepared from Kraft lignin and modified castor oil

*L. B. Tavares, C. V. Boas, G. R. Schleder, A. M. Nacas, D. S. Rosa, D. J. Santos**

Centro de Engenharia, Modelagem e Ciências Sociais Aplicadas, UFABC, Santo André, 09210-580 São Paulo, Brazil

Received 24 April 2016; accepted in revised form 26 June 2016

Abstract. Current challenges highlight the need for polymer research using renewable natural sources as a substitute for petroleum-based polymers. The use of polyols obtained from renewable sources combined with the reuse of industrial residues such as lignin is an important agent in this process. Different compositions of polyurethane-type materials were prepared by combining technical Kraft lignin (TKL) with castor oil (CO) or modified castor oil (MCO1 and MCO2) to increase their reactivity towards diphenylmethane diisocyanate (MDI). The results indicate that lignin increases the glass transition temperature, the crosslinking density and improves the ultimate stress especially for those prepared from MCO2 and 30% lignin content from 8.2 MPa (lignin free) to 23.5 MPa. Scanning electron microscopy (SEM) micrographs of rupture surface after uniaxial tensile tests show ductile-to-brittle transition. The results show the possibility to develop polyurethane-type materials, varying technical grade Kraft lignin content, which cover a wide range of mechanical properties (from large elastic/low Young modulus to brittle/high Young modulus polyurethanes).

Keywords: *mechanical properties, reinforcements, Kraft lignin, lignopolyurethane materials, modified castor oil*

1. Introduction

Increasing concerns about depletion of petroleum-based resources and environmental problems caused by petroleum-based materials have led to considerable efforts to develop materials based on renewable resources such as vegetable oils, cellulose, lignin, starch, etc. [1]. The use of renewable raw materials can significantly contribute to sustainable development due to degradability and low toxicity of the resulting products. Conventional polyurethanes (PU) are usually synthesized by a polyaddition reaction between polyols, which are petrochemical in origin and polyisocyanate, which forms urethane linkages [2] resulting in a crosslinked polymer. Nevertheless, polyurethanes can be obtained by using renewable sources such as vegetable oils and can replace fossil fuel-derived oligomers partially or totally.

Castor oil is a major candidate in these replacement efforts due to its inherent advantages over other vegetable oils [3]. Besides its renewability, low cost and easy availability in large quantities, castor oil is not edible, and does not compete with food, and has free secondary hydroxyl groups. Approximately 90% of fatty acids in castor oil are ricinoleic acid (C18:1), which have a hydroxyl functional group at the 12th carbon. This provides a hydroxyl value of between 160 and 180 mg KOH g^{-1} [4, 5]. However, this low hydroxyl value along with the presence of secondary hydroxyls results in low functionality and low reactivity [6, 7], leading to low crosslinking density, which consequently produces semi-flexible and semi-rigid materials among other limitations [8]. Sharma *et al*. [7] investigated flexible polyurethane foams synthesized partially and completely from castor oil. They showed that foams made from 100% of castor oil

*Corresponding author, e-mail: demetrio.santos@ufabc.edu.br

were unstable and collapsed indicating the inferior reactivity of castor oil with isocyanate. The modification of castor oil increases its hydroxyl value and hard segment composition to improve the rigidity, physical and mechanical properties and crosslinking density of the final PU products [9]. Nevertheless, the hydroxyl value of modified castor oil is limited.

A renewable and promising source for sustainable chemicals and bio-based polymeric materials is lignin. Its phenylpropanoic structure and high content of diverse functional groups (such as phenolic and aliphatic hydroxyls, carbonyls, carboxyls) allow it to be used as an alternative for polymer development especially in the substitution of petroleum-based polyols in polyurethane synthesis. Many tons of lignin are generated as by-products of industrial processes such as pulp and paper. Most of the lignin extracted from pulp and paper operations is burned during pulp-spent liquor treatment. This offers energy recovery and regeneration of pulping chemicals with less than 2% recovered for utilization as a chemical product [10]. However, the amount of lignin produced exceeds the requirements for energy generation. The type of pulping process determines the type of lignin industrially available because it unavoidably modifies the lignin structure from that in the original feedstock. To increase the potential applications of lignin in polymeric materials, some chemical modifications have been developed [11, 12], but these add stages to the process and/or raise their costs considerably. Therefore, the direct use of industrial lignin is the most favorable option because it is a relatively cheap raw material. Unmodified lignin has poor stability [13] and difficult melt processing [14], which make its direct use uncompetitive. However, many studies have focused on the incorporation of lignin in polymer materials by blending it with synthetic or other bio-based polymers [15–17].

Current studies have shown increasing interest in diversifying the sources of the hydroxyl groups. Mohamed *et al*. [18] successfully synthetized an eco-friendly waterborne polyurethane dispersion, from castor oil and aromatic polyamide sulfone, via copolymerization reaction. Alternatively, combining lignin and castor oil as polyols for polyurethanic materials is promising. This can produce diversified materials with varied properties and applications. de Oliveira *et al*. [19] characterized polyurethanic materials based on sulfonated lignin (unmodified and modified by oxypropylation) and castor oil. The DMA results pointed out that the glass transition temperature (T_g) of the samples increased and thus the degree of crosslinking with the increase of hydroxyl groups derived from different combinations of sulfonated lignin/sulfonated ligin oxypropylated/castor oil as polyols. Cinelli *et al*. [20] characterized flexible polyurethanes foams from liquefied lignin and two different chain extenders: castor oil and poly(propylene glycol) (PPG). The single use of unmodified or modified castor oil as a polyol is already consolidated [3, 21]. Modified lignins have also been studied for this application [22, 23]. However, the combination of modified castor oil (MCO) and unmodified industrial lignin shows an interesting opportunity for renewable and low cost polyols for preparation of PU.

The aim of this work is to develop and to characterize polyurethane obtained from renewable sources by using polyols including modified castor oil and unmodified paper and pulp residue lignin. The influences of the basic chemistry reactions formed from different combinations were investigated. Fourier transform infrared spectroscopy (FTIR) was used to identify functional groups of the polymers. The thermal and mechanical properties were studied using thermogravimetric analysis (TGA), dynamic mechanical analysis (DMA) and tensile property measurements. Our research efforts focused on the development of novel 100% renewable polyols able to synthetize polyurethanes with a wide range of glass transition temperature (T_g) and mechanical properties. The wide range of lignin-containing polyurethane mechanical properties can make it suitable for the replacement of petroleum-based PU on several applications.

2. Experimental section

2.1. Materials

Technical Kraft lignin (TKL) was obtained as a byproduct of pulp and paper production. It was kindly supplied by Suzano Papel e Celulose (Suzano, SP, Brazil) with the following characteristics: brown color, M_w = 3388 g·mol^{-1} (obtained by gel permeation chromatography) pH 8.1, solid content = 92.5%, ashes = 10% and total hydroxyl index equivalent to

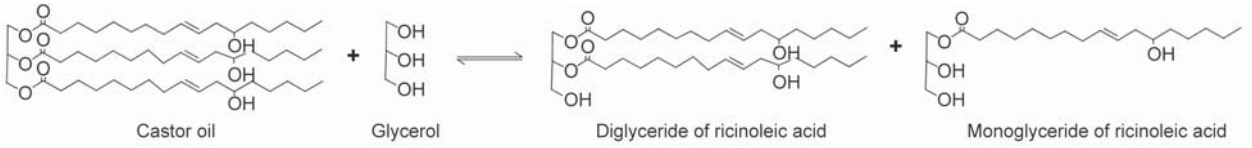

Figure 1. Schematic drawing of castor oil modification reaction

243 mg KOH g^{-1} (determined by ^{31}P nuclear magnetic resonance). The TKL was dried at 80 °C for 6 h before polyol preparation.

Castor oil (CO) and two types of modified castor oil (MCO1 and MCO2) were provided by CPA Brazil (Diadema, SP, Brazil) with a hydroxyl index of 159, 237 and 286 mg KOH g^{-1} and acid index of 0.95, 3.87 and 4.25 mg KOH g^{-1}, respectively (determined by titration). MCO1 and MCO2 were synthetized using a stainless steel industrial reaction kettle equipped with mechanical stirring, temperature monitoring, cooling control system and N_2 inlet. Castor oil was modified by reacting with glycerol and $Ca(OH)_2$ (1% of reactant total mass) at 230 °C for 8 h. Varying castor oil/glycerol ratios gave modified castor oils with different hydroxyl index. The reaction scheme of castor oil modification is shown in Figure 1.

Diphenylmethane diisocyanate (MDI) was acquired for polyurethane preparation from Kalium Chemical (São Paulo, SP, Brazil). It contained 30 and 32% (minimum and maximum) NCO group values.

2.2. Polyurethane preparation

Natural renewable source lignin-containing polyols were obtained by adding 10, 20 or 30 wt% of technical Kraft lignin (TKL) with castor oil (CO) or with modified castor oils (MCO1 or MCO2). Lignin-containing polyols were obtained by stirring 50 g of CO, MCO1 or MCO2 and the respective lignin weight ratios. Polyol preparation was carried out under air at room temperature, for 10 min at 80 rpm in a 200 mL beaker. Polyurethanes (PU-CO, PU-MCO1 and PU-MCO2) were prepared by mechanically mixing MDI and the natural renewable source lignin-containing polyols (NCO/OH equivalent molar ratio of 1.2) for 2 min at 20 rpm in a 200 mL beaker [19]. Polyol compositions are presented in Table 1.

The mixed polyurethane was poured into the cavities of an open silicon mold, with cavity dimensions according to ASTM D638-10 specimens Type I. The cure was carried out at room temperature for 7 days. Figure 2 shows representative reaction schemes between TKL/MDI/modified castor oil, which elucidates the urethane group formation and consequent polymeric structure.

2.3. Characterizations

2.3.1. Fourier transform infrared spectroscopy (FTIR)

The spectroscopic measurements in the infrared regions (FTIR) were performed in a Thermo Nicolet Nexus 4700 spectrometer in transmittance mode; 10 scans were performed from 4000–500 cm^{-1} with a resolution of 4 cm^{-1} in each sample.

2.3.2 Thermogravimetric analysis (TG)

Thermogravimetric analysis (TG) was carried out using Netzsch equipment model STA 449F3. The samples (11.0 mg) were heated from 25 to 800 °C under nitrogen atmosphere and 50 mL·min^{-1} flow and a heating rate of 10 °C·min^{-1}.

Table 1. Nomenclature and compositions of developed polyols according to TKL and oil wt%

	PU-CO	**PU-CO/L10**	**PU-CO/L20**	**PU-CO/L30**
TKL [wt%]	0	10	20	30
CO [wt%]	100	90	80	70
	PU-MCO1	**PU-MCO1/L10**	**PU-MCO1/L20**	**PU-MCO1/L30**
TKL [wt%]	0	10	20	30
MCO1 [wt%]	100	90	80	70
	PU-MCO2	**PU-MCO2/L10**	**PU-MCO2/L20**	**PU-MCO2/L30**
TKL [wt%]	0	10	20	30
MCO2 [wt%]	100	90	80	70

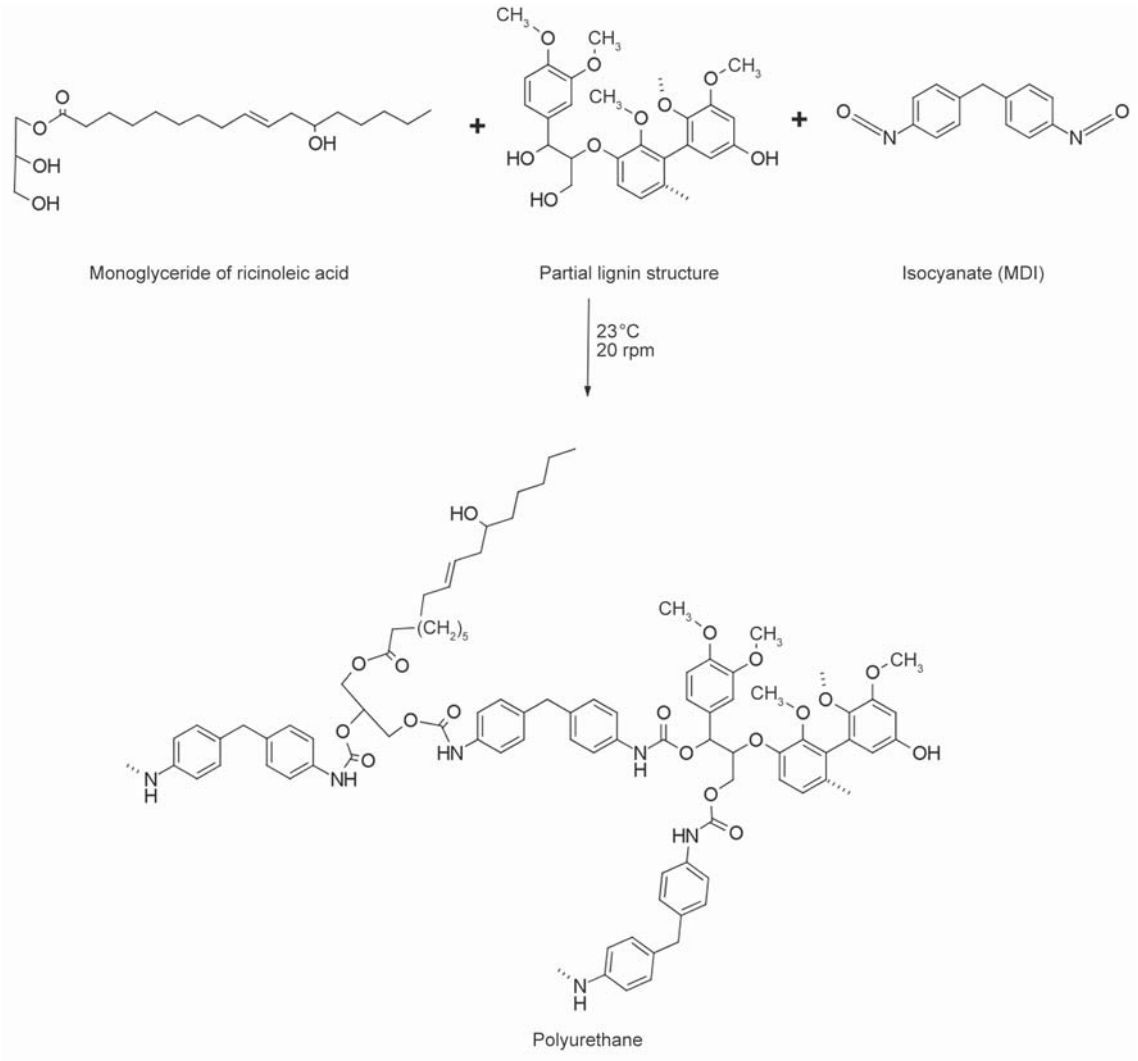

Figure 2. Schematic drawing of polyurethane groups formation from TKL/MDI/MCO reaction

2.3.3. Dynamic mechanical analysis (DMA)

Glass transition temperature (T_g) of renewable polyol based polyurethanes was investigated by DMA using a thermal analyzer model Pyris Diamond, Perkin Elmer. Measurements were carried out in flexural mode (single cantilever) with a temperature range from –50 to 150 °C, frequency of 1 Hz, oscillation amplitude of 10 mm and heating rate of 2 °C·min^{-1}. The dimension of specimens was 30 mm×12 mm× 2 mm, which were obtained by casting PU into the cavities of an open silicon mold. Storage modulus at rubbery plateau (E'_R) was used to calculate crosslinking density.

2.3.4. Mechanical properties

The mechanical properties (5 specimens for each condition) were tested according to ASTM D638 with Type I test specimens using an Instron universal testing machine model 5569 (CECS, Federal University of ABC, Santo André, SP, Brazil) with a crosshead speed of 50 mm·min^{-1} and a non-contact extensometer (Instron SVE). Type I test specimens presented following dimensions: overall length (165 mm), width of narrow section (13 mm), overall thickness (5 mm) and gage length (50 mm).

2.3.5. Scanning electron microscopy (SEM)

After mechanical testing, SEM was used to observe the cross sectional morphology of the fractured surfaces of the samples using a Jeol 6460LV scanning electron microscope with an electron beam at an accelerating voltage of 25 kV. The samples were set on the SEM sample holder and sputter coated with a thin layer of gold.

3. Results and discussion

3.1. Fourier transform infrared spectroscopy (FTIR)

Figure 3 shows the FTIR analysis for CO, MCO1 and MCO2 oils. All spectra present the characteristic peak at 3400 cm^{-1}. This corresponds to the hydroxyl group. MCO1 and MCO2 show increase in this band intensity (Figure 3b), which is related to hydroxyl value increasing after modification. Other characteristic absorption bands are observed at 2920 cm^{-1} (methyl), 2850 cm^{-1} (methylene), 1740 cm^{-1} (esters) and 1161 cm^{-1} (C–O–C) [23-26].

Figure 4 compares the FTIR spectra of PU-CO, PU-MCO1 and PU-MCO2. A characteristic band of urethane stretching at 3330 cm^{-1} is present on all samples, which corresponds to hydrogen bonded N–H group in disordered form [19, 24]. The increasing intensity of this band (Figure 4b) shows the increased amount of urethane groups for PU-MCO1 and PU-MCO2, which might be associated with reaction of NCO with increased hydroxyl level of MCO1 and MCO2. The absence of NCO stretching at 2260 cm^{-1} indicates that the isocyanate groups have been entirely reacted [19, 24, 27]. Other main absorption bands confirm polyurethane formation including absorptions in the region between 1704–1709 cm^{-1} (carbonyl group hydrogen bonding to the urethane group) and 1215 cm^{-1} (urethane linkages) [19, 23, 27].

Figure 5 shows the FTIR spectra of lignin-containing polyurethanes (varying the TKL wt% into the polyurethanes) and of TKL (Figure 5b, 5d and 5f). The band at 3425 cm^{-1}, TKL spectrum (Figure 5b, 5d and 5f), is characteristic of its aromatic and aliphatic OH bond stretching [15, 28, 29]. The presence of lignin in polyurethane resulted into the formation of a wider band in the 3330–3425 cm^{-1} region due to merging of the bonded NH band (3330 cm^{-1}) with lignin OH bond stretching (3425 cm^{-1}) [27]. It can be observed in parts b, d and f of Figure 5 that the intensity of the merged region increases with the increasing of lignin quantity for all samples.

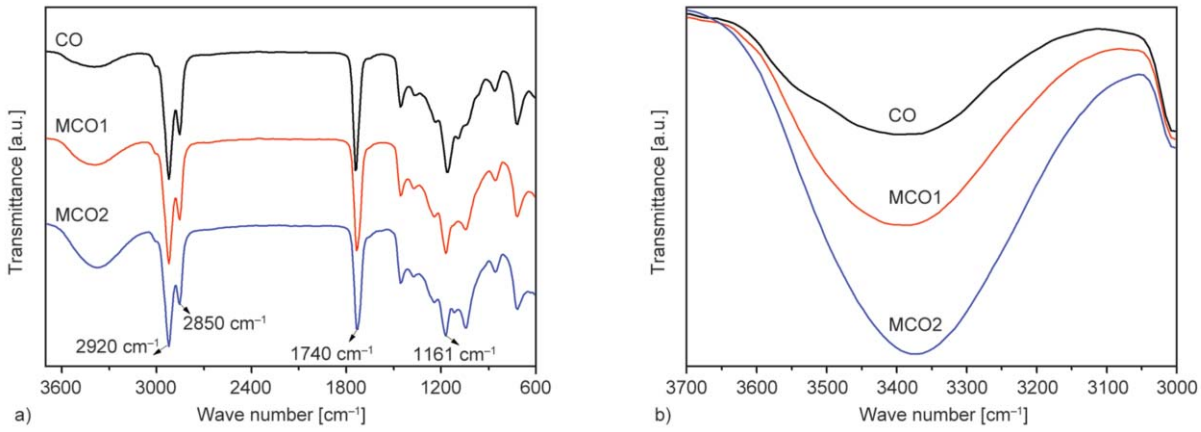

Figure 3. FTIR spectra of vegetable oils (CO, MCO1 and MCO2) (a) from 3700 to 600 cm^{-1} and (b) from 3700 to 3000 cm^{-1}

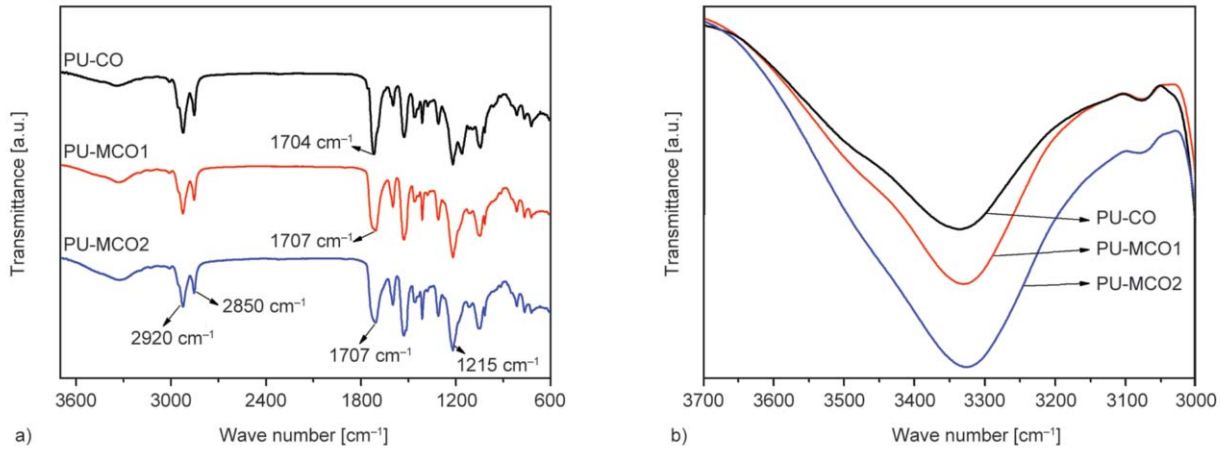

Figure 4. FTIR spectra of PU-CO, PU-MCO1 and PU-MCO2 (a) from 3700 to 600 cm^{-1} and (b) from 3700 to 3000 cm^{-1}

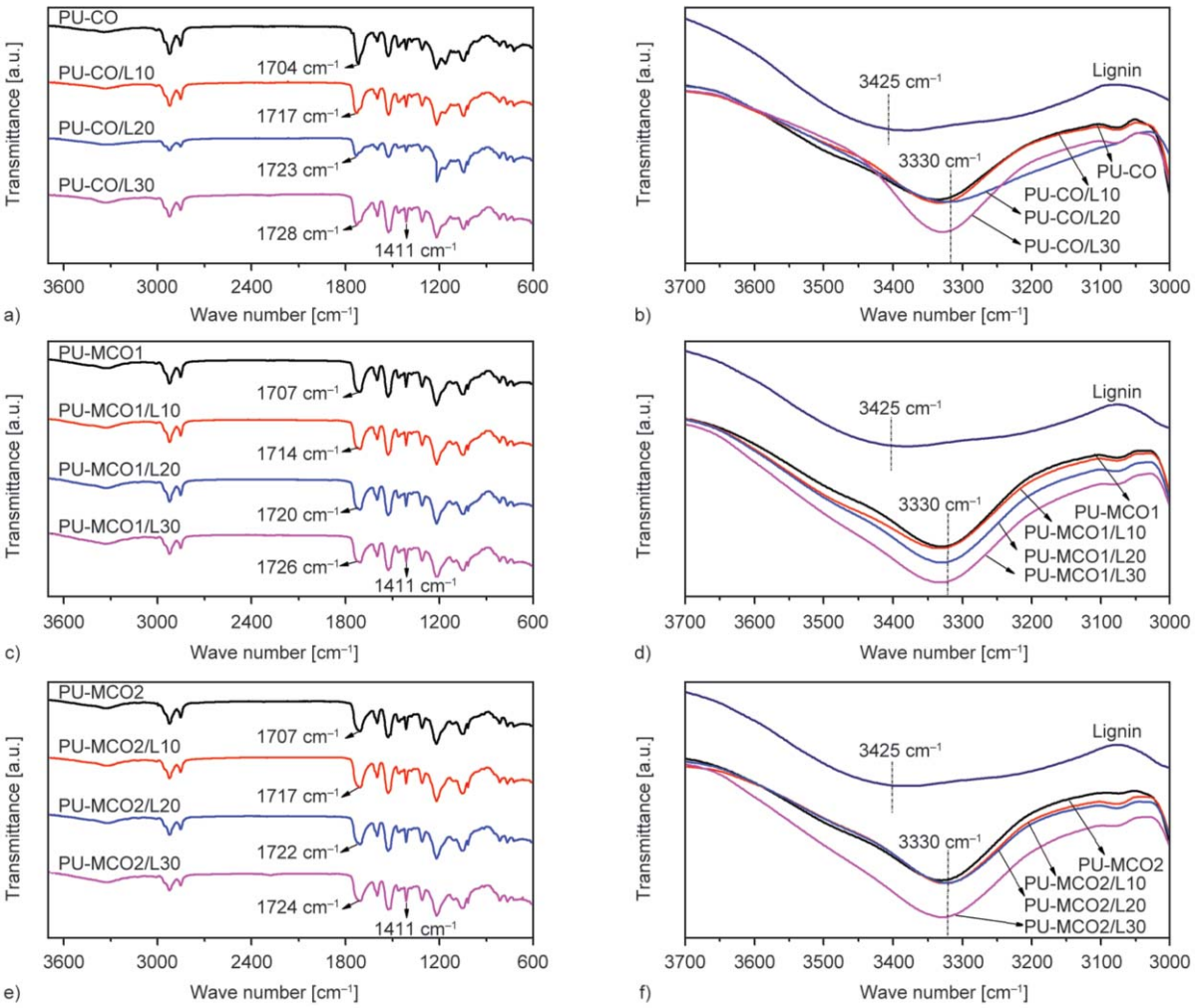

Figure 5. FTIR spectra of PU-CO/lignin compositions (a) from 3700 to 600 cm^{-1}, (b) PU-CO/lignin and lignin (TKL) from 3700 to 3000 cm^{-1}; of PU-MCO1/lignin compositions, (c) from 3700 to 600 cm^{-1}, (d) PU-CO1/lignin and lignin (TKL) from 3700 to 3000 cm^{-1}; and PU-MCO2/lignin (e) from 3700 to 600 cm^{-1}, (f) PU-CO2/lignin and lignin (TKL) from 3700 to 3000 cm^{-1}

As can be seen in Figures 5a, 5c and 5e the spectra of lignin-containing polyurethanes show that as the lignin content increases, the peak of the carbonyl stretching vibration (around 1700 cm^{-1}) gradually shifted to higher wavenumbers. Carbonyl bands of polyurethane can be divided on three main regions: the hydrogen bonded carbonyl in ordered crystalline domains at 1700–1709 cm^{-1} [19, 24, 27], the hydrogen bonded carbonyl in disordered amorphous conformations at 1714–1720 cm^{-1} [19, 30] and the free carbonyl groups (non bonded) at 1731–1745 cm^{-1} [23, 31]. The carbonyl band shifting indicates that the presence of lignin induces the change from a hydrogen bonded ordered crystalline domain (PU-CO, PU-MCO1 and PU-MCO2) to a disordered amorphous conformation and to the formation of free carbonyl groups (PU-CO/lignin, PU-MCO1/lignin and PU-MCO2/lignin) [27]. The absence of NCO stretching at 2260 cm^{-1} in all lignin-containing polyurethane spectra indicates that the isocyanate groups have been entirely reacted [19, 24, 27].

3.2. Thermogravimetric analysis (TGA)

The TGA and derivative TG curves for castor oil-based PU and castor oil/lignin-based PU are presented in Figures 6 and 7. The stability of the PU is related to the hard segment nature (rigid aromatic ring of MDI and TKL), soft segment (introduced by flexible chains of castor oil) and the molar ratio of the hard segment to soft segment [32]. In general, the thermal degradation of polyurethane occurs in a two to three steps, and the composition of the decomposed products depends on the structure of the PU material [33].

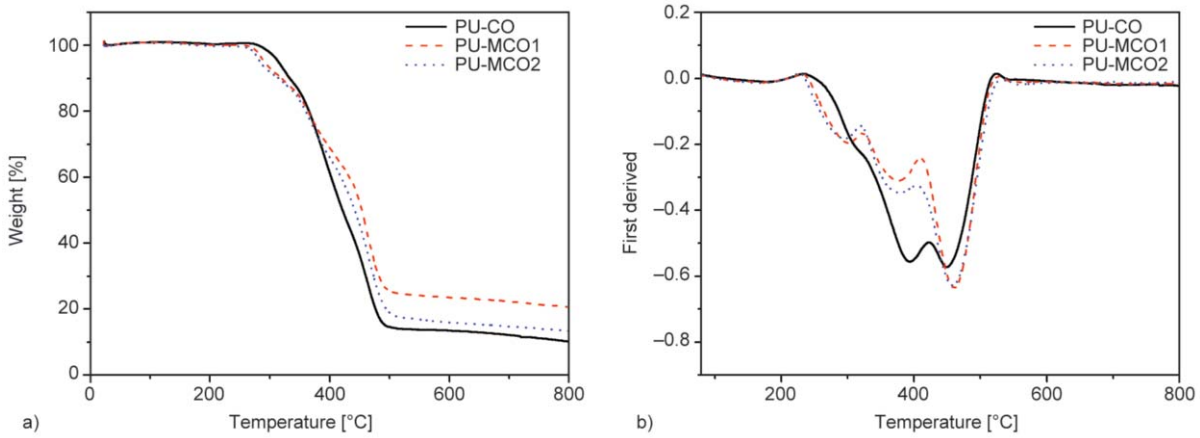

Figure 6. (a) TGA curves of PU-CO, PU-MCO1 and PU-MCO2 and (b) DTG curves of PU-CO, PU-MCO1 and PU-MCO2

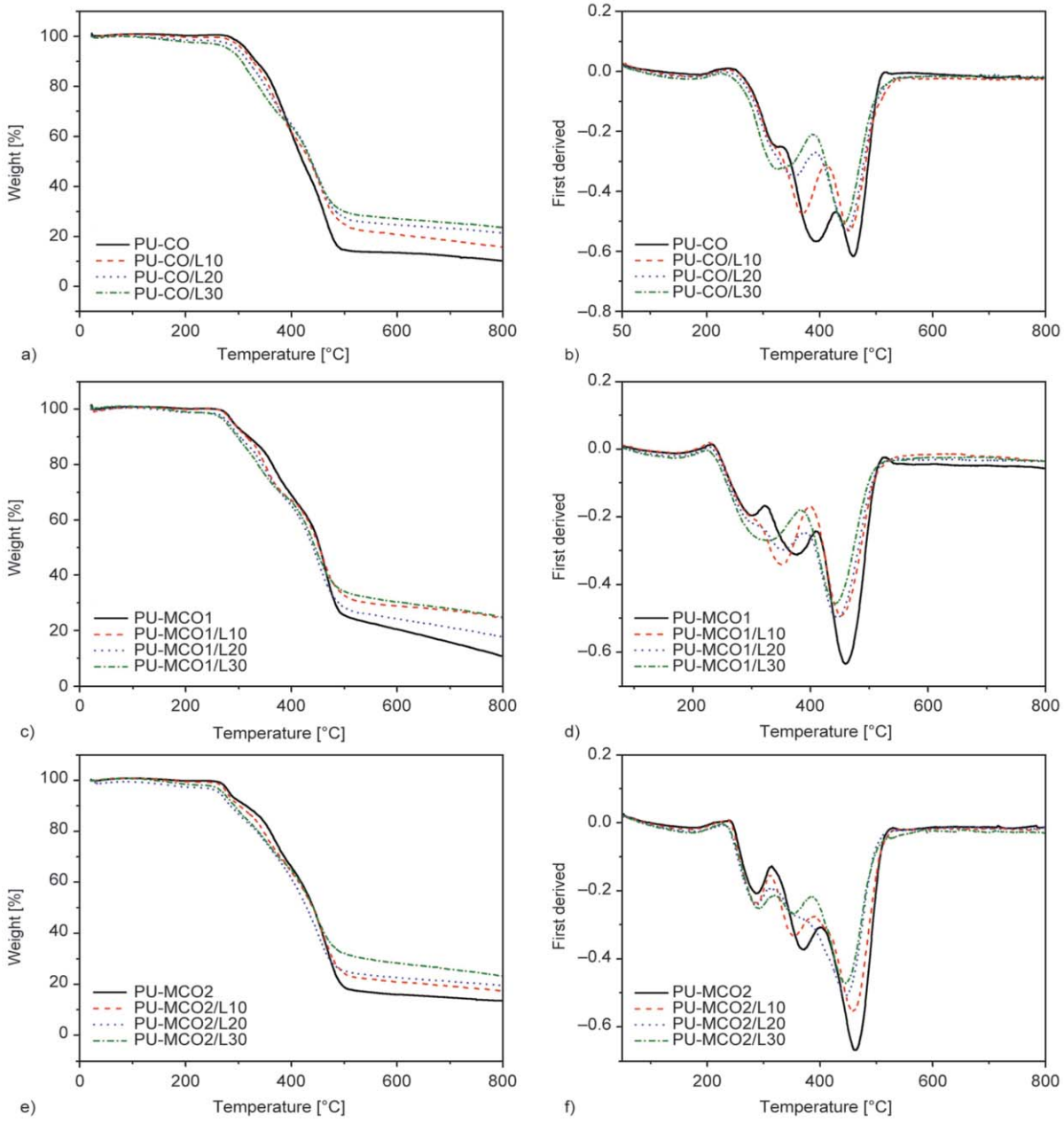

Figure 7. (a) TGA curves of PU-CO and PU-CO/lignin, (b) DTG curves of PU-CO and PU-CO/lignin, (c) TGA curves of PU-MCO1 and PU-MCO1/lignin, (d) DTG curves of PU-MCO1 and PU-MCO1/lignin, (e) TGA curves of PU-MCO2 and PU-MCO2/lignin and (f) DTG curves of PU-MCO2 and PU-MCO2/lignin compositions

A first step decomposition is observed around 270 °C and is related to the thermal decomposition of unstable urethane bonds [27]. The second step occurs above 320 °C. The mass loss occurs at a fast rate in this step. It is associated to the soft segment and depends on its structure and three-dimensional arrangement [33]. The third one is above 380 °C and is also related to other remaining structures formed after the second decomposition, diisocyanate and lignin aromatic rings [1, 25, 34].

Figure 6 shows the TGA and derivative curves of PU-CO, PU-MCO1 and PU-MCO2, respectively. The PU-MCO2 and PU-MCO1 showed lower degradation temperature for first step decomposition (maximum peaks at 289.3 and 294.2 °C, respectively) and presented higher mass loss compared to PU-CO (320.0 °C) due to increasing urethane groups that were improved by castor oil modification. The second step decomposition may correspond to the chain scission of CO (PU-CO 393.6°C, PU-MCO1 372.3 °C, and PU-MCO2 370.9 °C), the soft polyurethane segment, also observed by Hablot *et al*. [35]. In the third step of decomposition, DTG peaks are shown at 448.5 °C for PU-CO, 457.1 °C for PU-MCO1, and 459.4 °C for PU-MCO2.

Figure 7 shows TGA and DTG curves of PU-CO/lignin, PU-MCO1/lignin and PU-MCO2/lignin compositions. The presence of lignin for all conditions decreased the onset of thermal decomposition. The degradation onset in the 250–290 °C temperature range corresponds to the decomposition of unstable urethane bond from hard segment, but also the cleavage of unstable ether linkages of lignin (Figure 7a, 7c and 7e) [23]. Derivative curves for PU-CO/L20, PU-CO/L30 and PU-MCO1/L30 revealed two decomposition peaks, as can be seen in Figure 7b and 7d. The two first stages, hard and soft segment degradations, became close resulting in one larger peak, also observed by Zhang *et al*. [23]. The larger peaks have shifted to lower temperature and smaller intensity, compared to the second step decomposition of lignin free polyurethane, at 300–400 °C range. Lignin incorporation did not significantly affect the degradation behavior but it rather increased the amount of char formation, observed in TGA curves above 500 °C. It was found that the char residue of lignin-containing polyurethanes increases as the lignin concentration increases. Table 2 presents additional thermogravimetric parameters, including initial decomposition temperature for degradation step (T_{onset}), final decomposition temperature for degradation step (T_{offset}), temperature for 50% mass loss ($T_{50\%}$) and % mass of remaining char at 750 °C.

Table 2. Thermogravimetric parameters of PU-CO/lignin, PU-MCO1/lignin and PU-MCO2/lignin

	T_{onset} [°C]	$T_{50\%}$ [°C]	T_{offset} [°C]	Char residue [%]
PU-CO	290.7	421.5	484.6	11.2
PU-CO/L10	287.7	434.8	485.9	17.0
PU-CO/L20	284.2	438.1	480.9	22.2
PU-CO/L30	282.3	437.2	478.8	24.6
PU-MCO1	267.1	453.7	486.3	13.3
PU-MCO1/L10	265.6	452.6	487.9	19.5
PU-MCO1/L20	264.8	440.9	486.3	26.1
PU-MCO1/L30	264.3	444.9	477.8	26.5
PU-MCO2	267.3	441.8	492.6	13.9
PU-MCO2/L10	263.6	440.9	488.7	18.4
PU-MCO2/L20	258.0	429.0	480.3	20.3
PU-MCO2/L30	259.9	441.5	485.5	24.6

3.3. Dynamic mechanical analysis (DMA)

The evolution of tan δ as function of temperature is presented in Figure 8 and might be attributed to the glass transition temperature (T_g) [23]. A wide T_g range might be obtained for polyurethanes, which is dependent on polymer segment, hard and soft nature, and composition [19].

Figure 8a shows the glass transition temperature of PU-CO and PU-CO/lignin conditions. Tan δ values shifted to higher temperature as TKL wt% increases. PU-CO presented the T_g at –0.76 °C and is mainly related to soft segments [19]. Increasing lignin content shifted the T_g to a maximum value of 47.5 °C for PU-CO/L30, mainly due to lignin rigid segment movements [19]. Lignin mass percentage and T_g shifting presented a linear dependence. Lignin mass fraction increasing also induced the tan δ peak broadening, which implies in the sample heterogeneity and might be related to augment of molecular weight of polyol component [36]. In this study, it might have been induced by high molecular weight and heterogeneous molecular structure of TKL added.

Tan δ curves of PU-MCO1 and PU-MCO2 based polyurethanes are presented in Figures 8b and 8c. As general tendency, the T_g shifted to higher temperatures as TKL content increased. It can be seen in Figures 8a, 8b and 8c that all lignin-containing polyure-

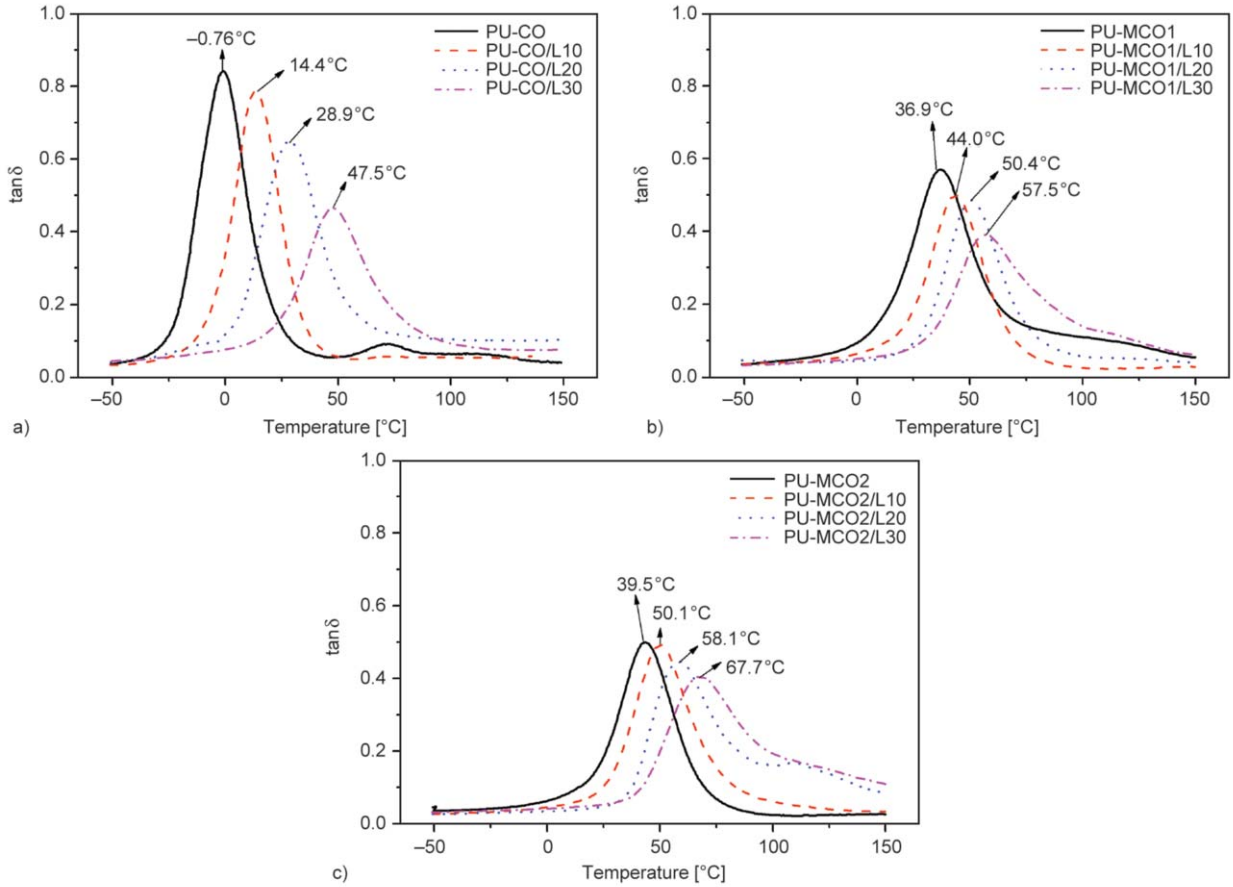

Figure 8. DMA curves (tan δ) of (a) PU-CO/lignin, (b) PU-MCO1/lignin and (c) PU-MCO2/lignin

thanes show a single tan δ peak, which is an indicative of polyol components miscibility. PU-CO is the only condition that presented a small secondary peak, which might be associated to a slight phase separation between soft and hard segments in this composition.

It is of interest to evaluate the effects of CO modification and TKL addition on polyurethane crosslinking density (ν), which can be calculated using storage modulus at rubbery plateau [36]. The crosslinking density can be obtained, for samples submitted to normal stress (tensile and flexural operation mode), Equation (1) [37]:

$$\nu = \frac{E'_R}{3RT} \tag{1}$$

where R is the gas constant, E'_R is the storage modulus at rubbery plateau and T the absolute temperature. Storage modulus at rubbery plateau and calculated crosslinking density are presented in Table 3. Castor oil modification increased polyurethane crosslinking density from 293 mol·m^{-3} (PU-CO) to

Table 3. Storage modulus at rubbery plateau and crosslinking density of PU-CO/lignin, PU-MCO1/lignin and PU-MCO2/lignin

	PU-CO	**PU-CO/L10**	**PU-CO/L20**	**PU-CO/L30**
E'_R [MPa]	2.5	6.1	6.9	13.2
ν [mol·m^{-3}]	293	670	731	1360
	PU-MCO1	**PU-MCO1/L10**	**PU-MCO1/L20**	**PU-MCO1/L30**
E'_R [MPa]	3.2	13.4	19.1	22.4
ν [mol·m^{-3}]	331	1365	1919	2209
	PU-MCO2	**PU-MCO2/L10**	**PU-MCO2/L20**	**PU-MCO2/L30**
E'_R [MPa]	5.4	9.1	13.1	14.6
ν [mol·m^{-3}]	560	918	1288	1407

560 mol·m^{-3} (PU-MCO2). The crosslinking density increasing of PU-CO/lignin, PU-MCO1/lignin and PU-MCO2/lignin is a direct response of TKL wt% rising. However, PU-MCO1/lignin presented higher crosslinking density than PU-MCO2/lignin, besides the higher crosslinking density value for PU-MCO2 in comparison to PU-MCO1.

3.4. Scanning electron microscopy (SEM)

Lignin-containing PU-COs presented a smooth transition from a ductile fracture (smooth grooves, white arrows) to a brittle one (sharp surfaces, black arrows) [38] near the TKL concentration value of 30 wt%, as illustrate in Figure 9a and 9b; for the PU-MCO1, there is a change in fracture mechanism at 20 wt%

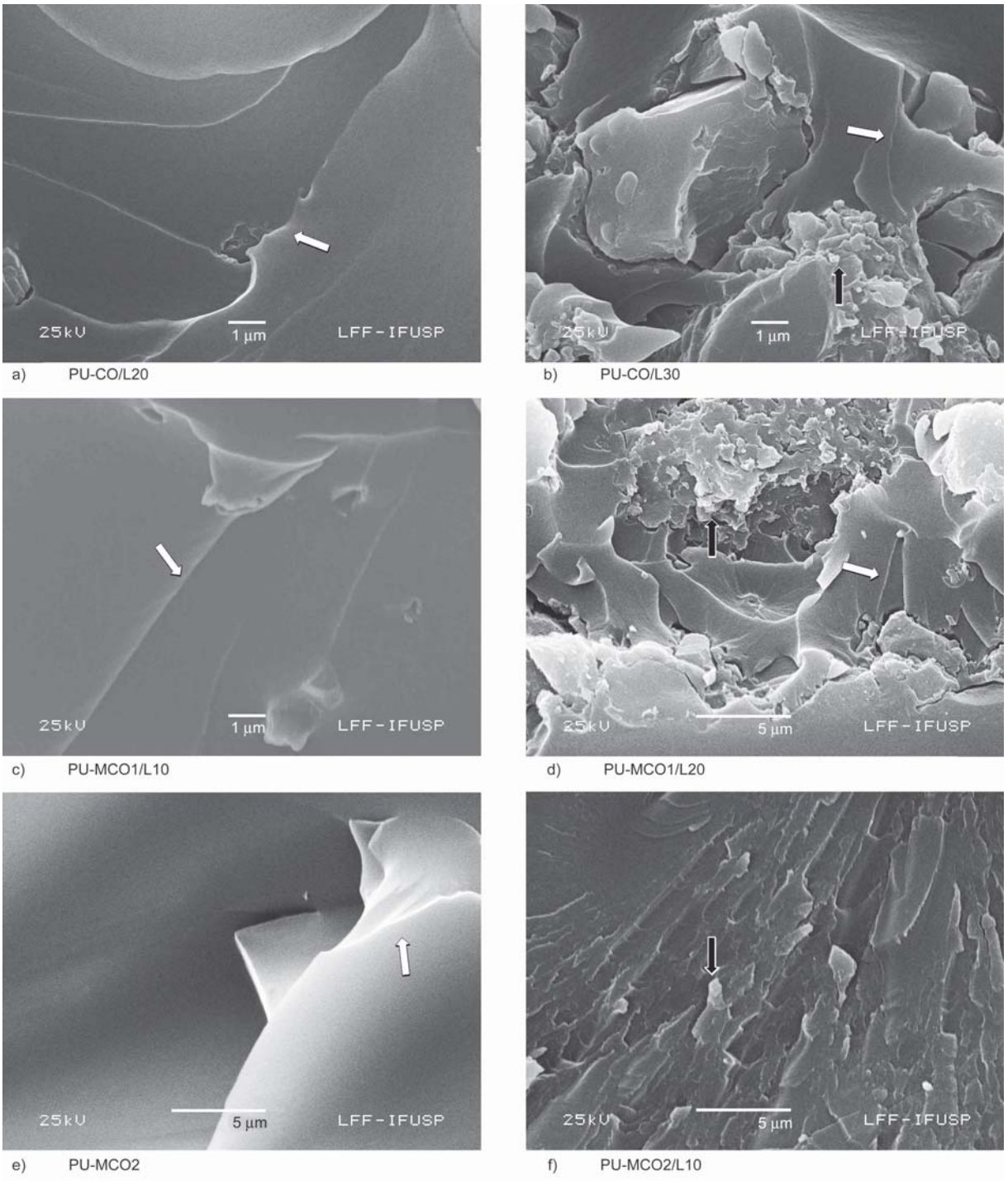

Figure 9. SEM images of the fractured surface of the lignopolyurethanes with magnification of 10000× (a, b and c) and 5000× (d, e and f)

TKL content (Figure 9c and 9d). This behavior is similar for PU-MCO2, where the value is 10 wt% lignin content (Figure 9e and 9f). It reveals that for PU-MCO1 and PU-MCO2 this behavior is anticipated due to lower lignin content.

3.5. Mechanical properties

Figure 10 summarizes the mechanical behavior of the polyurethanes. First, the increased hydroxyl index from CO to MCO1 and MCO2 substantially increased the ultimate tensile stress (Figure 10a) and the Young modulus (Figure 10c) of PU-MCO1 and PU-MCO2 versus PU-CO. Polyurethane mechanical behavior is mainly determined by the crosslinking density given by the functionality of its reactants and the stoichiometry between them [11, 39].

Figures 10b and 10d allow analyzing the effects of increasing hydroxyl index on strain. Higher hydroxyl indices decreased elastic strain (Figure 10d), which might be associated to higher amounts of rigid segments and higher crosslinking density in the polymer structure [11, 24]. Comparison of Figure 10b and 10d highlights the presence of plastic deformation in PU-CO, PU-MCO1 and PU-MCO2 before rupture. Considering that plastic deformation of thermosets starts after chain scission and is not governed by the crosslinking density [40, 41], a comparison of the increasing hydroxyl index and the ultimate strain is not feasible.

The introduction of TKL in the polyol strongly affected the mechanical behavior and increases the ultimate tensile stress (Figure 10a) and Young's modulus (Figure 10c) of lignin-containing polyurethanes. The maximum tensile stress was 23.50 MPa, and the maximum Young's modulus was 2.00 GPa for PU-MCO2/L30. The hardening effect caused by introduction of TKL might be elucidated by two mechanisms: i) Besides its participation as a co-monomer, lignin has a reinforcement role derived from its characteristics (aromatic rigid structure and Young's modulus between 2.31–4.65 GPa) [20, 39, 42, 43]; ii) Crosslinking density increasing [11, 20, 44].

The ultimate strain for PU-CO and PU-MCO1 increased by adding TKL up to 20 and 10 wt%, respectively. As TKL weight contents rises for these compositions, the ultimate strain decreases. This ultimate strain trend inversion converges to ductile-to-brittle transition, as shown in Figure 9, and is related to more rigid segments and consequently to glass transition temperature shifting. The ductile-to-brittle transition

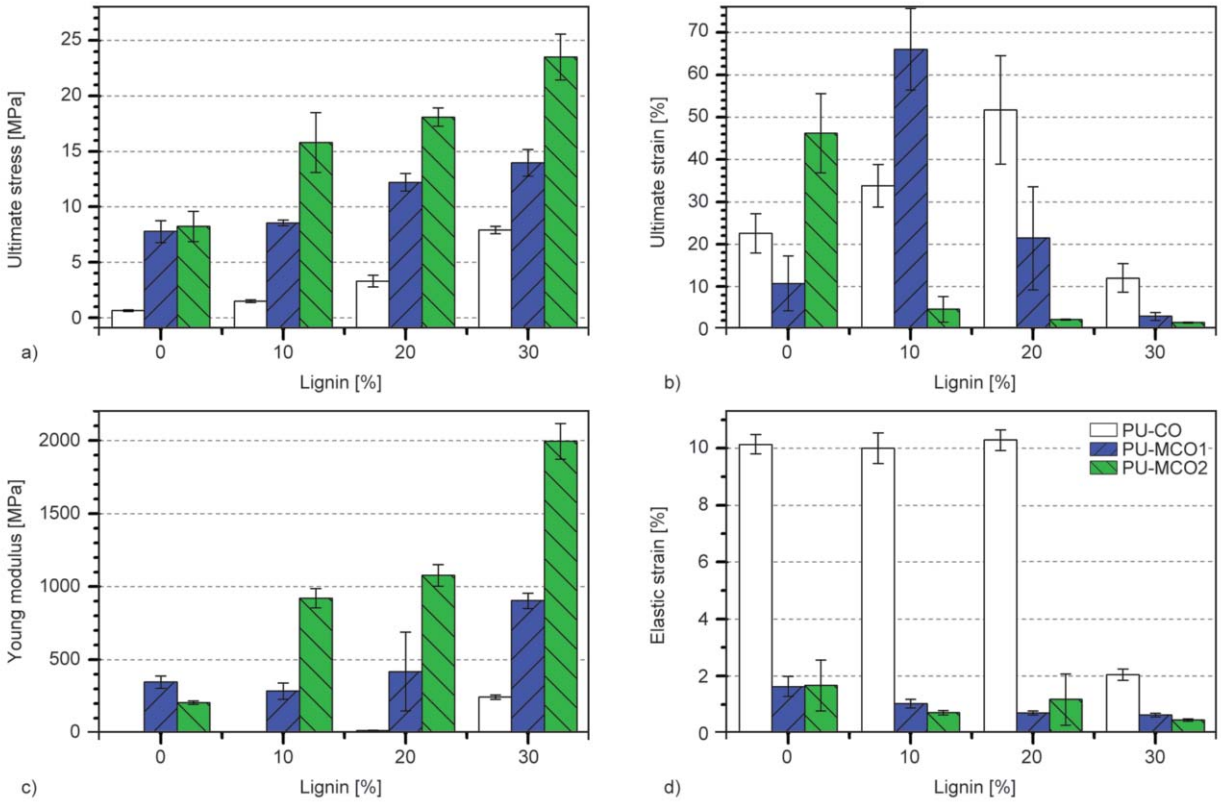

Figure 10. Mechanical results of samples with different amounts of lignin: (a) ultimate stress, (b) ultimate strain, (c) Young modulus and (d) elastic strain

occurred around 45 °C for lignin-containing polyurethanes, based on CO or MCOs, as can be observed in DMA results.

Results pointed out that the mechanical properties of lignin-containing polyurethane are in agreement with the mechanical properties of petroleum based polyurethanes, such as polyurethane adhesives (Young modulus: 0.73 to 2.25 MPa; ultimate tensile stress: 17.84 to 40.03 MPa) [45, 46] and crosslinked polyurethanes (typical ultimate tensile stress: 1.70 to 41.00 MPa) [47–49]. PU-MCO2/L30 presented the highest Young modulus in comparison with recent published results concerning 100% bio-based polyols based polyurethanes [23, 50, 51].

4. Conclusions

Polyurethanes based on renewable raw materials (technical Kraft lignin, castor oil and modified castor oil) were prepared. The results indicated that the starting materials change the polymer's properties. The oil modification process improved hydroxyl concentration and lead to polyurethanes with enhanced mechanical properties versus ones synthesized from unmodified castor oil. The introduction of TKL increased the glass transition temperature of the materials from –0.76 °C for PU-CO to 47.5 °C for PU-CO/L30 and had a twofold effect on the mechanical properties. The reinforcement co-monomer and further increase in hydroxyl content led to a higher crosslinking density. The products show the feasibility of developing polyurethane-type materials with large property range, by using an industrial low cost, unmodified and largely available residue combined with no edible renewable source oil.

Acknowledgements

The authors thank FAPESP/CNPq and acknowledge UFABC (Federal University of ABC) for the doctoral fellowship of L.T. and A.N., the master fellowship of C.B. and G.S. and financial support.

References

[1] Bernardini J., Cinelli P., Anguillesi I., Coltelli M-B., Lazzeri A.: Flexible polyurethane foams green production employing lignin or oxypropylated lignin. European Polymer Journal, **64**, 147–156 (2015). DOI: 10.1016/j.eurpolymj.2014.11.039

[2] Huber G. W., Iborra S., Corma A.: Synthesis of transportation fuels from biomass: Chemistry, catalysts, and engineering. Chemical Reviews, **106**, 4044–4098 (2006). DOI: 10.1021/cr068360d

[3] Zhang L., Zhang M., Hu L., Zhou Y.: Synthesis of rigid polyurethane foams with castor oil-based flame retardant polyols. Industrial Crops and Products, **52**, 380–388 (2014). DOI: 10.1016/j.indcrop.2013.10.043

[4] Karak N., Rana S., Cho J. W.: Synthesis and characterization of castor-oil-modified hyperbranched polyurethanes. Journal of Applied Polymer Science, **112**, 736–743 (2009). DOI: 10.1002/app.29468

[5] Zhang M., Pan H., Zhang L., Hu L., Zhou Y.: Study of the mechanical, thermal properties and flame retardancy of rigid polyurethane foams prepared from modified castor-oil-based polyols. Industrial Crops and Products, **59**, 135–143 (2014). DOI: 10.1016/j.indcrop.2014.05.016

[6] Gallezot P.: Conversion of biomass to selected chemical products. Chemical Society Reviews, **41**, 1538–1558 (2012). DOI: 10.1039/C1CS15147A

[7] Sharma C., Kumar S., Unni A. R., Aswal V. K., Rath S. K., Harikrishnan G.: Foam stability and polymer phase morphology of flexible polyurethane foams synthesized from castor oil. Journal of Applied Polymer Science, **131**, 8420–8427 (2014). DOI: 10.1002/app.40668

[8] Mutlu H., Meier M. A. R.: Castor oil as a renewable resource for the chemical industry. European Journal of Lipid Science and Technology, **112**, 10–30 (2010). DOI: 10.1002/ejlt.200900138

[9] Mosiewicki M. A., Dell'Arciprete G. A., Aranguren M. I., Marcovich N. E.: Polyurethane foams obtained from castor oil-based polyol and filled with wood flour. Journal of Composite Materials, **43**, 3057–3072 (2009). DOI: 10.1177/0021998309345342

[10] Lora J.: Industrial commercial lignins: Sources, properties and applications. in 'Monomers, polymers and composites from renewable resources' (eds: Belgacem M. N., Gandini A.) Elsevier, Amsterdam, 225–241 (2008). DOI: 10.1016/B978-0-08-045316-3.00010-7

[11] Duval A., Lawoko M.: A review on lignin-based polymeric, micro- and nano-structured materials. Reactive and Functional Polymers, **85**, 78–96 (2014). DOI: 10.1016/j.reactfunctpolym.2014.09.017

[12] Kandula M., Schwenke T., Friebel S., Salthammer T.: Effect of ball milling on lignin polyesterification with ε-caprolactone. Holzforschung, **69**, 297–302 (2015). DOI: 10.1515/hf-2014-0053

[13] Braun J. L., Holtman K. M., Kadla J. F.: Lignin-based carbon fibers: Oxidative thermostabilization of kraft lignin. Carbon, **43**, 385–394 (2005). DOI: 10.1016/j.carbon.2004.09.027

[14] Norberg I., Nordström Y., Drougge R., Gellerstedt G., Sjöholm E.: A new method for stabilizing softwood kraft lignin fibers for carbon fiber production. Journal of Applied Polymer Science, **128**, 3824–3830 (2013). DOI: 10.1002/app.38588

[15] Gordobil O., Delucis R., Egüés I., Labidi J.: Kraft lignin as filler in PLA to improve ductility and thermal properties. Industrial Crops and Products, **72**, 46–53 (2015). DOI: 10.1016/j.indcrop.2015.01.055

[16] Schorr D., Diouf P. N., Stevanovic T.: Evaluation of industrial lignins for biocomposites production. Industrial Crops and Products, **52**, 65–73 (2014). DOI: 10.1016/j.indcrop.2013.10.014

[17] Spiridon I., Leluk K., Resmerita A. M., Darie R. N.: Evaluation of PLA–lignin bioplastics properties before and after accelerated weathering. Composites Part B: Engineering, **69**, 342–349 (2015). DOI: 10.1016/j.compositesb.2014.10.006

[18] Mohamed H. A., Badran B. M., Rabie A. M., Morsi S. M. M.: Synthesis and characterization of aqueous (polyurethane/aromatic polyamide sulfone) copolymer dispersions from castor oil. Progress in Organic Coatings, **77**, 965–974 (2014). DOI: 10.1016/j.porgcoat.2014.01.026

[19] de Oliveira F. D., Ramires E. C., Frollini E., Belgacem M. N.: Lignopolyurethanic materials based on oxypropylated sodium lignosulfonate and castor oil blends. Industrial Crops and Products, **72**, 1–10 (2015). DOI: 10.1016/j.indcrop.2015.01.023

[20] Cinelli P., Anguillesi I., Lazzeri A.: Green synthesis of flexible polyurethane foams from liquefied lignin. European Polymer Journal, **49**, 1174–1184 (2013). DOI: 10.1016/j.eurpolymj.2013.04.005

[21] Yeganeh H., Mehdizadeh M. R.: Synthesis and properties of isocyanate curable millable polyurethane elastomers based on castor oil as a renewable resource polyol. European Polymer Journal, **40**, 1233–1238 (2004). DOI: 10.1016/j.eurpolymj.2003.12.013

[22] Huo S-P., Nie M-C., Kong Z-W., Wu G-M., Chen J.: Crosslinking kinetics of the formation of lignin-aminated polyol-based polyurethane foam. Journal of Applied Polymer Science, **125**, 152–157 (2012). DOI: 10.1002/app.35401

[23] Zhang C., Wu H., Kessler M. R.: High bio-content polyurethane composites with urethane modified lignin as filler. Polymer, **69**, 52–57 (2015). DOI: 10.1016/j.polymer.2015.05.046

[24] Das S., Pandey P., Mohanty S., Nayak S. K.: Influence of NCO/OH and transesterified castor oil on the structure and properties of polyurethane: Synthesis and characterization. Materials Express, **5**, 377–389 (2015). DOI: 10.1166/mex.2015.1254

[25] Gurunathan T., Mohanty S., Nayak S. K.: Isocyanate terminated castor oil-based polyurethane prepolymer: Synthesis and characterization. Progress in Organic Coatings, **80**, 39–48 (2015). DOI: 10.1016/j.porgcoat.2014.11.017

[26] Wong C. S., Badri K. H.: Chemical analyses of palm kernel oil-based polyurethane prepolymer. Materials Science and Applications, **3**, 78–86 (2012). DOI: 10.4236/msa.2012.32012

[27] Luo X., Mohanty A., Misra M.: Lignin as a reactive reinforcing filler for water-blown rigid biofoam composites from soy oil-based polyurethane. Industrial Crops and Products, **47**, 13–19 (2013). DOI: 10.1016/j.indcrop.2013.01.040

[28] García A., Erdocia X., González M. A., Labidi J.: Effect of ultrasound treatment on the physicochemical properties of alkaline lignin. Chemical Engineering and Processing: Process Intensification, **62,** 150–158 (2012). DOI: 10.1016/j.cep.2012.07.011

[29] Nada A-A. M. A., Yousef M. A., Shaffei K. A., Salah A. M.: Infrared spectroscopy of some treated lignins. Polymer Degradation and Stability, **62**, 157–163 (1998). DOI: 10.1016/S0141-3910(97)00273-5

[30] Pietrzak K., Kirpluks M., Cabulis U., Ryszkowska J.: Effect of the addition of tall oil-based polyols on the thermal and mechanical properties of ureaurethane elastomers. Polymer Degradation and Stability, **108**, 201–211 (2014). DOI: 10.1016/j.polymdegradstab.2014.03.038

[31] Sormana J-L., Meredith J. C.: High-throughput discovery of structure–mechanical property relationships for segmented poly(urethane–urea)s. Macromolecules, **37**, 2186–2195 (2004). DOI: 10.1021/ma035385v

[32] Corcuera M. A., Rueda L., Fernandez D'Arlas B., Arbelaiz A., Marieta C., Mondragon I., Eceiza A.: Microstructure and properties of polyurethanes derived from castor oil. Polymer Degradation and Stability, **95**, 2175–2184 (2010). DOI: 10.1016/j.polymdegradstab.2010.03.001

[33] Chattopadhyay D. K., Webster D. C.: Thermal stability and flame retardancy of polyurethanes. Progress in Polymer Science, **34**, 1068–1133 (2009). DOI: 10.1016/j.progpolymsci.2009.06.002

[34] D'souza J., Camargo R., Yan N.: Polyurethane foams made from liquefied bark-based polyols. Journal of Applied Polymer Science, **131**, 1–10 (2014). DOI: 10.1002/app.40599

[35] Hablot E., Zheng D., Bouquey M., Avérous L.: Polyurethanes based on castor oil: Kinetics, chemical, mechanical and thermal properties. Macromolecular Materials and Engineering, **293**, 922–929 (2008). DOI: 10.1002/mame.200800185

[36] Kang S. M., Lee S. J., Kim B. K.: Shape memory polyurethane foams. Express Polymer Letters, **6**, 63–69 (2012). DOI: 10.3144/expresspolymlett.2012.7

[37] Calvo-Correas T., Gabilondo N., Alonso-Varona A., Palomares T., Corcuera M. A., Eceiza A.: Shape-memory properties of crosslinked biobased polyurethanes. European Polymer Journal, **78**, 253–263 (2016). DOI: 10.1016/j.eurpolymj.2016.03.030

[38] Nair M. N. R., Sukumar P., Jayashree V., Nair M. R. G.: Mechanical properties and fractography of block copolymers based on NR and MDI-based polyurethanes. Polymer Bulletin, **65**, 83–96 (2010).
DOI: 10.1007/s00289-010-0251-8

[39] Ionescu M.: Chemistry and technology of polyols for polyurethane. Rapra, Shawbury (2007).

[40] Jang B. Z., Pater R. H., Soucek M. D., Hinkley J. A.: Plastic deformation mechanisms in polyimide resins and their semi-interpenetrating networks. Journal of Polymer Science Part B: Polymer Physics, **30**, 643–654 (1992).
DOI: 10.1002/polb.1992.090300701

[41] Mullins M. J., Liu D., Sue H-J.: Mechanical properties of thermosets. in 'Thermosets: Structure, properties and applications' (ed.: Guo Q.) Woodhead, Oxford (2012).
DOI: 10.1533/9780857097637.1.28

[42] Elder T.: Quantum chemical determination of Young's modulus of lignin. Calculations on a β–O-4′ model compound. Biomacromolecules, **8**, 3619–3627 (2007).
DOI: 10.1021/bm700663y

[43] Li Y., Ragauskas A. J.: Kraft lignin-based rigid polyurethane foam. Journal of Wood Chemistry and Technology, **32**, 210–224 (2012).
DOI: 10.1080/02773813.2011.652795

[44] Mahmood N., Yuan Z., Schmidt J., Xu C.: Preparation of bio-based rigid polyurethane foam using hydrolytically depolymerized Kraft lignin *via* direct replacement or oxypropylation. European Polymer Journal, **68**, 1–9 (2015).
DOI: 10.1016/j.eurpolymj.2015.04.030

[45] Banea M. D., da Silva L. F. M., Carbas R. J. C., Campilho R. D. S. G.: Mechanical and thermal characterization of a structural polyurethane adhesive modified with thermally expandable particles. International Journal of Adhesion and Adhesives, **54**, 191–199 (2014).
DOI: 10.1016/j.ijadhadh.2014.06.008

[46] Clauss S., Gabriel J., Karbach A., Matner M., Niemz P.: Influence of the adhesive formulation on the mechanical properties and bonding performance of polyurethane prepolymers. Holzforschung, **65**, 835–844 (2011).
DOI: 10.1515/HF.2011.095

[47] Prisacariu C.: Polyurethane elastomers: From morphology to mechanical aspects. Springer, Viena (2011).
DOI: 10.1007/978-3-7091-0514-6

[48] Wang H. H., Mou J., Ni Y. H., Fei G. Q., Si C. L., Zou J.: Phase behavior, interaction and properties of acetic acid lignin-containing polyurethane films coupled with aminopropyltriethoxy silane. Express Polymer Letters, **7**, 443–455 (2013).
DOI: 10.3144/expresspolymlett.2013.41

[49] Kupka V., Vojtova L., Fohlerova Z., Jancar J.: Solvent free synthesis and structural evaluation of polyurethane films based on poly(ethylene glycol) and poly(caprolactone). Express Polymer Letters, **10**, 479–492 (2016).
DOI: 10.3144/expresspolymlett.2016.46

[50] Lee A., Deng Y.: Green polyurethane from lignin and soybean oil through non-isocyanate reactions. European Polymer Journal, **63**, 67–73 (2014).
DOI: 10.1016/j.eurpolymj.2014.11.023

[51] Madhukar B. S., Bhadre Gowda D. G., Annadurai V., Somashekar R., Siddaramaiah: Phase behaviors of PU/SPI green composites using SAXS profiles. Advances in Polymer Technology, **35**, 21526/1–21526/10 (2016).
DOI: 10.1002/adv.21526

eXPRESS Polymer Letters Vol.10, No.11 (2016) 941–949
Available online at www.expresspolymlett.com
DOI: 10.3144/expresspolymlett.2016.87

Non-destructive evaluation by terahertz spectroscopy for penetration of acid solutions into epoxy resin

M. Kusano[1*], *M. Kubouchi*[2], *D. S. Bulgarevich*[1], *M. Shiwa*[1]

[1]National Institute for Materials Science, 1-2-1 Sengen, Tsukuba, 305-0047 Ibaraki, Japan
[2]Tokyo Institute of Technology, 2-12-1, O-okayama, Meguro, 152-8550 Tokyo, Japan

Received 18 April 2016; accepted in revised form 27 June 2016

Abstract. Epoxy resins are used as high-performance thermosetting linings to protect substrates under corrosive environments. However, in a severe corrosive chemical solution, such protective layers may degrade with long time due to penetrations of solvent and solute molecules into resin network. In this regard, the terahertz time-domain spectroscopy (THz-TDS) is a promising tool for non-destructive evaluation of the penetrant amounts due to high transparency of such plastic materials and high sensitivity to the molecular vibrations in terahertz spectral range. In this work, the complex refractive indexes n and κ of epoxy specimens were measured after immersion into sulfuric acid solutions and compared with penetrated mass fractions of water and acid ions. It was found that n and κ depended linearly with water and sulfuric acid mass fraction in specimens, and κ of sulfuric acid immersed specimens was lager at higher frequency. While the calculated $\Delta\kappa$ agreed well with THz-TDS measurement by THz-TDS, the calculated Δn was higher than the measurement. The difference may be attributed to the water and sulfuric states in the specimen.

Keywords: *thermosetting resins, terahertz spectroscopy, complex refractive index, epoxy resin, sulfuric acid*

1. Introduction

Epoxy resins have excellent properties such as adhesion, corrosion resistance, and mechanical strength. Therefore, they are classified as high-performance thermosetting resins for coatings and linings. In particular, the amine-cured epoxies can cure at ambient conditions and are known as the most common coatings for metal equipment and concrete constructions under corrosive environments [1]. When these coatings are used in chemical solutions such as process fluids in chemical plants and sewage water in communities, the water and solute molecules gradually penetrate into the epoxy resins, especially under low pH acid conditions [2–7]. After the penetrants reach the interface between the resin coating and the substrate, the substrate can be corroded by the penetrants. In order to use these protective materials for a long-term, it is important to non-destructively evaluate the amounts and depths of the penetrants in the polymer coatings/lining. However, there are only a few non-destructive testing (NDT) methods that can measure the amounts of water and solutes inside coatings/linings. For example, the ultrasonic test (UT), which is one of the most common NDT methods, can measure the variation of the sound velocity in degraded samples [8]. However, it is still difficult to estimate the penetrants in resin by UT. On the other hand, with portable FT-IR Attenuated Total Reflection (ATR) spectroscopy, it is possible to non-destructively detect water, sulfate, or other penetrant in plastics [9, 10], but the depth of FT-IR ATR measurement into plastics is only submicron at most [11, 12], which is much smaller than typical thickness of resin coatings/linings (typically more than 1 mm). Therefore,

*Corresponding author, e-mail: KUSANO.Masahiro@nims.go.jp

FT-IR ATR spectroscopy is also not suitable for the NDT method of coatings/linings.

The terahertz frequency ranges between 0.1 and 10 THz correspond to the spectral region between microwave and far-IR. Due to the progress in terahertz time-domain spectroscopy (THz-TDS), it has received an increased interest during the past decade. The main advantages of THz-TDS for NDT studies are the high penetration of THz electromagnetic waves into polymers [13–18], high sensitivity to the inter/intra molecular vibrations (especially for water) [18–26], and ability to estimate the materials dielectric properties without direct contact [27–29].

The THz spectra of various thermoplastics [13–15] and thermosets [16, 17] measured by THz-TDS were reported. In contrast with FT-IR spectra, the THz spectra shows a few clear features to distinguish polymer molecular structures. However, THz spectroscopy can be useful for monitoring the glass transition of the polymer because the polymer chain motion above and below the glass transition temperature affects the THz refractive index [14]. In addition, owing to the significant difference of dielectric properties between polymers and other materials, spectral features of inclusions such as inorganic fillers [15] and carbon nanotubes [17] in polymer materials were also recognized in the THz spectra.

The dielectric properties of liquid water, aqueous solutions, and water in materials were also studied with to understand hydrogen bonding state i.e. 'free water' and 'bound water' [23–26]. Although free and bound water was experimentally studied by FT-IR [10, 30, 31], NMR [32], thermomechanical analysis [31, 32] etc., it is still a highly controversial subject. Since the interactions of the bound water and free water show slightly different dielectric properties [14, 20, 22–25, 29], THz-TDS could have an advantage to distinguish these two states of water. In fact, the THz dielectric spectra of bulk water is composed of several spectral peaks related to the different relaxation times and intermolecular stretching vibration of water [23, 24].

The detection and imaging of liquid water and moisture in materials by THz spectroscopy had been previously studied and various applications had been demonstrated on medical, agricultural, food, and other products [20, 27]. Note that water molecules in material can also exist as both 'free' and 'bound' water and it is difficult to separate experimentally the contributions from bound and free water to the THz spectra [20]. In certain cases, the assumption that only bound water exists in a material makes it possible to measure its content [18, 20]. For example, the amounts of water in polyamide and wood plastic composites were estimated with THz-TDS by measuring the complex refractive index as a function of water content [18]. In the case of wood materials in humid environment, the real and imaginary parts of the complex dielectric function of the samples strongly correlated with density and moisture content [21].

As described above, the interpretation of THz spectra for penetrants in polymer still remains unclear but if penetrants such as sulfuric acid in polymer affect THz spectra, THz spectroscopy may help to nondestructively monitor polymer degradation by corrosive solution penetration and evaluate the penetrant content in polymer. To the best of our knowledge, there is no study with THz spectroscopy on penetrants in polymeric materials except for water.

In this work, the epoxy resin immersed in sulfuric acid aqueous solutions was observed by THz-TDS. It was shown that the imaginary part of the complex refractive index in THz range was correlated linearly and independently with the amounts of water and sulfuric acid in epoxy resin.

2. Experimental

2.1. Specimens and immersion environments

Epoxy resin (EP) specimens were prepared in the following manner. Firstly, a bisphenol-A-type epoxy resin (EPOMIK® R140, Mitsui Chemicals, Inc., Japan) was mixed with equivalent ratio of curing agent (polyether amine, JEFFAMINE® D-230, Huntsman Corporation, Japan). The mixture was evacuated in a deforming device to remove air bubbles, then it was cast into a metal mold and placed into an oven at appropriate temperature until curing was completely finished. After that, the broad cured EP plate 2 mm thick was taken out from the mold and cut into specimens with 30×30 mm dimensions.

Ion-exchanged water and 2.0 M sulfuric acid aqueous solutions (Kanto Chemical Co., Inc., Japan) were used as environmental solutions. The beakers with such solutions were set in a water bath at 70 ºC. The EP specimens were immersed into solutions and then taken out periodically. Then, they were wiped off

with paper towel to measure their mass by an analytical balance, thickness by a micrometer, and transmission spectrum by THz-TDS. After these measurements, the specimens were dried in air at 50 ºC until their masses remained constant for a day. Then, their mass, thickness, and transmission spectrum were measured again.

2.2. Degradation analysis

In acid aqueous solutions, the water and acid could penetrate into the immersed resin specimen with time [4–6]. In order to evaluate the amounts of penetrants, the mass of the specimen was measured soon after removal from the solution (m_{wet}) and after drying in air at 50 °C (m_{dry}). The wet (M_{wet}) and dry (M_{dry}) mass fractions were determined by Equations (1) and (2):

$$M_{wet} = \frac{m_{wet} - m_0}{m_0} \tag{1}$$

and

$$M_{dry} = \frac{m_{dry} - m_0}{m_0} \tag{2}$$

where m_0 was the initial mass.

After drying, the specimens were cut and their cross sections were analyzed by energy dispersive X-ray spectroscopy, EDS (equipped on JSM-6510 LA, JEOL Ltd., Japan). The sulfur element mapping on the cross section provides the penetration depth of sulfuric acid.

2.3. Terahertz time-domain spectroscopy

The THz-TDS instrument with bound IR-spectra software (IRS-2000, Aispec Co. Ltd., Japan) was used to measure transmission spectra of the EP specimens. Figure 1 displays typical transmission-type THz-TDS setup [28, 29]. In this optical arrangement, the modulated femtosecond laser pulse of about 10 fs duration at a wavelength of 780 nm is split into the pump and probe beams. The pump beam helps to generate ultrashort current flow inside illuminated photoconductive substrate in the gap between biased antenna electrodes (a low-temperature-grown Ga–As film). Then, the broadband THz radiation from this gap is reshaped spectrally and redirected spatially by antenna electrodes and optical elements towards sample. Finally, THz radiation arrives to the second identical photoconductive antenna (PCA) at the same time with the laser probe beam. As a result, the modulated current is generated at the PCA detector gap and registered with lock-in amplifier. In order to record the time-domain signal of the pump beam, the optical length of the probe beam is changed by moving a corner reflector as indicated by an arrow in Figure 1 (in other words, the time the probe beam arrives at the PCA is changed). As a consequence, THz waveform can be digitized at fine time intervals.

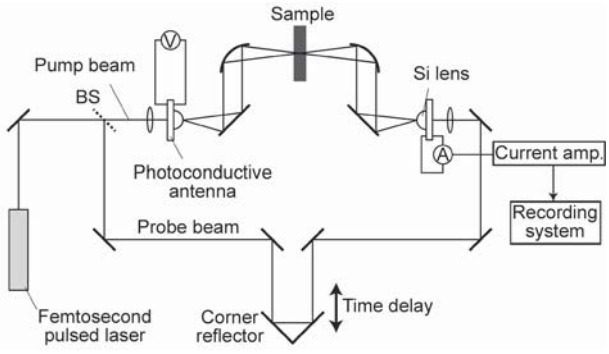

Figure 1. The scheme of the THz-TDS system used in experiments

The THz waveform transmitted through specimens was measured under ambient conditions (24 ºC, ~40% RH). In addition, the waveform without specimens at the same ambient conditions was also measured as a reference every time. Since the THz beam focuses on sample and the beam width at sample is less than 10 mm, the dimensions of the EP specimens were large enough not to consider whether the edge of the specimen affected the transmission spectra in this study. The measured waveforms were converted into the frequency domain THz transmission spectrum and phase delay data by fast Fourier transform (FFT). From the spectrum and phase delay data of specimen and reference, IR-spectra software calculates the complex refractive indexes ($\tilde{n} = n - i\kappa$) of the EP specimens in THz range. The mathematical algorithm is described in detail elsewhere [28, 29]. Since the transmittance of electromagnetic waves through a 2 mm thick epoxy specimen rapidly decreases with increasing frequency above 1 THz, the effective frequency range is limited up to 1 THz. For the same reason, the range is also limited to above 0.2 THz.

3. Results

3.1. EP immersed in water

Firstly, the EP specimen after immersion in ion-exchanged water was observed. Figure 2 shows M_{wet} of the EP specimen with immersion times in ion-exchanged water. As shown in this figure, M_{wet} increases proportionally with square root of immersion time due to penetration of the water molecules into EP network by Fick's law of diffusion [2, 3]. After about 900 hours (37.5 days), the M_{wet} reached to a saturation level. The mass after drying in air at 50 ºC, m_{dry} returns to the initial value, m_0 because water molecules in EP have completely evaporated.

Figure 3 shows the spectral change of n and κ of EP through water immersion from 0 to 49 days. Both of them are shifted vertically and incrementally with immersion time. After drying, such spectra return to their initial values (0 days). In order to correlate the complex refractive index with water content in EP, n and κ at 0.4 and 0.6 THz as representative values are plotted with M_{wet}. As shown in Figure 4, both n and κ at 0.4 and 0.6 THz increase linearly with M_{wet}. The slopes of n at 0.4 and 0.6 THz and those of κ at 0.4 and 0.6 THz are also the same, respectively. This behavior is in a good agreement with the complex refractive index spectrum of polyamide (PA) immersed in water reported by Jördens *et al*. [18] even though PA absorbs more water than EP and saturates at about 10 mass%.

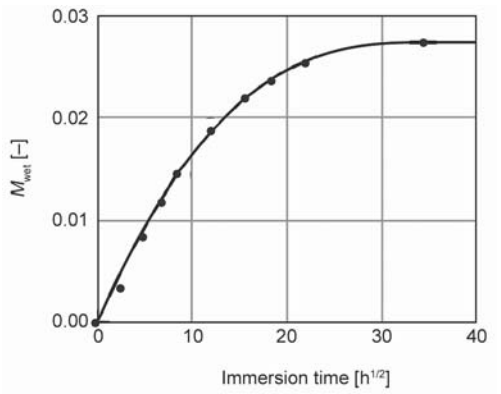

Figure 2. The wet mass fraction of the EP specimen with immersion times in ion-exchanged water

3.2. EP immersed in sulfuric acid solution

In addition to water, sulfuric acid solutions are also known to penetrate into the EP network [4–6]. Therefore, EP specimens after immersion in the sulfuric acid solution and after drying are studied gravimetrically and spectroscopically. Up to about 150 hours, M_{wet} increases linearly with square root of immersion time (see Figure 5) as the same tendency as the specimens immersed in water shown in Figure 2. After about 150 hours (6.3 days), the M_{wet} becomes constant due to saturation with water and sulfuric acid. On the other hand, the mass after drying in air at 50 ºC decreases to some extent but m_{dry} does not return to m_0. M_{dry} also increases linearly with square root of immersion time and becomes constant after 150 hours. While water molecules evaporate completely from EP network through the drying process, sulfuric acid remains due to its much lower volatility. Therefore, M_{dry} indicates the sulfuric acid mass fraction M_S in the specimen.

The EDS mapping of the sulfur element for the cross section of the specimen is shown in Figure 6. This EP specimen was immersed in the sulfuric acid solution for 84 hours. The image represents that sulfuric acid penetrates into the specimen and distribute

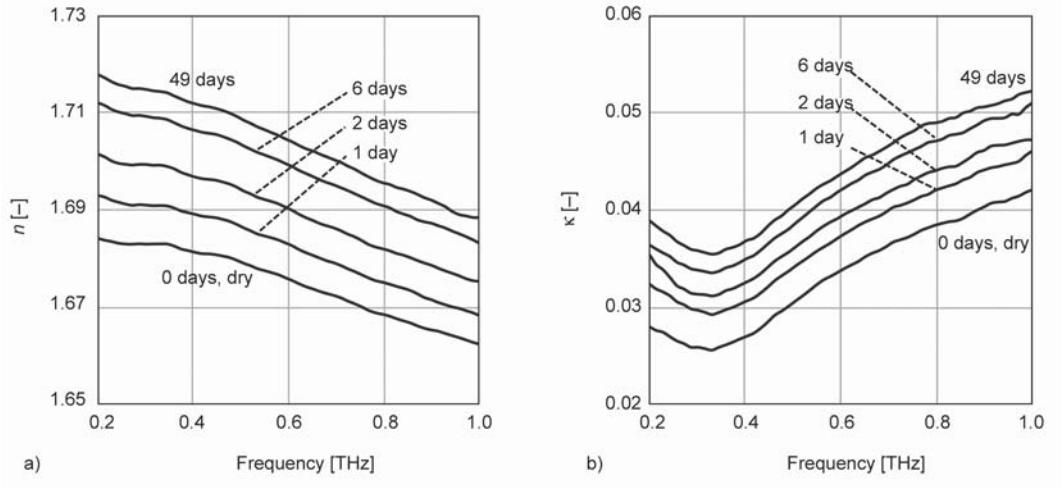

Figure 3. (a) The real and (b) imaginary parts of the complex refractive index for the EP specimen after immersion in water

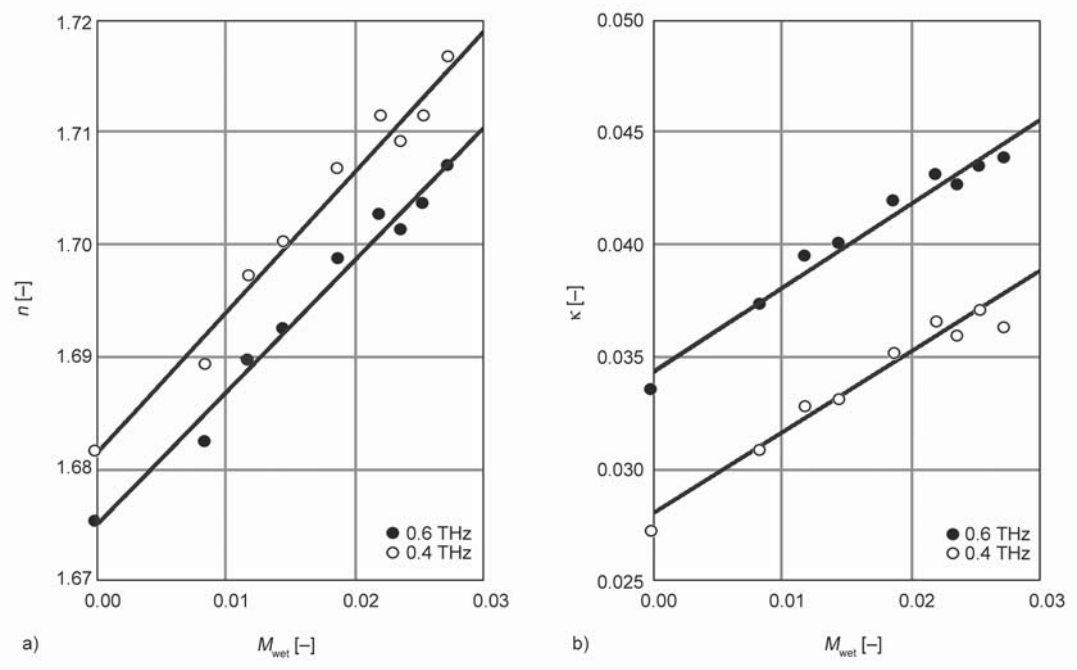

Figure 4. (a) The real and (b) imaginary parts of the complex refractive index at 0.4 and 0.6 THz for the EP specimen with water mass fraction

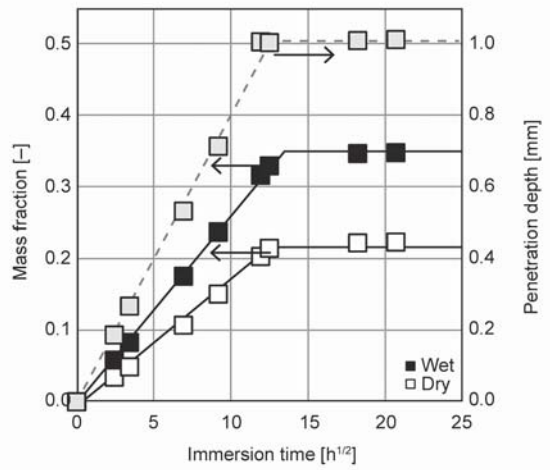

Figure 5. The wet and dry mass fractions of the EP specimen after immersion times in 2.0 M sulfuric acid solution. In addition, gray plots are penetration depth of sulfuric acid in the specimen measured by EDS (see Figure 6)

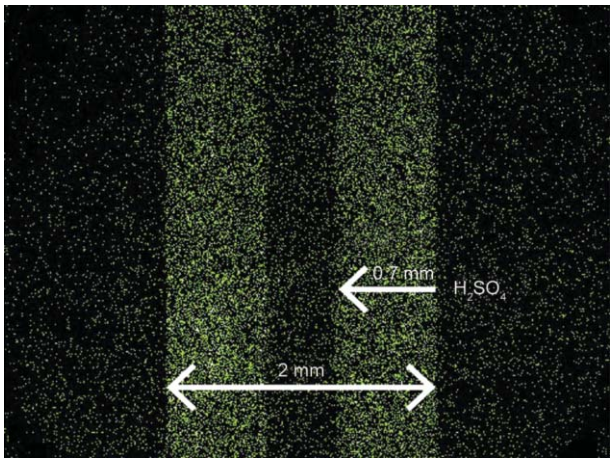

Figure 6. The EDS mapping of sulfur element at the cross section of the EP specimen (2 mm thick) after immersion in 2.0 M sulfuric acid solution for 84 hours. Sulfur element shows that sulfuric acid penetrates into the specimen from both surfaces and reached to 0.7 mm depth.

uniformly from both sides up to 0.7 mm depth. The depth with square root of immersion time is also shown in Figure 5. The depth also increases linearly with square root of time and leveled off at 150 hours because the acid penetrates to whole thickness at this immersion time. These observations are consistent with other reports [4–6]. In addition, epoxy resin itself scarcely changes in respect of the molecular structure or chemically degrade despite the penetration of sulfuric acid [5].

The *n* and κ spectra of the 'wet' specimens soon after removal from the sulfuric acid solution are shown in Figure 7. Although both spectra display increase with immersion time, the n spectra show almost parallel lines or constant increment at all frequencies. On the other hand, the increment of κ at higher frequency is larger than that of lower frequencies. Figure 8 shows *n* and κ spectra of the 'dry' specimens which are immersed in the solution and subsequently dried. Again,

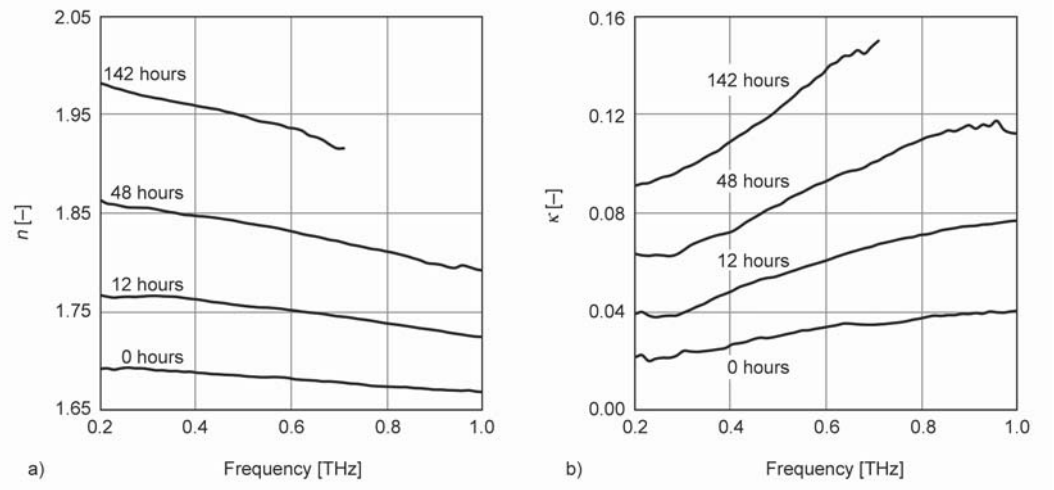

Figure 7. (a) The real and (b) imaginary parts of the complex refractive index of the EP specimen soon after removal from the 2.0 M sulfuric acid solution

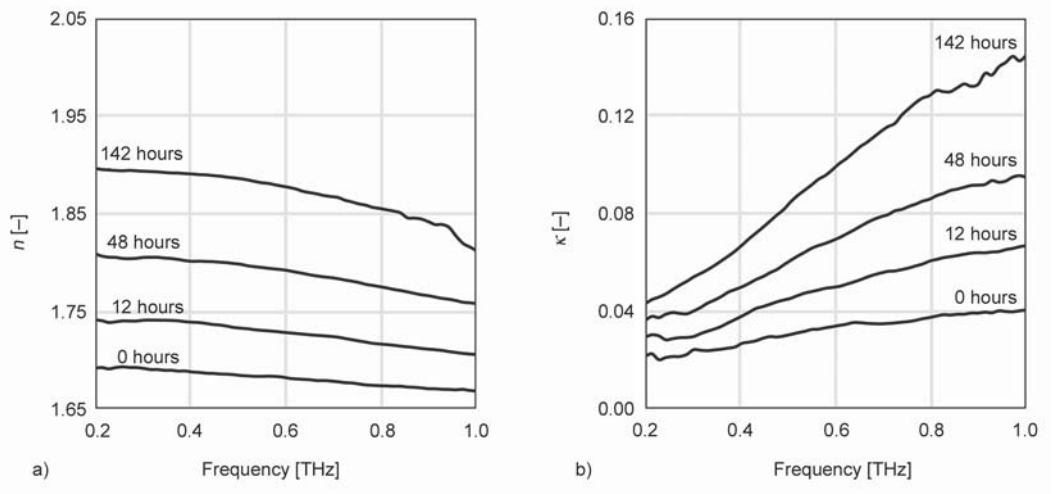

Figure 8. (a) The real and (b) imaginary parts of the complex refractive index of the EP specimen measured after immersion in the 2.0 M sulfuric acid solution and subsequent drying in air 50 °C

the κ at higher frequency displays larger increments and n does not show this tendency. This can be seen more clearly in Figure 9, where κ at 0.4 and 0.6 THz are plotted against M_{dry}. The figure demonstrates linear dependence with the same slope of n and with different slopes of κ at 0.4 and 0.6 THz. Such behavior is observed for sulfuric acid aqueous solutions with different concentrations [33]. These results indicate that penetrated sulfuric acid causes larger increase of the κ at the higher frequencies.

4. Discussion

As discussed in section 3.1, the $\tilde{n}$ of the EP specimen increased with the M_{wet}. Although the THz spectra of the $\tilde{n}$ of bulk water are already known [18, 23, 24, 34], as mentioned in section 1, it is challenging to separate experimentally the contributions from bound and free water in materials [18, 20]. In our study, some water molecules in the specimen can be bound to the amine and hydroxyl groups in the resin. As a result, the water state could be different from that of bulk water. This behavior is consistent with the trends observed for water immersed polyamide (PA) specimens reported by Jördens, *et al*. [18]

However, the $\tilde{n}$ of the epoxy specimen immersed in the sulfuric acid solution showed different changes from that immersed in water, especially for the κ at the higher frequencies. The $\tilde{n}$ increased with the fraction of the sulfuric acid in the specimen. As mentioned in section 3.2, the sulfuric acid does not cause the chemical decomposition of the epoxy network by hydrolysis and other reactions [5]. From these results, it is guessed that the change of the $\tilde{n}$ can be attributed mainly to the sulfuric acid in epoxy resin. The

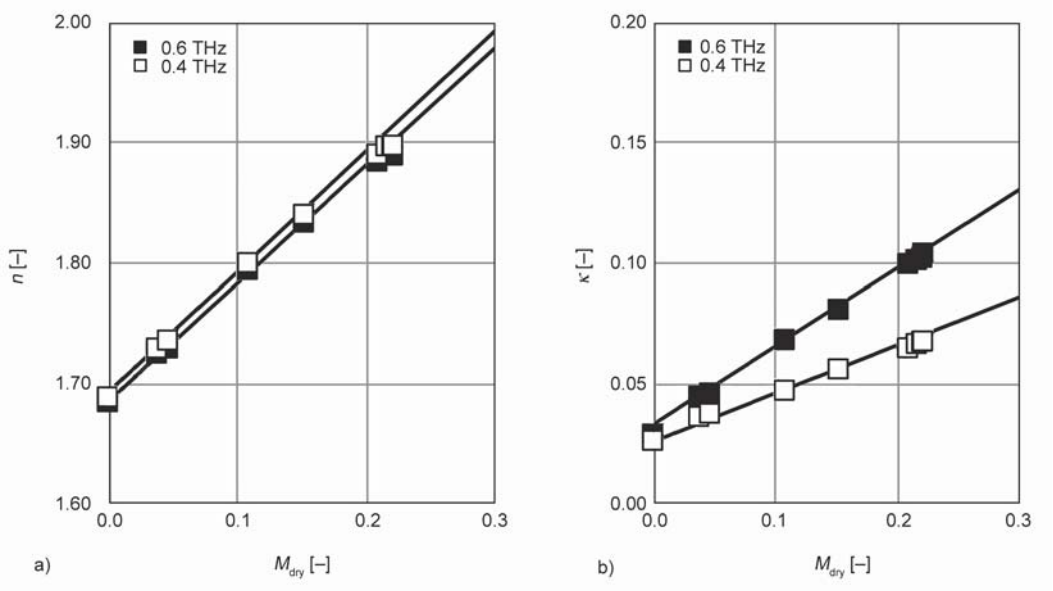

Figure 9. (a) The real and (b) imaginary parts of the complex refractive indexes at 0.4 and 0.6 THz with the mass fraction of sulfuric acid for the EP specimen, which were measured after immersion in the 2.0 M sulfuric acid solution and subsequent drying in air 50 °C.

lager κ at the higher frequencies can be attributed to the sulfuric acid spectral band above 1.0 THz with the tail extending to 0.2 THz. To understand this in more detail, the measurement at higher THz frequencies and with thinner samples are necessary (not a subject of the present work).

Since the increments of the $\tilde{n}$ in Figure 7 were caused by both water and acid, it is estimated that the increment Δn and $\Delta\kappa$ are decided by a linear equation of water and acid mass fractions in EP independently. Here, $I_{n,W}$ and $I_{n,S}$ are the corresponding slopes from Figures 4a and 9a, where subscripts *W* and *S* indicate water and sulfuric acid, respectively. While water mass fraction in EP specimen M_W is the difference between M_{wet} and M_{dry}, sulfuric acid mass fraction M_S is M_{dry}. The linear equation of Δn is described as Equation (3):

$$\Delta n_\omega = I_{n,W,\omega} M_W + I_{n,S,\omega} M_S \quad (3)$$

where the subscript ω indicates frequency. Likewise, $\Delta\kappa$ is described as Equation (4):

$$\Delta\kappa_\omega = I_{\kappa,W,\omega} M_W + I_{\kappa,S,\omega} M_S \quad (4)$$

Figure 10 represents comparison between the increments by measuring with THz-TDS (Figure 7) and by calculating with the linear Equations (3) and (4) at 0.4 THz. Both the measured and calculated $\Delta n_{0.4}$ and $\Delta\kappa_{0.4}$ increase with M_{wet}. While the calculated $\Delta\kappa_{0.4}$ agrees well with the measured $\Delta\kappa_{0.4}$, the calculated $\Delta n_{0.4}$ is higher than the measured $\Delta n_{0.4}$. These behaviors are observed at other frequencies. The difference between calculated and measured $\Delta n_{0.4}$ may be attributed to free and bound water in the specimen because THz radiation is sensitive to both water states [18–26]. Since amine cured EP resins have some hydrophilic groups such as hydroxyl groups and amine groups, water becomes bound to such groups to some extent. On the other hand, sulfuric acids react with amine groups in EP resins and form amine salt [4, 5]. Therefore, the state of water in the sulfuric acid immersed specimen may differ from that in the water immersed specimen so that calculated and measured $\Delta n_{0.4}$ does not show agreement with each other. THz-TDS and some complementary analyses such as FT-IR [10, 30, 31], NMR [32], thermomechanical analysis [31, 32] could help to determine penetrant states in the EP resin. Nevertheless, it is confirmed that THz spectroscopy is a promising method to evaluate sulfuric acid in epoxy resin.

5. Conclusions

The $\tilde{n}$ of the EP specimens were measured by THz-TDS after immersion in water and sulfuric acid solutions. It was found that *n* and κ depended linearly with water and sulfuric acid mass fraction in specimens, and $\Delta\kappa$ of sulfuric acid immersed specimens

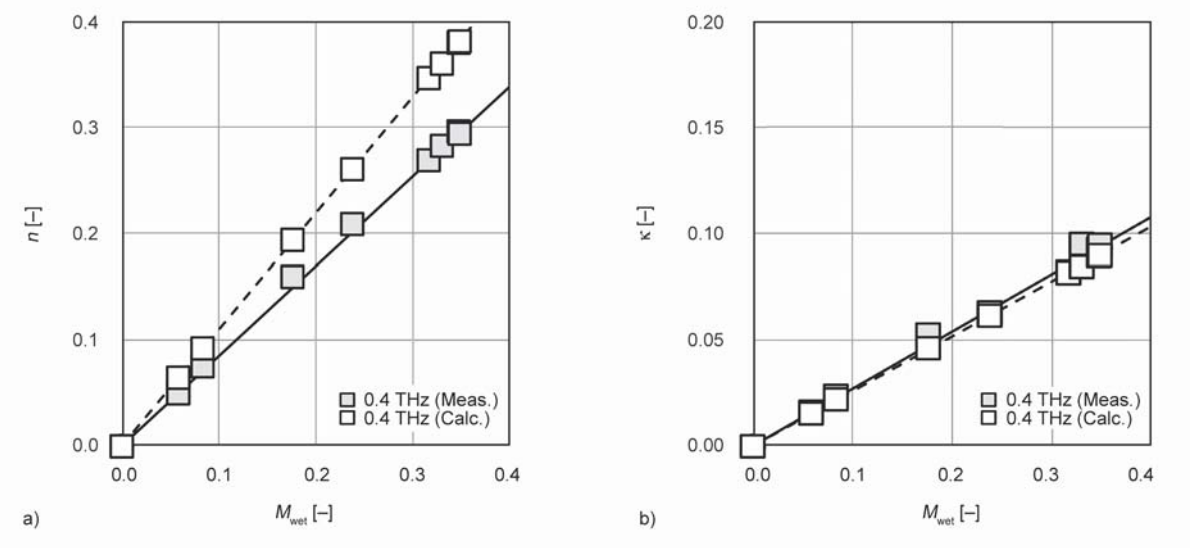

Figure 10. The increments of (a) the real and (b) imaginary parts of the complex refractive indexes at 0.4 THz: comparison between calculation by the linear equations (white plots) and the measurement by THz-TDS (gray plots)

was lager at higher frequency. THz-TDS can help to discern whether the specimen contains sulfuric acid. The increments of the $\tilde{n}$ were described with linear equations involving water and sulfuric acid mass fractions. As for $\Delta\kappa$, good agreement between calculation and measurement was observed. On the other hand, calculated Δn was higher than the measured Δn. The difference may be attributed to free and bound water in the specimen. Therefore, THz-TDS can help to find out penetrant states in the EP resin, making it a promising NDT method to evaluate the penetration of the corrosive chemicals into resin coatings.

References

[1] Weldon D. G.: Failure analysis of paints and coatings revised edition. Wiley, New York (2009).

[2] Maggana C., Pissis P.: Water sorption and diffusion studies in an epoxy resin system. Journal of Polymer Science Part B: Polymer Physics, **37**, 1165–1182 (1999). DOI: 10.1002/(SICI)1099-0488(19990601)37:11<1165::AID-POLB11>3.0.CO;2-E

[3] Wong T. C., Broutman L. J.: Water in epoxy resins part II. Diffusion mechanism. Polymer Engineering and Science, **25**, 529–534 (1985). DOI: 10.1002/pen.760250904

[4] Tsuda K., Kubouchi M.: Decomposition of polymeric materials. Zairyo-to-Kankyo, **44**, 104–111 (1995). DOI: 10.3323/jcorr1991.44.104

[5] Sembokuya H., Negishi Y., Kubouchi M., Tsuda K.: Corrosion behavior of epoxy resin cured with different amount of hardener in corrosive solutions. Journal of the Society of Materials Science, **9**, 230–234 (2003). DOI: 10.2472/jsms.52.9Appendix_230

[6] Nakayama M., Hosokawa Y., Muraoka Y., Katayama T.: Life prediction under sulfuric acid environment of FRP using X-ray analysis microscope. Journal of Materials Processing Technology, **155–156**, 1558–1563 (2004). DOI: 10.1016/j.jmatprotec.2004.04.252

[7] Amaro A. M., Reis P. N. B., Neto M. A., Louro C.: Effect of different acid solutions on glass/epoxy composites. Journal of Reinforced Plastics and Composites, **32**, 1018–1029 (2013). DOI: 10.1177/0731684413483886

[8] Yochev B., Kutzarov S., Ganchev D., Staykov K.: Investigation of ultrasonic properties of hydrophilic polymers for dry-coupled inspection. in 'Proceeding of The European Conference on Non-Destructive Testing. Berlin, Germany', pp. 1–10 (2006).

[9] Silverstein R. M., Webster F. X., Kiemle D. J., Bryce D. L.: Spectrometric identification of organic compounds. Wiley, New York (1998).

[10] Kusanagi H., Yukawa S.: Fourier transform infra-red spectroscopic studies of water molecules sorbed in solid polymers. Polymer, **35**, 5637–5640 (1994). DOI: 10.1016/S0032-3861(05)80037-0

[11] Harrick N. J., Carlson A. I.: Internal reflection spectroscopy: Validity of effective thickness equations. Applied Optics, **10**, 19–23 (1971). DOI: 10.1364/AO.10.000019

[12] Chen J., Gardella J. A.: Quantitative ATR FT-IR analysis of surface segregation of polymer blends of polystyrene/poly(dimethylsiloxane)-*co*-polystyrene. Applied Spectroscopy, **52**, 361–366 (1998). DOI: 10.1366/0003702981943824

[13] Wietzke S., Jansen C., Reuter M., Jung T., Kraft D., Chatterjee S., Fischer B. M., Koch M.: Terahertz spectroscopy on polymers: A review of morphological studies. Journal of Molecular Structure, **1006**, 41–51 (2011). DOI: 10.1016/j.molstruc.2011.07.036

[14] Wietzke S., Jansen C., Jung T., Reuter M., Baudrit B., Bastian M., Chatterjee S., Koch M.: Terahertz time-domain spectroscopy as a tool to monitor the glass transition in polymers. Optics Express, **17**, 19006–19014 (2009).
DOI: 10.1364/OE.17.019006

[15] Pastorelli G., Trafela T., Taday P. F., Portieri A., Lowe D., Fukunaga K., Strlič M.: Characterisation of historic plastics using terahertz time-domain spectroscopy and pulsed imaging. Analytical and Bioanalytical Chemistry, **403**, 1405–1414 (2012).
DOI: 10.1007/s00216-012-5931-9

[16] Rutz F., Koch M., Khare S., Moneke M., Richter H., Ewert U.: Terahertz quality control of polymeric products. International Journal of Infrared and Millimeter Waves, **27**, 547–556 (2007).
DOI: 10.1007/s10762-006-9106-7

[17] Macutkevic J., Seliuta D., Valusis G., Adomavicius R., Kuzhir P., Paddubskaya A., Shuba M., Maksimenko S., Coderoni L., Micciulla F., Sacco I., Bellucci S.: Terahertz time domain spectroscopy of epoxy resin composite with various carbon inclusions. Chemical Physics, **404**, 129–135 (2012).
DOI: 10.1016/j.chemphys.2012.02.002

[18] Jördens C., Wietzke S., Scheller M., Koch M.: Investigation of the water absorption in polyamide and wood plastic composite by terahertz time-domain spectroscopy. Polymer Testing, **29**, 209–215 (2010).
DOI: 10.1016/j.polymertesting.2009.11.003

[19] Nagai N., Kumazawa R., Fukasawa R.: Direct evidence of inter-molecular vibrations by THz spectroscopy. Chemical Physics Letters, **413**, 495–500 (2005).
DOI: 10.1016/j.cplett.2005.08.023

[20] Federici J. F.: Review of moisture and liquid detection and mapping using Terahertz imaging. Journal of Infrared, Millimeter, and Terahertz Waves, **33**, 97–126 (2012).
DOI: 10.1007/s10762-011-9865-7

[21] Inagaki T., Ahmed B., Hartley I. D., Tsuchikawa S., Reid M.: Simultaneous prediction of density and moisture content of wood by terahertz time domain spectroscopy. Journal of Infrared, Millimeter, and Terahertz Waves, **35**, 949–961 (2014).
DOI: 10.1007/s10762-014-0095-7

[22] Nagai M., Yada H., Arikawa T., Tanaka K.: Terahertz time-domain attenuated total reflection spectroscopy in water and biological solution. International Journal of Infrared and Millimeter Waves, **27**, 505–515 (2006).
DOI: 10.1007/s10762-006-9098-3

[23] Yada H., Nagai M., Tanaka K.: Origin of the fast relaxation component of water and heavy water revealed by terahertz time-domain attenuated total reflection spectroscopy. Chemical Physics Letters, **464**, 166–170 (2008).
DOI: 10.1016/j.cplett.2008.09.015

[24] Rønne C., Åstrand P-O., Keiding S. R.: THz Spectroscopy of liquid H_2O and D_2O. Physical Review Letters, **82**, 2888–2891 (1999).
DOI: 10.1103/PhysRevLett.82.2888

[24] Vinh N. Q., Sherwin M. S., Allen S. J., George D. K., Rahmani A. J., Plaxco K. W.: High-precision gigahertz-to-terahertz spectroscopy of aqueous salt solutions as a probe of the femtosecond-to-picosecond dynamics of liquid water. The Journal of Chemical Physics, **142**, 164502/1–164502/7 (2015).
DOI: 10.1063/1.4918708

[26] Koeberg M., Wu C-C., Kim D., Bonn M.: THz dielectric relaxation of ionic liquid:water mixtures. Chemical Physics Letters, **439**, 60–64 (2007).
DOI: 10.1016/j.cplett.2007.03.075

[27] Hochrein T.: Markets, availability, notice, and technical performance of Terahertz systems: Historic development, present, and trends. Journal of Infrared, Millimeter, and Terahertz Waves, **36**, 235–254 (2015).
DOI: 10.1007/s10762-014-0124-6

[28] Hangyo M., Nagashima T., Nashima S.: Spectroscopy by pulsed Terahertz radiation. Measurement Science and Technology, **13**, 1727–1738 (2002).
DOI: 10.1088/0957-0233/13/11/309

[29] Watanabe M., Kuroda S., Yamawaki H., Shiwa M.: Terahertz dielectric properties of plasma-sprayed thermal-barrier coatings. Surface and Coatings Technology, **205**, 4620–4626 (2011).
DOI: 10.1016/j.surfcoat.2011.03.144

[30] Kondo T., Sawatari C.: A Fourier transform infra-red spectroscopic analysis of the character of hydrogen bonds in amorphous cellulose. Polymer, **37**, 393–399 (1996).
DOI: 10.1016/0032-3861(96)82908-9

[31] Ping Z. H., Nguyen Q. T., Chen S. M., Zhou J. Q., Ding Y. D.: States of water in different hydrophilic polymers – DSC and FTIR studies. Polymer, **42**, 8461–8467 (2001).
DOI: 10.1016/S0032-3861(01)00358-5

[32] Hatakeyema T., Yamauchi A., Hatakeyema H.: Studies on bound water in poly(vinyl alcohol). Hydrogel by DSC and FT-NMR. European Polymer Journal, **20**, 61–64 (1984).
DOI: 10.1016/0014-3057(84)90223-4

[33] Kusano M., Aoki S., Kubouchi M.: Evaluation of acid and alkali aqueous solution penetration in polymeric materials by Terahertz time-domain spectroscopy. in 'The 11th European Conference on Non-Destructive Testing 2014. Prague, Czech Republic' p.9 (2014).

[34] Rungsawang R., Ueno Y., Ajito K.: Detecting a sodium chloride ion pair in ice using terahertz time-domain spectroscopy. Analytical Sciences, **7**, 917–920 (2007).
DOI: 10.2116/analsci.23.917

eXPRESS Polymer Letters Vol.10, No.11 (2016) 950–963
Available online at www.expresspolymlett.com
DOI: 10.3144/expresspolymlett.2016.88

Composite coating with synergistic effect of biomimetic epoxy thermoset morphology and incorporated superhydrophobic silica for corrosion protection

W. F. Ji[1], *C. W. Li*[1], *W. J. Huang*[1], *H. K. Yu*[1], *R. D. Chen*[2], *Y. H. Yu*[3], *J. M. Yeh*[1*], *W. C. Tang*[4], *Y. C. Su*[4]

[1]Department of Chemistry, Center for Nanotechnology and Center for Biomedical Technology at Chung-Yuan Christian University (CYCU), 32023 Chung Li, Taiwan, Republic of China
[2]Master Program in Nanotechnology and Center for Nanotechnology at CYCU, 32023 Chung Li, Taiwan, Republic of China
[3]Department of Chemistry, Fu Jen Catholic University, Hsinchung Dist., 24205 New Taipei City, Taiwan, Republic of China
[4]Division of Applied Chemistry, Material and Chemical Research Laboratories, Industrial Technology Research Institute, 30011 Hsinchu, Taiwan, Republic of China

Received 18 April 2016; accepted in revised form 27 June 2016

Abstract. In this work, potential anticorrosive coating resulted from the composite with synergistic effect of biomimetic epoxy thermoset (BET) morphology and incorporated superhydrophobic silica microspheres was presented. First of all, superhydrophobic methyl-modified silica (MS) microspheres were synthesized by performing the conventional base-catalyzed sol-gel process of MTMS and APTMS. The as-prepared MS microspheres were identified as having an average particle size of ~1 μm in diameter. The as-prepared MS microspheres were characterized by Fourier transform infrared spectrometry (FTIR), ^{29}Si and ^{13}C solid-state nuclear magnetic resonance (NMR) spectroscopy. Morphological properties of MS microspheres and BET-silica composite coating were studied by scanning electron microscopy (SEM). Subsequently, 3 wt% of MS microspheres were incorporated into an epoxy slurry of DGEBA/T-403 in dimetyl acetamide (DMAc), followed by performing the programmed heating through nanocasting technique with PDMS as soft template materials for pattern transfer by using leaf of *Xanthosoma Sagittifolium* as natural template, leading to the formation of artificial biomimetic composite coating. The appearance/dispersion capability of silica microspheres in BET coating was confirmed by the energy dispersive X-ray spectroscopy (EDX) and Si-mapping. The roughness level of BET and BEC-3% were detected by AFM. The BET-silica composite was found to exhibit a contact angle (CA) of ~153°, revealing the synergistic effect of biomimetic epoxy morphology and incorporated superhydrophobic MS microspheres, which is found to be more hydrophobic than that of neat epoxy thermoset (CA = 81°). Corrosion protection of as-prepared coatings was demonstrated by performing a series of electrochemical measurements (Tafel, Nyquists and Bode plots) upon CRS electrodes in saline condition. It should be noted that the BET coatings upon CRS electrode revealed an effectively enhanced corrosion protection as compared to that coatings without biomimetic morphology. Moreover, the BET coating with superhydrophobic MS microspheres upon CRS electrode was found to exhibit better corrosion protection as compared to a counterpart coating without MS microspheres.

Keywords: *polymer composites, biomimetic, methyl-modified silica microsphere, epoxy resin, corrosion protection*

1. Introduction

Corrosion is a significant research area for finishing of metallic industry. Therefore, protective organic/polymeric coatings are typically utilized as a primer to protect metal surface from corrosion [1–3]. In the past decades, different classic polymers, such as

*Corresponding author, e-mail: juiming@cycu.edu.tw

epoxy resin, [4, 5] polyurethane [6, 7] and polyimide [8, 9] have been used by the environmentally sheltered coatings to enhance the anticorrosive effect upon various metallic substrates. In order to facilitate the corrosion protection of various metallic substrates, versatile alternative practical coatings are being continuously developed such as conducting/electroactive polymers, [10, 11] conventional polymers containing filler with large aspect ratio [12, 13] and polymer coatings with superhydrophobic surface [14, 15].

Recently, great attention is paid to the potential of applications on bio-mimetic materials with super-hydrophobic surfaces structure due to their diverse potential and unprecedented hierarchical surfaces [16–26]. Moreover, the studies of anticorrosive polymer coatings with roughly superhydrophobic or biomimetic surface attracted intensive research interests [27–34]. For example, Liu *et al*. [35] found that the surface of copper block was found to display superhydrophobicity after treatment of n-tetradecanoic acid solution for a period of time, leading to the as-formed surface with better anticorrosion performance. Moreover, Wang *et al*. [36] demonstrated that the steel surface treated with specific surface modification to give coating with micro-/nano- hierarchical superhydrophobic structures upon steel, leading to an excellent corrosion protection property. Furthermore, Yang *et al*. [37] reported that the eletroactive polymer with the biomimetic topography also showing superhydrophobicity, which exhibited superior anticorrosive ability based on a series of electrochemical investigations in 3.5 wt% NaCl solution. Enhancement of corrosion protection of above-mentioned superhydrophobic coatings may be attributed to the trapped gas within the valleys between the hills of the superhydrophobic surface [35].

On the other hand, the research activity in terms of polymer coating incorporated with hydrophobic inorganic particles has also evoked great research interests [38–43]. For example, Sun *et al*. [44] had explored that the superhydrophobic surfaces covered with cauliflower-like cluster binary micro-nano coatings and promoted excellent corrosion resistance property in the 3.5 wt% NaCl solution. Moreover, Weng *et al*. [45] demonstrated that the as-prepared organic-inorganic superhydrophobic composite coating was found to boost the corrosion resistance property in saline condition (e.g., 3.5 wt% NaCl solution) based on a series of electrochemical corrosion measurements. Chang *et al*. [46] found that the UV-cured biomimetic composites containing thermoplastic PMMA and micro-silica particles was found to give the coating surface with increased roughness, which may effectively increase the superhydrophobicity and therefore facilitate the corrosion resistance of metallic substrates in saline.

In this work, the synergistic effect of biomimetic morphology and incorporated superhydrophobic silica microspheres is used to prepare the BET-silica composite anticorrosion coatings. First of all superhydrophobic methyl-modified silica (MS) microspheres were synthesized by sol-gel reactions and characterized by FTIR, ^{13}C and ^{29}Si NMR spectra. Moreover, nanocasting technique was utilized with PDMS (poly dimethyl siloxane) as pattern-transfer polymer by using natural leaf of *Xanthosoma Sagittifolium* as natural template, leading to the formation of artificial BET-silica composite coatings. Furthermore, 3 wt% of as-prepared superhydrophobic MS microspheres was added into BET to give the BET-silica composite coatings. SEM and contact angle measurements were applied to investigate the morphology and hydrophobicity of coating surface. Finally, anticorrosion performance of the developed BET-silica composite coatings upon CRS electrodes was evaluated by a series of electrochemical measurements (Tafel Nyquists and Bode plots) in 3.5 wt% NaCl aqueous solution.

2. Experiment

2.1. Materials and measurements

In this study, the bisphenol A diglycidyl ether (DGEBA; Aldrich; Japan) and trimethylolpropanetris [poly(propylene glycol), amine terminated] ether (T-403; Aldrich; American) were used as received without further treatment. Trimethoxy (methyl) silane (MTMS; Aldrich, 98.0%; American), (3-aminopropyl) trimethoxysilane (APTMS; Fluka, 98.0%; Switzerland) were used as sol-gel precursor and epoxy coupling agent, respectively. Ethanol (EtOH; Aldrich, 95%; American), ammonium hydroxide solution (NH_4OH; Aldrich, 28.0–30.0%; American), polyvinylpyrrolidone (PVP, M_w = 40,000, polymeric stabilizer, Aldrich), and *N*, *N*-dimethyl acetamide (DMAc; 99.0%, Aldrich; American) were used as received without further purification. The liquid com-

ponents (Sylgard 184) of polydimethylsiloxane (PDMS; American) were supplied by Dow Corning Corporation. All reagents were reagent grade unless otherwise stated.

Fourier-transform infrared (FTIR) spectra were recorded using an FTIR spectrometer (JASCO FT/IR-4200) operating at room temperature. The X-ray photoelectron spectroscopy XPS measurement was performed on Microlab MKII electron spectrometer with a base pressure of 10^{-10} Torr. The Sorvall RC-5C Plus Super-speed Centrifuge was used to separate methyl-modified silica (MS) particles by centrifugal force (7500 rpm). Both ^{13}C and ^{29}Si MAS solid-state NMR experiments were performed on a 400 MHz solid-state NMR spectrometer. ^{13}C MAS NMR spectra were obtained at 100.63 MHz with 7 kHz applying 90° pulses and 2.0 s pulse delays. To enhance carbon sensitivity, cross-polarization (CP) techniques were employed. ^{29}Si MAS NMR spectra were recorded at 79.49 MHz applying 90° pulses, 300 s pulse delays, and 5.0 ms contact time, with samples in 5.0 mm zirconia rotors spinning at 7 kHz. Surface morphologies of the superhydrophobic samples were observed by using SEM (JOEL JSM-7600F). Silica dispersion was detected by EDX (OxFord xmax 80). Contact angles were measured using a First Ten Angstroms FTA 125 at ambient temperature. Water droplets (about 4 μL) were carefully dropped onto the surfaces of samples, and contact angle was determined from the average of five measurements at various positions on the samples surface. Corrosion potential and corrosion current of sample-coated CRS electrodes were electrochemically measured using a VoltaLab 50 potentiostat/galvanostat. Electrochemical impedance spectroscopy (EIS) study was recorded on AutoLab (PGSTAT302N) potentiostat/galvanostat electrochemical analyzer.

2.2. Synthesis of methyl-modified silica (MS) microsphere

The MS microspheres were synthesized via conventional base-catalyzed sol-gel reactions of MTMS in the presence of APTMS molecules. A typical procedure to prepare the MS microspheres was given as follows: the surfactant (PVP, 0.1 g) and NH_4OH (0.1 mL) was dissolved in 40 mL of water and kept at 5 °C. The mixture of 2.04 g MTMS (20 mmole) and 0.136 g APTMS (1 mmole) was added drop-wise to the aqueous solution for about 1 hour at 5 °C. The sol-gel reaction was continued under magnetic stirring for 6 hours at room temperature. Finally, the as-prepared silica microspheres were washed repeatedly with ethanol (EtOH) and separated from the aqueous mixture by centrifugal sedimentation of 7500 rpm to remove the surfactant and re-dispersed in water.

2.3. Preparation of PDMS template

The PDMS pre-polymer was obtained by mixing the elastomer base and a curing agent at a specific weight ratio (10:1, w/w). The PDMS pre-polymer was poured into a mold of 6×6 cm^2 fixed to a piece of fresh, natural *Xanthosoma sagittifolium* leaf (veins of leaf were removed in area of about 6×6 cm^2) and cured in oven programmed at 60 °C for 6 hours. After curing process, the PDMS blocks were detached from the molds, to be used as a negative template for the following nanocasting process of pattern transferring [47].

2.4. Preparation of CRS electrode coated with biomimetic epoxy thermoset (BET)

The 1.024 g of DGEBA was dissolved in 5 g of DMAc under stirring for 1 hour, followed by adding 0.88 g of T-403 functioning as curing agent under stirring for 12 hours. Finally, the solution was cast onto the PDMS template, and then the cold-rolled steel (CRS) electrode was pressed against upon the surface of as-prepared epoxy slurry. Subsequently, the thermal curing process of epoxy thermoset was programmed at 50 °C for 1 hour, 120 °C for 2 hours and 140 °C for 0.5 hour. The CRS electrode coated with BET can be obtained by detaching from PDMS template.

2.5. Preparation of CRS electrode coated with biomimetic epoxy-silica composite (BEC-3 wt%)

The representative procedure for the preparation of CRS electrode coated with biomimetic epoxy-silica composite (BEC) was given as follows: 1.024 g of DGEBA and 0.075 g of the as-prepared MS particles were dissolved or dispersed into 5 g of DMAc under magnetic stirring for 1 hour, followed by introducing 0.5 g of T-403 for 6 hours under stirring. The mixed solution was eventually dropped and cast onto the PDMS template, the CRS electrode was then pressed

against the surface of mixing slurry. Subsequently, the thermal curing process of BEC was programmed at 50 °C for 1 hour, 120 °C for 2 hours and 140 °C for 0.5 hour. The CRS electrodes coated with BEC was then obtained by detaching from the PDMS template.

2.6. Electrochemical corrosion studies

Epoxy thermoset coatings of about 30 μm in thickness were obtained after drying in a fume hood for 24 hours. Edges of the coupons were locked on the artificial electrode for corrosion testing. The coated and uncoated coupons were connected to the working electrode of an electrochemical cell. For the anticorrosion measurement aspect, polarization curves were obtained by using cyclic voltammetry (VoltaLab 50 potentiostat/galvanostat) at an operational temperature of 30 °C. The three-electrode configuration was employed in the circuit, with the sample as the working electrode, the graphite rod as the counter electrode, and the saturated calomel electrode (SCE) as the reference electrode. 3.5 wt% aqueous solution of saline was utilized as the electrolyte. Open circuit potential (OCP) at the equilibrium state of system was used as the corrosion potential (E_{corr} in [V] vs. SCE). For the potentiodynamic polarization experiments, the potential was scanned from -500 to 500 mV at a scanning rate of 50 mV·s^{-1}. Corrosion current (I_{corr} [μA·cm^{-2}]) was determined by superimposing a straight line along the linear portion of the cathodic or anodic curve and extrapolating it through E_{corr} [mV]. All raw data were taken at least three times to ensure the reproducibility and statistical significance.

3. Results and discussion

A representative process of base-catalyzed sol-gel reactions of MTMS and APTMS was used to prepare superhydrophobic MS microspheres. Moreover, the typical procedure for the preparation of biomimetic epoxy incorporated superhydrophobic MS microspheres coatings by replicating fresh *Xanthosoma sagittifolium* leaf through nanocasting technique was used, as shown in Figure 1. It should be noted that a large amount of MTMS in the sol-gel process may lead to as-prepared silica microspheres with a considerable amount of methyl groups attached to the surface, resulting in better superhydrophobicity. On the other hand, a small amount of APTMS used in the sol-gel process indicates that few primary amine groups may adhere to the surface of silica microspheres, implying the formation of chemical bonding between primary amine and the epoxide ring of epoxy pre-polymer.

3.1. Characterization of superhydrophobic methyl-modified silica microspheres

Figure 2 show the representative NMR, FTIR spectroscopy and SEM image of MS microspheres. Solid-state ^{29}Si NMR provided quantitative information about the condensation reaction and solid-state ^{13}C NMR spectroscopy was particularly useful in

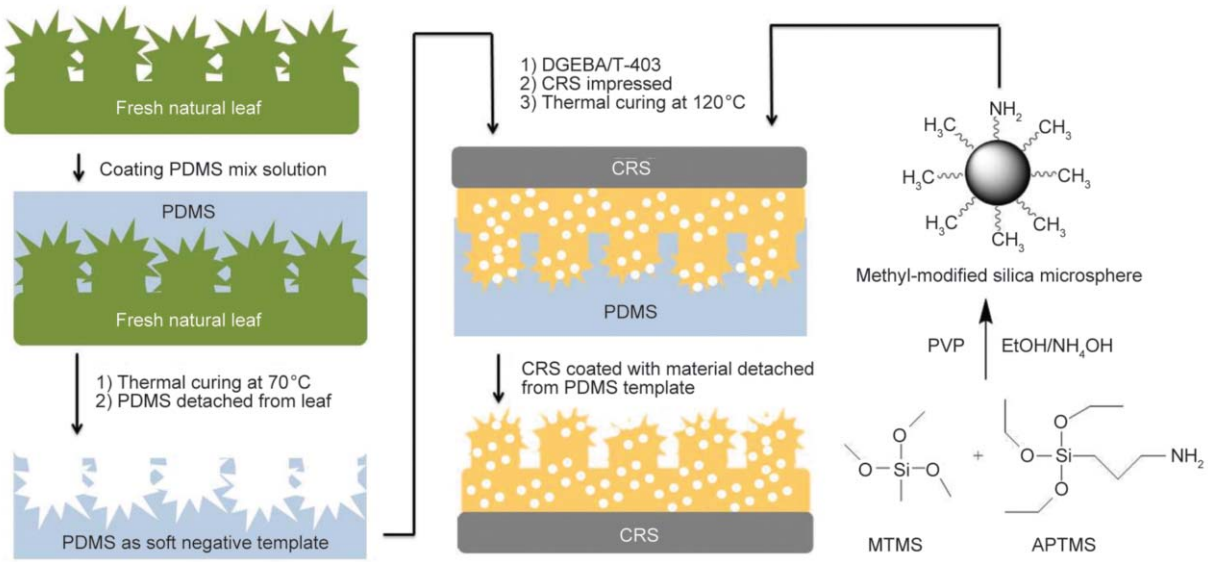

Figure 1. Preparation flow chart of superhydrophobic methyl-silica (MS) microsphere and incorporated superhydrophobic MS microspheres onto the biomimetic epoxy thermoset surface to manufacture the CRS coated with biomimetic epoxy thermoset composite

monitoring the hydrolysis reaction of sol-gel process. Figure 2a shows the ^{29}Si NMR spectrum, two clear resonance peaks derived from T_m (T_m = $RSi(OSi)_m(OH)_{3-m}$, m = 1–3; T_3 at δ = –65.2 ppm and T_2 at δ = –55.7 ppm) were observed [48]. T_1 peaks were too small to be analyzed in the photography. The formation of T_1 and T_0 species was insignificant, suggesting that non-reactive organically modified precursor was present. Figure 2b shows the results of ^{13}C NMR analysis. The sample exhibited three peaks with nearly equal intensity at the position around 11.1, 26.1, and 43.5 ppm. Three peaks could be attributed to three different kinds of Carbon atoms for the APTMS group, confirming the existence of APTMS bonded to silica. Figure 2c displays the FTIR spectrum of MS microspheres. The presence of characteristic bands of MS at wavenumber of 774 and 2979 cm^{-1} were attributed to the stretching vibrations of Si–C and C–H. The MS exhibited well-defined absorptions at ca. 1411 cm^{-1}, which belonged to the characteristic of symmetric deformations in Si–R groups. The presence of Si–O–Si linkages could be assigned to the absorptions at the location of 1136 and 1024 cm^{-1}. Moreover, the band occurring at the location of 1273 cm^{-1} showed a well-defined C–H absorption of Si–CH_3 [49]. Furthermore, the bond at 1531 cm^{-1} was due to N–H bending vibration. Because the mole ratio of MTMS/APTMS in sol-gel reaction was 20, meaning that the Si–CH_3 had a stronger absorption than N–H in MS, as shown in Figure 2c. Moreover, there were much more methyl groups providing the superhydrophobicity of the silica surface. Furthermore, the N–H group could provide the strong chemical bonding with epoxy. The Figure 2d shows the SEM image of the as-prepared MS microspheres at 10 000 magnification, revealing an average particle size of ~1 μm in diameter.

3.2. Investigating the thermal curing of epoxy thermosets by FTIR Spectroscopy and XPS analysis

FTIR was utilized to investigate the curing process of the epoxy thermoset. For example, FTIR spectra of epoxy slurry (before curing), biomimetic epoxy ther-

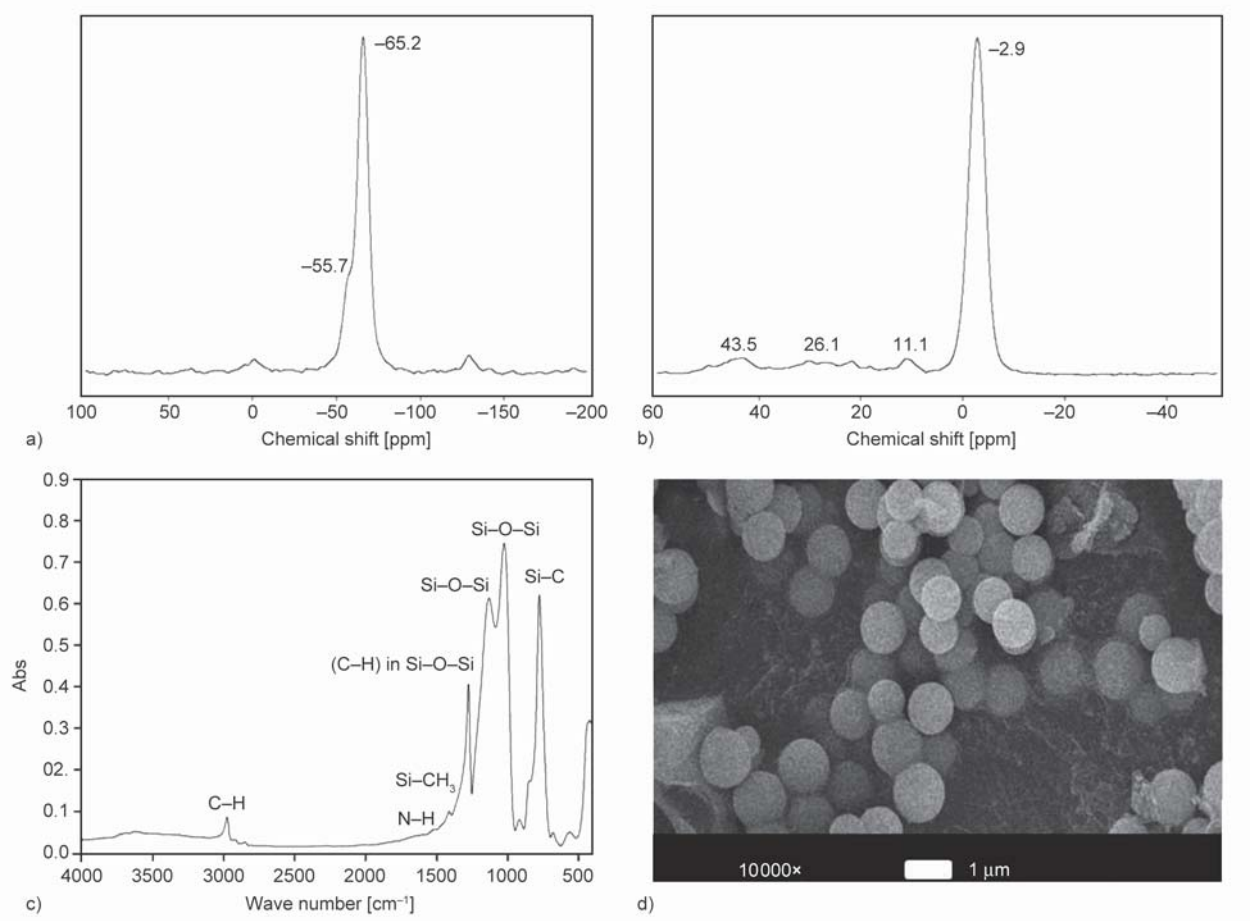

Figure 2. The identification of as-prepared superhydrophobic methyl-silica microsphere of (a) ^{29}Si NMR spectroscopy, (b) ^{13}C NMR spectroscopy, (c) FTIR spectroscopy and (d) image of SEM observation at magnification 10 000×

moset (after curing) and biomimetic epoxy-silica composite are shown in Figure 3. After the programmed heat treatment, the disappearance of characteristic peak of epoxide ring (915 cm^{-1}) and of the primary amine of epoxy thermoset could be identified as a proof of the accomplishment of the ring-opening polymerization, as shown in Figures 3b and 3c. Moreover, XPS was utilized to measure the characteristic peak of BET and BEC, as shown in Figure 4. From the Figure 4b, the Si 2p and Si s were found to be locatet at the positions of 102.9 eV (Si–O group) and 153.5 eV, indicating that the MS microspheres were randomly dispersed onto the BEC surface.

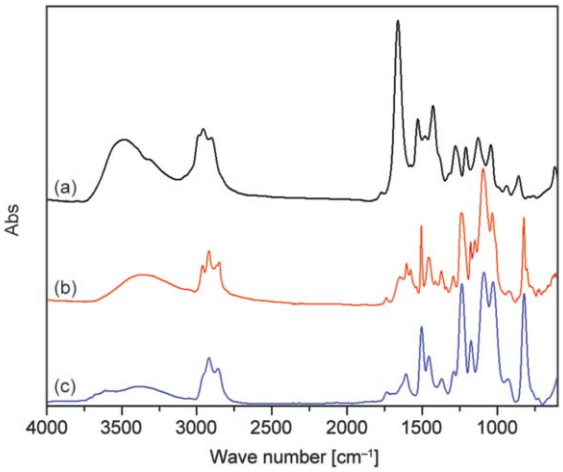

Figure 3. The identification of FTIR spectroscopy for (a) epoxy slurry (before curing), (b) epoxy thermoset (after curing) and (c) composite with biomimetic epoxy thermoset and incorporated superhydrophobic MS microspheres

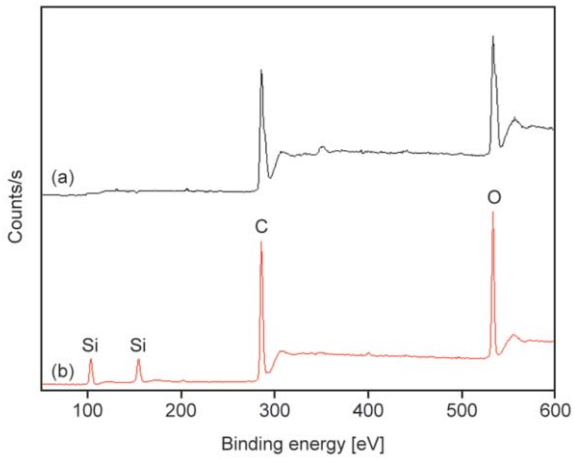

Figure 4. The identification of XPS for (a) biomimetic epoxy thermoset and (b) composite with biomimetic epoxy thermoset and incorporated superhydrophobic MS microspheres

3.3. Microscopic observations and EDX spectroscopy for biomimetic morphology

Macroscopic photograph of natural, fresh leaf of *Xanthosoma sagittifolium* is shown in Figure 5a. Moreover, microscopic SEM overview image at a magnification of 1000× for Figure 5b fresh natural leaf, Figure 5c PDMS soft negative template, Figure 5d biomimetic epoxy thermoset and Figure 5e composite with synergistic effect of biomimetic epoxy thermoset morphology and incorporated superhydrophobic MS microspheres. In Figure 5b, there were much smaller micro papillary hills and nano textures tan those found on the fresh natural *Xanthosoma sagittifolium* leaves. Moreover, the Figure 5c shows the SEM image of the cured PDMS negative template prepared by casting the liquid PDMS directly onto a natural and fresh *Xanthosoma sagittifolium* leaves. The Figure 5d was the SEM image of BET at magnification of 1000×. It should be noted that the morphology of BET is almost the same as that of fresh *Xanthosoma sagittifolium* leaves, implying that the nano-casting technique was successful in transferring the pattern of natural leaves. To well-understand the papilla-like and texture on the surface, Figure 5e shows the SEM image of BET at a magnification of 3000×. From the cross-section Figure 5f at a magnification of 5000×, the height of papilla-like was found to be 6–9 μm. This observation depicted that the template effectively replicated the structure of leaf surface.

For the morphology study of biomimetic epoxy silica containing 3 wt% composite (BEC-3%), the SEM image at a magnification of 1000× of BEC-3% images, Si mapping and EDX of the BEC-3% surface are presented in Figures 6. Morphology of BEC-3% was very similar to that of BET, implying that the majority of incorporated MS microspheres may be embedded into the BET matrix, as shown in Figure 6a. In Figure 6b, the lots of red spots representing the mapping of Si element of BEC was clearly found, indicating that the MS microspheres were randomly dispersed in the BET matrix. Moreover, the EDX showed that the appearance of peaks for Si, O and N element of BEC-3%, implying that the MS microspheres may probably be there inside or on the BET coating. Hydrophobicity enhancement of BEC-3% coating resulted from both the biomimetic morphol-

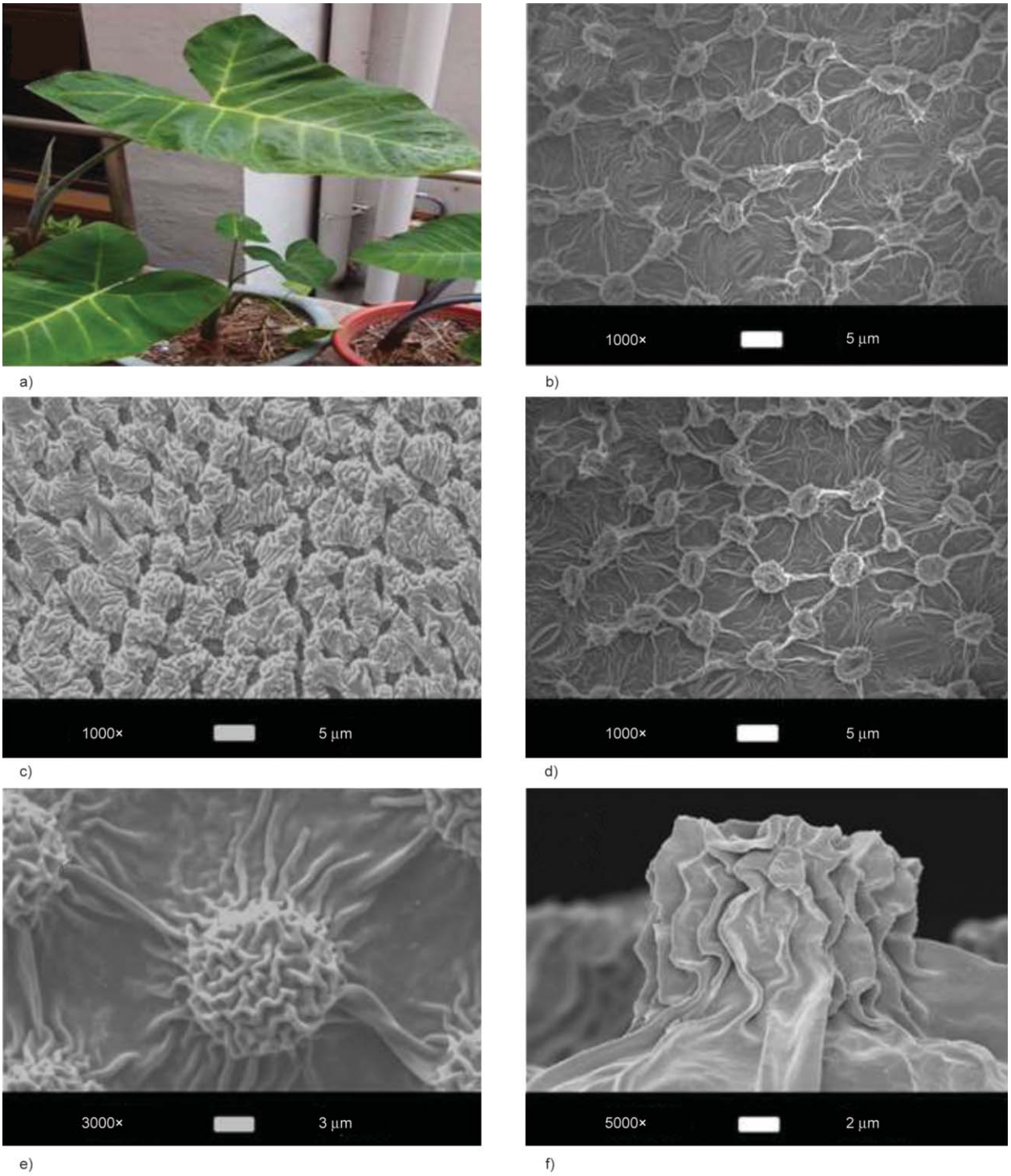

Figure 5. The morphology observations for (a) macroscopoc photograph of the fresh natural *Xanthosoma sagittifolium* leaves. Microscopic SEM overlook image at magnification of 1000× for (b) fresh natural leaf, (c) PDMS soft negative template, (d) biomimetic epoxy thermoset and (e) biomimetic epoxy thermoset at magnification of 3000× (f) cross-section for biomimetic epoxy thermoset at magnification of 5000×

ogy and incorporated MS microspheres, respectively, can be further identified by the contact angle measurement of water droplets and will be discussed in the following section.

3.4. Atomic force microscope

In Figure 7, the three dimensional AFM images of biomimetic epoxy thermoset and biomimetic epoxy silica containing 3 wt% composite on the CRS sub-

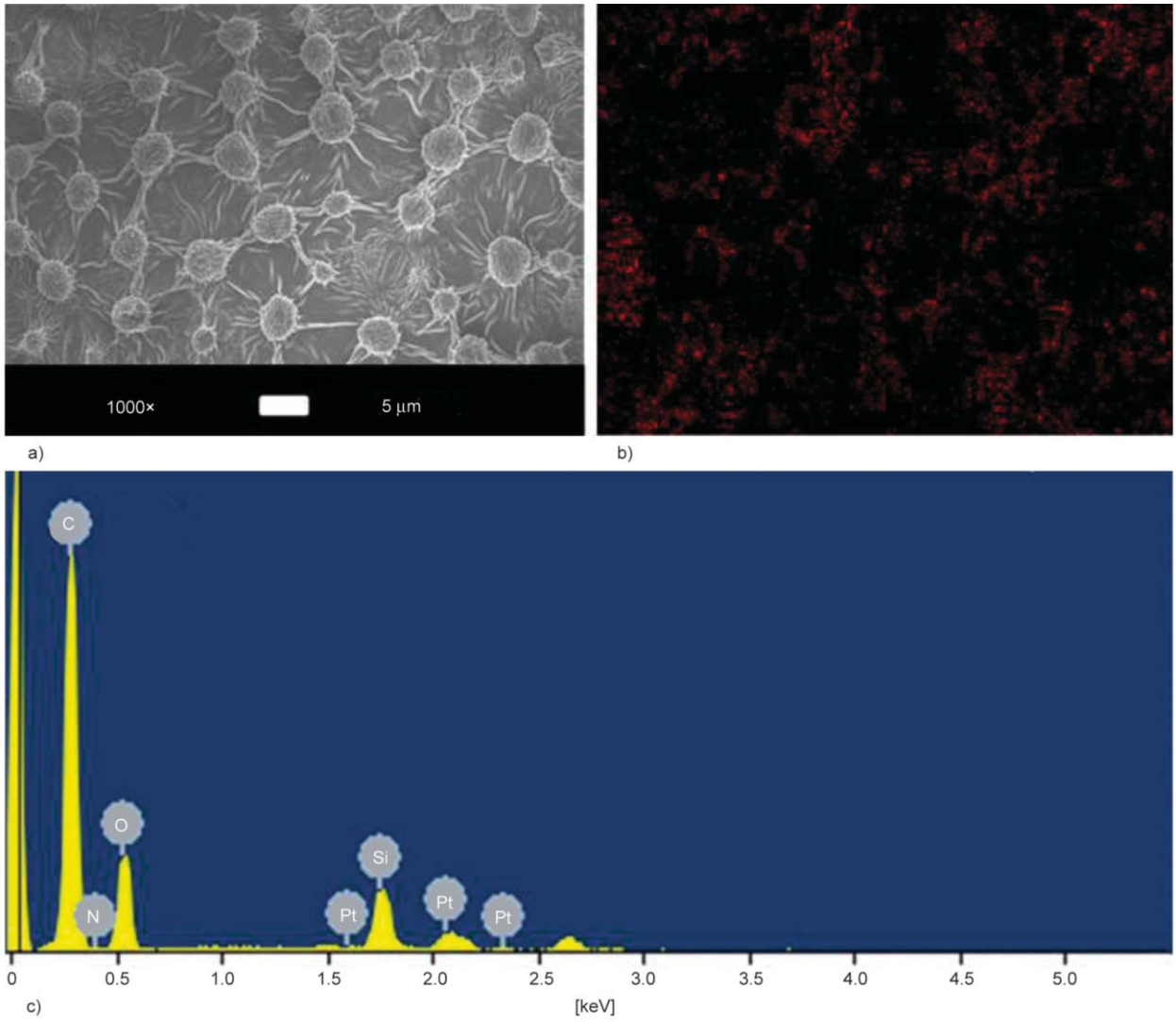

Figure 6. The surface studies of as-prepared biomimetic epoxy-silica composite of (a) SEM microscopic observation at magnification of 1000×, (b) Si mapping and (c) energy-dispersive X-ray spectroscopy

strate vividly showed higher surface roughness. From the AFM image, the surface morphology was coincident with the SEM observation. Moreover, well-understanding the surface roughness on the BET and BEC coatings, AFM was studied and performed in which height images were obtained and average roughness levels of the surfaces were determined [50]. The arithmetic average roughness, Ra levels of the BET and BEC-3% coatings were measured. The BEC-3% coating had the higher RMS roughness of 2.322 µm than BET coating (2.205 µm).

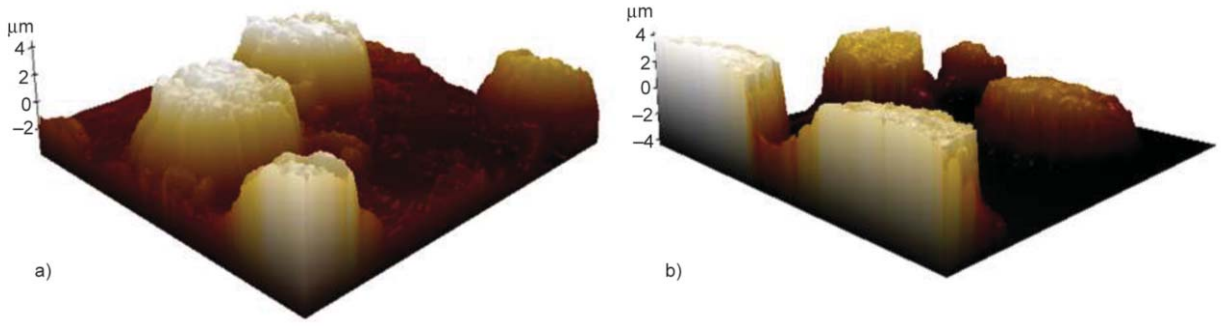

Figure 7. The surface roughness studies of three dimonsional morphology atomic force microscope for (a) CRS electrode coated with biomimetic epoxy thermoset and (b) CRS electrode coated with biomimetic epoxy-silica composite

3.5. Surface hydrophobicity of as-prepared coatings measured by contact angle

In this study, the contact angle (CA) of water droplets upon six different surfaces of coatings were illustrated in Figure 8. The CA for fresh leaf of *Xanthosoma sagittifolium* was 146°, as shown in Figure 8a. The CA for neat epoxy thermoset with smooth surface was 81°, as shown in Figure 8b. Moreover, the CA upon surface of BET was 123°, as shown in Figure 8c. It indicated clearly that the biomimetic morphology may increase the CA of neat epoxy thermoset by up to 42°, reflecting that the biomimetic morphology could effectively promote the hydrophobicity of neat material. Moreover, the CA of neat as-prepared dry fine powder coating of superhydrophobic MS microspheres on glass was found to be 158° because of the methyl group attached onto the surface, as shown in Figure 8d. With incorporated 1 wt% of MS microspheres into BET, the as-obtained BEC-1% with synergistic effect of biomimetic morphology and superhydrophobic silica microspheres was found to exhibit the CA = 137°, as shown in Figure 8e. Moreover, incorporated 3 wt% of MS microspheres into BET, the as-perpared BEC-3% was revealed the CA = 153°, as shown in Figure 8e. It indicated that introducing 3 wt% silica microspheres into BET coating may further promote the hydrophobicity of BET by further increasing the CA of coating by ~30°. In summary, the BEC coating with synergistic effect of biomimetic epoxy thermoset morphology and incorporated MS microspheres revealed an increment in CA of 72° as compared to that of neat epoxy thermoset with smooth surface, implying that this composite could be a potential candidate as corrosion protection coating, as discussed in the following section.

3.6. Potentiodynamic measurements

Polarization curves for the CRS electrode coated with neat epoxy thermoset, biomimetic epoxy thermoset and biomimetic epoxy-silica composite can be obtained by performing all the measurements in electrolyte of 3.5 wt % NaCl aqueous solution.

Corrosion current was obtained by extrapolating Tafel plots, from both the cathodic and anodic polarization curves for the respective corrosion process. Extrapolating the cathodic and anodic polarization curves to the point of intersection provides both the corrosion potential and corrosion current. Tafel plots for (a) bare CRS electrode, (b) CRS electrode coated with smooth epoxy thermoset, (c) CRS electrode coated with biomimetic epoxy thermoset, (d) CRS electrode coated with biomimetic epoxy-silica containing 1 wt% composite and (e) CRS electrode coated with biomimetic epoxy-silica containing 3 wt% com-

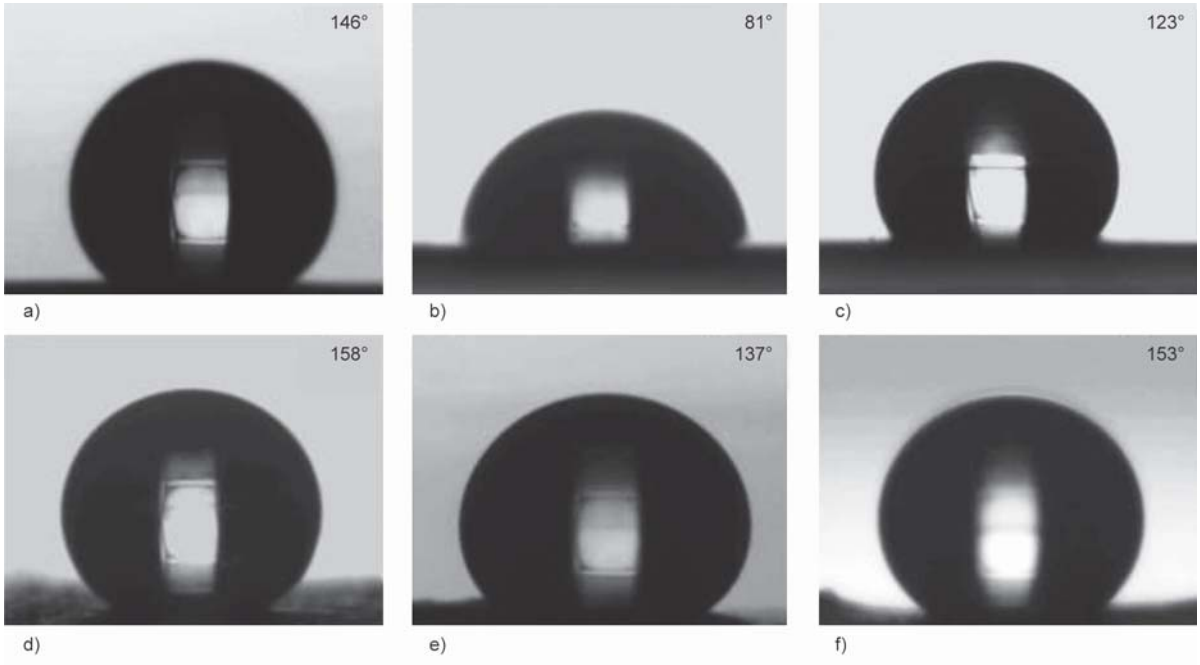

Figure 8. Water contact angle for (a) the fresh natural *Xanthosoma sagittifolium* leaves (b) RS electrode coated with smooth epoxy thermoset, (c) CRS electrode coated with biomimetic epoxy thermoset, (d) methyl-silica microsphere tablet, (e) CRS electrode coated with biomimetic epoxy-silica containing 1% composite and (f) CRS electrode coated with biomimetic epoxy-silica containing 3% composite

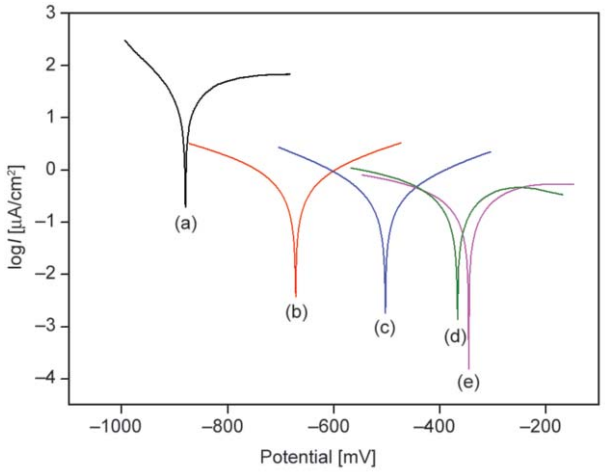

Figure 9. Tafel plots of electrochemical corrosion measurement for (a) bare CRS electrode, (b) CRS electrode coated with smooth epoxy thermoset, (c) CRS electrode coated with biomimetic epoxy thermoset, (d) CRS electrode coated with biomimetic epoxy-silica containing 1% composite and (e) CRS electrode coated with biomimetic epoxy-silica containing 3% composite

posite are shown in Figure 9 and the corresponding data were summarized and listed in Table 1.

Tafel plots of CRS electrode coated with all three samples exhibiting the corrosion potential (E_{corr}) was more positive than the bare CRS electrode. On the other hand, the corrosion current (I_{corr}) of the CRS electrode coated with samples was found to be lower than the bare CRS electrode. First of all, studies for the effect of biomimetic epoxy morphology on corresponding corrosion protection upon CRS electrode, it should be noted that the corrosion potential of CRS electrode coated with BET (E_{corr} = –504.0 mV) was found to be more positive than that of neat epoxy thermoset (E_{corr} = –672.5 mV). Moreover, the corrosion current of CRS electrode coated with BET (I_{corr} = 0.33 μA/cm^2) was found to be lower than that of neat epoxy thermoset (I_{corr} = 0.78 μA/cm^2). Based on the E_{corr} and I_{corr} data obtained from Tafel plots, the BET was found to show better corrosion protection upon CRS electrode than that of epoxy thermoset with smooth surface. The increase of anticorrosion performance of the coating may be attributed to the more hydrophobic surface (CA = 123°) of BET than that of neat epoxy thermoset (CA = 81°). Secondly, the further studies for the effect of incorporated superhydrophobic 1 wt% MS microspheres existing in BET on corrosion protection upon CRS electrode, it should be noted that the corrosion potential of CRS electrode coated with BEC-1% (E_{corr} = –387.2 mV) was found to be more positive than that of BET (E_{corr} = –504.0 mV). Moreover, the corrosion current of CRS electrode coated with BEC-1% (I_{corr} = 0.31 μA/cm^2) was found to be lower than that of BET (I_{corr} = 0.33 μA/cm^2). Afterward, incorporated superhydrophobic 3 wt% MS microspheres existing in BET on corrosion protection upon CRS electrode, it described that the corrosion potential of CRS electrode coated with BEC-3% (E_{corr} = –344.4 mV) was found to be more positive than that of BEC-1% (E_{corr} = –387.2 mV). Moreover, the corrosion current of CRS electrode coated with BEC-3% (I_{corr} = 0.19 μA/cm^2) was found to be lower than that of BET and BEC-1% (I_{corr} = 0.31 μA/cm^2). The BEC-3% was found to show better corrosion protection upon CRS electrode than that of BET and BEC-1% based on the conclusion obtained from the E_{corr} and I_{corr} data. The further increase of anticorrosion performance of coating may be associated with incorporated suitable amount MS microspheres enhance the hydrophobicity of BET and BEC-1% coating.

Enhancement of coatings in anticorrosion upon CRS electrode can be further confirmed by electrochemical impedance spectroscopy (EIS), as discussed in the following section.

Table 1. Contact angle and electrochemical corrosion measurements of bare CRS electrode, CRS coated with smooth epoxy thermoset, BET and BEC

Sample code	Electrochemical corrosion measurements				
	E_{corr} [mV]	I_{corr} [μA/cm^2]	Contact angle [°]	Hysteresis	Coating thickness [μm]
CRS	–852.8	220.5	–	–	–
Epoxy	–672.5	0.78	81±3	32	28±2
BET	–504.0	0.33	123±3	21	29±2
BEC-1%	–387.2	0.31	137±3	17	30±2
BEC-3%	–344.4	0.19	153±2	9	31±2

3.7. Electrochemical impedance spectroscopy measurements

In this study, EIS was utilized to evaluate the corrosion protection for CRS electrode coated with epoxy thermoset, BET and BEC. Generally, corrosion behavior of a metal can be modeled with an equivalent circuit which consists of a double-layered capacitor that is parallel with a charge transfer resistor and connected in series with an electrolyte solution re-

sistor. Impedance (Z) depends on the charge transfer resistance (R_{ct}), the solution resistance (R_s), the capacitance of the electrical double layer, and the frequency of the AC signal (ω).

The high-frequency intercept was equal to the solution resistance and the low-frequency intercept was equal to the sum of the solution and charge transfer resistances [51]. Figure 10 shows the Nyquist plots for (a) bare CRS electrode, (b) CRS electrode coated with smooth epoxy thermoset, (c) CRS electrode coated with biomimetic epoxy thermoset, (d) CRS electrode coated with biomimetic epoxy-silica containing 1% composite and (e) CRS electrode coated with biomimetic epoxy-silica containing 3% composite. The samples were immersed in 3.5 wt% NaCl aqueous electrolyte for 40 min before EIS measurements. The charge transfer resistances of all samples, as determined by subtracting the intersection of the high-frequency end from the low-frequency end of the semi-circle arc with the real axis, were 0.156, 574.8, 3140, 3961 and 5250 kΩ·cm^2, respectively.

EIS Bode plots (impedance vs. frequency) of all samples were shown in Figure 11. Z_{real} was also a measure of corrosion resistance. Low Z_{real} value could be performed from high capacitance to low resistance of the coating. The Bode magnitude plots for (a) bare CRS electrode, (b) CRS electrode coated with smooth epoxy thermoset, (c) CRS electrode coated with biomimetic epoxy thermoset, (d) CRS electrode coated

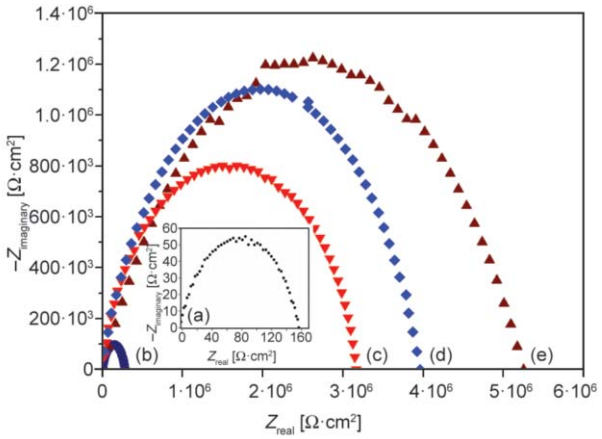

Figure 10. Nyquist plots of electrochemical corrosion measurement for (a) bare CRS electrode, (b) CRS electrode coated with smooth epoxy thermoset, (c) CRS electrode coated with biomimetic epoxy thermoset, (d) CRS electrode coated with biomimetic epoxy-silica containing 1% composite and (e) CRS electrode coated with biomimetic epoxy-silica containing 3% composite

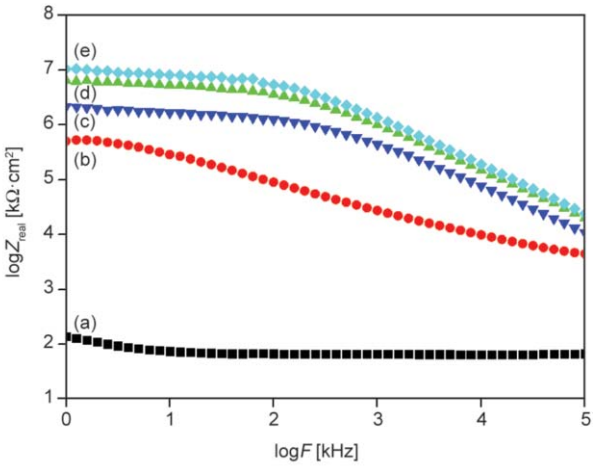

Figure 11. Bode plots of electrochemical corrosion measurement for (a) bare CRS electrode, (b) CRS electrode coated with smooth epoxy thermoset, (c) CRS electrode coated with biomimetic epoxy thermoset, (d) CRS electrode coated with biomimetic epoxy-silica containing 1% composite and (e) CRS electrode coated with biomimetic epoxy-silica containing 3% composite

with biomimetic epoxy-silica containing 1% composite and (e) CRS electrode coated with biomimetic epoxy-silica containing 3% composite showed Z_{real} values of 2.104, 5.724, 6.333, 6.814 and 7.017 kΩ·cm^2, respectively, at low frequency end. It should be noted that the result obtained from the EIS (Nyquist plots and Bode plots) was found to be consistent with the previous conclusion obtained from the Tafel plots. It also demonstrated that the composite with synergistic effect of biomimetic epoxy thermoset morphology and incorporated MS microspheres exhibiting better corrosion protection as compared to that of neat epoxy thermoset with smooth surface.

In this work, the superhydropobic composite coatings with synergistic effect of biomimetic epoxy thermoset morphology and incorporated MS microspheres had the best corrosion protection. The possible mechanism of enhancing corrosive protection prop-

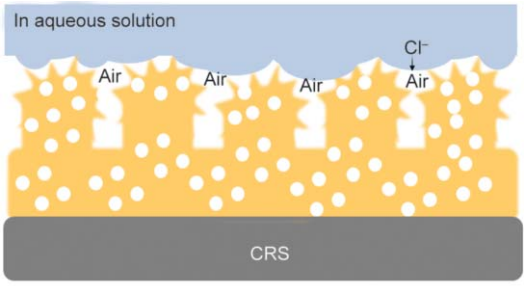

Figure 12. The mechanism of enhancing corrosive protection properties

erties was that superhydrophobic surface composed of hills trapped the gas within the valleys between the hills. Therefore, the free radical, O_2 and H_2O in the corrosion solution could not effectively separate and reach to metal substrates, as shown in Figure 12.

4. Conclusions

In this work, the coating of composite with synergistic effect of biomimetc epoxy thermoset morphology and incorporated superhydrophobic MS microspheres was found to reveal better anticorrosion performance on CRS electrode based on a series of electrochemical measurements (Tafel plots) in saline conditions. First of all, MS microspheres were prepared by performing the sol-gel reaction of MTMS in the presence of APTMS, followed by characterized through FTIR, ^{13}C NMR and ^{29}Si solid-state NMR spectroscopy. The PDMS was employed as negative soft template to duplicate the surface structures of natural leaf of *Xanthosoma sagittifolium*. Moreover, the coatings with surface of biomimetic epoxy thermoset and biomimetic epoxy-silica composite were prepared by pouring the corresponding epoxy and epoxy-silica slurry upon PDMS template, followed by a series of programmed heating treatment. The surface morphology study of coatings with biomimetic morphology was investigated by the SEM observations. The distribution of MS microspheres in BEC-3% coatings was identified by Si mapping and EDX studies, implying that the majority of MS microsphere was embedded in the BET coating. Moreover, the surface hydrophobicity of coatings with/without biomimetic morphology and with MS microspheres was confirmed by the measurements of contact angle (CA) of water droplets. It clearly indicated that the contact angle of BEC-3% (CA = 153°) and BET (CA = 123°) was found to be much higher than that of neat epoxy thermoset (CA = 81°). The CRS electrode coated with BET was found to exhibit better anticorrosion performance than that of neat epoxy thermoset based on a series of electrochemical measurements. This may be attributed to the higher surface hydrophobicity of BET, resulted from the biomimetic morphology, than that of neat epoxy thermoset. Moreover, the CRS electrode coated with BEC-3% was found to reveal better anticorrosion performance than that of BET. This may be related to the incorporated 3 wt% of superhydrophobic MS microspheres into BET to enhance the hydrophobicity of coating. In summary, the composite coating with synergistic effect of biomimetic epoxy thermoset morphology and incorporated superhydrophobic MS microspheres upon CRS electrode revealed significantly increased corrosion protection performance as compared to that of neat epoxy thermoset with smooth surface.

Acknowledgements

The authors acknowledge financial support from the Ministry of Science and Technology, Taiwan, R.O.C. (NSC 102-2632-M-033-001-MY3) and (MOST 104-2113-M-033-001-MY3); the Department of Chemistry at CYCU; and the Center for Nanotechnology and Center for Biomedical Technology at CYCU.

References

[1] Newman R. C., Sieradzki K.: Metallic corrosion. Science, **263**, 1706–1709 (1994).
DOI: 10.1126/science.263.5154.1708

[2] Ramezanzadeh B., Attar M. M., Farzam M.: A study on the anticorrosion performance of the epoxy–polyamide nanocomposites containing ZnO nanoparticles. Progress in Organic Coatings, **72**, 410–422 (2011).
DOI: 10.1016/j.porgcoat.2011.05.014

[3] Arefinia R., Shojaei A., Shariatpanahi H., Neshati J.: Anticorrosion properties of smart coating based on polyaniline nanoparticles/epoxy-ester system. Progress in Organic Coatings, **75**, 502–508 (2012).
DOI: 10.1016/j.porgcoat.2012.06.003

[4] Yeh J-M., Hsieh C-F., Jaw J-H., Kuo T-H., Huang H-Y., Lin C-L., Hsu M-Y.: Organo-soluble polyimde (ODA–BSAA)/montmorillonite nanocomposite materials prepared by solution dispersion technique. Journal of Applied Polymer Science, **95**, 1082–1090 (2005).
DOI: 10.1002/app.21317

[5] Ramezanzadeh B., Attar M. M.: An evaluation of the corrosion resistance and adhesion properties of an epoxy-nanocomposite on a hot-dip galvanized steel (HDG) treated by different kinds of conversion coatings. Surface and Coatings Technology, **205**, 4649–4657 (2011).
DOI: 10.1016/j.surfcoat.2011.04.001

[6] Yan X., Xu G.: Corrosion and mechanical properties of epoxy-polyurethane/bronze composite coatings with low infrared emissivity. Surface and Coatings Technology, **205**, 2307–2312 (2010).
DOI: 10.1016/j.surfcoat.2010.09.015

[7] Gurunathan T., Rao C. R. K., Narayan R., Raju K. V. S. N.: Synthesis, characterization and corrosion evaluation on new cationomeric polyurethane water dispersions and their polyaniline composites. Progress in Organic Coatings, **76**, 639–647 (2013).
DOI: 10.1016/j.porgcoat.2012.12.009

[8] Yu Y-H., Yeh J-M., Liou S-J., Chen C-L., Liaw D-J., Lu H-Y.: Preparation and properties of polyimide–clay nanocomposite materials for anticorrosion application. Journal of Applied Polymer Science, **92**, 3573–3582 (2004).
DOI: 10.1002/app.20400

[9] Huttunen-Saarivirta E., Yudin V. E., Myagkova L. A., Svetlichnyi V. M.: Corrosion protection of galvanized steel by polyimide coatings: EIS and SEM investigations. Progress in Organic Coatings, **72**, 269–278 (2011).
DOI: 10.1016/j.porgcoat.2011.04.015

[10] Yeh J-M., Liou S-J., Lai C-Y., Wu P-C., Tsai T-Y.: Enhancement of corrosion protection effect in polyaniline *via* the formation of polyaniline–clay nanocomposite materials. Chemistry of Materials, **13**, 1131–1136 (2001).
DOI: 10.1021/cm000938r

[11] Fang J., Xu K., Zhu L., Zhou Z., Tang H.: A study on mechanism of corrosion protection of polyaniline coating and its failure. Corrosion Science, **49**, 4232–4242 (2007).
DOI: 10.1016/j.corsci.2007.05.017

[12] Hung W-I., Chang K-C., Chang Y-H., Yeh J-M.: Advanced anticorrosive coatings prepared from polymer-clay nanocomposite materials. in 'Advances in nanocomposites – Synthesis, characterization and industrial applications' (ed.: Reddy B.) InTech, Rijeka, 561–582 (2011).
DOI: 10.5772/15355

[13] Chang K-C., Hsu M-H., Lu H-I., Lai M-C., Liu P-J., Hsu C-H., Ji W-F., Chuang T-L., Wei Y., Yeh J-M., Liu W-R.: Room-temperature cured hydrophobic epoxy/graphene composites as corrosion inhibitor for cold-rolled steel. Carbon, **66**, 144–153 (2014).
DOI: 10.1016/j.carbon.2013.08.052

[14] Ou J., Hu W., Xue M., Wang F., Li W.: Superhydrophobic surfaces on light alloy substrates fabricated by a versatile process and their corrosion protection. ACS Applied Materials and Interfaces, **5**, 3101–3107 (2013).
DOI: 10.1021/am4000134

[15] Momen G., Farzaneh M.: Facile approach in the development of icephobic hierarchically textured coatings as corrosion barrier. Applied Surface Science, **299**, 41–46 (2014).
DOI: 10.1016/j.apsusc.2014.01.179

[16] Yao H-B., Tan Z-H., Fang H-Y., Yu S-H.: Artificial nacre-like bionanocomposite films from the self-assembly of chitosan–montmorillonite hybrid building blocks. Angewandte Chemie International Edition, **49**, 10127–10131 (2010).
DOI: 10.1002/anie.201004748

[17] Cheng Q., Li M., Jiang L., Tang Z.: Bioinspired layered composites based on flattened double-walled carbon nanotubes. Advanced Materials, **24**, 1838–1843 (2012).
DOI: 10.1002/adma.201200179

[18] Wang J., Lin L., Cheng Q., Jiang L.: A strong bio-inspired layered PNIPAM–clay nanocomposite hydrogel. Angewandte Chemie International Edition, **51**, 4676–4680 (2012).
DOI: 10.1002/anie.201200267

[19] Cheng Q., Wu M., Li M., Jiang L., Tang Z.: Ultratough artificial nacre based on conjugated cross-linked graphene oxide. Angewandte Chemie International Edition, **52**, 3750–3755 (2013).
DOI: 10.1002/anie.201210166

[20] Cheng Q., Jiang L., Tang Z.: Bioinspired layered materials with superior mechanical performance. Accounts of Chemical Research, **47**, 1256–1266 (2014).
DOI: 10.1021/ar400279t

[21] Cui W., Li M., Liu J., Wang B., Zhang C., Jiang L., Cheng Q.: A strong integrated strength and toughness artificial nacre based on dopamine cross-linked graphene oxide. ACS Nano, **8**, 9511–9517 (2014).
DOI: 10.1021/nn503755c

[22] Wang J., Cheng Q., Lin L., Jiang L.: Synergistic toughening of bioinspired poly(vinyl alcohol)–clay–nanofibrillar cellulose artificial nacre. ACS Nano, **8**, 2739–2745 (2014).
DOI: 10.1021/nn406428n

[23] Yao H-B., Ge J., Mao L-B., Yan Y-X., Yu S-H.: 25th anniversary article: Artificial carbonate nanocrystals and layered structural nanocomposites inspired by nacre: Synthesis, fabrication and applications. Advanced Materials, **26**, 163–188 (2014).
DOI: 10.1002/adma.201303470

[24] Cheng Q., Duan J., Zhang Q., Jiang L.: Learning from nature: Constructing integrated graphene-based artificial nacre. ACS Nano, **9**, 2231–2234 (2015).
DOI: 10.1021/acsnano.5b01126

[25] Gong S., Cui W., Zhang Q., Cao A., Jiang L., Cheng Q.: Integrated ternary bioinspired nanocomposites *via* synergistic toughening of reduced graphene oxide and double-walled carbon nanotubes. ACS Nano, **9**, 11568–11573 (2015).
DOI: 10.1021/acsnano.5b05252

[26] Zhang Y., Gong S., Zhang Q., Ming P., Wan S., Peng J., Jiang L., Cheng Q.: Graphene-based artificial nacre nanocomposites. Chemical Society Reviews, **45**, 2378–2395 (2016).
DOI: 10.1039/C5CS00258C

[27] Xu Q. F., Wang J. N.: A superhydrophobic coating on aluminium foil with an anti-corrosive property. New Journal of Chemistry, **33**, 734–738 (2009).
DOI: 10.1039/B817130K

[28] Wang P., Zhang D., Qiu R., Hou B.: Super-hydrophobic film prepared on zinc as corrosion barrier. Corrosion Science, **53**, 2080–2086 (2011).
DOI: 10.1016/j.corsci.2011.02.025

[29] Yuan S., Pehkonen S. O., Liang B., Ting Y. P., Neoh K. G., Kang E. T.: Superhydrophobic fluoropolymer-modified copper surface via surface graft polymerisation for corrosion protection. Corrosion Science, **53**, 2738–2747 (2011).
DOI: 10.1016/j.corsci.2011.05.008

[30] de Leon A. C. C., Pernites R. B., Advincula R. C.: Superhydrophobic colloidally textured polythiophene film as superior anticorrosion coating. ACS Applied Materials and Interfaces, **4**, 3169–3176 (2012).
DOI: 10.1021/am300513e

[31] Lo T-Y., Huang Y-C., Hsiao Y-N., Chao C-G., Whang W-T.: Preparation of superhydrophobic polyimide films modified with organosilicasol as effective anticorrosion coatings. Surface and Coatings Technology, **258**, 310–319 (2014).
DOI: 10.1016/j.surfcoat.2014.09.008

[32] Liu Y., Li S., Zhang J., Liu J., Han Z., Ren L.: Corrosion inhibition of biomimetic super-hydrophobic electrodeposition coatings on copper substrate. Corrosion Science, **94**, 190–196 (2015).
DOI: 10.1016/j.corsci.2015.02.009

[33] Zhang X-F., Chen R-J., Hu J-M.: Superhydrophobic surface constructed on electrodeposited silica films by two-step method for corrosion protection of mild steel. Corrosion Science, **104**, 336–343 (2016).
DOI: 10.1016/j.corsci.2015.12.028

[34] Yilgor I., Bilgin S., Isik M., Yilgor E.: Facile preparation of superhydrophobic polymer surfaces. Polymer, **53**, 1180–1188 (2012).
DOI: 10.1016/j.polymer.2012.01.053

[35] Liu T., Chen S., Cheng S., Tian J., Chang X., Yin Y.: Corrosion behavior of super-hydrophobic surface on copper in seawater. Electrochimica Acta, **52**, 8003–8007 (2007).
DOI: 10.1016/j.electacta.2007.06.072

[36] Wang N., Xiong D., Deng Y., Shi Y., Wang K.: Mechanically robust superhydrophobic steel surface with anti-icing, UV-durability, and corrosion resistance properties. ACS Applied Materials and Interfaces, **7**, 6260–6272 (2015).
DOI: 10.1021/acsami.5b00558

[37] Yang T-I., Peng C-W., Lin Y-L., Weng C-J., Edgington G., Mylonakis A., Huang T-C., Hsu C-H., Yeh J-M., Wei Y.: Synergistic effect of electroactivity and hydrophobicity on the anticorrosion property of room-temperature-cured epoxy coatings with multi-scale structures mimicking the surface of *Xanthosoma sagittifolium* leaf. Journal of Materials Chemistry, **22**, 15845–15852 (2012).
DOI: 10.1039/C2JM32365F

[38] Chen H., Zhang X., Zhang P., Zhang Z.: Facile approach in fabricating superhydrophobic SiO_2/polymer nanocomposite coating. Applied Surface Science, **261**, 628–632 (2012).
DOI: 10.1016/j.apsusc.2012.08.071

[39] Kartsonakis I. A., Balaskas A. C., Koumoulos E. P., Charitidis C. A., Kordas G.: Evaluation of corrosion resistance of magnesium alloy ZK10 coated with hybrid organic–inorganic film including containers. Corrosion Science, **65**, 481–493 (2012).
DOI: 10.1016/j.corsci.2012.08.052

[40] Zhou C., Lu X., Xin Z., Liu J., Zhang Y.: Polybenzoxazine/SiO_2 nanocomposite coatings for corrosion protection of mild steel. Corrosion Science, **80**, 269–275 (2014).
DOI: 10.1016/j.corsci.2013.11.042

[41] Qing Y., Yang C., Hu C., Zheng Y., Liu C.: A facile method to prepare superhydrophobic fluorinated polysiloxane/ZnO nanocomposite coatings with corrosion resistance. Applied Surface Science, **326**, 48–54 (2015).
DOI: 10.1016/j.apsusc.2014.11.100

[42] Jie H., Xu Q., Wei L., Min Y.: Etching and heating treatment combined approach for superhydrophobic surface on brass substrates and the consequent corrosion resistance. Corrosion Science, **102**, 251–258 (2016).
DOI: 10.1016/j.corsci.2015.10.013

[43] Zhang D., Qian H., Wang L., Li X.: Comparison of barrier properties for a superhydrophobic epoxy coating under different simulated corrosion environments. Corrosion Science, **103**, 230–241 (2016).
DOI: 10.1016/j.corsci.2015.11.023

[44] Sun M., Luo C., Xu L., Ji H., Ouyang Q., Yu D., Chen Y.: Artificial lotus leaf by nanocasting. Langmuir, **21**, 8978–8981 (2005).
DOI: 10.1021/la050316q

[45] Weng C-J., Huang J-Y., Huang K. Y., Jhuo Y. S., Tsai M. H., Yeh J. M.: Advanced anticorrosive coatings prepared from electroactive polyimide–TiO_2 hybrid nanocomposite materials. Electrochimica Acta, **55**, 8430–8438 (2010).
DOI: 10.1016/j.electacta.2010.07.063

[46] Chang K. C., Chuang T. L., Ji W. F., Chang C. H., Peng Y. Y., Shih H., Hsu C. L., Yeh J. M., Tang W. C., Su Y. C.: UV-curable nanocasting technique to prepare bioinspired superhydrophobic organic-inorganic composite anticorrosion coatings. Express Polymer Letters, **9**, 143–153 (2015).
DOI: 10.3144/expresspolymlett.2015.15

[47] Cheng Q., Li M., Zheng Y., Su B., Wang S., Jiang L.: Janus interface materials: Superhydrophobic air/solid interface and superoleophobic water/solid interface inspired by a lotus leaf. Soft Matter, **7**, 5948–5951 (2011).
DOI: 10.1039/C1SM05452J

[48] Chong A. S. M., Zhao X. S.: Functionalization of SBA-15 with APTES and characterization of functionalized materials. The Journal of Physical Chemistry B, **107**, 12650–12657 (2003).
DOI: 10.1021/jp035877+

[49] Wang X., Lin K. S. K., Chan J. C. C., Cheng S.: Direct synthesis and catalytic applications of ordered large pore aminopropyl-functionalized SBA-15 mesoporous materials. The Journal of Physical Chemistry B, **109**, 1763–1769 (2005).
DOI: 10.1021/jp045798d

[50] Gadelmawla E. S., Koura M. M., Maksoud T. M. A., Elewa I. M., Soliman H. H.: Roughness parameters. Journal of Materials Processing Technology, **123**, 133–145 (2002).
DOI: 10.1016/S0924-0136(02)00060-2

[51] Park S-M., Yoo J-S.: Peer reviewed: Electrochemical impedance spectroscopy for better electrochemical measurements. Analytical Chemistry, **75**, 455A–461A (2003).
DOI: 10.1021/ac0313973